A Multi-Wavelength Study of Galaxy Cluster Cores

by

Victoria Helena Hamilton-Morris

Astrophysics and Space Research Group

School of Physics and Astronomy

The University of Birmingham

October 2011

Abstract

The study of Dark Matter, X-ray emitting intra cluster gas and the galaxies in Galaxy Clusters provides insight into the interplay between baryonic and Dark Matter. By relating observables to mass, scaling relations can be used to constrain cosmological parameters, and probe the global properties of the cluster population. Comparison of multi-wavelength observations can reduce systematics associated with different mass probes, and allow us to decipher the recent structural evolution of the clusters. With future, large scale surveys of clusters providing catalogues of thousands of clusters, new methods must be developed to efficiently analyse and catagorise the observed cluster population.

In this thesis I describe a statistically robust, standardised multi-wavelength study on 21 X-ray luminous cluster cores at $0.15 < z < 0.3$, spanning X-ray to near Infra-Red (IR) wavelengths. As part of this study I present a detailed structural analysis of 21 clusters using weak lens (WL) analysis of SNAPSHOT data from the Hubble Space Telescope Advanced Camera for Surveys. Substructures found in the "non-parametric" lensing mass maps are compared with K-band luminosity maps, and Chandra X-ray flux maps. Using the near-IR data as a prior on both the location and mass of substructures within the clusters, I then use a Bayesian method to fit multiple parameterised Dark Matter (DM) haloes to the shear data. I then use mass-observable scaling relations to explore segregation in cluster properties between cool core and non cool core clusters, relate the DM model properties to X-ray indicators of dynamical state, and discuss in-depth two clusters that exemplify the ability of my algorithm to efficiently identify 'bullet' type clusters and constrain complex DM structure of group and cluster scale objects.

This work shows that the spatial distribution of the gas, galaxies and DM is better constrained than the weak lens masses, which suffer a low mass bias due to systematics in the shear smoothing algorithm. However, by assuming a constant bias for a constant smoothing scale, I find that the K-band luminosity scales with mass similarly to the X-ray luminosity, suggesting a link between X-ray luminosity and red light in cluster cores. I find that the mass substructure fraction distribution suggests that the cluster population selected by X-ray luminosity is consistent with that with SL features. An in-depth study suggests that this algorithm may be capable of detecting clusters with strongly disturbed mass distributions worthy of further study (A 3364). For instance, in my analysis I have detected the weak lens signal of a galaxy group outside the HST:ACS field of view (A 3192). I conclude that the analysis algorithm in this thesis could be useful in the large batch analysis of cluster observations from future, large scale surveys, such as PANSTARRS and DES, and could also be applicable to efficiently constructing cluster samples for future observations from archival data.

To my beloved husband Robert

Acknowledgements

I would like to gratefully thank my supervisor, Graham Smith, for his support and guidance over the last 5 years. I also thank fellow PhD students Tim James and Paul May for keeping me sane in the office. I am grateful to the support and help provided by the Extragalactic Research group at Birmingham, by members current and past, in particular from Prof. Trevor Ponman and Dr. Somak Raychaudhury. I would also like to specially thank Tom Targett and Alastair Sanderson for their help with the IR and X-ray data. I am also grateful to the members of LoCuSS who I have collaborated and worked with, and give a very grateful thanks to Eiichi Egami and Yuying Zhang for their help and advice. In addition I thank Sarah Bridle, Phil Marshall and Jean-Paul Kneib for assistance with IM2SHAPE, LENSENT2 and LENSTOOL respectively. Not least I thank David Stops, Norma Simpson and so many members of the administrative staff in the School, without whom none of this could have been achieved.

I finally thank my husband for his neverending support and encouragement, and my parents and grandparents for their faith in me.

Statement of Originality

Chapter 1 and Chapter 2 are based on existing reviews, text books and the literature, and do not contain original research.

The reduction of the infrared data and production of initial object catalogues in Chapter 3 was performed by Tom Targett, whereas the reduction and analysis of the X-ray data was performed by Alastair Sanderson. Both are referenced in the text. The correction of the point spread function benefitted from previous programming work by Dermisha Patel and Graham Smith.

Chapter 6.1 has benefit from discussions with local X-ray astronomers and external feedback from Arif Babul and Yuying Zhang. Chapter 6.2 is a letter being prepared for publication, and the current list of co-authors has been given at the start of the chapter.

I promise that the reduction of the HST:ACS SNAPSHOTS and weak lens analysis, and derivation of results on the internal structures of cluster cores, is my own work, under the supervision of Dr Graham Smith, and aided by colleagues in LoCuSS and the School of Physics and Astronomy Extragalactic Research Group. Any non original work is fully referenced within the text. This work has not been previously submitted for a degree.

Contents

List of Figures

List of Tables

Chapter 1

Introduction

The vast majority of matter in our Universe is not contained in stars, galaxies or intergalactic gas clouds; it does not emit light, and can only be detected through its gravitational influence on the space around it. For this reason it is called dark matter (DM). In 1933, Zwicky applied the Virial theorem to the Coma Cluster, and found a discrepancy between the mass predicted by galaxy dynamics compared to that predicted by the light. He concluded that there must be a hidden mass component to make up the shortfall (Zwicky, 1933, 1937b). Later studies on the rotation curves of galaxies (Rubin & Ford, 1970; Rubin et al., 1980), showed that the speed of the stars on the edge of galaxies did not drop off as expected given the galaxy mass predicted from the luminosity distribution, providing more evidence for the existence of an invisible mass component. DM is now understood to comprise 80% of the mass in our Universe, forming the framework upon which galaxies and gas collect into groups and clusters. Understanding the distribution of DM and its relationship with the distribution of baryonic matter is vital in understanding the evolution of large scale structure.

The use of the gravitational impact to constrain the DM distribution in large structures continues today, principally via a technique called gravitational lensing (GL). A natural result of relativity, GL occurs when the geodesics along which light travels are distorted by the gravitational field of a mass lying along the line of sight. Instead of the original source, the observer sees a distorted and deflected image. Using knowledge of the source, and measurements of the deflection, the mass distribution in the lens can be reconstructed.

The strength of the distortion depends on how large the lens is and where the source lies

Figure 1.1: Strong lensing arc and multiple images around A370. The image is taken from the NASA public image gallery. (Credit: NASA, ESA, and the Hubble SM4 ERO Team and ST-ECF)

in the lens geometry. The Strong Lensing (SL) regime covers the creation of large, spectacular arcs (Fig. 1.1) and multiple images of background sources. Analysis of the shape and position of the arcs and images can probe the distribution of DM within 100kpc, in the cores of galaxy clusters. The Weak Lensing (WL) regime covers slight distortions in the images of background galaxies, where a statistically significant shear signal can only be obtained by averaging over the ellipticities of many images. Careful analysis of large catalogues of background galaxy images allows the mass distribution of a lens to be constrained within radii up to several Mpc, the scale of galaxy clusters.

Galaxy clusters are the largest gravitationally bound structures in the Universe today, and the only mass distributions large enough to produce a weak lensing signal capable of providing detailed constraints on individual cluster DM structure. Their large size means that the interplay between the baryonic and Dark Matter components of the clusters is easier to infer from the distributions and properties of the cluster galaxies, gas and Dark Matter. The cluster mass

function is closely linked to the density perturbations in the early Universe, and can provide constraints on the structure formation and Dark Energy. Accurately probing the matter distribution in galaxy clusters with weak lensing not only provides insight into the nature of the most mysterious and dominant matter component in our Universe, but can also contribute to determining how the Universe evolved after the Big Bang.

In this introduction I will briefly cover the Standard Cosmological Model, the history of the Universe, the impact of Dark Matter (DM) on the formation of structure, and how galaxy clusters represent ideal laboratories to study the nature of DM. For further reading, please see Narayan & Bartelmann (1996); Mellier (1999); Bartelmann & Schneider (2001); Schneider (2006a); Bartelmann (2010); Massey et al. (2010).

1.1 Cosmological Model

The physics of galaxy and cluster formation must be studied and understood within the framework of the evolution of structure in our Universe as a whole. Understanding how galaxies fall into groups, which fall into clusters, and the interplay between baryons and DM in the process, necessarily demands an explanation of why matter clumps together in the first place, and how the filamentary structure in the Universe came into being. This cosmological history is described by the Standard Model.

Observations, such as of the distribution of faint galaxies and the Cosmic Microwave Background, suggest that on large scales, the average properties of the Universe appear the same in every direction . This means the Universe has no preferred direction, and is *isotropic*. If we assume that the Earth is not at any favoured point in the Universe, then this isotropy must be true for an observer at any position in space. This means the Universe is also *homogeneous*. In order to construct a cosmological model, a space time metric is required that is motivated by

these two postulates, and forms a solution for Einstein's field equations,

$$G_{\alpha\beta} = \frac{8\pi G}{c^2} T_{\alpha\beta} + \Lambda g_{\alpha\beta} \tag{1.1}$$

which relate the gravitational tensor $G_{\alpha\beta}$ to the stress-energy tensor $T_{\alpha\beta}$ and the space time metric tensor $g_{\alpha\beta}$. The Λ factor was originally known as the Cosmological Constant, added by Einstein to ensure a static, infinite Universe remained a possible solution. However, the expansion of the Universe was observed in the 1920s by Hubble (Hubble, 1929). By noting a Doppler shift in the spectra of distant galaxies, Hubble realised that the recession velocity of distant galaxies was proportional to the distance to that galaxy. As the space through which the light ray is travelling expands, the wavelength of the light is stretched, resulting in the light appearing redder. The relation is given by Eq. 1.2,

$$\nu = H_0 D \tag{1.2}$$

where H_0 is the value of the Hubble Constant at the present time, and ν and D the recessional velocity and distance to the object. The Hubble Constant varies as a function of the scale factor, $a(t)$, which describes the size of the Universe as a function of time,

$$H(t) = \frac{\dot{a}}{a} \tag{1.3}$$

The shift Hubble observed is called the *redshift*, usually denoted z. It describes the extent to which the observed wavelength differs from the emitted wavelength,

$$z = \frac{\lambda_{obs}}{lambda_{emit}} - 1 \tag{1.4}$$

and as the change in the observed wavelength due to expansion is related to the scale factor, this can be rewritten as $z = \frac{a_{obs}}{a_{emit}} - 1$. The scale factor can be normalised such that $a_{obs} = a(0) = 1$, and we obtain,

$$z = \frac{1}{a} - 1 \; or \; a = (1+z)^{-1} \tag{1.5}$$

So not only must the space time metric abide by isotropy and homogeneity, it must also allow for the expansion of the Universe over time. The basis of such a metric is the Robertson-Walker Metric (Eq. 1.6) (Robertson, 1935; Walker, 1935),

$$ds^2 = c^2 dt^2 + a^2(t) dl^2 \tag{1.6}$$

where dl is defined as the spatial line element. This metric satisfies homogeneity and isotropy regardless of whether the geometry of the Universe is curved or flat. Using w as the comoving radial coordinate and θ, ϕ to denote positions on a unit sphere around the observer, the geometry can be expressed as,

$$ds^2 = c^2dt^2 - a^2(t)[dw^2 + F_K^2(w)(d\theta^2 + sin^2\theta d\phi^2)] \tag{1.7}$$

where ds is the proper time experienced by the observer, dt the time within the coordinate frame. Homogeneity and isotropy in combination with this metric allow for non flat Universes, and F_K is a function of the curvature of space time at $t = 0$, K,

$$ds^2 = c^2dt^2 - a^2(t)[dw^2 + f_K^2(w)(d\theta^2 + sin^2\theta d\phi^2)]F_K(w) = \begin{cases} K^{-\frac{1}{2}}sin(K^{\frac{1}{2}}w) & K > 0 \\ w & K = 0 \\ |K|^{-\frac{1}{2}}sinh(|K|^{\frac{1}{2}}w) & K < 0 \end{cases} \tag{1.8}$$

When K is negative, zero or positive the curvature is called hyperbolic (open), linear (flat) or trigonometric (closed) respectively. When Eq. 1.7 is used as a solution to Eq. 1.1, the field equation simplifies to Eq. 1.9 and Eq. 1.10 (where the stress-energy tensor is described in terms of pressure, $p(t)$, and density, $\rho(t)$) (Friedman, 1922; Friedmann, 1924),

$$\left(\frac{\dot{a}}{a}\right)^2 = \frac{8\pi G}{3}\rho - \frac{Kc^2}{a^2} + \frac{\Lambda}{3} \tag{1.9}$$

$$\frac{\ddot{a}}{a} = -\frac{4\pi G}{3}(\rho + \frac{3p}{c^2}) + \frac{\Lambda}{3} \tag{1.10}$$

Combining Eq. 1.9 and Eq. 1.10 gives the *adiabatic equation*, Eq. 1.11. If the scale factor $a(t)$ and metric ds satisfy the adiabatic equation and Eq. 1.9 then the metric is known as the Robertson-Walker-Friedmann-Lemâitre metric,

$$\frac{d}{dt}[a^3(t)\rho(t)c^2] + p(t)\frac{da^3(t)}{dt} = 0 \tag{1.11}$$

$\rho(t)$ and $p(t)$ describe the total matter density and pressure of the Universe. They are the sum of density and pressure contributions from the three major matter-energy components of the Universe: relativistic matter, non-relativistic matter, and the vacuum energy of the Universe.

Relativistic matter, more commonly called radiation, and including light, travels with thermal velocities close the the speed of light, c. Using the equation of state for radiation, $p_r = \rho c^2/3$, in the adiabatic equation, the radiation density can be related to the scale factor, as in Eq. 1.12,

$$\rho_r \propto a^{-4} \tag{1.12}$$

Matter that travels at velocities much less than the speed of light includes baryons, from which the visible matter in the Universe is made, and Cold Dark Matter (CDM), which will be explained below. As the velocities are much smaller than the speed of light, the pressure term of the adiabatic equation is negligible compared to the term containing the speed of light and the density. This reveals that the mass density is related to the scale factor by,

$$\rho_m \propto a^{-3} \tag{1.13}$$

Quantum physics implies that the vacuum can also have a non zero energy density. Such an energy density would have a constant and negative pressure, $p_\Lambda = \rho_\Lambda c^2$ which would accelerate expansion. After expansion was discovered in the 1920s, Einstein rejected his Cosmological Constant. However, if $\rho = \rho_m + \rho_r + \rho_\Lambda$ and $p = \rho_r c^2/3 - \rho_\Lambda c^2$ are substituted in the Friedmann equations a term like the Cosmological Constant reappears. Today, Λ is used to refer the vacuum energy density, where $\rho_\Lambda = \Lambda/8\pi G$, and the vacuum energy is more commonly known as Dark Energy (DE).

The critical density of the Universe is defined as $\rho_{CR} = 3H_0^2/8\pi G$, and using this obtain dimensionless matter densities, Ω_M, Ω_R and Ω_{lambda}, at the current epoch. The fate of the universe and these total matter densities are quite closely related. The curvature is described by $K \simeq (H_0/c)^2(\Omega_M + \Omega_\lambda - 1)$ (the radiation density at the current epoch is negligable compared to the matter density, and neglected). When $K = 0$, $\Omega_M + \Omega\lambda = 1$, the Universe is flat and expands forever. If K is less than 1, then the Universe is open, and also expands forever. If K is greater than 1, then the Universe is closed and will eventually contract in on itself due to gravity overcoming the expansion.

Observations of the Cosmic Microwave Background Radiation (CMBR) by the Wilkinson Matter Anisotropy Probe (WMAP) (Bennett et al., 2003a,b; Spergel et al., 2003; Hinshaw et al., 2007, 2009; Komatsu et al., 2009) have established that the Universe has a total density of $\Omega_M + \Omega_\lambda = 1$ within a 0.5% error. This means that the curvature of the Universe is zero, and that the Universe is flat: it will expand for all eternity. This conclusion holds when combined with constraints from type 1a Supernova observations (Komatsu et al., 2009), Baryonic Acoustic Oscillations (BAO) (Miller et al., 1999; Eisenstein et al., 2005) and the constraints on H_0 from the Hubble Key Project (Freedman et al., 2001). Using the conclusion of a flat Universe, the WMAP 5 year results suggest that the Universe has a DE density of $\Omega_\lambda = 0.726 \pm 0.015$ and a matter density of $\Omega_M h^2 = 0.1358^{+0.0037}_{-0.0036}$. Baryons make up a mere 5% of our Universe, while DM only 22%. For the flat Universe, the Hubble constant has been constrained to $70.5 \pm 1.3 \mathrm{kms}^{-1}\mathrm{Mpc}$, and the age of the Universe to $13.72 \pm 0.12 \mathrm{Gyr}$. Thus we live in a DE dominated Universe, and the majority of matter is invisible to us.

While this model satisfactorily describes the large scale, averaged properties of the Universe, it fails to describe why there is so much inhomogeneity on small scales. Why, if the Universe is homogeneous and isotropic, do structures like galaxies, clusters and filaments exist?

1.2 Structure Formation

The Universe is believed to have begun with an event called the Big Bang, a period of rapid expansion during which space time and all the components of the Universe were created. Evidence for the Big Bang comes from the fact the Universe is expanding, and the lack of observational evidence for collapse in the past, and from observations of the CMBR. The matter density of the Universe can be written as $\rho = \rho_{m,0} a^{-3} + \rho_{r,0} a^{-4}$. Assuming that at the Big Bang the scale factor reaches zero, then immediately after the Big Bang the Universe was dominated by radiation. When the radiation and mass densities were in equilibrium, the photons that were no longer being absorbed propagated through the Universe as radiation. A prediction of the Big

Bang theory is that this radiation would match the blackbody model, would persist through expansion on cosmological timescales, and should be observable in the modern Universe. The existence of the CMBR was confirmed in the 1960s (Penzias & Wilson, 1965). Observations of the CMBR (Hinshaw et al., 2009; Komatsu et al., 2009) have shown that it is isotropic over large scales, with relative photon temperature fluctuations $< 10^{-5}$. The temperature of the CMBR reflects the temperature of the Universe, and decreases over time and expansion by a factor of $(1+z)$. Therefore, as we travel back in time, the scale factor tends to zero, and the Universe gets hotter.

Although true on large scales, isotropy clearly does not hold on smaller scales, as stars, galaxies, galaxy clusters exist. The anisotropies in the CMBR suggest that modern structures evolved from random Gaussian fluctuations in the primordial Universe. So there must be some process by which current large structures evolved and grew from these initial density fluctuations as the Universe expanded. Linear growth is used to explain the existence of small scale structures, as small scale inhomogeneities had higher local densities than the surrounding space, and expanded slower, becoming comparatively more dense and centres of attraction for the mass around them.

However the evolution of galaxy and cluster scale structures is best described by non linear fluctuation growth models, although these are usually very complex and cannot be solved analytically. A simple example that can be described is spherical collapse. Consider a sphere of matter in the early Universe. The gravitational attraction of the matter within the sphere means it recedes more slowly than the matter outside the sphere. Thus the density contrast between the matter within the sphere and the matter around it increases. At some point this contrast reaches the point where the gravitational attraction at the centre of the sphere is stronger than the pull of the expansion and the matter at the centre starts to collapse. The collapse then spreads to the outer regions of the sphere. Smaller objects collapse and form first near the centre, with larger objects forming later. This is the basis for the model of hierarchical assembly. Anisotropies in

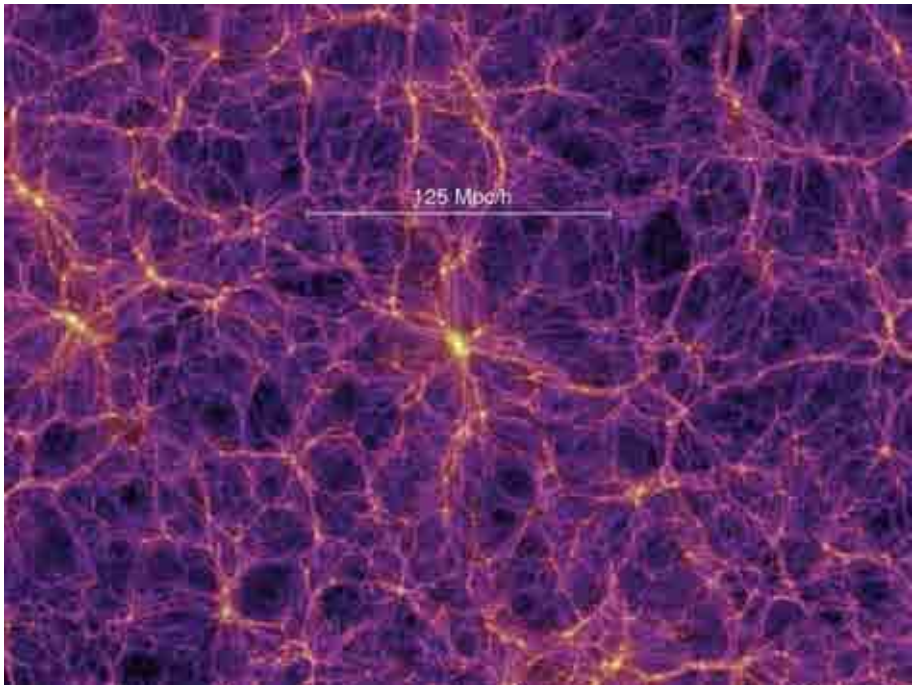

Figure 1.2: CDM filamentary structure from the Millenium Simulations (Springel et al., 2005). Clusters lie in the dense centres, yellow in this image, with smaller structures infalling along the filaments. Image Credit: (http://www.mpa-garching.mpg.de/ mpa/research/current_research/hl2004-8/hl2004-8-en.html)

the distribution of the matter within the sphere will result in the formation of substructures.

Further evidence for DM comes from the formation of structure in our Universe. For a baryon only Universe, structure formation would not have been possible until the Universe was cool enough for the first atoms to form. Assuming linear or non linear growth, the size of the anisotropies in the CMBR are too small to have grown into the galaxy and cluster scale structures evident in the modern Universe within the time from that epoch until now. A further mass component is needed to accelerate structure growth. As DM is expected to only interact gravitationally, it would have started collapsing before the first baryonic atoms formed. Thus DM formed a scaffold for the baryons to collapse onto once atoms were formed (Fig. 1.2).

The nature of the DM can further be constrained by observations of structure in the Universe today. DM can be divided into two possible types: Hot Dark Matter (HDM) with relativistic

velocities, and Cold Dark Matter (CDM) with non relativistic velocities. HDM structure formation models result in the formation of large structures first, as the fast moving HDM particles smooth out smaller structures. Observations show galaxies forming when the Universe was only 10% of its current age (Bouwens et al., 2011), in conflict with this model. CDM is now considered to be the dominant component of DM.

1.2.1 Dark Energy

Dark Energy (DE) also impacts structure formation. The isotropy seen in the distribution of faint galaxies found in redshift surveys and in the CMBR on large scales requires that the horizon size of these regions at the epoch of recombination was connected. This means that the horizon size was small enough that information could have been transmitted across the space within the horizon size within that time epoch. However, assuming linear expansion suggests that the horizon size at that is too large to be connected: the matter on one side could not have been connected with the matter on the other side and thus there is no reason for isotropy to hold. Inflation is the theory that the vacuum energy density is non zero, and dominated the very early Universe. The negative pressure resulted in a period of inflationary expansion, allowing a small, connected horizon size at the epoch of recombination to grow to the large scales on which isotropy and homogeneity hold today. DE is described in modern cosmology using an equation of state ω, which relates pressure to density. WMAP has constrained this value to $-0.14 < 1+\omega < 0.12(95\%CL)$, where $\omega = -1$ represents a constant Cosmological Constant. Constraining the nature of DE will not only shed light on structure formation and the physics of inflation, but also determine the ultimate fate of our Universe.

1.3 Galaxy Clusters

The largest structures formed by hierarchical assembly are formed from the oldest galaxies, and due to their long formation history, reflect the matter properties of the Universe at the time of the start of their formation. These are galaxy clusters, the largest virialized structures at the current epoch. The earliest clusters have been observed at redshifts of $1.4-1.6$ (Jee et al., 2009; Brodwin et al., 2011; Santos et al., 2011). Clusters are made of three components: gas and galaxies, both baryonic forms of matter, residing within a large DM potential. Only 1% of a cluster's mass is in its galaxies: the X-ray emitting gas in cluster, called the Intra Cluster Medium (ICM), provides $\sim 10\%$ of the mass, and the remainder is made up of the invisible Dark Matter. Because of their size and the long time scales involved in their formation, clusters are very rare, sitting at the junctions between filaments of DM carrying much smaller structures such as groups and individual galaxies.

Their size and complexity results in clear signatures in multiple observational methods, allowing the study of different physical processes within the clusters, which can be combined to interpret how these processes impact each other and overall cluster and galaxy evolution. As rarities clusters can be treated as isolated systems, acting as laboratories for testing predictions based on Cold Dark Matter (CDM) simulations and hierarchical assembly. With high overdensities of galaxies, gas and DM, clusters are useful for studying galaxy evolution and DM-baryon interplay. Their number densities reflect the power spectrum of density fluctuations in the early Universe and can be used to constrain cosmological parameters such as the amplitude of density fluctuations, σ_8, at $t = 0$, and the DE equation of state, ω (Press & Schechter, 1974; Viana et al., 2003; Voit, 2005). By constructing a cluster mass function, cosmologists can test different cosmological predictions against the observed cluster abundances. Constraining these parameters requires accurate mass determination of clusters in order to obtain the cluster mass function. Cluster masses are observed using mass-observables, such as X-ray temperature or luminosity, and masses obtained from these using models with assumptions on the dynamic state of the cluster, or scaling relations. For example, Vikhlinin et al. (2009) used the X-ray

masses of 37 clusters, in combination with WMAP, BAO and the supernova studies mentioned previously, to improve constraints on the Dark Energy equation of state, ω, by factors of 1.5 and 2 for statistical and systematic errors respectively. However, if there is scatter in the scaling relations relations, from measurement error or the impact of dynamical state and physical processes within the cluster, the cluster mass function will be biased, as will the derived cosmological parameters. It is thus important not only to accurately constrain cluster masses, but also to determine the sources of scatter in the mass-observable scaling relations.

1.3.1 Cluster Galaxies

Galaxies and clusters were first detected by William Herschel in the 18th century. At this point telescopes could only show the clusters and galaxies as diffuse luminous regions. It wasn't until the 20th century that optical surveys in the 1950s (Abell, 1958) spurred research into galaxy clusters and their matter distributions. Abell searched for overdensities in the galaxy distribution, and defined clusters based on the magnitude and number of galaxies within a radius of $\sim 1.5h^{-1}$Mpc. This is today known as the cluster richness, with clusters having a richness of 30 or more galaxies with magnitudes brighter than the magnitude of the third brightest galaxy plus 1.

Hierarchical assembly states that smaller structures form first. Baryons fell into the initial gravitational wells established by DM and these co-evolved into the earliest galaxies. As clusters take so long to form the large, passively evolving elliptical galaxies at the centre of clusters are among the oldest in the Universe. They are called early type galaxies (ETGs). Star formation (SF) in these ancient galaxies has longed been diminished by their morphological transformation and surrounding environment, and as result they have a higher fraction of old, red stellar populations (Kauffmann et al., 2003). The galaxy colour can be detected by comparing the magnitudes from two different band filters. Due to their red stellar popultaions, ETGs form the Red Sequence on a colour-magnitude diagram (Fig. 1.3.1), useful for identifying galaxy clusters in the field (Gladders & Yee, 2005; Gladders, 2004; Demarco et al., 2010; Gilbank et al.,

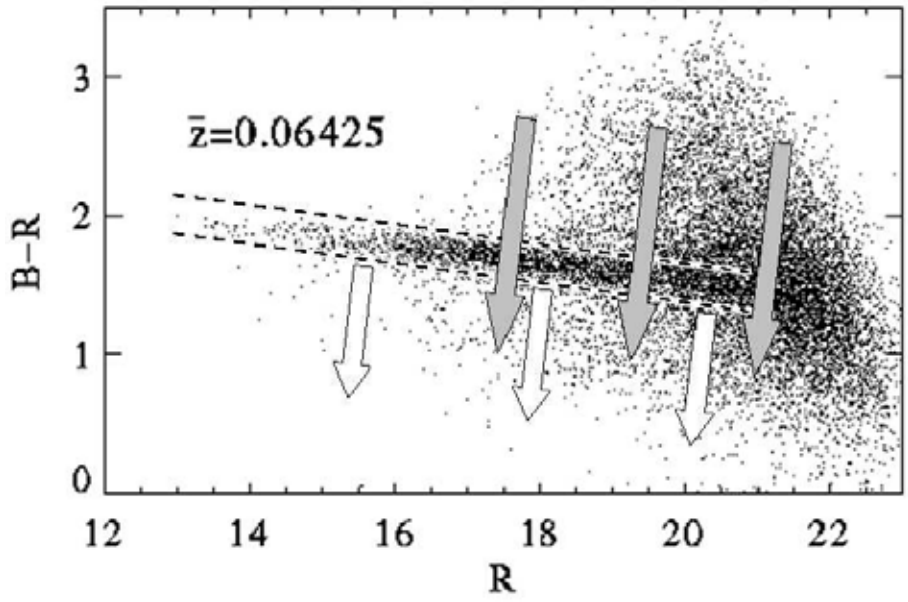

Figure 1.3: Example of the red sequence on a colour-magnitude diagram from Gladders (2004). The red sequence is shown bounded by the two diagonal lines. The grey arrows represent the typical positions of background galaxies to the cluster, and the white arrows represent the typical positions of foreground galaxies to the cluster. The cluster used is constructed of galaxies within $0.5h_{-1}$Mpc of the cores of ~ 40 low redshift, X-ray selected, Abell clusters.

2011). On the edges of clusters, at a few Mpc, lie infalling spirals. Close to the centre of the DM potential well will lie the brightest cluster galaxy (BCG).

Galaxies in galaxy clusters are subject to gravitational stresses and harassment that galaxies in the field are not. As a cluster grows richer and more compact, the denser and crowded internal environment of the cluster contributes to the morphological transformation of galaxies as they fall through the core, thus lowering the fraction of spirals (Dressler et al., 1997; Bahcall, 1999). As mentioned above, an indicator of this processes is quenching of star formation, resulting in dominance of older stellar populations on the galaxy light, and a redder colour. The closer to the core, the brighter and redder the cluster galaxies, and as a result the Red Sequence is tilted downward at fainter magnitudes. Galaxy-galaxy interactions are more likely than mergers in clusters due to the high velocity dispersion, and these, in combination with the tidal effects of the cluster potential, strip and truncate the DM haloes of cluster members, observed by studying the weak lensing signal of cluster members and the cluster itself (Natarajan et al., 2002; Limousin et al., 2007a; Natarajan et al., 2009). These environmental processes, including ram

pressure stripping of the cold, inter stellar gas from infalling galaxies by the cluster hot X-ray emitting gas and mutual harassment between galaxies flaring and quenching star formation, result in a unique environment that impacts galaxy evolution and morphology.

Identifying and studying clusters using the galaxy distributions suffers from issues such as projection effects, which can only be alleviated using expensive redshift surveys or multiple filter imaging to create red sequence diagrams. Galaxies also only account for $\sim 1\%$ of the mass in clusters. As galaxies are expected to reside in DM gravitational potentials, it follows that mass should follow light, but to understand all the process affecting structure formation and evolution in clusters, the X-ray emitting gas and DM distributions must be constrained.

1.3.2 The Intra Cluster Medium

The Intra Cluster Medium (ICM) consists of hot, X-ray emitting gas that surrounds the cluster galaxies. Clusters were first detected at X-ray wavelengths in the 1970s, (Forman et al., 1972; Gursky et al., 1972), and are now known to be some of the brightest X-ray emitters in the Universe. The hot gas that permeates the space between the clusters galaxies emits Bremsstrahlung radiation. During infall into the cluster core, the gas is shock heated to $T_X \sim T_{vir} \sim 1-10keV$, or $2-100\times10^6K$(Mushotzky, 2004). X-ray emission goes as the density of the gas squared, so large clusters will have extremely bright X-ray temperatures compared to smaller clusters. As a result, X-ray surveys suffer far less from projection effects compared to optical surverys, and have become one of the most reliable methods of detecting clusters (Vikhlinin et al., 1998; Ebeling et al., 2000), with a high degree of completeness compared to the contamination that plagued optical surveys.

The ICM gas is expected act as a fluid, whereas the cluster galaxies and DM are expected to act as collisionless particles (Markevitch et al., 2002). This means that during a merger the galaxies and DM will only interact gravitationally, while the ICMs of each merging component

will impact each offer. The offset between the BCG and the peak of the X-ray distribution, and deviations of the X-ray temperature profiles from symmetry, can give a strong indication of the dynamical state of the cluster (Sanderson et al., 2009). Other features of the ICM can be used to catagorise clusters and act as possible indicators of dynamical state. A cooling flow occurs as when the emission of X-rays causes the gas in the centre of the cluster to lose energy and cool (Fabian, 1994). A cluster with such a region of cooling gas is called a 'cool core cluster'. While mergers and significant substructure infall may disrupt the cooling flow and the associated cool core, it has been suggested that the cool core survives or reforms afterwards (Poole et al., 2006). Studying cool core clusters with evidence of merging and recent infall can provide greater understanding of the interaction between the baryonic and non baryonic components in clusters.

Both the X-ray temperature and X-ray luminosity scale with total cluster mass. Using the virial theorem, $T_X \propto M_{vir}^{2/3}$, while $L_X \propto M$ for masses at fixed overdensities (Kaiser, 1986). Assuming spherical symmtery and hydrostatic equilibrium, $\Delta P = \rho_{gas} \Delta \phi$, where ϕ is the gravitational potential, P the pressure and ρ_{gas} the density of the gas. X-ray observations of the ICM radial profile can be used to constrain the mass of clusters (Sarazin, 1988; Voit, 2005; Vikhlinin et al., 2006). These assumptions require that the radial profile of the ICM is the same in every direction from the peak of the X-ray emission, and that the gravitational compression of the gas is matched by the pressure of the gas. However, the X-ray properties of clusters are not only impacted by gravitational heating. Strong shock fronts in merging clusters, such as in the Bullet Cluster (Markevitch et al., 2002) and the impact of bulk gas motions in cluster outskirts provide non-thermal pressure support on large scales (Rasia et al., 2006; Nagai et al., 2007), resulting in the X-ray mass being underestimated. This is a critical issue when masses from X-ray temperatures are used to construct the cluster mass function, and thus constrain cosmological parameters. The impact of the dynamical state of the cluster on this function needs to be tested using alternate mass probes if X-ray masses are to be used to probe cluster physics.

1.3.3 Dark Matter in Galaxy Clusters

DM is the dominant mass component of galaxy clusters. Under the CDM paradigm, DM is currently considered collisionless, with very low self and baryon interaction cross sections. The main impact on the galaxies and gas is gravitational, the DM forming a deep potential well in which the baryonic components reside. The overall cluster DM profile is predicted, from CDM only simulations, to follow a universal profile (Navarro et al., 1997, 2010). However, other simulations and observations suggest the that inner core profile of the cluster, on scales below the maximum resolution of the previous simulations, is not universal, and may depend on cluster mass and infall history, and the impact of the presence of baryons on DM (Jing & Suto, 2000; Sand et al., 2002, 2004; Navarro et al., 2004; Sand et al., 2008). Within the cluster halo exist substructures. These substructures, such as infalling haloes belonging to groups or galaxies, are tidally stripped and become truncated after passing through the core. These subhaloes tend to persist within the main halo, a consequence of CDM (Natarajan et al., 2007). Detection of such substructure can be indicative of recent infall and structure formation, while the evolution of substructures has been linked to look back time as a test of cosmological parameters and as a signature of cluster formation history (Evrard et al., 1993; Smith & Taylor, 2008). Modelling substructure in clusters can not only provide details on structure evolution, but also test CDM predictions about the universality of the DM halo profile, and the behaviour of DM in the presence of baryonic matter.

Although DM was first detected in clusters using galaxy dynamics, a more accurate method of constraining DM structure is the analysis of the impact the cluster potential has on the light from background galaxies. That clusters could act as strong lenses was first suggested by Zwicky (1937a,c). Strong lensing (SL) is the most obvious lens effect detected, and clusters with high masses ($10^{14}-10^{15}M_{\odot}$) and strongly concentrated cores, combined with choice alignment with background sources, have resulted in spectacularly distorted arcs (Fig. 1.4), as first observed detected by Soucail et al. (1988). SL can be used to constrain the core mass profile within 100kpc, and if the lens itself is well known, the high magnification of background sources

Figure 1.4: Strong lensing features in $A2218$. (Credit: Andrew Fruchter (STScI) et al., WFPC2, HST, NASA Digitally reprocessed: Al Kelly).

in cluster cores allows for the detection and study of high redshift galaxies. However, SL is not useful for constraining the cluster mass at radii comparable to the virial radius ($\sim 1.5h^{-1}$Mpc), and not all clusters are observed with the chance alignments that produced SL.

The gravitational potential of clusters is strong enough to weakly shear the images of faint background galaxies, which, depending on depth of the observations, can be detected out to radii up to a few Mpc. The image of every galaxy behind the cluster will be slightly distorted by all mass distribution between the galaxy and the observer, including the cluster. Although the extent to which the background galaxy image is sheared by the cluster potential is smaller than the intrinsic ellipticities of the background population, over large numbers of faint galaxies the intrinsic ellipticities average to zero, while the weak lens signal remains detectable. Weak lensing in clusters was first detected in the early 90s i.e. Tyson et al. (1990). Since Kaiser & Squires (1993) developed an algorithm for reconstructing the mass of galaxy clusters using weak shear information, clusters have been used as testing grounds for weak lens mass reconstruction. The large size of clusters means they have the signal necessary for individual weak lens analysis: smaller structures, such as groups, require stacking in order to obtain strong enough signal to

noise for analysis, again assuming the objects have spherical symmetry (Hoekstra et al., 2001, 2003, 2004; Mandelbaum et al., 2006; Leauthaud et al., 2010).This means that the scatter in relations between lens properties and other mass tracers such as X-ray can be investigated, whereas in a stacked analysis the impact of dynamical state or DM substructure may be lost. This strong signal also allows for substructures in the DM halo to be detected and modelled. Both SL and WL can provide constraints on the projected cluster mass that are independent about assumptions on the dynamical state of matter within the clusters, but are sensitive to other mass distributions along the line of sight. The mass estimates and distributions can also be impacted by assumptions of spherical symmtery Clowe et al. (2004a); Corless & King (2007), and for parameterised models, assumptions made about the complexity of the mass distribution. In the following section I discuss the observed discrepancies between X-ray and lensing cluster mass estimates, some possible source of bias in both probes, and how, by combination with other multi-wavelength data, these impact of these biases can be improved and our insight into cluster formation history and the interplay deepened.

1.3.4 Multi-wavelength Cluster Studies

The study of galaxy clusters is one area that can greatly benefit from the comparison of multi-wavelength data. It is through the comparison of X-ray, luminosity and DM mass reconstructions that we can start to accurately interpret the evolution of and interaction between the different cluster components. Interactions and mergers between clusters and cluster members help to constrain the physics of the interplay between baryonic and DM, and also constrain the nature of DM itself.

Comparing X-ray temperature to lensing masses or cluster luminosity can help categorise clusters. If several clusters lie on the same scaling relation, then they are assumed to have similar formation histories and dynamics (Schaeffer et al., 1993). Thus studying outliers and segregation in scaling relations can help identify cluster subtypes, such as dynamically disturbed

or relaxed clusters. For example, Smith et al. (2005) found strong segregation between 10 disturbed and undisturbed clusters in the $M_{SL} - T_X$ relation. The disturbed, multi-modal clusters dominated the sample and the scatter in the relation. Constraining the slope and normalisation of scaling relations is therefore very important for predicting cluster properties. When the mass based relations are well constrained they can be used to estimate systematic errors in other mass probes. One application in particular is in the comparison of cluster masses obtained from lensing analysis, and those masses obtained from X-ray observations.

Miralda-Escude & Babul (1995) found that cluster masses from strong lensing were 2-3 times mass estimates from X-ray. Although the X-ray and lens mass esimates were in agreement within large errors, Squires et al. (1996) also found considerable discrepancy between the estimates. Early on there was suggestion that any difference could be due to the impact of merging and departure from HSE (Squires et al., 1997), while other studies suggested that the disruption of cooling flows in the ICM could be a possible cause (Allen, 1998). Simulated X-ray and lensing observations in the second half of the 2000s demonstrated that assuming HSE in clusters where there is additional pressure support does result in underestimated M_X, especially in disturbed, complex clusters (Rasia et al., 2006), and shows this discrepancy increasing with r (Nagai et al., 2007). By this point improvements in observation and analysis had reduced the average discrepancy (Zhang et al., 2008), with good agreement at higher overdensities, but with increasing discrepancy between X-ray and lensing mass estimates as r, the distance from the cluster centre, increased (Mahdavi et al., 2008; Zhang et al., 2010), as predicted by the simulated results. Non thermal pressure support could cause X-ray estimates of mass assuming HSE to be underestimated, while shock heating during mergers could alternately cause M_X to be overestimated. One interesting result from Mahdavi et al. (2008) was that the discrepancy in this study was not correlated with cool core status, which, if the discrepancy is caused by pressure support from physical processes associated with merging and dynamical disturbance, supports that notion that cool core status is not connected to dynamical state.

All masses obtained from lensing are projected onto a 2D plane at the position of the cluster, and thus are sensitive to contributions from non related mass distributions along the line of sight (Hoekstra, 2003). Such limitations could explain the excess in initial fitted concentrations from lensing analysis of cluster cores, in contrast to predictions from simulations (Broadhurst et al., 2005). There is growing evidence that clusters are not spherically symmetric but triaxial, and that this can cause bias in cluster concentration and mass parameters depending on the DM halo orientation (Shaw et al., 2006; Clowe et al., 2004a; Corless & King, 2007). If a prolate cluster mass distribution is viewed along its major axis, and reconstructed assuming spherical symmetry, it may be interpreted as having a very high concentration (Gavazzi, 2005). Substructure within the DM distribution can also result in simpler models having boosted masses and concentrations, especially if that substructure is along the line of sight. Deviations from spherical symmetry which will also cause the average shear signal within a circular aperture to be suppressed. This may further cause systematic underestimation of weak lensing mass if not properly modelled (Meneghetti et al., 2010). Richard et al. (2010) concluded that clusters with higher DM substructure fractions have higher $M_{SL} - M_X$ discrepancy, possibly due to substructure being indicative of recent infall that may have provided additional, non thermal pressure support, which invalidates HSE. Substructure, projection effects and modelling restrictions all complicated the determination of total cluster mass using lensing, and may also be indicative of processes that can impact other mass probes.

IR observations of cluster galaxies are less impacted by dust than observations in optical and UV filters, and thus are good for observing the large, red cluster galaxies as opposed to infalling spirals and recent SF, which both have a bluer colour. The spirals are less likely to trace the dominant DM structure, located at the edges of the cluster, whereas the red cluster galaxies are more likely to trace structure in the central region of the clusters. Study of the IR light from the BCGs in clusters has shown that higher mass clusters are more likely to have fewer, yet brighter cluster galaxies per unit mass than low mass clusters, which have higher dim galaxy proportions. This may be a result of mergers, as fainter cluster galaxies are cannibalized by the

BCG, which primarily grows by merging with other galaxies (Lin et al., 2004; Lin & Mohr, 2004). Comparing IR imaging of clusters with X-ray allows scientists to probe the relationship between the cluster galaxies and the ICM. Such comparison have revealed that the stellar mass fraction decreased with cluster mass, while the ICM to stellar mass fraction increases, suggesting star formation is less efficient in higher mass clusters (Lin et al., 2003).

But the weaknesses of some observational mass probes are the strength of others. While gravitational lensing in independent of the dynamical state of the cluster, and doesn't require assumptions about HSE, X-ray observations are less hindered by the projection effects that can boost the lensing signal. X-ray observations are useful for constructing cluster samples, as clusters have a distinct signature at X-ray wavelengths (Gladders, 2004). Comparison of the 2D projected distributions of the DM, ICM and galaxies has produced constraints on the interaction cross section of DM (Markevitch et al., 2004; Randall et al., 2008; Bradač et al., 2008), and in some cases has been vital to the interpretation of anomalous results, such as the discovery of two clusters merging along the line of sight from comparing X-ray and DM observations, that explained the unusually high concentration obtained when fitting the DM alone (Czoske et al., 2002). Using such comparisons to obtain offsets between the centre of the DM, galaxies and ICM distributions can be indicative of recent infall and mergers, while comparison with galaxy dynamics can reveal the infall trajectories of galaxies, and thus insight into the recent merger and formation history of the clusters. The best interpretation of any set of observations is obtained using comparison with multi-wavelength data. The strengths of one data set can constrain the systematics of the other, motivate new interpretations and provide normalisation of other results. Complex lensing models of DM structure motivated by, and interpreted using multi-wavelength data are necessary to provide the strongest constraints on cluster mass and DM structure, and to compensate for limitations and bias involved in different observational mass probes.

1.4 Cosmic Train Wrecks

A principled study of a large sample of clusters allows for the detailed study of mass-observable scaling relations, and the interaction between the different mass components of the clusters. Analysis with multi-wavelength data such as lensing, optical and X-ray further allows for the identification of "extreme" individual clusters, the study of which offer unique insights into the interplay of DM and baryons.

Such studies were motivated by the discovery of the Bullet Cluster (1E 0657-56) (Markevitch et al., 2002; Clowe et al., 2004b; Bradač et al., 2006; Clowe et al., 2006). A major merger in the plane of the sky, two clusters have collided and then continued on their original paths, with each component reacting differently to the merger. While the galaxies and DM of each cluster has passed through the contact point as collisionless particles, the X-ray emitting gas has been strewn between the two systems. The smaller cluster has been almost completely stripped of its gas, and the interaction has caused in a prominent shock front in the gas from this cluster. The DM is still associated with the separate clusters, but each halo is strongly elongated in the NS plane (Fig. 1.5, left panel). By determining the offsets between the peak of the X-ray, DM and luminosity distribution, constraints can be put on the Dark Matter self-interaction cross section of $< 1\mathrm{cm}^2\mathrm{g}^{-1}$. The Bullet Cluster represents an example of the differing behaviours of different components of merging cluster providing constraints on the nature of Dark Matter.

Since the Bullet Cluster result, other extreme clusters have been identified and analysed. The Baby Bullet (MACS J0025.4-1222) (Bradač et al., 2008) (Fig. 1.5, right panel) is a similar example to the Bullet Cluster, another high speed merger in the plane of the sky. Although there is no obvious shock front in the X-ray gas, the peak of the gas is clearly offset from the two, separate, cluster DM and galaxy distributions. The gas mass fraction and mass-to-light ratio for all the DM, gas and galaxy components combined are normal for a cluster of this size, suggesting that global cluster properties may not be reliable in identifying extrema clusters. The mass-to-light ratios of the individual peaks are also typical for clusters of this size, evidence that

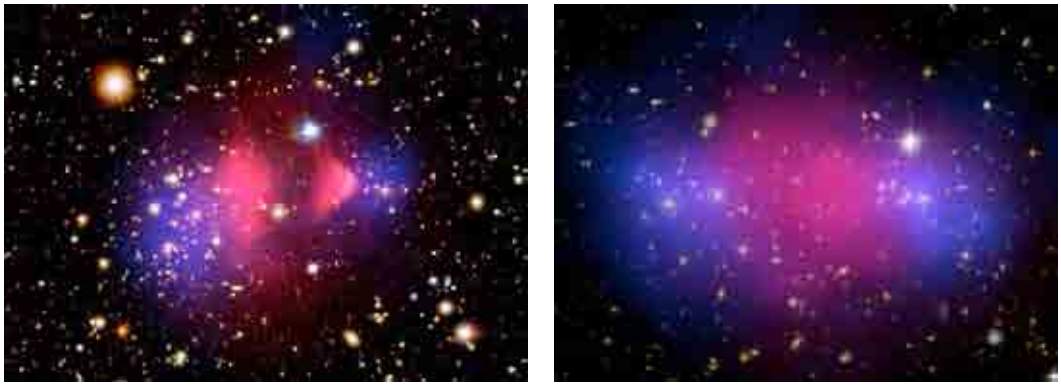

Figure 1.5: Left: The Bullet Cluster, with X-ray overlayed in pink, and the total weak lens mass distribution overlaid in blue. (Credit: X-ray: NASA/CXC/M.Markevitch et al. Optical: NASA/STScI; Magellan/U.Arizona/D.Clowe et al. Lensing Map: NASA/STScI; ESO WFI; Magellan/U.Arizona/D.Clowe et al). Right: The Baby Bullet, with the same colour overlays as the Bullet Cluster. (Credit: NASA, ESA, CXC, M. Bradac (University of California, Santa Barbara), and S. Allen (Stanford University))

the DM was not stripped or lost from either peak. The spatial correlation between the galaxy and DM distributions compared to the X-ray emitting gas suggests that DM acts collisionless, with an estimate self interaction cross section of $< 4\text{cm}^2\text{g}^{-1}$.

However, not all extreme clusters appear to support entirely collisionless DM. In 2007, Mahdavi et al. (2007), published the weak lens reconstruction of $A520$, a rich cluster at $z = 0.201$ (Fig. 1.6, left panel). The most interesting feature in this cluster was a 'dark' core, a peak in the cluster core with a very high mass-to-light ratio ($721 h_{70} M_{\odot}/L_{\odot_b}$), with a low mass-to-light region 500kpc east of this position, matching a shock feature in the radio emission. As with the Baby Bullet, the fraction of mass attributed to the X-ray emitting gas, $0.15 h_{70}^{-1.5}$%, and total cluster mass to cluster light ratio, $232 \pm 25 h_{70} M_{\odot}/L_{\odot B}$, were considered normal for this cluster total mass, further evidence that not all extreme clusters are identifiable from their global properties. Mahdavi et al. proposed that, in accordance with CDM, the dark peak is the result of a complex multi-body merger, or that in conflict with CDM, the low mass-to-light peak (peak 5. in Fig. 1.6) and dark core (peak 3. in Fig. 1.6) had a common precursor that was 'stripped' of DM during a previous merger. Other studies on $A2744$ (Fig. 1.6, left panel, (Owers et al., 2011; Merten et al., 2011) report a variety of over massive and under massive multi-wavelength substructures within a multiple merger, suggesting as the cause of separation between DM and

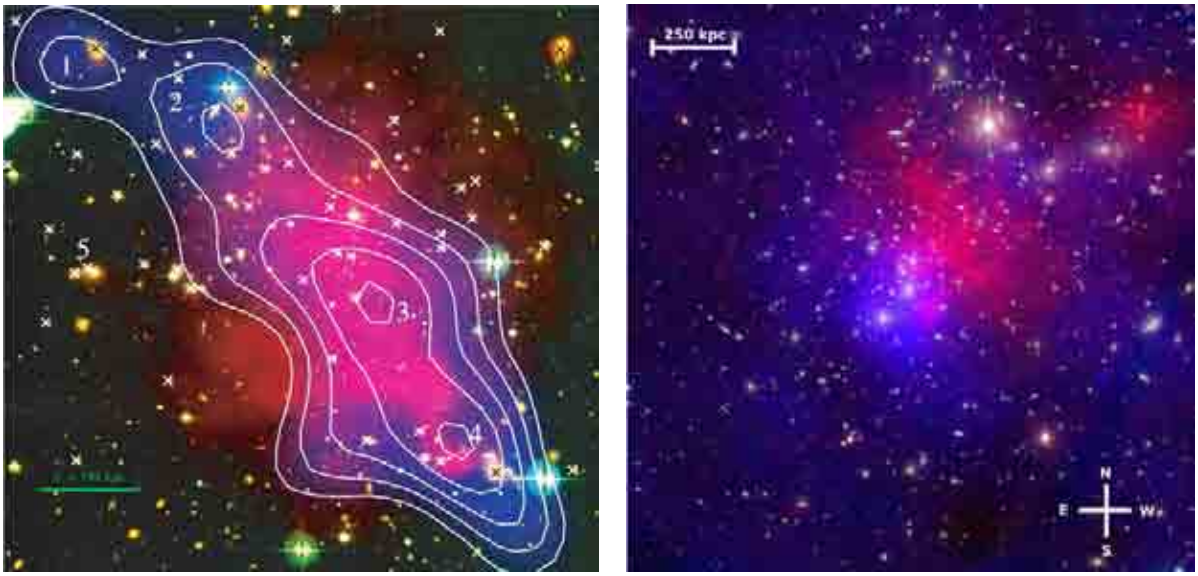

Figure 1.6: Left: *A*520, with X-ray overlaid in red and the matter distribution from lensing overlaid in blue. The white contours show the DM reconstruction with $3, 3.5, 4, 4.5, 5\sigma$ intervals. Crosses denote spectroscopically confirmed cluster members, orange crosses those on the Red Sequence. (Credit: Mahdavi et al. (2007)). Right: *A*2744, with X-ray in red and the DM distribution in blue. (Credit: Merten et al. (2011)).

light the dynamics of multi-body systems.

In all of these examples, it was the combination of multi-wavelength data and careful modelling of the spatial distributions of the different cluster components that lead to greater insight on the merging processes. The conflicting pictures from different extreme clusters suggests that a larger sample is required to test systematics in the merger population, and obtain stronger constraints on the nature of DM. However, as clusters themselves are rare, and as such interactions between cluster scale systems even rarer, developing a catalogue of such objects could be very difficult and expensive in term of survey time. Attempts to circumvent the rarity by averaging over the substructure offsets of apparently less disturbed clusters, in order to obtain an estimate of 'bulleticity' where the individual component offsets are not significant but the overall offset could be (Massey et al., 2011) may work, but also require large catalogues of clusters with obvious substructure.

1.5 The Local Cluster Substructure Survey: LoCuSS

LoCuSS is a systematic, multi-wavelength survey of over 100 X-ray luminous, $2 \times 10^{44} \leq L_X \leq 3 \times 10^{45} ergs^{-1}$, local galaxy clusters at redshifts between $0.15 < z < 0.3$, selected from the ROSAT All Sky Survey catalogue, (Böhringer et al., 2004a; Ebeling et al., 2000, 1998). Involving collaborators and observatories world wide, the survey seeks to investigate the impact of hierarchical formation on the baryon and DM physics within galaxy clusters, with the goal of constraining the scatter induced in mass-observable scaling relations by differing cluster evolution and merger history. Using a combination of lensing mass maps, X-ray, Sunyaev Zel-Dovich (SZE) and IR observations, the effect of structure infall on the dynamical evolution of cluster galaxies and the ICM is probed in order to provide insight into the relation between the baryonic and DM matter, and provide further constraints on the relationships between different mass and structure tracers.

A pilot study by Smith et al. (2005) (Smith et al., 2001, 2002a,b, 2003) of 10 cluster cores ($R < 250 h^{-1} kpc$) found 7/10 were disturbed (multimodal, with a large discrepancy between the mass and X-ray peaks, and $f_{sub} \sim 0.1-0.6$), and that these clusters dominated the scatter on the mass-T_X relation, with the normalisation of the mass-temperature relation for the disturbed clusters being $\sim 40\%$ hotter than that for the undisturbed clusters. This conclusion contradicted the established paradigm from theory and X-ray studies that the mass-temperature relation had little scatter and that the majority of clusters were undisturbed Evrard et al. (1996); Finoguenov et al. (2001); Borgani et al. (2004). Such a bold statement required a larger sample to obtain robust statistics on the cluster demographics.

LoCuSS aims to investigate the results of the pilot study and improve the statistics on the segregation of the cluster population by increasing the size of the sample by an order of magnitude, while studying the mechanics of hierarchical assembly and its relation to the evolutionary history of galaxies within the cluster and of the cluster itself. The survey has several goals

related to this aim: to obtain demographics on the local population of galaxy clusters, in order to constrain the proportion of disturbed clusters; to investigate the structural segregation of the mass-temperature relation, determine whether this segregation is evident in other mass-observable scaling relations, and constrain the resultant scatter to improve cluster cosmology experiments; and investigate the assembly history of clusters using multi-wavelength comparisons of structure maps, with the aim of using this intermediate cluster population as a baseline for studying higher redshift cluster populations.

In order to investigate these goals, LoCuSS has amassed a considerable database of multi-wavelength cluster observations, from X-ray observations from XMM-Newton and Chandra, to IR observations from CTIO, Kitt Peak and Palomar, optical imaging for lensing analysis from Subaru and the Hubble Space Telescope, SZE observations from the Sunyaez Zel-dovich Array, and most recently, constraints on star formation from the Herschel Telescope. Some of the key results from LoCuSS are as follows;

(i) Evidence of structural segregation in the mass observable scaling relations (Zhang et al., 2010; Richard et al., 2010; Okabe et al., 2010c), with the scatter and normalisation at odds with results from with numerical simulations (Zhang et al., 2008; Marrone et al., 2009).

(ii) Scatter in X-ray mass at fixed observables in scaling relations is half that of the WL mass (Zhang et al., 2008), while the scatter in the WL mass at fixed Y_{SZE} is less than at fixed T_X (Marrone et al., 2009), and the mass of the X-ray emitting gas, M_{gas}, has lowest scatter in WL mass compared to other X-ray observables (Okabe et al., 2010c).

(iii) The discrepancy between SL and X-ray mass estimates is related to the amount of mass substructure and the dynamical state, with disturbed clusters having larger discrepancies (Richard et al., 2010). Mergers appear to cause departure from HSE, perturbing the cool cores (Sanderson et al., 2009; Richard et al., 2010).The agreement between the WL and X-ray mass estimates is found to improve as the overdensity at which the mass is measured increases (Zhang et al., 2010).

(iv) Star formation is enhanced in the infall regions of clusters, with rates above those predicted by numerical simulations, possible due to environmental triggering. The fraction of SF

galaxies doesn't depend on dynamical state, with the majority of SF taking place in the outer regions of the cluster, away from merging activity in the core. SF has been detected in galaxies associated with substructure in the X-ray, lensing and NIR (Haines et al., 2009, 2010; Pereira et al., 2010).

However, even with such a comprehensive dataset there is still disagreement within the survey itself on results such as the dependence of gas mass fraction on the dynamical state of the cluster, with Zhang et al. (2010) concluding that it is not related to dynamical state, whereas Sanderson et al. (2009) found that it was related to the offset between the BCG and peak of the X-ray emission, which itself was found to be related to the dynamical state.

These results have relied upon weak and strong lensing analysis of the LoCuSS cluster sample (Smith et al., 2005; Okabe et al., 2010b; Richard et al., 2010) to provide estimates of the 'true' mass of the cluster to compare with mass tracers such as X-ray temperature. The constraints on the DM distribution is especially interesting as the fraction of mass substructure in the cluster can be used to infer the cluster assembly history (Smith & Taylor, 2008).

My thesis aimed to use the weak lensing analysis of shallow, single filter imaging from the Hubble Space Telescope to constrain the internal structure of a large number of cluster cores, for comparison with similar constraints from X-ray and NIR data, in order to investigate the structural segregation in the mass-temperature relation and the spatial distribution of the different cluster components. These observations contributed some of the strong lens constraints to Richard et al. (2010), and the clusters were also observed by Chandra. By utilising the LoCuSS multi-wavelength data this work has attempted to decipher the recent assembly histories of 21 galaxy clusters, by comparing the spatial distribution of subtructures in the IR, mass and X-ray flux maps, by comparison of the cool core strength with the fraction of substructure in the cluster core, and by studying the properties of the mass-temperature relation for cool core and non cool core clusters.

Many previous studies have focussed on the indepth analysis of a single, or small sample of clusters. While the deeper data and individualised analysis may provide tighter constraints for individual examples, these studies are less appropriate for constraining the scatter in mass-temperature scaling relations, or determining the relation between substructure fraction and other global properties. A large sample is required to reduce the statistical errors on weak lens mass scaling relations, and test whether the skew towards disturbed clusters seen in Smith et al. (2005) is evident in the larger cluster population.

Future surveys, such as PANSTARRS (Kaiser et al., 2010) and the Dark Energy Survey (DES) (Flaugher, 2005; Sánchez & the Des collaboration, 2010), will produce massive datasets of groups and clusters for studying clustering and the growth of cosmic structure. This will require large amounts of telescope time and extensive analysis, thus it is important for future surveys to efficiently construct cluster samples that probe the issues of most interest to the survey. A standardised analysis pipeline is required to process the large amount of data coming from these surveys, and also to identify those clusters that can skew the results from the general cluster population, such as extreme mergers like the Bullet Cluster. The methods developed to detect the weak lens signal in shallow, noisy data will be applicable to the analysis of those parts of the surveys with poor coverage, and for the detection of weaker signals from galaxy groups, or for measuring the cosmic shear. In addition, for the investigation of merging clusters as windows into the interaction between baryons and DM, such a pipeline could be used in conjunction with archival observations to identify extreme clusters for detailed analysis with deeper observations.

My thesis demonstrates that we have succeeded in the constraining the 2D DM structure for a large (21) sample of clusters, via a principled analysis. We have obtained robust parameterised and non-parameterised maps of the DM distribution using weak lensing, and have provided comparisons with luminosity density and X-ray emission distributions. We have obtained estimates for the systematics of our pipeline using comparisons with the literature on

the Bullet Cluster, and have identified an 'extreme' Bullet type cluster. We have also detected a group scale structure using WL information alone, out side of the field of view of the WL observations, and have thus disentangled a foreground group detection, A 3192, from a background cluster, RXC J0358. Although the smoothing of the faint galaxy catalogues require further research to alleviate a low mass bias in the total cluster masses, this analysis represents a systematic method for cheaply obtaining cluster merger histories, identifying extreme clusters and probing the relation between gas, light and DM using weak lensing.

I will briefly describe the observatories from which the data for this analysis were taken at the end of this Introduction. I will introduce lensing theory and the weak lens mass reconstruction methods used in this analysis in Chapter 2. I will then describe my reduction and initial analysis of the Hubble Space Telescope observations in Chapter 3, as well as summarising the reduction and analysis of the near-IR and X-ray observations performed by my colleagues, Tom Targett and Alastair Sanderson. In Chapter 4 I cover the non parameterised and parameterised weak lens mass reconstruction of the data, and then discuss the individual cluster and sample results in Chapter 5. I describe two clusters, A 1392/RXC J0358 and A 3644, in detail in Chapter 6. Finally I summarise my results and discuss the implications of my thesis and the applicability of the pipeline described within to the large scale analysis and construction of future surveys.

1.5.1 Observatories

Hubble Space Telescope: Advanced Camera for Surveys

The Hubble Space Telescope (HST) was launched in 1990, and provides astronomical imaging from the Ultra Violet (UV) to Near Infra-Red (NIR) (Fig. 1.7). A primary benefit of observing from space is that observations are not impacted by the Earth's atmosphere. The turbulent motions of the atmosphere limit observing times and cause a spreading distortion in images of distant stars and galaxies. This distortion is called the seeing. By avoiding this effect, the HST

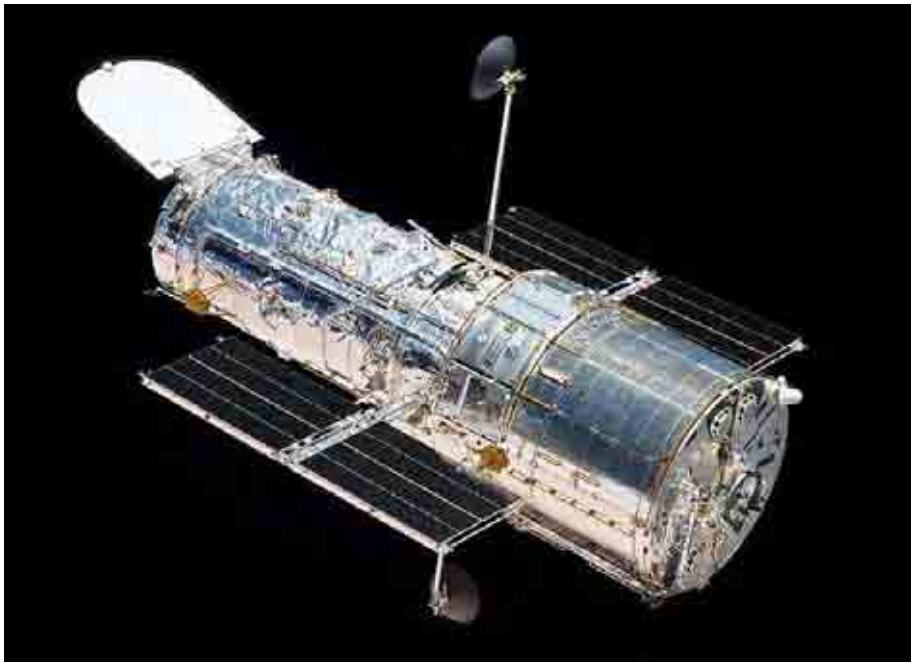

Figure 1.7: The Hubble Space Telescope, after being released from the space shuttle Atlantis, after a servicing mission in 2009 (Image Credit: NASA, http://hubblesite.org /gallery/spacecraft/25/)

provides sharper imaging better suited for measuring weak shear in faint galaxy shapes around clusters and groups. Such benefits in observing conditions is reponsible for the HST receiving between $7000-12000$ proposals a year, of which only $1/5$ can be filled.

The Advanced Camera for Surveys (ACS) is a 16 Mpixel CCD camera designed for wide field surveying in the visible to NIR wavelengths and imaging in the UV to IR wavelengths. It was installed in the HST in March 2002, and suffered an severe CCD electronics fault in January 2007.

The Wide Field Channel (WFC) of the ACS aims to provide high throughput, wide field imaging in visible wavelengths, from $370-1100$ nm. It has a $202x202''$ field of view, and typically achieves a seeing FWHM of $0.1-0.14''$. The ACS:WFC camera was used to obtain SNAPSHOT images of the LoCuSS galaxy clusters for weak shear analysis.

Figure 1.8: The Mayall (left) and Blanco (right) 4 metre telescopes at Kitt Peak, USA and Cerro Tololo, Chile, respectively. (Image Credits: NOAO/AURA/NSF, http://www.noao.edu/outreach/media/photo/kpno/mayall/02106.med.jpg, http//www.noao.edu/image_gallery/images/d2/02360a.jpg)

Near Infra-Red Observatories

The near Infra-Red (NIR) observations were taken at three different observatories: the 4 metre Mayall and Blanco telescopes at Kitt Peak and Cerro Tololo respectively, and on the Hale telescope at Palomar.

The Mayall and Blanco telescopes are identical, with the Mayall seeing first light in 1973, and the Blanco in 1974, and are part of the National Optical Astronomy Observatory (NOAO) (Fig. 1.8). Both are primarily used for NIR and faint visible light observations. On the Mayall, the Flamingos IR Imaging Spectrometer is a wide field image and multi-slit spectrometer. It can provide imaging in the J, H, K and Ks band filters, with a FWHM of $0.6-1.0''$, over the telescope field of view of 10 by 10 arcminutes. The NIR imager on the Blanco telescope is the Infrared Side Port Imager (ISPI). Similar to the Flamingos, it has a $0.3''$ per pixel resolution, and a FWHM of $0.6-1.0''$, a field of view of ~ 10.5 by 10.5 arcminutes and provides imaging in the J, H, K and Ks band filters.

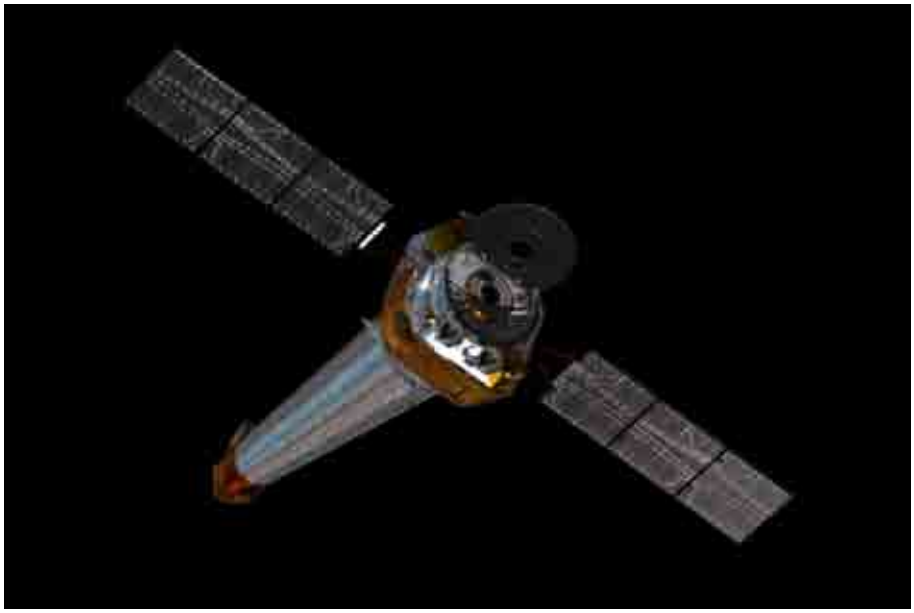

Figure 1.9: Chandra observatory, an artist's impression. (Image Credit: NASA/CXC/D.Berry, http://chandra.si.edu/graphics/resources/illustrations/chandra_bshot6_300.jpg)

The Palomar 200 inch Hale telescope saw first light in 1948. The Wide Field Infra-Red Camera (WIRC) has a resolution of $0.25''$ per pixel, and field of view of 8.7 by 8.7 arcminutes. As with the other two observatories, this instrument provides imaging in a range of IR filters, including J, H and Ks.

Chandra X-ray Telescope: AXAF CCD Imaging Spectrometer

Chandra is an X-ray telescope, orbiting the Earth in order to detect X-ray emission from exploded stars and extra-galactic sources which is absorbed by the atmosphere (Fig. 1.9. Originally known as the Advanced X-ray Astrophysics Facility (AXAF), Chandra was designed for high resolution X-ray imaging and spectromety, and was launched in 1999.

The AXAF CCD Imaging Spectrometer (ACIS) provides 17 by 17 arcminute wide field imaging with an energy resolution of 130 eV at 1.49 keV or 280 eV at 5.9 keV. The imager works by recording the position, energy and arrival time of each X-ray photon that hits the detector. It allows for an imaging resolution of $\sim 1''$, and was used to provide 2D X-ray flux maps

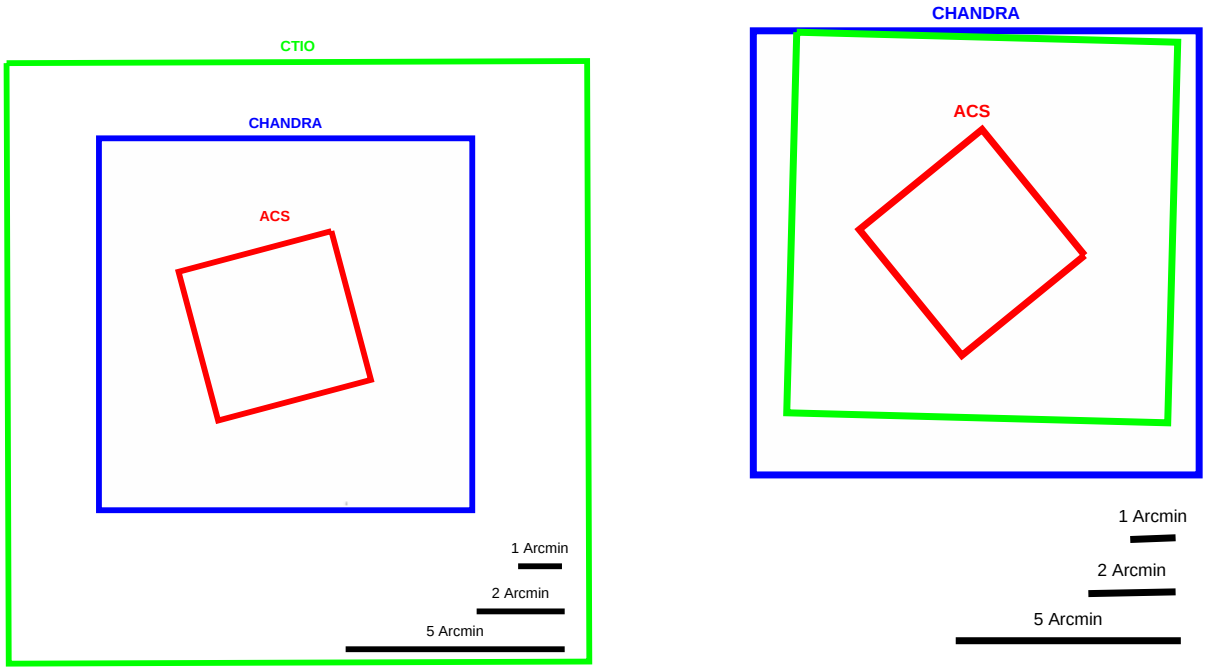

Figure 1.10: Schematics showing the field of view of the observatories described in this section. The blue field of view is that of the AXAF imager on the Chandra telescope, the green fields represent the Flamingos/ISPI (left) and WIRC (right) field of views and the red box shows the field of view of the ACS camera on the HST.

for the clusters in this study.

In Fig. 1.10 I give a schematic of the field of views of the AXAF imager on Chandra (blue), the ACS camera on the HST (red) and the Flamingos/ISPI field of views (green, on left schematic) and WIRC field of view (green, on right schematic).

Chapter 2

Lens Theory

2.1 Gravitational Deflection of Light

Lensing describes the bending of light due to the mass of a foreground system gravitationally distorting the local space time geodesics. The term covers a wide range of effects, from micro-lensing, used to find planets orbiting distant stars, through weak lensing Tyson et al. (1990), where almost imperceptible distortions of the light from background galaxies can be used to constrain foreground DM distributions, to strong lensing Soucail et al. (1988), where the shear field deflects the light into multiple images of the same source. One of the most interesting features of lensing is that it only depends on the gravitational properties of the lens, and not on the state or type of matter the lens is made of. This not only allows for gravitational lensing to be easily described mathematically, but allows for assumptions about physical processes in the lenses to be tested. Because the distances over which the light travels are much greater than the scale of either the source or lens, gravitational lensing reduces to a geometric problem. Then as well as being able to study the properties of the lens and source, we can also study the geometry of the Universe (Lombardi & Bertin, 1999b). As the number of lenses in the Universe depends on this geometry, we can use the probability that a lens event will occur to determine cosmological parameters.

Clusters act as the most impressive lenses in the Universe; their large and complex potentials produce a variety of lensing effects, from weak to strong lensing. The ability to combine constraints from both types of lensing and thus constrain the DM distribution both in the core

and at the virial radius makes the lensing study of clusters very rewarding. Additionally, by acting as strong lenses, clusters magnify distant galaxies, allowing scientists to investigate galaxy formation in the early Universe (Smail et al., 1993; Kneib et al., 2004; Richard et al., 2011).

Lensing analysis of a cluster can produce a model for the total mass distribution on scales of 10kpc (strong lensing) to 5Mpc (weak lensing)(Smail, 2004). Such models can be used to probe the interplay between DM and baryons (Markevitch et al., 2004), or probe the cluster formation history, especially in combination with other mass and structure probes (Czoske et al., 2001). As the lens effect only depends on the gravitational potential of the cluster and not the type of matter (dark/luminous) or dynamical state, not only have lensing mass estimates of cluster provided support for the existence of DM (Clowe et al., 2004b), but they can also be used to test assumptions on internal cluster physics employed other mass probes such as X-ray temperature (Meneghetti et al., 2010). With the higher resolution imaging available from future telescopes, and large scale cluster surveys, lensing mass reconstructions will continue to provide important results to the field of cluster mass reconstruction.

In this chapter I will cover lensing theory, with an emphasis on weak lensing by clusters. I will also describe various statistical methods by which weak shear information is used to reconstruct the DM distribution of the cluster, and discuss the development of parameterised and non-parameterised mass reconstruction methods. Finally I will cover observational difficulties in using weak lensing to constrain cluster properties. For more indepth reviews, see Narayan & Bartelmann (1996); Bartelmann & Schneider (2001); Petters et al. (2001); Meylan et al. (2006).

2.2 The Lens Equation

Once the multiple images or shear effects of a lensing potential have been observed, the lens equation can be applied to probe the properties of either the lens or the source, for example the cluster or background galaxies. Lensed images of the source are distorted in shape by the

shearing impact of the tidal gravitational field, and magnified by focusing due to the shear and local matter density. Retracing from multiple images of the same source back to its original position is fairly straightforward once the lensing distribution is known, while the reverse is more difficult as one source can produce multiple images. In order to simplify the mathematics, the gravitational field is modelled as weak and stationary, in order to allow the local linearisation of General Relativity, which simplifies the relations between the deflection angle and the potential of the lens. This Thin Lens Approximation allows geometric optics to be applied to the lensing system. As the distances between the observer and the lens, and between the lens and the source are of the order of several Gpc compared to the physical extent of the lens itself, which at the most massive (ie. cluster scale) is only a few Mpc, this approximation means lensing mass distribution can be approximated as a 2D projection of the 3D mass distribution (Narayan & Bartelmann, 1996).

For example, consider a source of light at a distance D_s from the observer. A large mass positioned in between the observer and the source, at D_d, distorts the local flat spacetime, resulting in a deflection in the paths along which light rays from the source travel, called *null geodesics*. Due to this distortion the position of the image of the source is deflected by $\hat{\alpha}$, as in Fig. 2.2.

The distance between the source and the lens at the source plane, given by η, can be expressed in terms of θ and α using small angle approximations,

$$\eta = D_s\theta - D_{ds}\hat{\alpha} = \frac{D_s}{D_d}\xi - D_{ds}\hat{\alpha}(\xi) \tag{2.1}$$

where $\xi = D_d\theta$. Then the approximation of $\eta = D_s\beta$ allows this to be rearranged to,

$$\beta = \theta - \frac{D_{ds}}{D_s}\hat{\alpha}(\underline{\xi}) = \theta - \alpha(\theta) \tag{2.2}$$

where $\alpha(\theta) = \frac{D_{ds}}{D_s}\hat{\alpha}(D_d\theta)$ is the scaled deflection angle. Now consider Fermat's Principle: a light ray travelling between two points will traverse the path that takes the least time. Due to the gravitational distortion of the geodesics, the arrival time of each light ray package will be

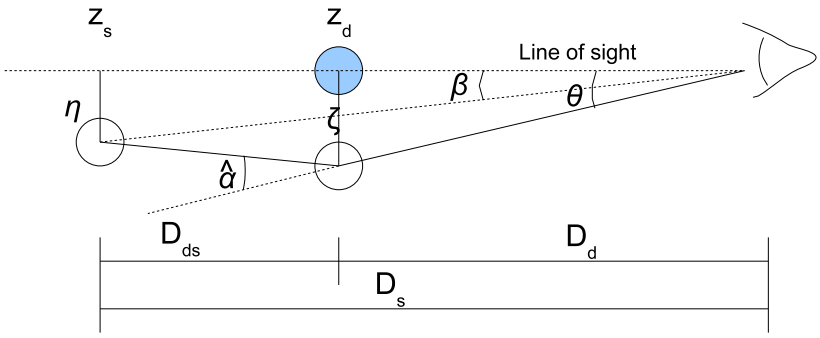

Figure 2.1: Light rays from the source at angular diameter distance D_s are lensed by a mass at D_d, so the observer sees the image deflected by $\hat{\alpha}$. The white circles represent the source and the deflection of light rays from the source at the lens plane. The distance between the lens and the source at the source plane is given by η, and the distance between the image position and the lens at the lens plane is given by ξ. It should be noted that over cosmological distances $D_d + D_{ds} != D_s$

delayed. This arrival time is given by

$$\tau_a = \frac{1}{c}\int(1-\frac{2\Phi}{c^2}).dl = \frac{l}{c} - \frac{2}{c^3}\int \Phi.dl \tag{2.3}$$

where Φ is the three dimensional Newtonian potential of the lens, and dl the line integral of the light path. From Fig. 2.2, and the fact that all the angles are very small,

$$l = l_I + l_S = D_d + \frac{D_d\theta^2}{2} + D_{ds} + \frac{(D_d\theta - D_s\beta)^2}{2D_{ds}} \tag{2.4}$$

We can neglect the constants in this equation as Fermat's Principle means we are only interested where the derivative of t_a with respect to θ vanishes. The second term becomes the projected two-dimensional Newtonian potential, ϕ,

$$\int \Phi dl = \phi(\xi) = D_d^2\phi(\theta) \tag{2.5}$$

Then differentiating the arrival time with respect to θ and considering the minimal case gives

$$\frac{D_d(D_d\theta - D_s\beta)}{D_{ds}} + D_d\theta - \frac{2D_d^2}{c^2}\nabla_\theta\phi(\theta) = 0 \tag{2.6}$$

By rearranging Eq. 2.1, $D_d\theta - D_s\beta = (\hat{\alpha} - \theta)D_{ds}$ then this term delivers the deflection angle,

$$\hat{\alpha}(\xi) = \frac{2D_d}{c^2}\nabla_\theta\phi(\theta) = \frac{D_d}{D_{ds}}\nabla_\theta\varphi(\theta) \tag{2.7}$$

where φ is the deflection potential,

$$\varphi = \frac{2D}{c^2}\phi \quad and \quad D = \left(\frac{D_d D_{ds}}{D_s}\right) \tag{2.8}$$

Then we can use the scaled deflection angle α from Eq. 2.2 to obtain

$$\alpha = \nabla\varphi \tag{2.9}$$

Another quantity related to the lensing potential is the dimensionless surface mass density, κ, also known as the convergence. κ can be used to quantify the strength of the lensing effect, i.e. strong ($\kappa \geq 1$) or weak ($\kappa << 1$). κ is defined using the critical mass density, Σ_{CR},

$$\kappa = \frac{\Sigma(\xi)}{\Sigma_{CR}} \quad where \quad \Sigma_{CR} = \frac{c^2}{4\pi G}\frac{D_s}{D_d D_{ds}} \tag{2.10}$$

The critical density is an indicator of the strength of the lens effect for the given source and lens redshifts. In the strong lensing regime the lens is classed as super critical, and the lens effect is strong enough to generate multiple images of the source. This regime is found near the centre of the lens, where the gravitational potential is deepest, and the local surface mass density is more likely to exceed the critical density. The dimensionless convergence is related to the second derivatives of the lensing potential by Laplace's equation,

$$\nabla^2\varphi = 2\kappa \tag{2.11}$$

The lens equation can be linearised if the angular scale of the source is much less then the angular scale of the variance of the lens potential. This means the distortion of the lensed image can be described by a coordinate transformation from the source plane to the image planes, expressed as a Jacobian matrix, whose elements are expressed in terms of the convergence κ and shear γ,

$$A(\theta) = \frac{\delta\beta}{\delta\theta} = \begin{pmatrix} 1-\kappa-\gamma_1 & -\gamma_2 \\ -\gamma_2 & 1-\kappa+\gamma_1 \end{pmatrix} \tag{2.12}$$

where γ_1 and γ_2 are components of complex shear, $\gamma = \gamma_1 + i\gamma_2$, with

$$\gamma_1 = \frac{1}{2}(\varphi_{11} - \varphi_{22}) \quad \gamma_2 = \varphi_{12} \tag{2.13}$$

and the convergence κ can be expressed as (Schneider, 2006b; Narayan & Bartelmann, 1996),

$$\kappa = \frac{1}{2}(\varphi_{11} - \varphi_{22}) = \frac{1}{2}tr\varphi_{ij} \tag{2.14}$$

2.3 Lensing Magnification

Gravitational lensing does not alter the surface brightness of the source, only the resultant flux $S_{\nu,\theta}$ by transforming the solid angle of the flux. Thus the magnification can be found by using the ratio of the solid angle from the image, $d\omega_\theta$, and the solid angle from the source, $d\omega_\beta$.

$$|\mu| = \frac{S_{\nu,\theta}}{S_{\nu,\beta}} = \frac{d\omega_\theta}{d\omega_\beta} = \frac{d^2\theta}{d^2\beta} \tag{2.15}$$

The magnification tensor is defined as the inverse of the lensing Jacobian, $M(\theta) = A^{-1}$. The modulus of the magnification μ can be defined as

$$\mu = det|A| \tag{2.16}$$

2.4 Strong Lensing and the Einstein Radius

Strong lensing occurs when the surface mass density at some point θ exceeds the critical surface mass density, $\Sigma \geq \Sigma_{CR}$, i.e. $\kappa \geq 1$ and $\det(A) \leq 0$, usually detected near the core of the cluster. This generates caustics in the lensing potential. A distortion of a source near a caustic may result in more than one null geodesic and the light travelling down each solution geodesic forms a different image of the source for the observer. The placement of the source with respect to the caustic then determines the shape and complexity of these images, and whether one or more images are produced. When the source lies on the caustic, it produces an extended arc, and when the caustic is a cusp, three images merge to form the largest and most impressive arcs, as in Fig. 2.4. Ideal alignment between source, lens and observer means a quadruplet of images will merge together, forming a arc around the lens called an Einstein ring.

In cluster cores, strong lensing, such as arcs and multiple images, can provide constraints on the total mass within a radius of a few tens to a hundred kpc. Tangential arcs occur at tangential critical curves of the lens, within which the mean surface mass density is close to the critical surface mass density. Assuming circular symmetry, a simple estimate of the mass within the

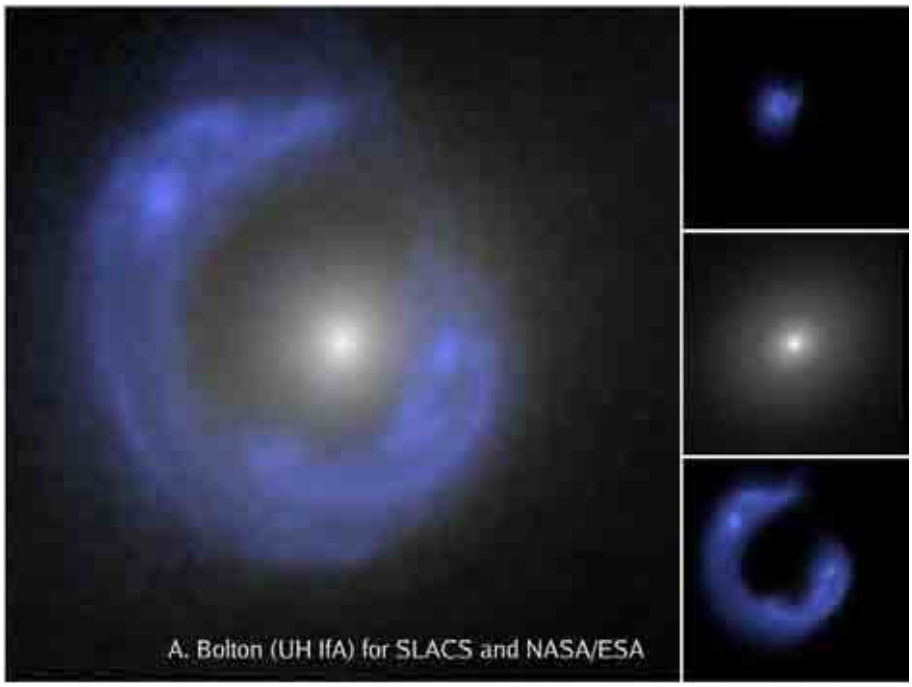

Figure 2.2: SDSSJ1430: The image background galaxy is warped around the lensing galaxy in the centre, forming an Einstein Ring. The panels on the right show the different components separately, and a recreation of what the image of the background galaxy would look like unlensed. (Credit: A. Bolton (UH/IfA) for SLACS and NASA/ESA)

Einstein radius is given by (Narayan & Bartelmann, 1996),

$$M(\theta) = \Sigma_{CR}\pi(D_d\theta)^2 \tag{2.17}$$

2.5 Weak Lensing

Weak lensing encompasses minor distortion (a signal to noise ratio per per galaxy image of ≈ 0.3) of background sources, when $\kappa, \gamma << 1$, and the Jacobian $A(\theta)$ approaches the unit matrix. The sources used in weak lensing studies are distant faint galaxies in the optical or near IR bands, around $z \sim 0.7-1.5$ for clusters at $z \sim 0.2$. Weak lensing information can be classified into two effects: shear and magnification. Using observations of the faint background galaxies, the net distortion effect on the ellipticities of the background galaxy images can be used to obtain the projected mass distribution; this can also be obtained from magnification data by studying background galaxy number densities. Individual ellipticity measurements for the background sources are too small to be considered individually, so many lensed sources have to

be considered, and the shearing effect statistically derived. To obtain constraints from lensing magnification knowledge of the unlensed number counts of background galaxies is required. Number counts in the field can be used but may miss any line of sight clumping behind the cluster (Schneider et al., 2000). Another problem plaguing lensing mass reconstruction is the *mass sheet degeneracy* (§ 2.5.1). Briefly, a scalar, constant convergence field can be added to any solution for the shear field, without affecting the observations.

Weak lensing effects can be analysed to study the mass distribution of clusters on larger scales, angular resolutions of $\theta > 0.5'$ whereas strong lensing covers the range $\theta \sim 0.5-1'$. Weak lens constraints combined with strong lens core constraints, either within their respective regimes or with the strong len masses used to scale the weak lens result, can produce accurate mass profiles and measurement estimates for clusters (Bradač et al., 2004b; Bradač, 2004; Bradač et al., 2006; Cacciato et al., 2006).

From the observed shapes of the background galaxies it is possible to obtain an estimate for the ellipticity of an image,

$$\epsilon = \left(\frac{1-\frac{b}{a}}{1+\frac{b}{a}} \right) \exp(2i\phi) \tag{2.18}$$

where a is the semi-major axis, b the semi-minor axis and ϕ the position angle of the image. The reduced shear, g, is defined as,

$$g(\theta) = g_1 + ig_2 = \frac{\gamma(\theta)}{1-\kappa(\theta)} \tag{2.19}$$

which allows the Jacobian to be rewritten as,

$$A(\theta) = (1-\kappa) \begin{pmatrix} 1-g_1 & -g_2 \\ g_2 & 1+g_1 \end{pmatrix} \tag{2.20}$$

The reduced shear $|g| \approx |\epsilon| = (1-b/a)/(1+b/a)$, thus

$$\langle \epsilon \rangle = \langle g \rangle = \left\langle \frac{\gamma}{1-\kappa} \right\rangle \tag{2.21}$$

In the weak lensing limit this means that the measured ellipticity directly gives the shear.

The detection of weak lensing requires deep observations of the clusters in order to obtain background galaxy number counts of around $N_{gal} \sim 60-100$ square arcminutes for ground based observations (Smith et al., 2005), as the background galaxies that are weakly distorted are very small, and the shears resulting from ellipticities may be hard to extract if the signal to noise ratio is too low, or the image suffers from bad seeing. The accuracy of the results depend on the number of sources detected and the precision of the shape measurement. This precision is also greatly affect by instrumental effects such as the *Point Spread Function* (PSF) of the telescope. The PSF must be measurable, in order to remove this effect from the measured galaxy shapes. This can be achieved by measuring the ellipticities of the images of stars. If there are enough stars in the image, a PSF map can be generated, which can then be used to correct for the PSF in the measured ellipticities of the background galaxies (Jarvis & Jain, 2004; Jain et al., 2006). Another source of errors in weak lensing shear measurement is the intrinsic ellipticities of the galaxies themselves. Compensating for these errors is part of the development of the mass reconstruction methods (detailed in § 2.6).

2.5.1 Mass Sheet Degeneracy

Finally, the reduced shear found from the observations is independent of a scaling factor applied to the original lensing Jacobian. Consider a transformation $A \mapsto \lambda A$, where λ is some scalar constant. Then the convergence κ and the shear γ scale as,

$$1-\kappa' = \lambda(1-\kappa) \quad \gamma' = \lambda\gamma \tag{2.22}$$

and the reduced shear becomes,

$$g' = \frac{\gamma'}{1-\kappa'} = \frac{\lambda\gamma}{\lambda(1-\kappa)} = \frac{\gamma}{1-\kappa} = g \tag{2.23}$$

This problem is known as the Mass Sheet Degeneracy (Falco et al., 1985; Schneider & Seitz, 1995; Bradač et al., 2004a) as it can be considered as $\kappa(\theta)$ plus a constant mass sheet of $(1-\lambda)$. It can be broken by either finding the redshift distribution of the sources and solving for different lens geometries, by considering the magnification of the sources, as $\mu' = \det A^{-1} =$

$((1-\kappa'^2)-\gamma'^2)^{-1} \propto \lambda^{-2}$, or it can be broken by mass constraints from strong lensing in the cluster core region to normalised the weak lens masses (Narayan & Bartelmann, 1996; Bartelmann & Schneider, 2001; Kochanek, 2004; Schneider, 2006b,c).

2.6 Weak Lens Mass Reconstruction

A wide variety of methods now exist for weak lensing reconstruction, and can be divided in several types. The most fundamental categorisation is parameteric versus non-parametric. Parametric techniques use a physically motivated model to fit to the data. Non-parametric methods use no model, and allow great freedom in the form of the reconstructed potential. Non-parametric methods can further be classified as direct and indirect. Direct methods obtain the potential directly from the shear measurements, by inverting the lens potential and shear relation in fourier space, while indirect methods test the likelihood of a probable potential model by comparing the predicted shear field against the observed shear field.

Non-parameterised methods are useful for developing spatial mass distribution maps where little is known about the underlying cluster complexity. However, the result is not constrained by physics and can be unrealistic. Parameterised methods offer control over the form of the mass distribution, but require simplifying assumptions to be made about the cluster complexity and symmetry. Using the non-parameterised methods to develop priors on the distribution of the mass and then refitting with parameterised models can utilise the advantages of both techniques.

Indirect and direct non-parameterised can be used in conjunction to provide even tighter constraints on the reconstructed distribution, and break the mass sheet degeneracy (Seitz et al., 1998). While the direct methods deliver computationally fast results, the maximum likelihood methods results suffer less from boundary artifacts. One such method is LENSENT2 (Bridle et al., 1998; Marshall et al., 2002), a maximum entropy based technique that produces a reconstruction of the cluster potential from weak lensing shear data and estimates of the total cluster

mass. Parameterised models can be considered in a similar fashion by changing the potential to be optimised with a model described by a set of parameters. LENSTOOL, (Jullo et al., 2007) is ray tracing software that can find the best fit parameters for many different types of model to a catalogue of faint galaxy shears. Both LENSENT2 and LENSTOOL use Bayesian statistics to find the most probable mass distribution, and employ Monte Carlo Markov Chain algorithms to converge on the result. Using Bayesian statistics provides a goodness of fit parameter that can be used to determine the most optimum model characteristics to include: for example, in LENSENT2, this could be the smoothing width that characterises the large scale cluster potential, whereas in LENSTOOL, this can be the form of the model (isothermal, elliptical) or the model complexity.

In this section I introduce Bayesian statistics, used by both parameterised and non-parameterised methods, and then the parameterised and non-parameterised methods, and their application to our data, are described in more detail.

2.6.1 Bayesian Statistics

In this section I will give an overview of Bayes' Theorem and its application in model and parameter fitting, introduce maximum entropy analysis for non-parameterised systems. For more indepth information, I refer the reader to Sivia (2008); Norris (2007).

Bayes Theorem (Eq. 2.25) describes the posterior *probability distribution function* (PDF) of a model or set of parameters (θ), given the data (D) and some prior knowledge (I), in terms of the likelihood of obtaining the data given the model and the prior information, and the likelihood of the model given the prior information. The likelihood of the data given the prior information is a normalization constant, and is usually used to determine the suitability of the prior information, and is called the *evidence*. Bayes Theorem follows easily from the basic laws of probability,

starting with the product rule,

$$\begin{gathered} prob(\theta, D|I) = prob(\theta|D, I) \times prob(D|I) \\ prob(\theta, D|I) = prob(D, \theta|I) \therefore \\ prob(\theta|D, I) \times prob(D|I) = prob(D|\theta, I) \times prob(\theta|I) \end{gathered} \tag{2.24}$$

which rearranges to

$$prob(\theta|D, I) = \frac{prob(D|\theta, I) \times prob(\theta|I)}{prob(D|I)} \tag{2.25}$$

Maximum Likelihood and Least Squares

If the model is well defined, with a fixed set of parameters to optimise, Bayes' theorem can be combined with a *maximum likelihood* treatment to obtain the results. This approach depends on some simplifying assumptions. First, the prior is set to be a constant, indicating that not much about the model is known before hand. As a result the posterior PDF becomes proportional to the likelihood function, and the analysis reduces to finding the model or set of parameters that maximises this side of the relation. The second assumption is that the distribution of errors on the data is Gaussian. Then for each data point, the likelihood function can be written as Eq. 2.26.

$$prob(D_i|\theta, I) = \frac{1}{\sigma_i \sqrt{2\pi}} \exp\left[-\frac{(\bar{D}_i - D_i)^2}{2\sigma_i^2}\right] \tag{2.26}$$

where σ_i represents the error on point i and $\bar{D}_i$ is the noiseless data measurement. The relation of $\bar{D}_i$ to D_i and the size of σ_i should be predicted as part of the prior information, θ, I. If we then assume that each data point i is independent, the total likelihood function is the product of the likelihoods of all N data points,

$$\begin{gathered} prob(D|\theta, I) \propto \exp\left[-\tfrac{(\bar{D}_1 - D_1)^2}{2\sigma_1^2}\right] \times \ldots \times \exp\left[-\tfrac{(\bar{D}_N - D_N)^2}{2\sigma_N^2}\right] \\ prob(D|\theta, I) \propto \exp\left[-\tfrac{(\bar{D}_1 - D_1)^2}{2\sigma_1^2} + \ldots + -\tfrac{(\bar{D}_N - D_N)^2}{2\sigma_N^2}\right] \\ prob(D|\theta, I) \propto \exp\left[-\textstyle\sum_i^N \tfrac{(\bar{D}_i - D_i)^2}{2\sigma_i^2}\right] \end{gathered} \tag{2.27}$$

The exponent is equivalent to the sum of the squares of the residuals, or χ^2. Thus the likehood function can be rewritten as Eq. 2.28,

$$prob(D|\theta, I) \propto \exp\left(-\frac{\chi^2}{2}\right) \tag{2.28}$$

Going back to our assumption of a uniform(flat) prior, then the logarithm of the PDF becomes,

$$\log_e prob(\theta|D,I) = C - \frac{\chi^2}{2} \tag{2.29}$$

The PDF is maximised when χ^2 is minimised. This is called *least squares* and this formalisation is common in data analysis.

Maximum Entropy

In some situations parameterising the problem is very difficult, such as when trying to reconstruct the 2D surface mass density using weak shear measurements. In this case, assuming the physical quantity you are trying to reconstruct is positive and additive, it is easier to interpret the problem as trying to determine the amplitude at different points on a grid, j. Then the prior PDF is no longer uniform, and can be described by an entropic prior, Eq. 2.30.

$$prob(a_j|m_j,\alpha,I) \propto \exp(\alpha S) \tag{2.30}$$

where a_j describes the amplitude in each bin j, S is the entropy of a_j relative to m_j, the *lebesgue measure*, and α is the entropic regularization parameter, controlling how much amplitude in total is allowed into the system, and preventing overfitting too small scale perturbations.

The posterior PDF then becomes Eq. 2.31, which can be seen as constrained minimisation of χ^2, with the entropic prior acting as a regularizer.

$$prob(a_j|D_i,m_j,\alpha,I) \propto \exp\left[\alpha S - \frac{\chi^2}{2}\right] \tag{2.31}$$

The result,$\hat{\kappa}$ is found by maximising $\alpha S - \frac{\chi^2}{2}$ for each bin j on the grid. Examples of weak lensing mass reconstruction methods using maximum likelihood and maximum entropy algorithms are discussed below.

2.6.2 Non-parameterised Methods

In this section I will discuss the development of non-parameterised mass reconstruction methods, and the differences between direct inversion and indirect techniques.//

Multiple mass reconstruction methods have been developed since Kaiser & Squires first developed their inversion technique in 1993. The early methods sought to improve on the KS method, correcting for boundary artefacts and the mass sheet degeneracy (Seitz & Schneider, 1996). Bartelmann et al. (1996) developed a maximum likelihood technique, based on a χ^2 fit of a model to the data. In 1998, Bridle et al. and Seitz et al. used entropy as the regulating factor in a new maximum likelihood technique. Bridle et al. first developed LENSENT, a package to perform maximum entropy mass reconstruction. Then in 1999 Lombardi & Bertin derived a direct method from variational principles, that was also independently described by Seitz & Schneider (2001), that allowed for fast direct techniques that improved on the computational cost of the previous direct finite field method. (Marshall et al., 2002) modified LENSENT to treat each galaxy individually, producing LENSENT2.

Ideally a cluster mass reconstruction based on lensing needs to break the mass sheet degeneracy, return a unique model for the two-dimensional mass distribution and minimise the impact from the intrinsic ellipticities of the background sources and PSF problems. Kaiser & Squires (1993) formulated a model independent inversion technique for mass reconstruction. While the problem had been solved for a theoretical shear field, this paper solved it for a solution in real space, considering not only continuous fields, but also discrete galaxy catalogue data. Kaiser and Squires did this by solving for the continuous distortion field case, then using a practical estimator to convert this method to real space. The drawback of this method is that the intrinsic galaxy ellipticities causes infinite noise when applying the estimator, which requires filtering to compensate.

Given a lensing deflection potential φ we can define the shear γ and convergence κ as

$$2\kappa = \nabla^2\varphi(\bar{\theta}) = \varphi^2_{,11} + \varphi^2_{,22} \quad \textit{and} \quad \gamma = \{(\varphi^2_{,11} - \varphi^2_{,22})/2, \varphi_{,12}\} \tag{2.32}$$

both are linear combinations of φ, so γ can be expressed as a convolution of κ with a kernel D, where D describes the shear created by a point mass,

$$\gamma(\theta) = \frac{1}{\pi}\int_{\Re^2} d^2\theta' D(\theta-\theta')\kappa(\theta') \tag{2.33}$$

where the kernel is given by,

$$D = -\frac{\theta_1^2-\theta_2^2+2i\theta_1\theta_2}{|\theta^4|} \tag{2.34}$$

Then the Fourier transforms of the shear, convergence and kernel are given by,

$$\hat{\gamma_1}(\bar{k}) = -\frac{1}{2}(k_1^2-k_2^2)\hat{\varphi}(\bar{k}) \qquad \hat{\gamma_2}(\bar{k}) = -k_1k_2\hat{\varphi}(\mathrm{a}\bar{r}k) \tag{2.35}$$

$$\hat{\kappa}(\bar{k}) = -\frac{1}{2}(k_1^2+k_2^2)\hat{\varphi}(\bar{k}) \tag{2.36}$$

$$\hat{D}(\bar{k}) = \pi\frac{|k_1^2-k_2^2+2ik_1k_2|}{|k^2|} \tag{2.37}$$

then the convolution can be written in Fourier space as,

$$\hat{\gamma}(\bar{k}) = \frac{1}{\pi}\hat{D}(\bar{k})\hat{\kappa}(\bar{k}) \tag{2.38}$$

where $k \neq 0$. This relation can be inverted to give

$$\hat{\kappa}(\bar{k}) = \frac{1}{\pi}\hat{D}^*(\bar{k})\hat{\gamma}(\bar{k}) \tag{2.39}$$

where * denotes the complex conjugate. Then performing an inverse Fourier transform gives the result,

$$\kappa(\bar{\theta}) = \kappa_0 + \frac{1}{\pi}\int_{\Re^2} d^2\theta' D^*(\theta-\theta')\gamma(\theta') \tag{2.40}$$

which can be converted to consider discrete shear measurement from a catalogue,

$$\kappa(\bar{\theta}) = \kappa_0 + \frac{1}{n\pi}\sum_g D^*(\theta-\theta_g)\epsilon \tag{2.41}$$

and ϵ is the measured ellipticity of galaxy image denoted by g (Kaiser & Squires, 1993; Squires & Kaiser, 1996; Narayan & Bartelmann, 1996; Schneider, 2006c). This method is limited in that it only applies to weak data, as strong lensing is non linear and makes the inversion method complicated, and assumes the field is infinite. If applied to the more realistic finite field, i.e. the field of a camera on a telescope, the method generates boundary effects. Seitz &

Schneider (1996) (hereafter SS96) derived a finite field version of the above inversion method by considering a finite field kernel that minimised the observational noise. It was based on their previous work which extended the Kaiser and Squires method into the strong lensing regime (Seitz & Schneider, 1995; Schneider & Seitz, 1995). Consider the vector field $\underline{u}$, defined as the gradient of $K = \ln(1-\kappa(\theta))$,

$$\underline{u} = \nabla K(\theta) \tag{2.42}$$

SS96 found that u is not completely a gradient field; that due to noise from intrinsic image ellipticities and the discrete data approximation, it has a rotational component.

$$\underline{u} = \nabla \widetilde{K}(\theta) + rot\ s(\theta) \tag{2.43}$$

Here $s(\theta)$ is a scalar field. The various finite field methods differ in how they treat this noise component. SS96 minimised this by imposing two conditions: the mean of $rot\ s(\theta)$ is zero over the data field U to remove the systematic noise component, and $rot\ s(\theta)$ is zero if $\underline{u}$ is a gradient field. The two conditions can be satisfied by setting s equal to zero on the boundary δU of U. As the noise component is random, then the mean difference between $\nabla\widetilde{K}$ and ∇K is zero, while the mass sheet degeneracy means K has an additive constant, denoted $\bar{K}$. Now SS96 introduce their finite field noise minimising kernel H,

$$K(\theta) - \bar{K} = \int H(\theta', \theta) \cdot u(\theta') . d^2\theta'_U \tag{2.44}$$

A unique solution for this kernel is obtained by setting H to be a gradient field with the Neumann boundary conditions,

$$cH(\theta', \theta).n(\theta) = 0 \qquad on\ \ \delta U \tag{2.45}$$

$$\nabla \cdot H(\theta', \theta) = -\delta(\theta' - \theta) + \frac{1}{A} \tag{2.46}$$

where A is the area of the field. They found that estimator was slightly more noisy then the Kaiser and Squires method, but was less noisy then other finite field methods, and removed the boundary effects in the original Kaiser and Squires method. However, evaluating H is very costly in computer time, and so the maximum grid size that it can be reconstructed on is limited. This means that large fields or those that have an irregular shape take impractical lengths of time

to analyze. Seitz & Schneider (2001) improved on their earlier method by finding a simpler way to solve for K.

$$\nabla^2 K = \nabla \cdot \underline{u} \tag{2.47}$$

As in the 1996 method, $s(\theta)$ equals a constant on the boundary of U, then this rotational component is perpendicular to the normal vector $\underline{n}$ on this boundary, and

$$\underline{n} \cdot \nabla K = \underline{n} \cdot \underline{u} \tag{2.48}$$

Now K is obtained by solving the Neumann problem, instead of H. This can be applied to any type of field U and the computational methods for solving this are faster then those needed to evaluate H. Further numerical tests showed the noise restriction was comparable to the 1996 method.

But while a direct method such as this and the KS93 method are computationally very fast, they cannot account very easily for magnification or strong lensing constraints, which makes it hard to break the mass sheet degeneracy, and the choice of smoothing parameter can be arbitrary.

Bartelmann et al. (1996) developed a maximum likelihood method based on a least χ^2 fit of a two-dimensional cluster potential to an observed shear pattern. Once the observed shears and sizes are averaged locally and smoothed, then for a grid of cells (k,l), each have a reduced shear value g_i and magnification μ. Then as both the shear and the convergence are related to φ (Eq. 2.13, 2.14) the second partial derivations of φ are converted into second order finite difference approximations, and the χ^2 function can be written as

$$\chi^2 = \sum_{k,l} \frac{1}{\sigma_g(k,l)} [g_i(k,l) - \hat{g}_i(k,l)]^2 + \frac{1}{\sigma_r(k,l)} [r(k,l) - \hat{r}(k,l)]^2 \tag{2.49}$$

where $r = \mu^{-1}$, $\hat{g}$ and $\hat{r}$ are the values obtained from model φ and σ_g, σ_r are estimated from the data. Then χ^2 is minimised to produce the potential model parameters that best fit the shear data.

The reconstruction was then tested and compared with a simulated cluster model. As seen Fig 2.6.2, (Bartelmann et al., 1996), the maximum likelihood method accurately reproduced

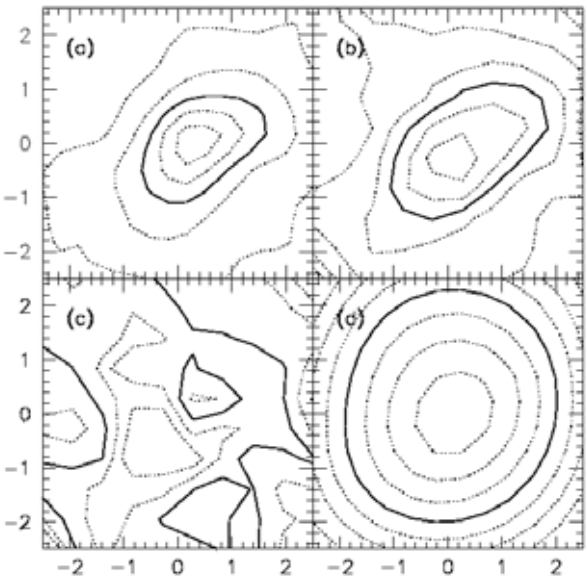

Figure 2.3: Original caption (Bartelmann et al., 1996): "Four contour plots showing the original cluster model in panel(a), the reconstruction in panel (b), the difference between the two in panel(c), and the dimensionless two-dimensional potential in panel(d). Contours in panels (a) and (b) a respaced by 0.1 and the heavy contour follows $\kappa = 0.5$. In panel(c) the contours are spaced by 0.05 and the heavy contour follows $\Delta\kappa = 0$. The potential is kept fixed at $\varphi = 0$ at three corners. The heavy line in panel(d) follows the arbitrary contour $\varphi = 5$ and the contours are spaced by 1.5. The side length of the fields is 5'."

the mass distribution of the cluster. The inclusion of magnification data breaks the mass sheet degeneracy, and by focusing on recovering the potential rather then the shear field, as shear and convergence are related to each other through the potential, this method also limits the noise. These inverse methods are more accurate then the direct methods (the Kaiser and Squires Inversion, and all methods based upon it) above, but take much more computation time.

Squires & Kaiser (1996) addressed the increased noise of the Seitz and Schneider method compared to the 1993 KS method. KS96 constructed an exact inverse gradient operator in Fourier space that performed favourably compared to previous finite field methods. They also expanded on the maximum likelihood method, finding the best results included a Fourier space regulariser, which demanded that the mass density coefficients be taken from a Gaussian distribution. One of the benefits of this method was that unlike using a usual Laplacian regulariser, the noise components were small at all frequencies. The method was also very fast, and could conserve spatial resolution. An important feature was it could also be extended to include strong

lensing constraints, leading to more accurate modelling of the mass distribution in the core of the cluster.

The maximum likelihood method with Fourier regulariser is a case of maximum entropy reconstruction (Bridle et al., 1998). Seitz et al. (1998) (hereafter SSB98) and Bridle et al. (1998) (hereafter B98), in 1998, both considered the case of maximum entropy reconstruction. Where Seitz et al. sought to reconstruct the lensing potential, Bridle et al. sought to reconstruct surface mass density at the grid points.

SSB98 notes that the integral noise in the ellipticity measurements is due to the intrinsic ellipticity distribution of the sources. When performing a maximum likelihood fit, this noise causes the model to try and fit to small scale fluctuations rather then the actual distribution. SSB98 compensates for this by using an entropic regulariser, which dampens the noise signal. This method seeks to minimise

$$E(\{\varphi\}) \doteq -\frac{1}{N_g}\ln L(\{\varphi\}) + \eta R(\{\varphi\}) \tag{2.50}$$

where L is the likelihood function, η weights the smoothness and R, the entropic regulariser, is,

$$R = \sum_{i,j=1}^{N_x N_y} \hat{\kappa}_{ij} \ln\left(\frac{\hat{\kappa}_{ij}}{b_{ij}}\right) \tag{2.51}$$

Here $\hat{\kappa}$ is the normalised surface density at grid points, and the prior b is found by using a direct reconstruction as the initial prior, minimising E a few times, then using a smoothed version of the resulting distribution as the ultimate prior. The resulting algorithm was faster than Bridle's grid based method, could be adapted to any geometry, and could even include magnification information, strong lensing constraints, and information on observational errors.

In B98, the inversion is regularised by an entropic prior, $S(\kappa, \underline{m})$ (Eq. 2.52). This prior describes the cross entropy between the real shear field, κ, and the model shear field, m,

$$S(\kappa, \underline{m}) = \sum_{j=2}^{L} \kappa(j) - m(j) - \kappa(j)\ln\left[\frac{\kappa(j)}{m(j)}\right] \tag{2.52}$$

and the probability of obtaining the observed ellipticities given a convergence κ, assuming Gaussian errors and non correlated observed data, is given by Eq. 2.31, as in § 2.6.1. This method was particularly useful when reconstructing the mass of clusters for which the observing field is an odd shape or smaller then usual, as previously this required using more grid points and was very expensive computationally.

So far these inversion methods have required regularization to prevent over fitting, and in most cases the data is binned before being analysed. Marshall et al. (2002), like SSB98, took the inversion technique of Bartelmann et al. (1996) and B98 and extended it to consider each background galaxy measurement discretely, rather than taking a local average. To do this they chose the reconstruction grid to have one galaxy per pixel, and denoted the observed ellipticity of that galaxy as ϵ_i. A predicted reduced shear field was generated using a model mass distribution and the relations used in KS93:

$$g(\theta) = \frac{1}{1-\kappa(\theta)} \cdot \frac{1}{\pi} \int D(\theta-\theta')\kappa(\theta')d^2\theta' \tag{2.53}$$

Then the likelihood of the data given the model can be written as

$$Pr(data|\Sigma) = \frac{1}{z_L} \exp -\frac{\chi^2}{2} \tag{2.54}$$

$$\chi^2 = \sum_{i=1}^{N} \sum_{j=1}^{2} \frac{(\epsilon_{j,i} - g_{j,i})^2}{\sigma^2} \tag{2.55}$$

where the error σ takes into account both the observational error and intrinsic ellipticities of the sources, and z_L is a normalisation factor. Finally, to account for the model of a cluster as a smooth extended distribution, an *intrinsic correlation function* (ICF) is used, which replaces the smoothing used in the previous methods. This maximum entropy method was originally applied in the program LENSENT (B98), and was very successful at reconstructing accurate mass distributions. In 2002 an improved version, LENSENT2, was released (Marshall, 2001; Marshall et al., 2002; Bradač et al., 2004b; Bradač, 2004; Bradač et al., 2006), and this version was used to obtain non-parameterised mass reconstructions of the clusters in our sample.

The Aperture Mass Statistic and Densitometry

The other, main non-parameterised method of obtaining information on the DM density field from weak shear data is the Aperture Mass Statistic (AMS), and its use in determining the 2D mass distribution and mass peak positions, called Aperture Mass Densitometry. The AMS measures the convergence, κ, within an aperture, which is proportional to the mass within that aperture, by relating it to observable local faint galaxy shear (Eq. 2.56) (Fahlman et al., 1994; Kaiser, 1995; Schneider, 1996; Clowe et al., 1998),

$$\xi(_1) = \bar{\kappa}(r < r_1) - \bar{\kappa}(r_1 < r < r_{max}) = 2\left(1 - \frac{r_1^2}{r_{max}^2}\right)\int_{r_1}^{r_{max}} < \gamma_T > dlnr \qquad (2.56)$$

The mass can then derived using the relation $M(< r_1) = \pi D_L^2 r_1^2 \Sigma_{crit} \xi(_1)$. By placing multiple apertures over the field, this statistic can be used to locate mass peaks and assess their significance with respect to the κ background, far more simply than the complex direct and indirect algorithms described above (Schneider et al., 1998). The AMS can be to provide lower bounds on the mass within the aperture, and is very useful for detecting structures in weak lens surveys where the centre of the mass distribution is not known, or for detecting large scale structure, where there low signal and extended shape means a sharply significant central mass peak is hard to locate (Jarvis et al., 2004). In this thesis work I focus on the maximum entropy based LENSENT2 algorithm, and do not use this statistic.

2.6.3 Parameterised Methods and LENSTOOL

The previous methods are parameter free, focusing on either directly finding κ from the shear measurements or fitting the most likely potential to the shear data. While parameter free methods allow more freedom in fitting disturbed or unusual clusters,the interpretation of the results suffers from the fact that the potential recovered may have no physical basis; it is just the solution that best fits the data. Parameterised methods allow the models to be fitted with generally fewer free parameters then non-parametric methods. Physical assumptions, such as symmtery, model complexity (possibly motivated by a non-parameterised reconstruction) and centering

the mass distribution on the BCG, make the interpretation of the results clearer. The models can be constructed so it is easier to extract meaningful physical quantities from the results, such as mass or velocity dispersion. Another advantage of parameterised models is the use of 'stacking' to obtain averaged weak lens mass distributions of structures, such as groups and galaxies, that would be too undermassive to have a significant shear signal for non-parameterised reconstruction (Hoekstra et al., 2001, 2003, 2004; Mandelbaum et al., 2006; Leauthaud et al., 2010). But parameterised models require some prior understanding of the existing structure in the cluster, otherwise information on complexity in the mass distribution may be lost if the model fitted to the data is too simple. Similar stacking only returns an average distribution that will have necessarily assumed symmetry and a model with limited complexity.

Early implementation of parameterised modelling included Kochanek (1990), who investigated fitting a parameterised model to the observed ellipticities in A370, in order to extract the global potential of the cluster. Miralda-Escude followed in 1991, but probing the accuracy to which the parameters could be obtained via fitting. Both concluded that while this accuracy was severely limited by the intrinsic ellipticity distribution, they could reconstruct the mass distribution of a cluster with parameterised fitting. Much progress has since been made on constraining the systematics in parameterised modelling, and investigating the impact of DM substructure and projection effects.King et al. (2001) found that adding substructure to the underlying mass distribution increased the error in the best fit parameters by 3%, and even doubling the amplitude of the substructure caused only a 10% increase in the parameter dispersion. Hoekstra (2003) noted that this result did not take into account line of sight large scale substructure, and found that the errors in M_{200} and c were twice as large than when this was accounted for.

Other systematics can be introduced when using an inappropriate model to fit that data. King et al. (2002) used a shear maximum likelihood analysis to fit a 3 parameter Singular Isothermal Ellipsoid (SIE) (Kormann et al., 1994) and a 2 parameter Navarro-Frenk-White (NFW) (Navarro et al., 1997) profile to A1689. They found the NFW proved a better fit, and found that fitting

the deviation from the isothermal profile was more fundamental than fitting the non circular symmetry. Corless & King (2007) found that when ellipticity of the cluster was extended along the line of sight, the mass of the cluster was overestimated by 50% and the concentration c was doubled. Clowe et al. (2004a) concluded that the dominant effect causing parameter variation was ellipticity along the line of sight, whereas substructure along the line of sight had only a minor influence.

Finally, SL and WL in combination with parameterised modelling can provide constraints on the entirety of the cluster DM profile, and on the mechanics of structure formation. Kneib et al. (2003) used strong lensing constraints from CL0024+1654 to obtain a core mass measurement, then combined this with weak lensing data to test the fit of a NFW-like halo on the scales of $0.1-5$Mpc. They found that the NFW profile best fitted the cluster, and that the mean mass to light ratio of the cluster was constant over this range. From these results they concluded that the clusters primarily grow via accretion of groups, not individual galaxies.

The parameterised modelling can be performed in several ways. The tangential shear can be binned as a function of radius, and then a χ^2 analysis performed to obtain the best fit parameters for the model. This method assumes spherical symmetry and uses radial binning, which may not be appropriate depending on the geometry of the cluster. Alternatively, the log-likelihood function can be minimised to obtain the best fit parameters for a particular model (Schneider, 2006c),

$$-\ln\ell = \sum_{i=1}^{N_g} \frac{|\epsilon_i - g(\theta_i,\{a,b,c,...\})|^2}{\sigma_i^2(\theta_i,\{a,b,c,...\})} + 2\ln\sigma_i(\theta_i,\{a,b,c,...\}) \tag{2.57}$$

where σ_i is based on assuming the intrinsic ellipticities follow a Gaussian with width σ_ϵ, then,

$$\sigma_i \approx \sigma_\epsilon(1-|g(\theta_i,\{a,b,c,...\})|^2) \tag{2.58}$$

and $\{a,b,c,...\}$ represents the set of parameters of the model to be fitted. Depending on the choice of model, the fit returns different parameters.

LENSTOOL (Jullo et al., 2007)[1] uses Bayesian optimisation to find the best fit parameters to a chosen model. An important feature of LENSTOOL is using the difference between the logged evidence to determine the optimum model: $\Delta(ln(E_i) - ln(E_j) > 1$ implies that model i is significantly more likely than model j (Jeffreys, 1961).

LENSTOOL convergences on the posterior PDF using Monte Carlo Markov Chains (MCMC). At each step in the optimisation, ten random samples are taken from the current estimate of the posterior PDF, one for each MCMC. The likelihood of each sample is calculated, and those with the worst likelihoods are rejected, while those with the best likelihoods are replicated so each chain has a sample. The duplicated samples are then randomly shifted in the parameter space to ensure each chain is independent. The ten samples are then added to the chains and used as the basis for the next calculation of the posterior PDF. The random selection of samples at step is designed to prevent the optimisation from falling into a local maxima. As a result, the output from LENSTOOL is a list of samples from the posterior PDF, but with more samples from where the PDF is highest.

In order to ensure enough samples are drawn in order to constrain the parameters being fitted, LENSTOOL uses an *annealing* cooling factor, γ (Eq. 2.59) At the start of the optimisation, γ is increased from zero to one at each step, by increments of $\delta\gamma$. $\delta\gamma$ is found by calculating the maximum and mean likelihoods of 10 randomly drawn samples, and applying this factor to a rate parameter set by the user, $\delta\gamma \sim RATE/(ln(L_{max}) - ln(\hat{L}))$. At the start of the convergence, and whenever the sample likelihoods are very disparate, $\delta\gamma$ becomes very small, and the convergence slows down. The smaller the rate parameter, the slower the convergence, and the optimisation is more accurate. However, very small rate parameters make the optimisation computationally expensive.

$$Pr(\theta|D,M) = \frac{Pr(D|\theta,M)^{\gamma} Pr(\theta|M)}{Pr(D|M)} \tag{2.59}$$

[1] LENSTOOL is available from http://www.oamp.fr/cosmology/lenstool/

Although the use of parameterised models means small scale complexity is lost, and essentially imposes a smoothing of the potential, with the correct prior information, large scale structure within the cluster can be constrained. LENSTOOL has had success in reconstructing the mass profiles of clusters (Smith et al., 2005; Limousin et al., 2007b; Richard et al., 2007), and can include strong lens constraints, and so was chosen for the parameterised fitting in this analysis, details of which are discussed in depth in § 4.

Pseudo Isothermal Elliptic Mass Distributions

Pseudo Isothermal Elliptic Mass Distributions (PIEMD) (Kassiola & Kovner, 1993) are used in this analysis to describe the cluster and cluster galaxy DM haloes. The PIEMD accounts for ellipticity in the mass distribution, yet also matches the isothermal slope in the SL region of the core, while also being analytically integrable and not too computationally expensive to do so. The truncated PIEMD (Kneib et al., 1996) consists of a superposition of two PIEMD haloes, and chosen to take into account tidal stripping of subhaloes within clusters (Limousin et al., 2005) and for ease of comparison with (Smith et al., 2005). The truncated PIEMD is described below, using the notation in (Kneib et al., 1996).

$$\Sigma(x,y) = \Sigma_0 \frac{r_c r_{cut}}{r_{cut} - r_c} \left(\frac{1}{\sqrt{r_c^2 + \rho^2}} - \frac{1}{\sqrt{r_{cut}^2 + \rho^2}} \right) \tag{2.60}$$

where ρ and M_{tot} are defined as follows,

$$\begin{aligned} \rho^2 &= \tfrac{x^2}{(1+\epsilon)^2} + \tfrac{y^2}{(1-\epsilon)^2} \\ \epsilon &= (a-b/a+b) \\ M_{tot} &= \tfrac{\pi}{G} \sigma_0^2 r_{cut}^2 \end{aligned} \tag{2.61}$$

Here r_{cut} is the truncation radius, with the surface mass density falling as r^{-3} if $r >> R_{cut}$. Between r_{core} and r_{cut} the slope is isothermal (density falling as r^{-2}).

2.6.4 Complications in Weak Lens Observing

Point Spread Function

The Point Spread Function (PSF) of a telescope causes a distortion of all sources it images, and is the result of a combination of distorting effects: atmospheric dispersion, the diffraction pattern of the telescope, focussing issues, etc. The distortion characterised by weak shear can be a degree of magnitude smaller than the distortion caused by the PSF, thus accurate modelling of the PSF is vital to obtaining good measurement of the galactic shears.

The PSF is corrected for by creating a model of the distortion and then deconvolving its impact from the observed sources' shapes. Constructing the PSF model is done by finding the distortion in the shapes of stars. Stars should be observed as point sources on the sky, and therefore can be described using a δ-function. The PSF causes the images of the stars to be blurred and measuring the degree of this smearing on stars that sample the full field of view of the image means we can build a map of the PSF distortion. However, problems arise when there are few stars in the image, or when the positions of the stars doesn't evenly sample the field of view. For many observatories, PSF correction can be achieved by using images of globular clusters, where the high density of stars means the PSF can be accurately modelled over the whole image. Alternatively, if the PSF is stable, then the stars from several images with similar observing conditions can be combined to create an average PSF map for the sample.

The PSF of the Advanced Camera for Surverys on the Hubble Space telescope (HST:ACS) is a particular challenge to model as the PSF changes over time as the telescope changes temperature and ages, thus making it difficult to use standard PSF models from images of globular clusters, or from combining star catalogues from a set of observations (Rhodes et al., 2007). The observations were taken over a period of several months, therefore we could not stack the images to obtain an average PSF. Instead, we individually modelled the PSF in each image, then used the average ellipticities of the stars to match clusters with similar PSFs, and thus augmented the PSF modelling with stars from both images. To do so we used a Bayesian shape

fitting code called IM2SHAPE(Bridle et al., 2002)[2].

IM2SHAPE uses Bayesian parameter estimation to fit *N* Gaussians to object images. It starts by taking in a list of object positions, and takes a snapshot of each object in the list. Then each object is treated as a convolution of a PSF made from *N* Gaussians, and a galaxy shape made from *M* Gaussians, each Gaussian described by its position, ellipticity, angle, size and amplitude. This treatment makes it easier to deconvolve the PSF from the measured shape. IM2SHAPE then creates Monte Carlo Markov Chains, i.e. computer simulated random walks, for a preset number of steps, and the maximum likelihood method, to converge on the PDF and obtain samples of the parameters. The most probable parameters are then found by obtaining the mean and standard deviation from each set of parameter samples.

The degree to which IM2SHAPE can correct for the PSF was tested as part of the Shear Testing Programme (STEP) (Heymans et al., 2006; Massey et al., 2007). This tested the ability of several different shape measurement and non-parameterised weak lens reconstruction methods to correct for the PSF and detect cosmic shear, the weak lensing of faint galaxy sources from all structure along the line of sight. The programme found that IM2SHAPE performed well, and successfully removed the PSF, measuring the cosmic shear to an accuracy of 4%. It noted that the number of iterations that IM2SHAPE uses to converge on the shape PDF can bias the shape parameter distributions if this number if too low. The programme recommended increasing the number of iterations until the shape parameters converged, as I demonstrate my results do in § 3.5.

;Our PSF correction was performed by using IM2SHAPE to fit a double Gaussian to the stars. The stellar shapes were then compared to a δ-function, and the ;residuals were smoothed to form a map of the PSF. The smoothing scale was dependent on the number of stars and the width of the field of view. After the initial PSF map ;construction, the map was used to correct the stellar ellipticities without refitting them. For those clusters with very few stars, or a poorly sampled field of view, ;the correction combined with stars from one other cluster was also investigated.

[2]IM2SHAPE is available from http://www.sarahbridle.net/im2shape/

Where the correction was improved the final PSF map was made with the augmented star ;catalogue. IM2SHAPE could then use this map when fitting the a single Gaussian to the shapes of the galaxies, to obtain PSF corrected shear measurements accurate ;enough to constrain the DM distribution.

Cluster Contamination

Weak shear analysis requires a catalogue of background galaxies whose images have been impacted to a greater or lesser degree by the lensing power of a foreground system, in our case a galaxy cluster. Cluster contamination refers to the situation where faint cluster members are accidentally included in the background galaxy catalogue. Unlike the background galaxies, the cluster galaxies are randomly orientated, and this, combined with the likelihood that the cluster members are among the brighter background galaxies and thus are likely to have smaller measurement errors, leads to the overall shear signal being diluted. This dilution can be as severe as a factor of 2-5 at $R \leq 400\text{kpc}\,h^{-1}$ (Broadhurst et al., 2005), depending on the observations and the redshift of the cluster.

To reliably remove cluster members from a catalogue, it is necessary to identify the Red Sequence. By obtaining imaging in two separate filters, the Red Sequence galaxies can be removed from the background catalogues (Okabe et al., 2010a,b). However contamination may still be an issue from faint, blue cluster members. The dilution of the weak shear signal in comparison to the signal from galaxies redder than the Red Sequence can be used to create limits on a colour-colour diagram that has had success in producing weak lensing constraints in close agreement with strong lensing constraints (Medezinski et al., 2010; Umetsu et al., 2010), while careful analysis of the dilution effect could be used to further constrain the luminosity profile of the cluster itself (Medezinski et al., 2007)

In the analysis described in this thesis, observations were only available in one filter, V_{606}.

The background galaxy catalogues were constructed using only a magnitude cut, thus cluster contamination will have an impact on the degree to which we can constrain the masses of the clusters. The literature suggests the degree of low mass bias is proportional to the fraction of cluster members and foreground galaxies contaminating the background sample, and is worse when analysing the dense cores of clusters (Medezinski et al., 2007; Umetsu & Broadhurst, 2008). In response, we have modelled the correction in our results assuming varying degrees of cluster contamination in order to fully assess the impact on our cluster mass constraints. For full details see § 4.2.3.

Chapter 3

Observations and Analysis

As established in the Introduction, multi-wavelength analysis of clusters is very important for interpreting their infall history and structural evolution. One of the goals of this thesis is to provide 2D maps of X-ray, Infra-Red and mass structure for comparison, and to use different observational probes to support the weak lens analysis. To this end, Infra-Red, X-ray and optical observations were analysed as part of this thesis work.

In this chapter I describe the galaxy cluster sample selection, and the reduction and initial analysis of the HST:ACS SNAPSHOTS and the multi wavelength data. This includes correction for instruments errors in the ACS, the construction of the PSF corrected faint galaxy shear catalogues, the IR cluster galaxy catalogues, the generation of K-band luminosity based DM distribution priors for the LENSTOOL weak lens modelling, and obtaining projected Hernquist masses from the X-ray data.

3.1 Optical Imaging with the Hubble Space Telescope

3.1.1 Sample Selection

The LoCuSS galaxy cluster sample from which our subsample was drawn consists of over 100 X-ray luminous local galaxy clusters selected from the ROSAT All Sky Survey catalogue, (Böhringer et al., 2004a; Ebeling et al., 2000, 1998), within constraints of $2 \times 10^{44} < L_X < \times 10^{45} \mathrm{ergs}^{-1}$. The redshift range of $0.15 < z < 0.3$ was chosen to be as local and narrow

as possible, to maximise the efficiency of lensing as a tool to probe the cluster mass distribution, avoid considerable evolution within the sample, yet allow $>\sim 100$ clusters in order to get reasonable statistics on cluster complexity and dynamics segregation in the mass-observable scaling relations. Further selection criteria included restriction to those clusters viewable from Hawaii and Chile, $-70^o \leq \delta \leq +70^o$, and a limit on column density to minimise contamination by bright stars ($n_H \leq 7 \times 10^{20}\mathrm{cm}^{-2}$) (Smith, 2006).

Of these > 100 clusters, 21 are studied as part of this thesis work. These clusters have X-ray luminosities ranging from 1.8×10^{44} to $12.3, 26.6 \times 10^{44}\mathrm{ergs}^{-1}$ (the extrema is the Bullet Cluster), and lie between redshifts of 0.1483 and $0.2984, 0.42$ (the extrema is A 3192, which will be discussed in § 6.2), consistent with the original sample. This subsample was selected based on those clusters the HST:ACS was able to observe before it's critical failure in January 2007. This clusters were observed as part of a SNAPSHOT program: shallow observations with short overhead times are slotted into the HST observing schedule where there is time and when the telescope is pointing in the correct direction in the sky. This means that these 17 were not preferentially selected for their mass or luminosity, but for their position on the sky, which should not bias the sample. As one of the goals of this thesis was to improve the statistics on structural segregation of the cluster population by increasing the sample sized used in the Pilot Study, it was decided to search the archives after the ACS failed. Thus the 4 remaining clusters in the subsample were selected from the HST:ACS archive, based on the observations having similar observing conditions and filter choices as the 17 clusters observed explicitly for LoCuSS. Such a heterogenous sample allows us to study the mass distribution of a large range of cluster types, and matches the original aims of the LoCuSS sample construction. While the sample size is not as big as originally planned, it is increased by a factor > 2 compared to the Pilot Study, and thus the statistics will be marginally improved.

3.1.2 Data description

Weak lensing shears are characterised by such small distortions that a significant detection requires many measurements of galaxy ellipticities to be averaged. As a result the measurement of the individual galaxy shape distortions are particularly sensitive to any form of systematics in the observation process. Ground based telescopes suffer from airmass distortion due to differential refraction in the upper atmosphere: the same effect that makes stars twinkle makes it hard to observe fainter objects clearly. Space based observations avoid this problem entirely, allowing data deep enough for weak shear analysis to be obtained with lower exposure times. The *Hubble Space Telescope* (HST) has famously revolutionised space based observation in this respect, and the SNAPSHOT survey program allows for quick and efficient observation of large cluster samples.

As part of HST SNAPSHOT Proposal 10881 (Smith, 2006), seventeen clusters were observed with Advanced Camera for Surveys (ACS), between the 15th of August 2006 and the 26th January 2007. Each cluster was observed for a total $1.2ksec$, split into 3 exposures of $400sec$, through the F606W filter (hereafter V_{606}). Each set of observations followed the ACS WFC line dither pattern, with a shift of ~ 0.3" between each exposures. The archival observations of $A611$, $Z2701$ and $A2537$ from Proposal 9270 (Allen, 2002), were also observed with HST:ACS using the F606W filter, between 22nd October and 3rd December, 2002, for between $2-2.2ksec$. These observations followed the ACS WFC box filter, with 4 pointings each and a 0.265" shift between exposures. The two Bullet Cluster frames, from Proposal 10200 (Jones, 2004) were observed on 21st October 2004, for a total of ~ 2.3 ksec each, split between 4 exposures and using two different line patterns with shifts of 3.0" and 1.265". General cluster and observation details are given in Table 3.1, while the general observation details are listed below, to assist those readers wishing to repeat or assess the reduction.

(i) Gain: 2

(ii) Saturation: $84700e^{-}$

(iii) Zeropoint: M_{F606W} = 32.90 magnitudes for Proposal 10081, M_{F606W} = 33.23 magnitudes for Proposal 9270, M_{F606W} = 33.31 magnitudes for Proposal 10200

3.1.3 Data Reduction

MULTIDRIZZLE (Koekemoer et al., 2002) was used to reduce all 21 clusters. Drizzling is the process of reducing the flat field science products of the ACS into single images, at the same time correcting for the spatial distortion of the camera and removing image defects. The name comes from the 'drizzling' of the observed pixels onto their true positions on the output image. The process involves first drizzling each flat fielded (FLT) science image separately, applying corrections for any image distortions, incorporating sky subtraction and using the result to construct temporary bad pixel masks and weight maps. The separate images are then stacked to create a median image to test and improve the bad pixel detection and improve the image alignment. This median image is then *blotted* to produced a smoothed image, used to detect and remove cosmic rays. Finally the seperate drizzled images are redrizzled onto a combined image with geometric distortion corrected for, cosmic rays removed and bad pixels masked. The drizzling process produces a science and a weight image, with weight based on the exposure time associated with each pixel. The reduction of the observations is described in detail below.

Reduction of Proposal 10081 Observations

The clusters observed for Proposal 10081 were dithered using the *ACS-WFC-DITHER-LINE* pattern with 3 pointings, each offset by $(0.00, 3.01)''$ ($(0, 60)$ pixels at $0.05''/pixel$) from the previous position. Dithering involves taking exposures at different positions on the field of view. Using this method, longer total exposure times can be obtained without over-saturation of pixels. Telescope-specific discrepancies in the image can be identified and corrected for, and cosmic ray detections removed. Sub-pixel shifts also allow resampling of the PSF of the telescope, and for a higher resolution image to be reconstructed.

Table 3.1: Cluster Sample

Cluster	Redshift	RA	DEC	Proposal ID	T_{exp} $[s]$	L_x $[10^{44} ergs\ s^{-1}]$	Alternate Name
A 2813	0.2924	00 43 25.13	-20 37 01.4	10881	1200	8.80	RXC J0043.3-2037
A 0141	0.2300	01 05 37.17	-24 40 49.7	10881	1200	6.66	RXC J0105.5-2439
A 2895	0.2275	01 18 11.04	-26 58 11.7	10881	1200	6.43	RXC J0118.1-2658
RXC J0220.9-3829	0.2280	02 20 56.57	-38 28 48.0	10881	1200	5.82	
A 0368	0.2216	02 37 27.80	-26 30 29.1	10881	1200	4.94	RXC J0237.4-2630
A 3084	0.2192	03 04 04.01	-36 56 27.0	10881	1200	4.68	RXC J0304.1-3656
A 3088	0.2537	03 07 02.19	-28 39 56.9	10881	1200	8.04	RXC J0307.0-2840
RXC J0331.1-2100	0.1880	03 31 05.87	-21 00 32.7	10881	1200	5.04	RBS 0436
A 3140	0.1729	03 36 15.84	-40 37 45.2	10881	1200	5.30	RXC J0336.3-4037
A 3192	0.42	03 58 54.16	-29 55 31.6	10881	1200	2.71	RXC J0358.8-2955
A 3292	0.1501	04 49 56.47	-44 40 24.1	10881	1200	3.29	RXC J0449.9-4440
RXC J0528.2-2942	0.1582	05 28 15.14	-29 43 03.9	10881	1200	2.87	
A 3364	0.1483	05 47 37.79	-31 52 24.9	10881	1200	4.67	RXC J0547.6-3152
AS 0592	0.2266	06 38 45.23	-53 58 23.3	10881	1200	12.27	RXC J0638.7-5358
1ES0657-558	0.296	06 58 35.39	-55 56 57.18	10200	2336	26.63	RXC J658.5-5556
A 611	0.2880	08 00 55.92	36 03 39.6	9270	2160	8.05	
A 781	0.2984	09 20 25.13	30 31 31.9	10881	1200	10.19	
Z 2701	0.2140	09 52 47.52	51 53 27.6	9270	2280	6.32	ZwCL 0949.6+5207
RX J1000.5+4409	0.1530	10 00 31.16	44 08 42.5	10881	1200	1.82	RBS 0819
A 2187	0.1825	16 24 14.08	41 14 36.7	10881	1200	3.11	
A 2537	0.2950	23 08 23.20	-02 11 31.0	9270	2080	11.76	RXC J2308.3-0211

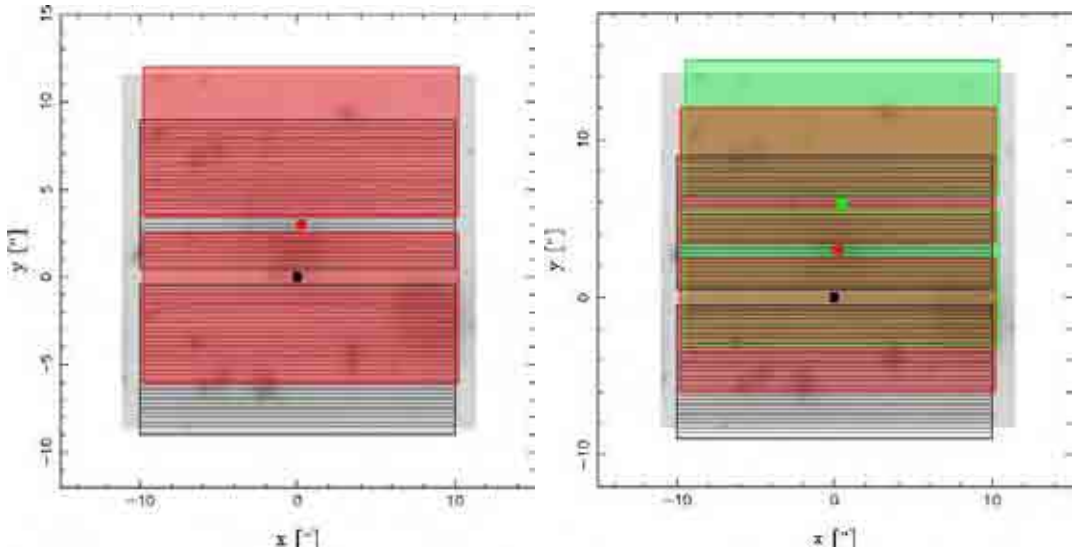

Figure 3.1: Left: 2-point line dither pattern. The different exposures are given in red and black stripes. Although the interchip gap is covered with an observation, it is only singly observed, and artefacts such as hot pixels and cosmic rays cannot be removed. Right: 3-point line dither pattern. An extra dither pointing, in green, means the interchip gap is observed twice over and can be corrected for various phenomena.

Invoking a large dither shift has particular issues for *ACS:WFC* observations due to off-optical inclination of the detector causing changing distortion across the chipset: the larger the shift, the large the change in distortion for any pixel. However, in order to obtain good weak lensing constraints, the shear field needed to be sampled as completely as possible around the cluster, and the clusters were centred just above the interchip gap between the top and bottom *WFC* chipsets. Although the interchip gap can be covered using only 2 dither positions, by using 3 dither positions, the gap is covered by at least 2 exposures, allowing for removal of cosmic rays and for resampling of the PSF in this area. 3-point dither programs optimise the balance between obtaining observations that be cleaned of defects and the limited observation time associated with SNAPSHOTS. Fig. 3.1 shows the coverage of the 2 and 3 dither observation programs. The dithering process results in a poorly sampled region around the edge of the final drizzled image, which ultimately was excluded from analysis.

MULTIDRIZZLE was initially run with the parameters given in MDRIZTAB, a multidrizzle pipeline configuration file from *S*TSDAS. Inspection of the reduced frames revealed a systematic background bias in each quadrant of the image, and long column like features (Fig. 3.2, top

and bottom left). The background issues were traced to differing background levels on the FLT frames. Each frame had two science images, corresponding to the top half and bottom half of the ACS observation. Each science image had a very mild bias between the left and right half of the image that, after reduction, produced the prominent effect found in the drizzled images. The correction of this effect proceeded as follows: the background of each half flat fielded science image was sampled randomly, producing a 3σ clipped average designed to exclude contributions from features in the image. This value was then subtracted from the half science image, and the drizzle process repeated. MULTIDRIZZLE includes its own background correction protocols, and repeated drizzling showed that this performed unsuccessfully when the background was completely subtracted beforehand. By correcting for the bias in the FLT images and then normalising the background to approximately the same value as the entire image, the drizzling process was successful in removing the background (Fig. 3.2, top right).

The removal of the column like features in the images was more involved. These bad columns were found occur in all the cluster science images, and were traced to vertical bad pixel-width columns in the FLT images, which, when drizzled, produced narrow 'tramlines' on the images due to their dithered positions. It was decided to augment the bad pixel masks included in the FLT images to allow MULTIDRIZZLE to remove the columns during the drizzling process. The column data was extracted by averaging all the FLT science 1 and 2 images with 2σ clipping, using the IRAF tool *imcombine*. The images were then smoothed using *rmedian* with a 11 pixel width. This removed the small scale features in the averaged image, leaving only the cluster galaxy contribution. Subtracting this information from the original averaged maps allowed for the large scale features in the summed images to be removed, leaving only the bad pixel columns common to each observation. This process is shown in Fig. 3.3. Using *imexpr*, this information was then added to the existing bad pixel masks. The success of the removal after drizzling using the augmented masks is shown in Fig. 3.2, bottom right. The correction for the background bias and the bad columns was applied to all the archival observations as well, as part of an reduction pipeline applied to all ACS observations.

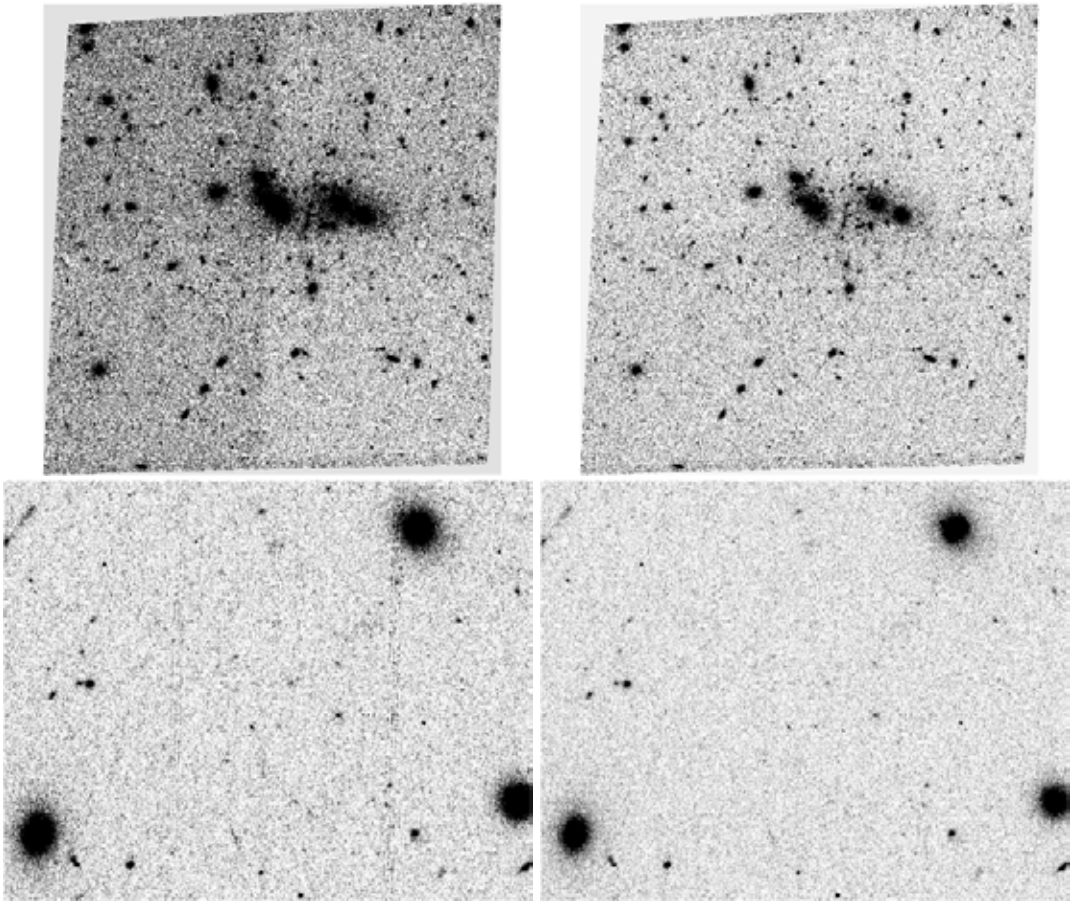

Figure 3.2: Top: chip bias in ACS image of A2813. The left hand image shows the background bias effect, while the right hand image shows the results of the background correction before drizzling. Bottom: As above, but for 'tramlines' caused by bad pixel columns in the undrizzled FLT images.

The output pixel scale was set to $0.03''/pixel$, allowable due to the pixel sub-sampling of the dither process. This pixel scale optimised the sampling, and later correction, of the PSF. The kernel that determines the way the pixel flux is distributed on to the output image was chosen to be *square*, however it should be noted that a Gaussian kernel is now considered more appropiate for weak lens analysis (Rhodes et al., 2007).

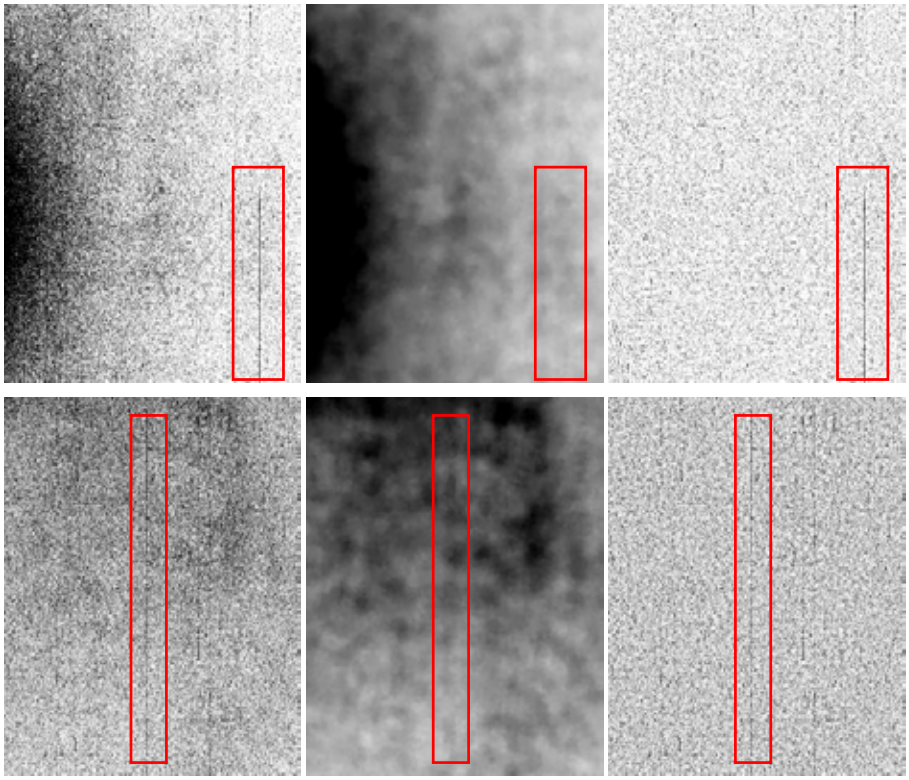

Figure 3.3: Left to right: Averaged FLT science images, this image smoothed and the result of subtraction of the smoothed image from the averaged image. The two rows show the results from the two science images in each FLT image. The cluster was centred on the top two chips of the detector.

Reduction of Proposal 9270 Observations

The clusters observed as part of Proposal 9270 were not centred on the field of view, but were centred on the top *ACS:WFC* chipset. As a result removing the interchip gap was less of a concern and these observations followed a *ACS-WFC-DITHER-BOX* dither pattern with 4 pointings following a parallelogram. The smaller offsets of $(0.187, 0.265)''$ ($\sim (3.74, 5.3)$ pixels at $0.05''/pixel$) in the dither pattern mean these observations will suffer less from the varying pixel distortions of *WFC*, and have a more consistent subpixel sampling across the image. However the placement of the cluster BCG means we are unable to sample nearly half the weak shear field, which makes our ultimate constraints on the shape of the DM halo much weaker. The background bias and bad column correction was applied to these observations as above, although their science frames were not included in the mask generation.

Reduction of the Bullet Cluster Observation

The Bullet Cluster was observed as part of Proposal 10200. The observation was split into two frames to focus on the two known components of this cluster. The overlap between the frames was almost half a frame. Both frames followed two dither patterns: a primary line pattern, and the second the *ACS-WCS-DITHER-LINE*. Both patterns used shifts in the y-axis, $3.0''$ and $1.265''$ respectively. Given that the two frames are aligned along the y-axis, it is likely this dithering pattern was chosen to cover the interchip gap and also temper the distortion effect from very large shift. Apart from combining the catalogues once the faint galaxies were extracted from each frame individually, these observations required no special treatment and were reduced as before.

3.2 Ground Based Near Infra-Red Observations

The Near IR imaging was obtained using ISPI at CTIO, Flamingos at Kitt Peak and WIRC at Palomar, between 2003 and 2008, and was reduced by Tom Targett. Full observation details are given in Tables 3.2, 3.3.

Adjusting for different observatories, the reduction was performed in the standard manner using IRAF packages. The observations from Palomar were not normalised or sky subtracted due to observational issues. For those images that were normalised, dark frames taken with equal integration time to the science images were used to create dark-subtracted science image. Normalized flat-field images were created using a scaled, σ-clipped median combination of neighbouring science frames. The dark-subtracted images were divided by these flat-field images, and the frame offsets found using bright stars. Bad pixels were excluded during image reduction, as were cosmic rays. After the initial reduction, the source flux was masked out, and improved flat-field images created from the masked science frames. The reduction process outlined above was then repeated to produce the final science frames (Targett et al., 2011).

3.3 X-ray Observations from *Chandra*

X-ray observations from *Chandra* existed for 20/21 of the clusters, from a combination of LoCuSS proposal and archival data. *A*3192 was rejected from the LoCuSS *C*HANDRA proposal due to an improved redshift measurement of 0.42 placing the cluster beyond the sample limits of this study. The ROSAT All Sky Survey image of this cluster was obtained for a simple comparison. Reduction and analysis details for the rest of the sample can be found in Sanderson et al. (2009) and Sanderson & Ponman (2010). Briefly, the *chandra* data analysed using CIAO 3.4 and CALDB 3.4.2 in order to remove flares and point sources. Variation in the high energy background was corrected for using blank sky observations normalized to cluster events. The Galactic foreground emission was accounted for following Sanderson et al. (2006). The cluster

X-ray properties are summarised in Table 3.4.

3.4 Analysis of Multi Wavelength Data

3.4.1 Infra-Red Analysis

SEXTRACTOR (Bertin & Arnouts, 1996) was used to extract sources from both the J and K-band reduced images, if they had at least 4 adjoining pixels with a 1.5σ detection. The astrometric calibration had RMS $\sim 1.3 pixels$, with an astrometric solution derived from 2MASS with a precision of $\sim 0.1''$ (0.33 pixels). The filter catalogues were matched based on the object World Coordinate System (WCS) positions, with selected sources in K having an associated source in J within a circle of radius $2''$ (7 pixels). Sources with magnitude errors in excess of $\delta K = 0.1$ were rejected, as were sources within the low S/N edges of the field, or with a stellarity> 0.8.

For each cluster, the J,K-band matched IR catalogue was used to create a colour-magnitude diagram. The cluster galaxy population is dominated by red elliptical galaxies, and these form an identifiable Red Sequence on the colour-magnitude diagram. Colour limits based on the $J-K$ distribution were manually applied to create cluster galaxy catalogues for the parameterized lens modelling and for the construction of luminosity density maps, in order to study the spatial distribution of the cluster members and to extract position priors for the DM haloes in the lens models. Figs. 3.4-3.24 show the colour magnitude (left) and $J-K$ distribution (right) for each cluster in the sample. The filled points are those with $\delta K < 0.1$, the vertical blackline with the $m_{K*}+1$ magnitude limit applied to remove faint and poorly constrained cluster members. The catalogues were also constrained by the ACS field of view.

The Red Sequence is not flat in the IR, but has a negative slope. The flat limits obtained by inspection above, and applied manually, do not reflect this slope, and may result in some

Table 3.2: Infra-Red Cluster Properties and Observation Details

Cluster	Filter	Obs.	Inst.	t_{exp} [ksec]	Image Z_p (Vega)	FWHM [″]	Saturation [ADU]	$N''/pixel$	Mag_{lim} $d_{aper} = 2 \times FWHM$
A 2813	J	CTIO	ISPI	1.74	21.1693	1.4	550	0.3	20.35
	K	CTIO	ISPI	1.8	21.5508	1.5	3000	0.3	19.88
A 0141	J	CTIO	ISPI	1.8	21.8563	1.1	550	0.3	20.56
	K	CTIO	ISPI	1.8	21.7573	1.3	3000	0.3	20.24
A 2895	J	CTIO	ISPI	1.8	21.4087	1.5	550	0.3	21.06
	K	CTIO	ISPI	1.8	21.5439	1.4	3000	0.3	19.97
RXC J0220.9-3829	J	CTIO	ISPI	1.02	21.873	1.0	550	0.3	21.67
	K	CTIO	ISPI	1.56	21.799	0.9	3000	0.3	20.36
A 0368	J	CTIO	ISPI	0.96	21.843	1.0	550	0.3	21.67
	K	CTIO	ISPI	1.02	21.880	0.9	3000	0.3	20.29
A 3084	J	CTIO	ISPI	1.02	21.882	0.9	550	0.3	21.73
	K	CTIO	ISPI	1.08	21.842	0.8	3000	0.3	20.37
A 3088	J	CTIO	ISPI	1.8	21.7380	1.3	550	0.3	21.43
	K	CTIO	ISPI	1.8	21.6677	1.3	3000	0.3	20.19
RXC J0331.1-2100	J	CTIO	ISPI	1.8	21.5677	1.8	550	0.3	21.64
	K	CTIO	ISPI	1.8	21.7087	1.2	3000	0.3	20.2
A 3140	J	CTIO	ISPI	1.02	21.868	1.1	550	0.3	21.66
	K	CTIO	ISPI	1.62	21.868	1.1	3000	0.3	20.31
A 3192	J	CTIO	ISPI	1.02	21.871	1.0	550	0.3	21.78
	K	CTIO	ISPI	1.02	21.871	0.9	3000	0.3	20.32
A 3292	J	CTIO	ISPI	1.02	21.867	0.9	550	0.3	21.71
	K	CTIO	ISPI	1.02	21.857	0.9	3000	0.3	20.09
RXC J0528.2-2942	J	CTIO	ISPI	1.8	21.7084	1.2	550	0.3	21.94
	K	CTIO	ISPI	1.8	21.7620	1.0	3000	0.3	20.21

Table 3.3: Infra-Red Cluster Properties and Observation Details

Cluster	Filter	Obs.	Inst.	t_{exp} [ksec]	Image Z_p (Vega)	FWHM [″]	Saturation [ADU]	$N''/pixel$	Mag_{lim} $d_{aper} = 2 \times FWHM$
A 3364	J	CTIO	ISPI	1.8	21.7018	1.3	550	0.3	20.73
	K	CTIO	ISPI	1.08	21.899	0.8	3000	0.3	20.46
AS 0592	J	CTIO	ISPI	1.8	21.7482	1.2	550	0.3	21.72
	K	CTIO	ISPI	2.28	21.7068	1.1	3000	0.3	20.21
1ES0657-558	J	CTIO	ISPI	1.8	21.6506	1.4	550	0.3	21.77
	K	CTIO	ISPI	2.7	21.6513	1.2	3000	0.3	18.41
A 0611	J	Palomar	WIRC	0.12	27.555	1.4	1E6	0.2487	20.40
	K	Palomar	WIRC	0.04	26.137	1.2	1E6	0.2487	19.57
A 0781	J	Kitt Peak	FLAMINGOS	1.5	21.527	1.8	750	0.3165	20.94
	K	Kitt Peak	FLAMINGOS	1.56	21.825	1.5	1500	0.3165	19.99
Z 2701	J	Palomar	WIRC	0.12	28.083	1.6	1E6	0.2487	20.75
	K	Palomar	WIRC	0.03	26.329	1.5	1E6	0.2487	19.97
RX J1000.5+4409	J	Palomar	WIRC	0.12	28.083	1.8	1E6	0.2487	20.65
	K	Palomar	WIRC	0.04	26.688	1.8	1E6	0.2487	19.91
A 2187	J	Kitt Peak	FLAMINGOS	1.5	21.724	1.2	750	0.3165	21.23
	K	Kitt Peak	FLAMINGOS	1.56	21.921	1.1	1500	0.3165	20.48
A 2537	J	Palomar	WIRC	0.12	28.08	1.4	1E6	0.2487	—
	K	Palomar	WIRC	0.02	25.88	1.4	1E6	0.249	—

Table 3.4: X-ray Cluster Properties and *Chandra* Observation Details

Cluster	α_X	δ_X	T_X [kev]	L_X [$10^{44} ergs\ s^{-1}$]	$\delta L_X / L_X$
A 2813	00:43:24.55	-20:37:26.76	6.51 (5.8-7.4)	8.80	0.156
A 0141	01:05:34.42	-24:38:04.20	6.48 (5.2-8.1)	6.66	0.157
A 2895	01:18:11.30	-26:57:59.76	8.08 (6.9-9.8)	6.43	0.140
RXC J0220.9-3829	02:20:56.53	-38:28:49.30	4.23 (3.8-5.0)	5.82	0.118
A 0368	02:37:27.66	-26:30:28.30	6.59 (5.5-8.3)	4.94	0.154
A 3084	03:04:03.00	-36:56:31.74	4.29 (3.7-5.2)	4.68	0.155
A 3088	03:07:01.92	-28:39:56.12	7.71 (6.4-9.9)	8.04	0.173
RXC J0331.1-2100	03:31:06.03	-21:00:32.18	5.68 (4.9-6.7)	5.04	0.245
A 3140	03:36:15.57	-40:37:42.10	5.32 (4.7-6.2)	4.30	0.154
A 3192	—	—	—	2.71	0.133
A 3292	04:49:56.55	-44:40:22.15	3.60 (3.2-4.1)	3.29	0.137
RXC J0528.2-2942	05:28:14.81	-29:43:13.69	4.21 (3.7-4.8)	2.87	0.376
A 3364	05:47:38.10	-31:52:09.08	7.65 (6.6-9.1)	4.67	0.075
AS 0592	06:38:48.40	-53:58:26.08	9.89 (8.0-13.5)	12.27	0.081
1ES0657-558	06:58:30.63	-55:56:35.84	13.24 (12.5-14.7)	26.63	0.079
A 0611	08:00:56.81	+36:03:23.69	7.94 (6.9-9.2)	8.05	0.06
A 0781	09:20:26.25	+30:29:56.26	4.70 (3.7-6.2)	10.19	0.08
Z 2701	09:52:49.26	+51:53:04.38	5.08 (4.7-5.5)	6.32	0.08
RX J1000.5+4409	10:00:31.54	+44:08:42.43	3.37 (3.0-3.8)	1.82	0.06
A 2187	16:24:14.00	+41:14:37.25	8.20 (6.9-10.0)	3.11	0.05
A 2537	23:08:22.10	-02:11:26.63	6.65 (5.8-7.6)	11.76	0.143

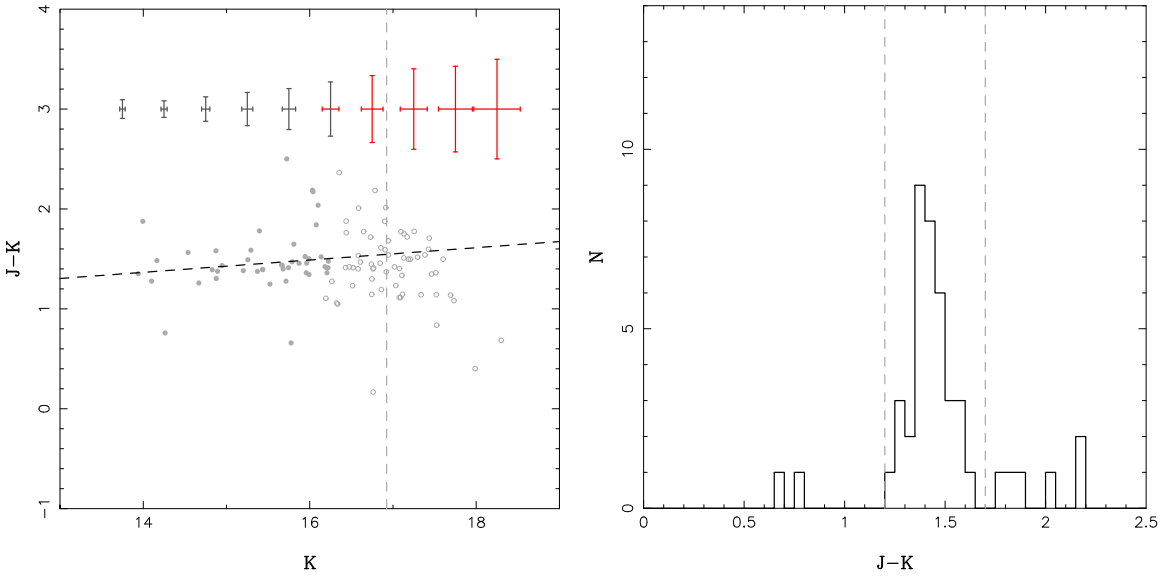

Figure 3.4: *A*2813: Colour magnitude diagram (left) and the $J-K$ colour distribution (right). The filled points on the colour magnitude diagram are those objects with $\delta K < 0.1$, the vertical line denotes the $m_{K*}+1$ limit and the fit shown uses a biweighted linear regression. The error bars at the top of the image show the binned average error in colour and magnitude. The errors bars turn red when $\delta K > 0.1$ or $\delta(J-K) > 0.3$. The colour distribution includes all galaxies with $\delta K < 0.1$. The vertical lines on the $J-K$ colour distribution denote the minimum and maximum colours used to extract the cluster galaxies.

faint, blue cluster galaxies being excluded, and red, non cluster galaxies contaminating the catalogue. While such limits may be acceptable for the simple extraction and analysis performed for this thesis, for more rigid constraints on the galaxy distribution and mass position prior, a future improvement to the analysis would be to automate this selection. This could be done either by applying Red Sequence constraints from models, based on the cluster redshifts, or by fitting a Red Sequence slope to the data. For the latter point, an attempt was made to fit the Red Sequence using a bi-weighted linear regression, however this was unsuccessful, and the fitted relations are shown for completeness only, and did not influence the cluster galaxy selection or analysis.

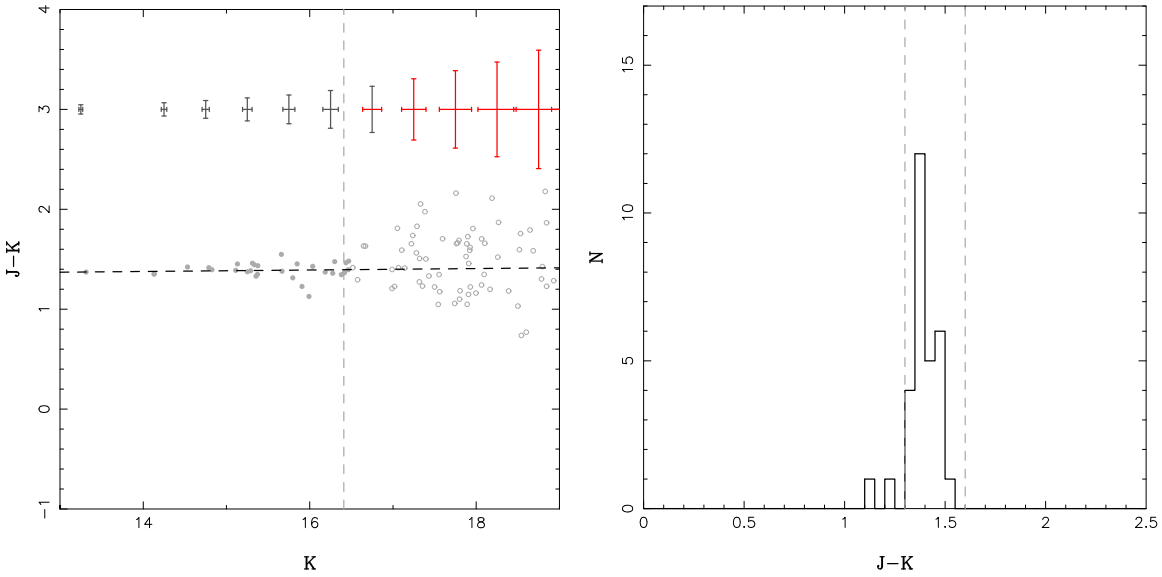

Figure 3.5: *A*0141: as for *A*2813.

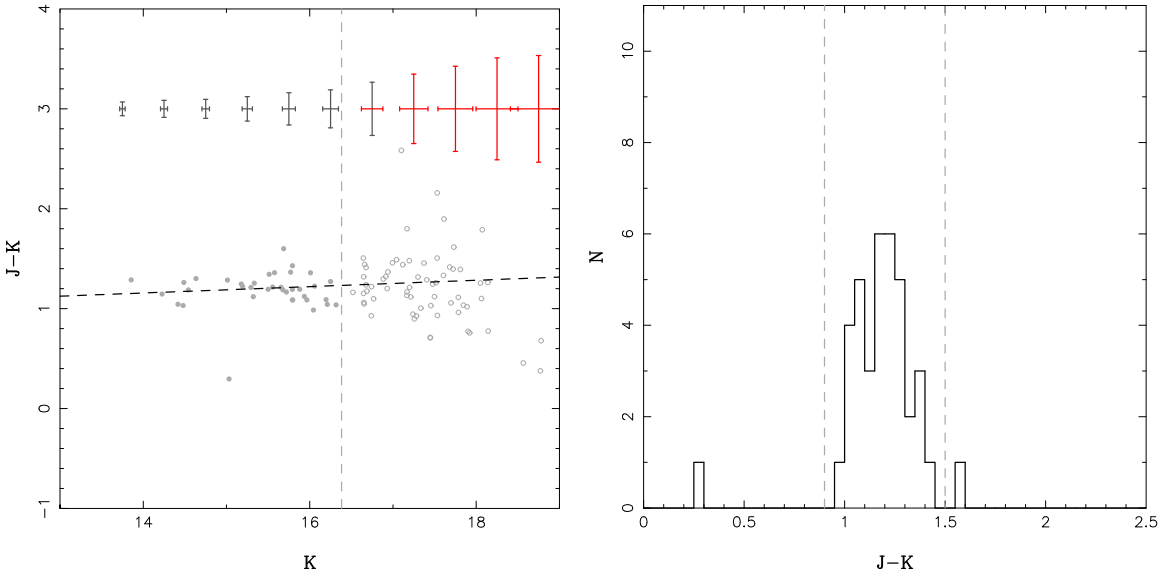

Figure 3.6: *A*2895

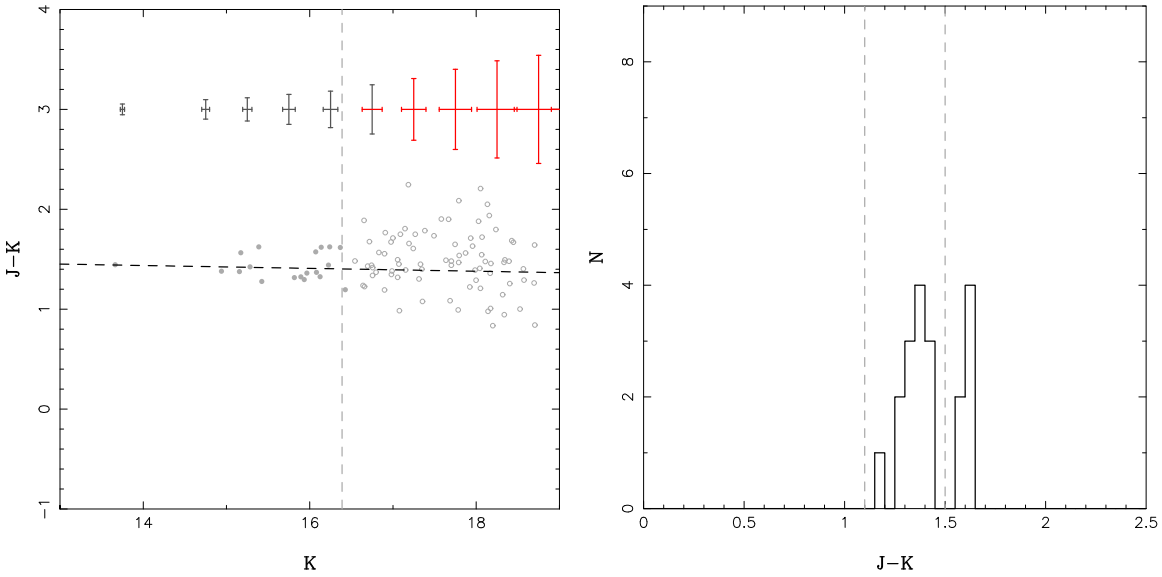

Figure 3.7: *RXCJ*0220.93829

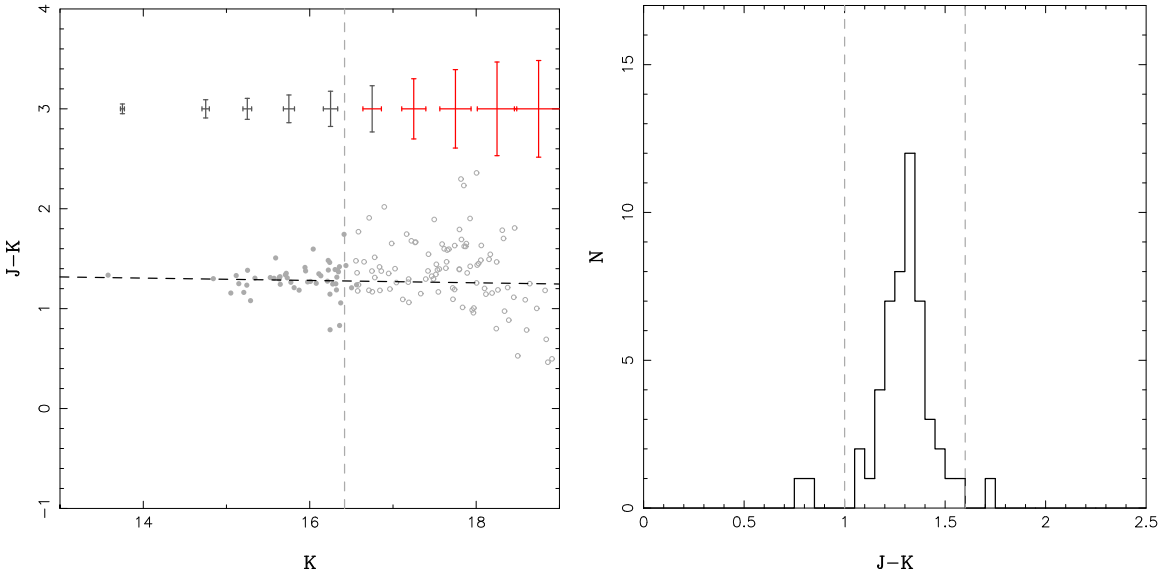

Figure 3.8: *A*0368

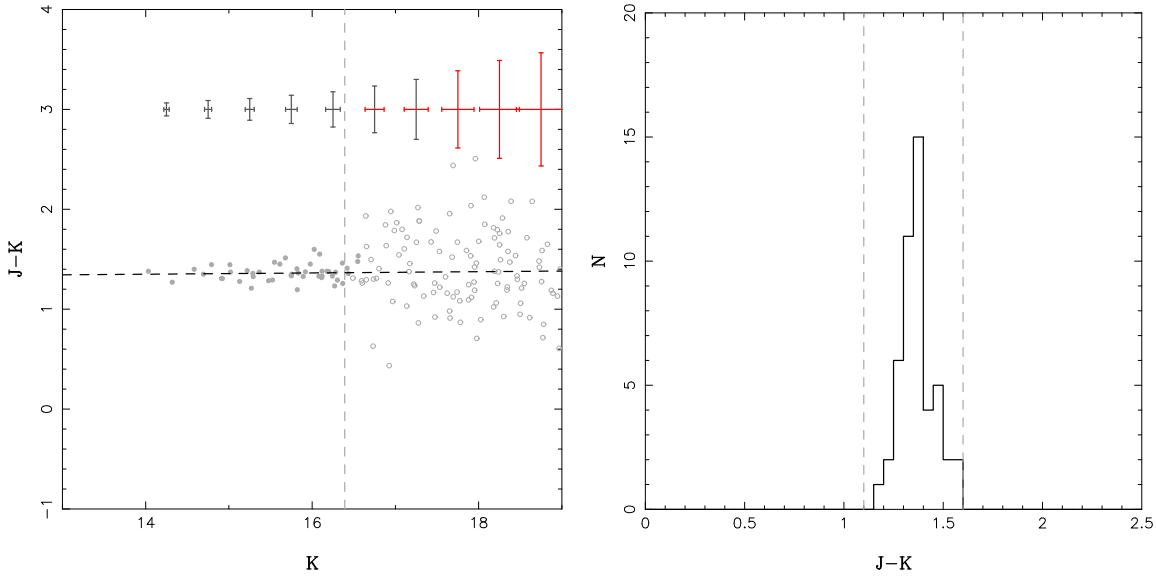

Figure 3.9: *A*3084

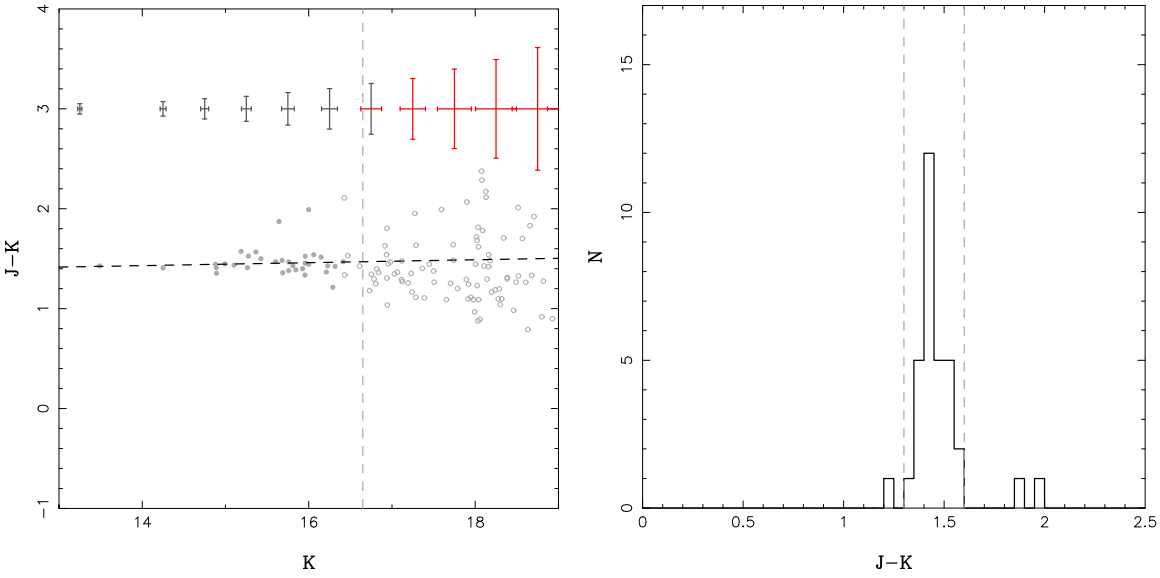

Figure 3.10: *A*3088

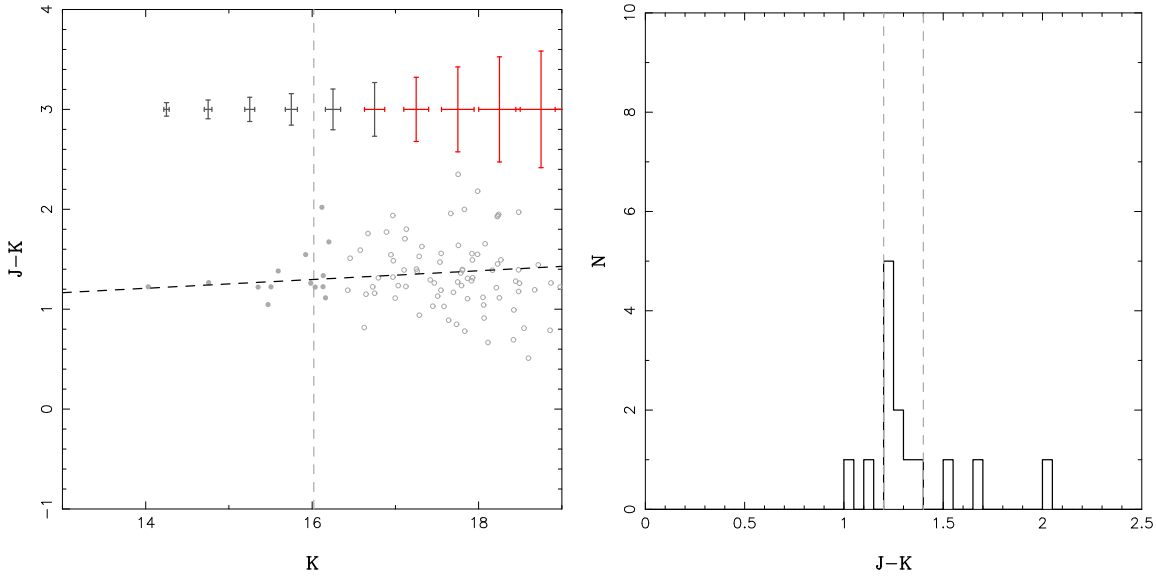

Figure 3.11: *RXCJ*0331.12100

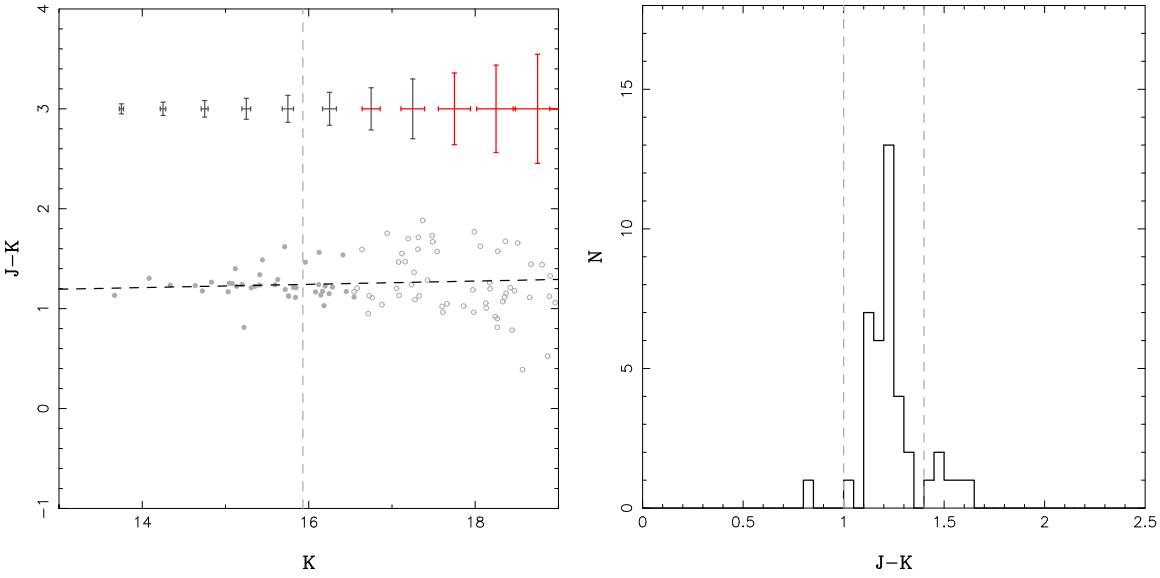

Figure 3.12: *A*3140

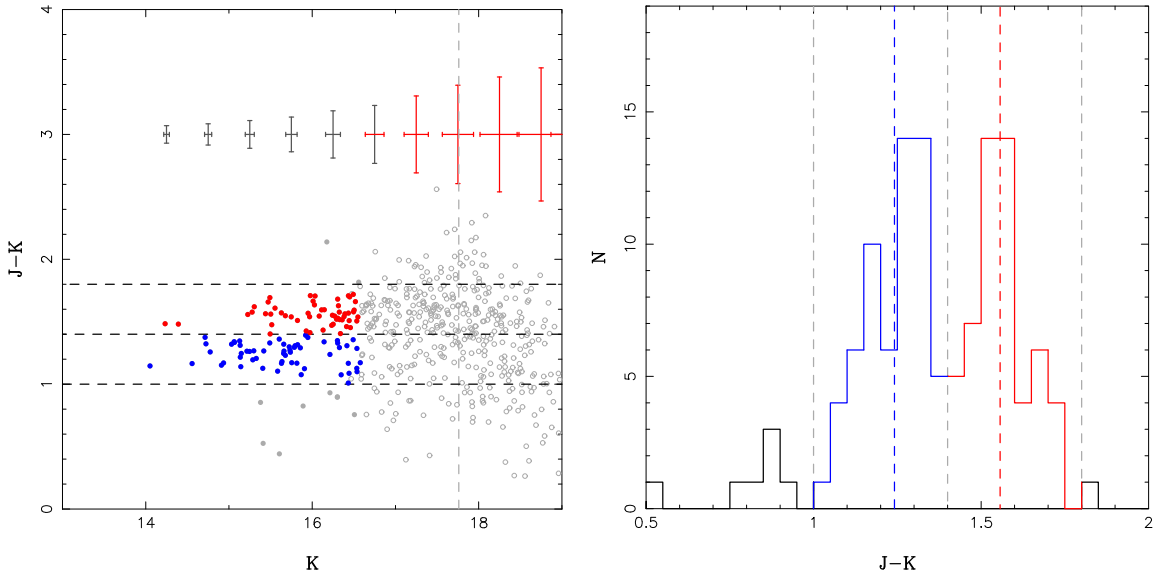

Figure 3.13: *A*3192: as for *A*2813, however the blue and red limits on the $J-K$ distribution denote the foreground group and background cluster galaxy selection respectively. For the LENSTOOL models that used the cluster galaxies, only the background, cluster (red) population was used.

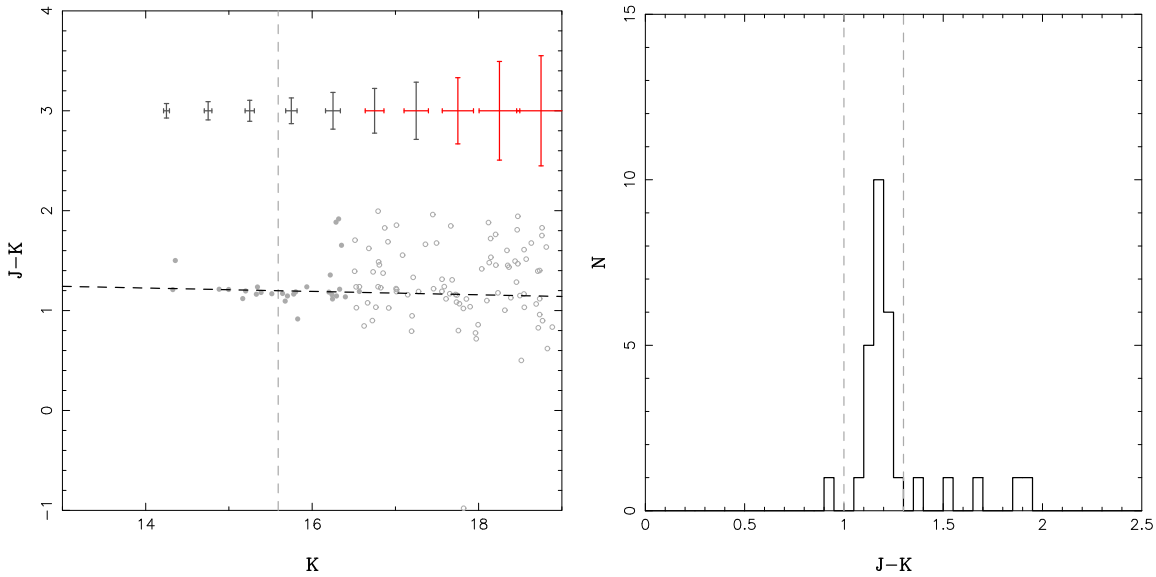

Figure 3.14: *A*3292

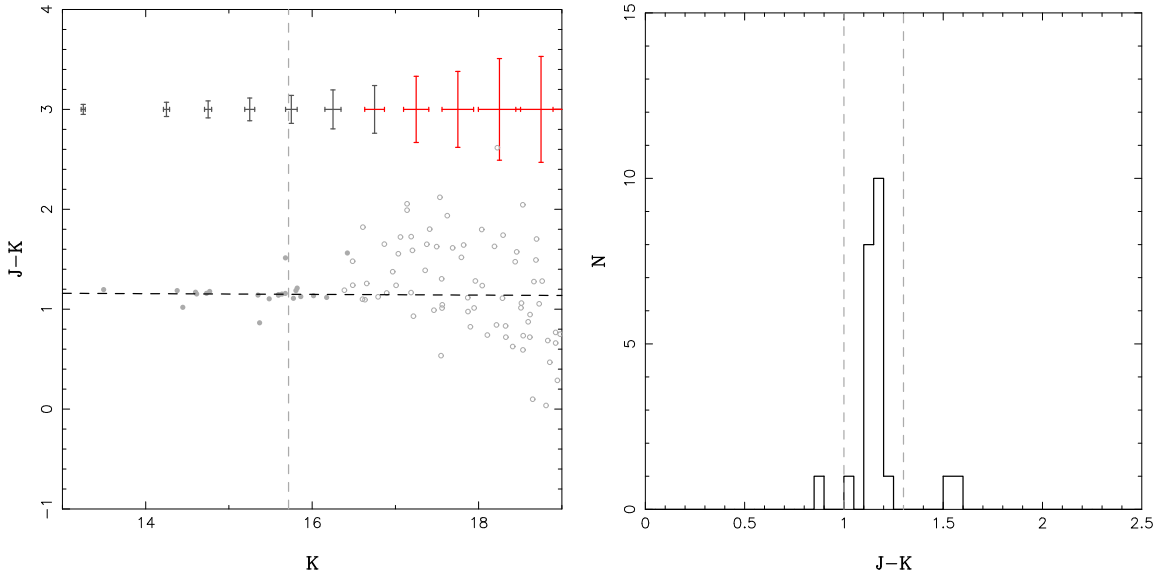

Figure 3.15: *RXCJ*0528.22942

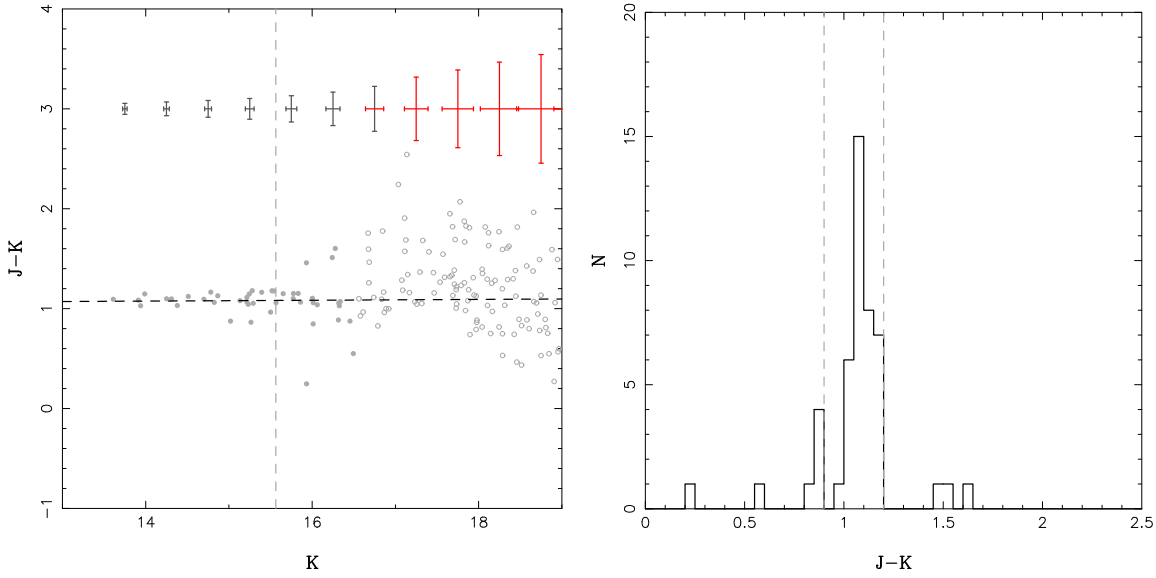

Figure 3.16: *A*3364

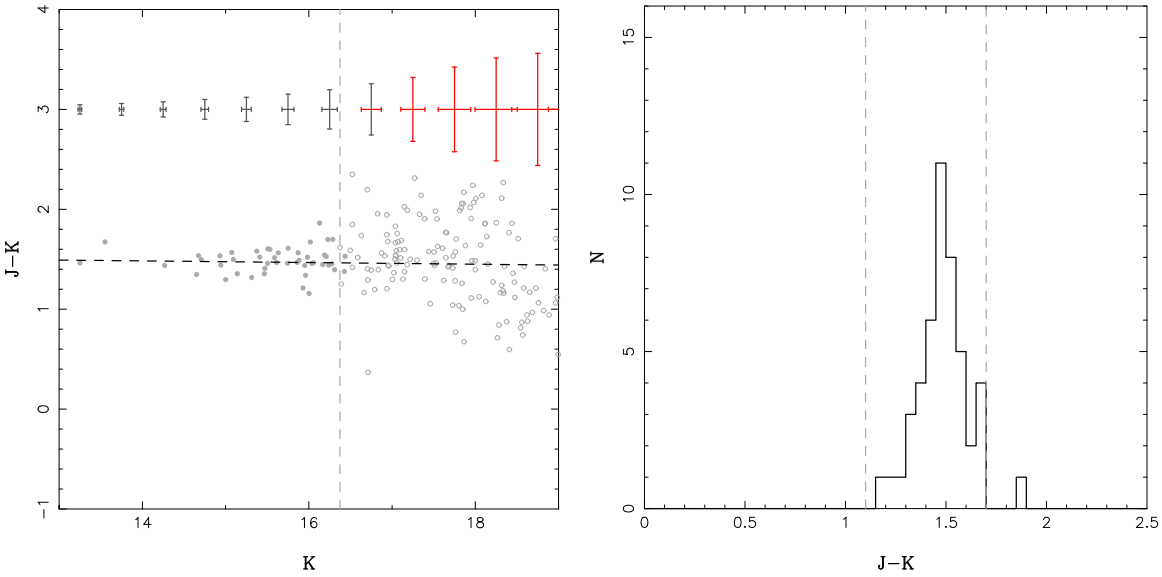

Figure 3.17: *AS*0592

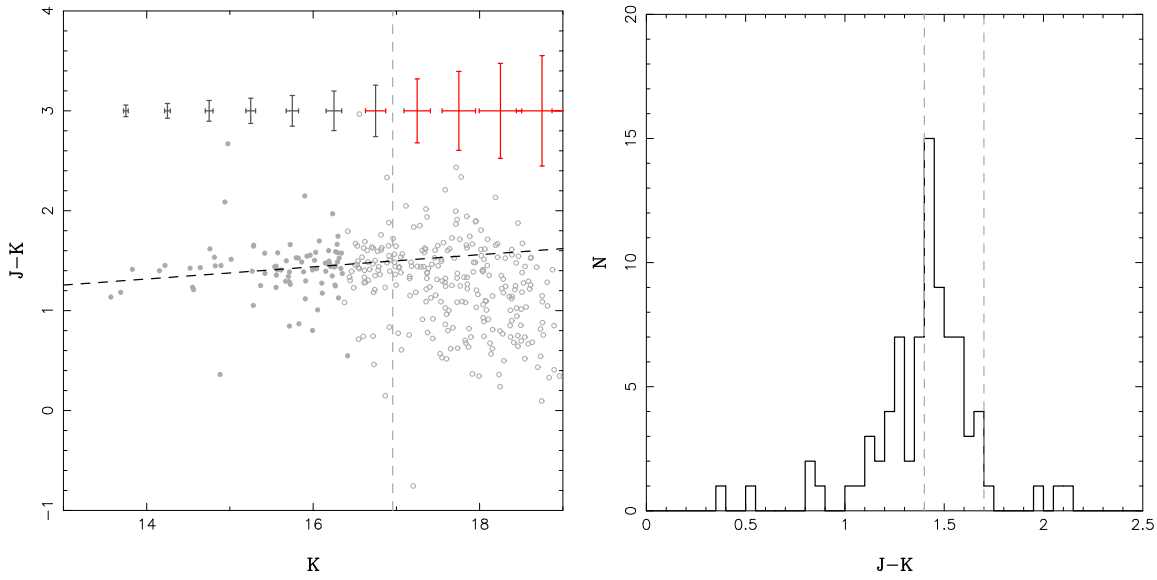

Figure 3.18: 1*ES*0657558

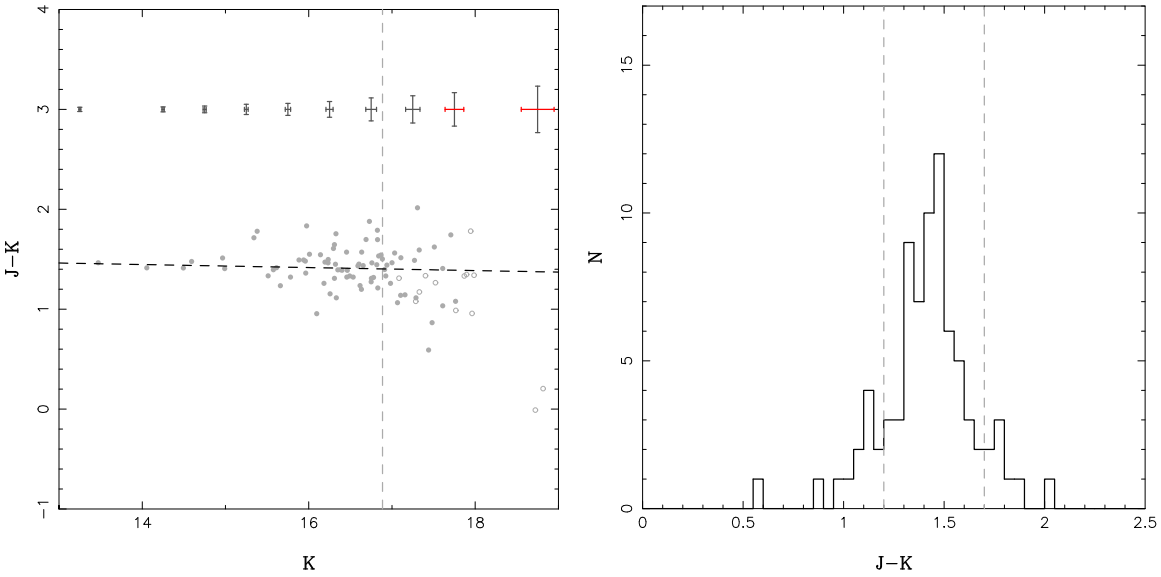

Figure 3.19: *A*0611

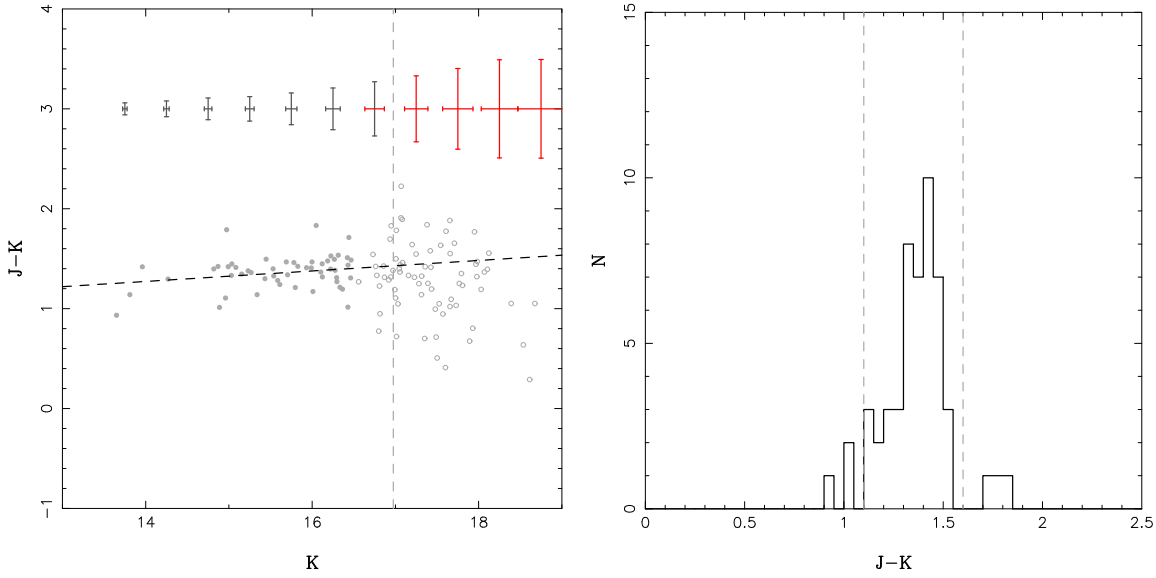

Figure 3.20: *A*0781

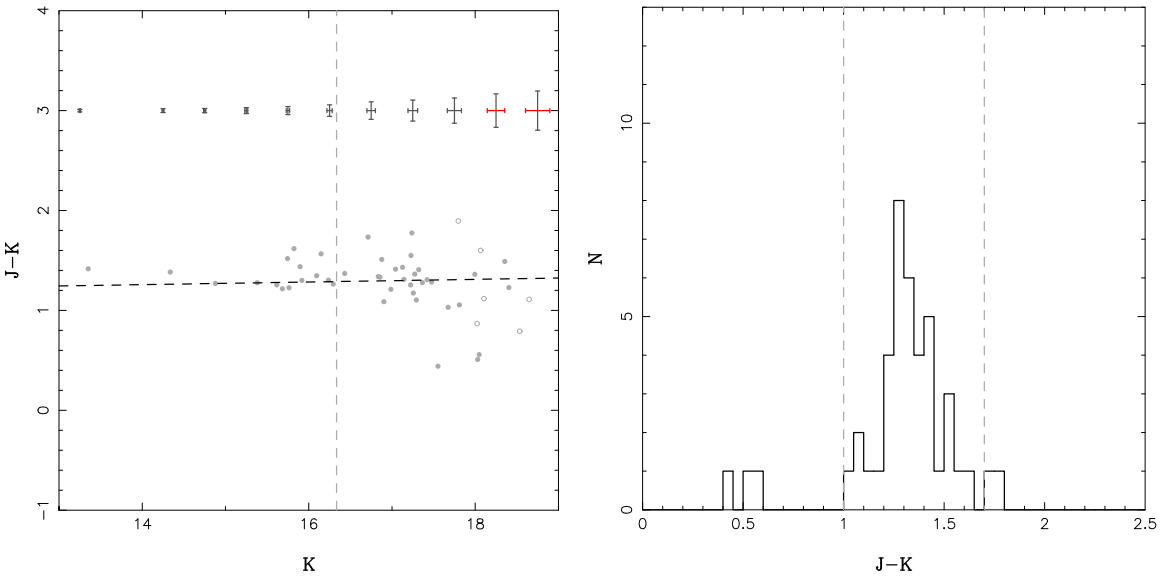

Figure 3.21: *Z* 2701

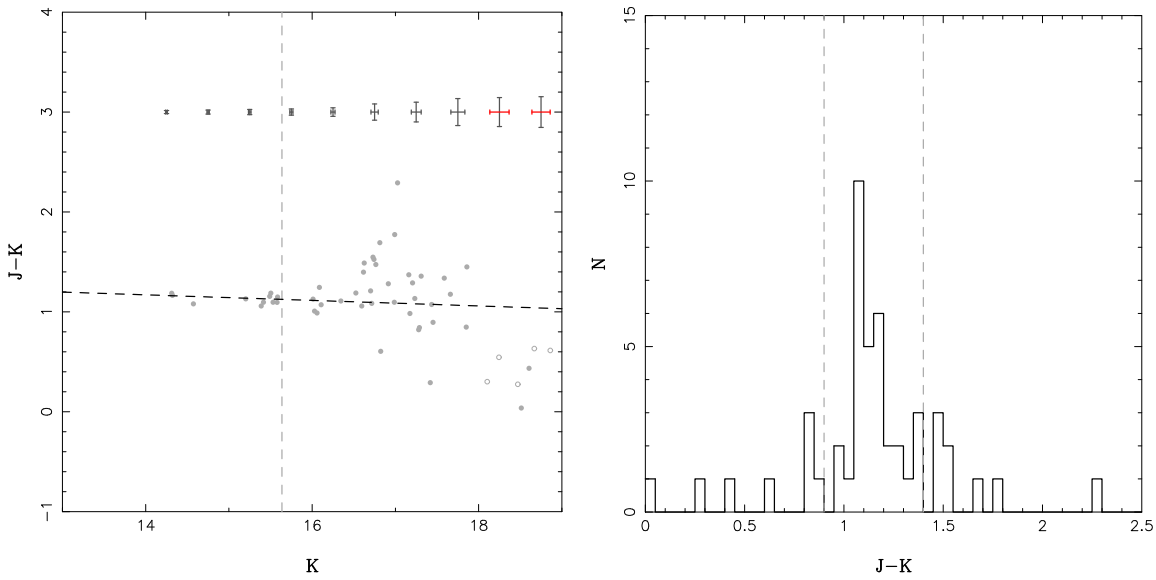

Figure 3.22: *RXJ* 1000.5+4409

The constraint on δK was found to be unnecessary for the majority of the clusters, as the magnitude limit $m_{K*}+1$ removed the cluster galaxies with $\delta K > 0.1$. However, for a subset of clusters, $A2813, A3088, A3192$ and the Bullet Cluster, this was not the case. In order to maintain a standardized analysis, for clusters, with the exception of $A3192$, the δK limit was increased to 0.2 to ensure that all galaxies within the colour limits and brighter than magnitude limit were included in the cluster galaxy catalogues (Fig. 3.25). The original colour selection limits remained the same. $A3192$ was not reanalysed with the new catalogue. This cluster was found to have been misidentified at being at a redshift of 0.1681, and actually lay at 0.42, outside the range of our sample. The confusion was found to be due to a foreground galaxy group lying almost along the line of sight at $z = 0.1681$, just outside the ACS field of view. The requirement of a multi-redshift lens plane to analyse this cluster, and the restriction within LENSTOOL to a single redshift lens plane would make it difficult to use the cluster and group galaxies as a prior within the LENSTOOL modelling itself. The primary analysis of $A3192$ was performed using models that did not include subhaloes corresponding to the cluster galaxies, albeit still utilising the luminosity map peak position prior, and is described in detail in § 6.2.

The K-band luminosity of the cluster members was found from the K-band magnitudes, and

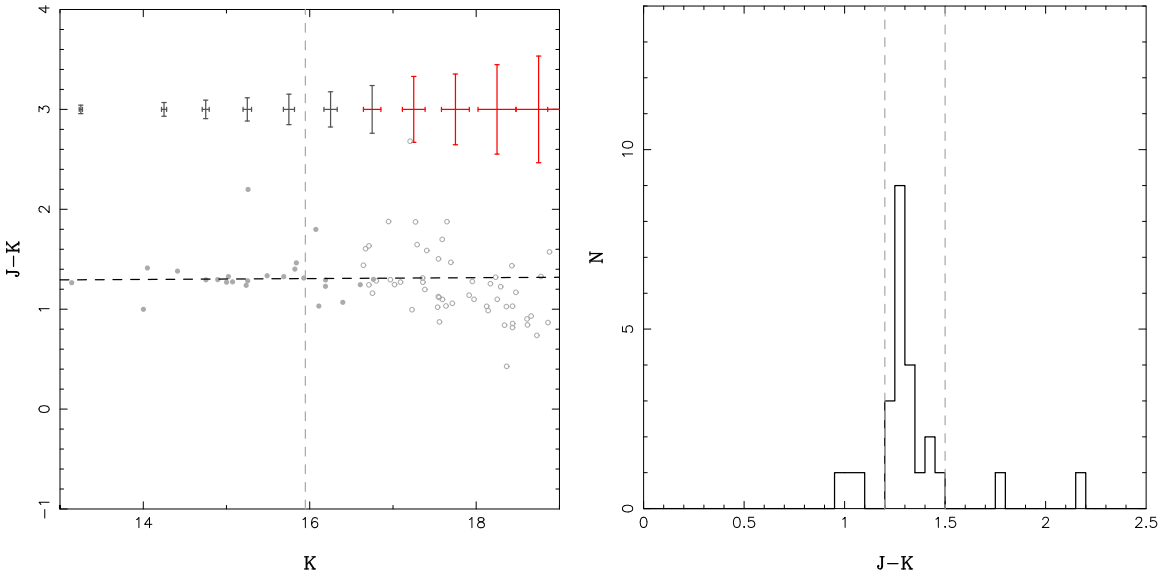

Figure 3.23: *A*2187

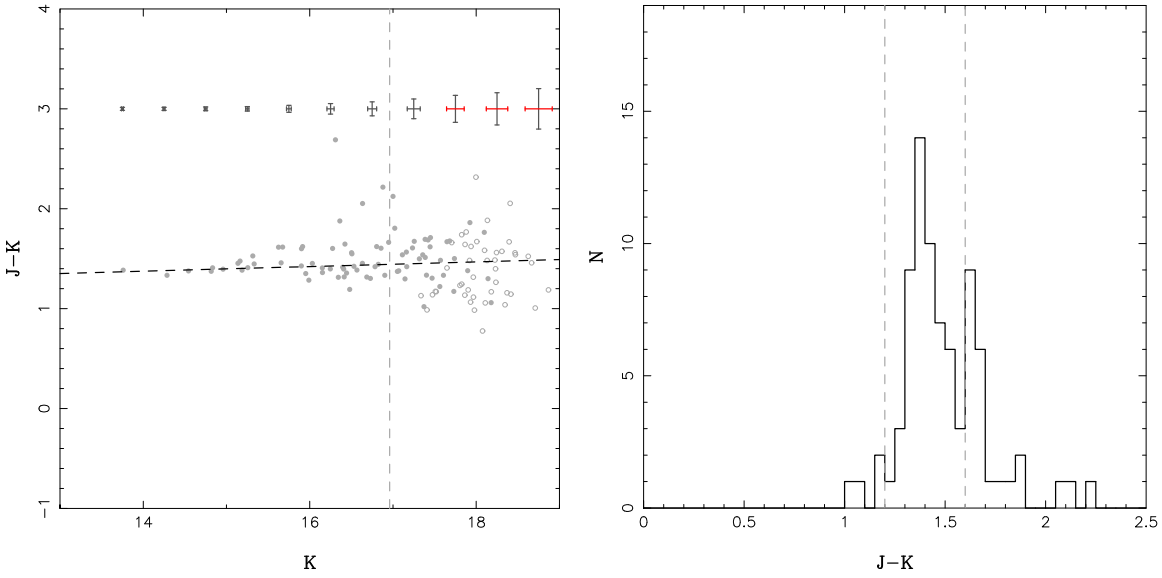

Figure 3.24: *A*2537

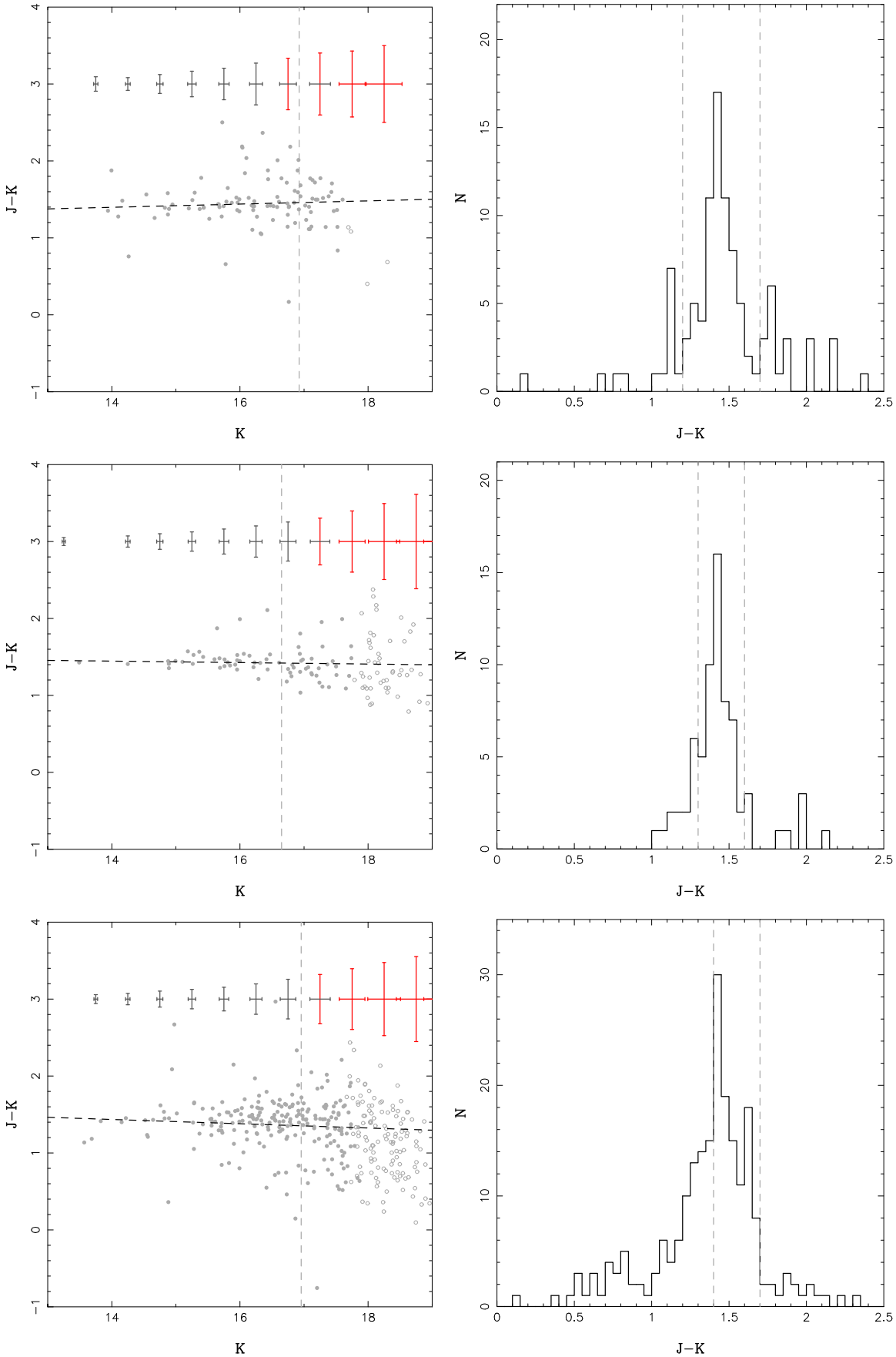

Figure 3.25: Colour-magnitude diagrams and colour distributions for all galaxies with $\delta K < 0.2$, for $A2183, A3088$ and $1ES0657558$. The original cluster galaxy colour selection limits still apply. The error bars on magnitude in the lefthand plots now turn red when $\delta K > 0.2$.

these smoothed using a Gaussian filter on scales of 100 kpc, chosen to match the most common optimum smoothing scale from the LENSENT2 analysis, which uses a smoothing scale to characterise large scale potentials in the weak lens map (§ 4.1). Individual cluster luminosity maps are shown in the top left hand panel of Figs. A.1-A.21, with examples in Fig. 3.26.

In order to obtain information on the cluster core structure, further luminosity maps were reconstructed on the smaller smoothing scale of $75kpc$. SEXTRACTOR was then used to extract the prominent clump positions from these maps, along with associated total luminosities within apertures of $150kpc$. These luminosities were then used to order the clump positions, and remove any positions with total luminosities less than L^*. Only the 5 brightest or fewer clumps were used to construct the parameterised models, with the single halo model always using the BCG position. For clump extraction, the luminosity maps for $A2183, A3088$ and $1ES0657558$ used the $\delta K < 0.1$ cluster galaxy catalogues, with the Bullet Cluster also using wider cluster galaxy selection limits. IR properties are given in Table 3.5, and extracted halo positions are given, in order of brightness (with BCG associated position always given first as 0,0) in Table 3.6.

3.4.2 X-ray Analysis

The 0.5-2.0 keV raw X-ray images from *C*HANDRA were analysed by Alastair Sanderson to produced smoothed surface brightness maps, based on the wavelet reconstruction described in Vikhlinin et al. (1998). The algorithm removes significant features at increasing scales, producing maps at the different scales that do not include bright X-ray points sources and small scale features. The images are then added together to create a surface brightness map. This method reproduces areas of low surface brightness extended emission, in spite of bright embedded point sources (Sanderson et al., 2009).

Once the smoothed X-ray images had been obtained from Alastair Sanderson, they were

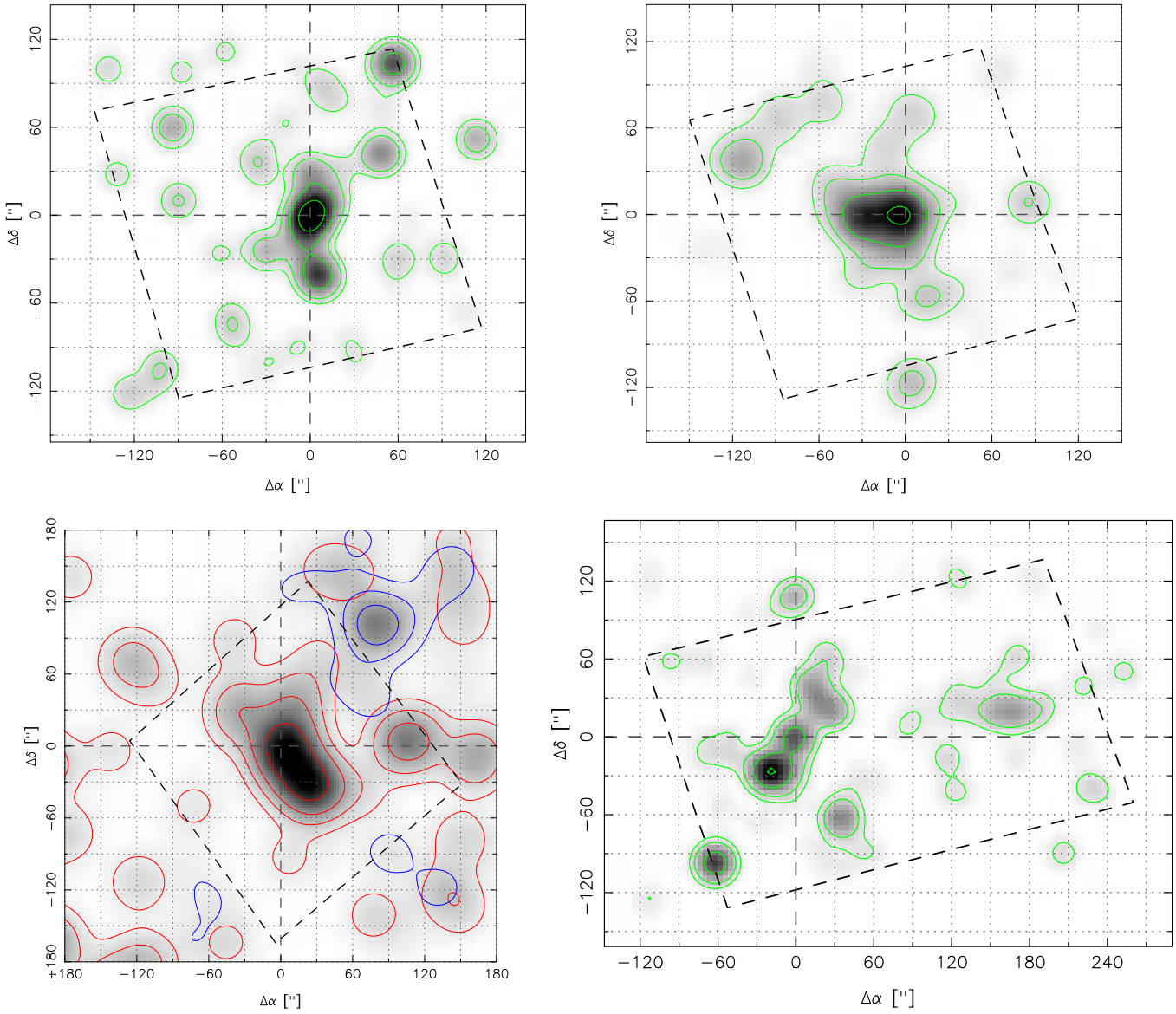

Figure 3.26: From top left, clockwise: $A2183, AS0592, A3192$ and the Bullet Cluster. Contours show $1, 2, 5 \times 10^{13}$ and 1×10^{14} solar luminosities per square Mpc. The blue and red contours $A3192$ show $0.2, 0.5, 1, 2, 5 \times 10^{13}$ and 1×10^{14} solar luminosities for the foreground group and background cluster galaxy populations respectively. These clusters were ultimately identified as multimodal in the lens modelling. Luminosity density distributions for each cluster in the sample can be found in the respective top left panels of the comparison figures in § A.

swarped to match the pixel scale and grid size of the LENSENT2 κ images, and plotted with contours in logarithmic steps. Individual cluster maps are shown in the top right hand panel of Figs. A.1-A.21, with examples in Fig. 3.27.

We obtained projected masses at $R_{aper} = 250kpc$, which were calculated with the best fit Hernquist parameters from A. Sanderson's analysis of the smoothed X-ray images, using Eq. 3.1 (Hernquist, 1990).

$$M_p(< R_{aper}) = M_h s^2 \frac{(X_s - 1)}{(1 - s^2)} \tag{3.1}$$

M_h is the total Hernquist mass, $s = \frac{R_{aper}}{a}$, were a is the scale radius, and X_s is given by Eq. 3.2.

$$\begin{aligned} s <= 1 \quad X_s &= \frac{sech^{-1}(\sqrt{1-s^2})}{(\sqrt{1-s^2})} \\ s > 1 \quad\;\; X_s &= \frac{sec^{-1}(\sqrt{s^2-1})}{(\sqrt{s^2-1})} \end{aligned} \tag{3.2}$$

The error on the projected mass was found by similarly computing masses for 100 MC fits of the Hernquist Mass and scale radius, then finding the standard deviation of the distribution. The slope, Hernquist masses and projected masses from the X-ray analysis are summarised in Table 3.7.

3.5 Construction of faint galaxy catalogues

The HST:ACS reduced frames were analysed with SEXTRACTOR (Bertin & Arnouts, 1996). A source was extracted if there were at least 5 (0.0045arcsec^2) adjoining pixels, each with a 1.5σ detection over the background isophote μ_{606} = 23.0 mag/arcsec^2. The selection used a three pixel Gaussian smoothing filter, approximating the ACS $1.0-1.2$ arcsecond seeing, with the major SEXRACTOR parameters listed below. 72114 sources were initially selected from all 21 clusters. Fig. 3.28 shows the number density of all sources from all catalogues as a function of magnitude. The sample is reasonably complete around $V_{606} \sim 26-27$. Sources close to diffraction spikes of stars or with magnitudes within 2σ of local background were removed from the catalogues before faint galaxy selection. The majority of sources near diffraction spikes

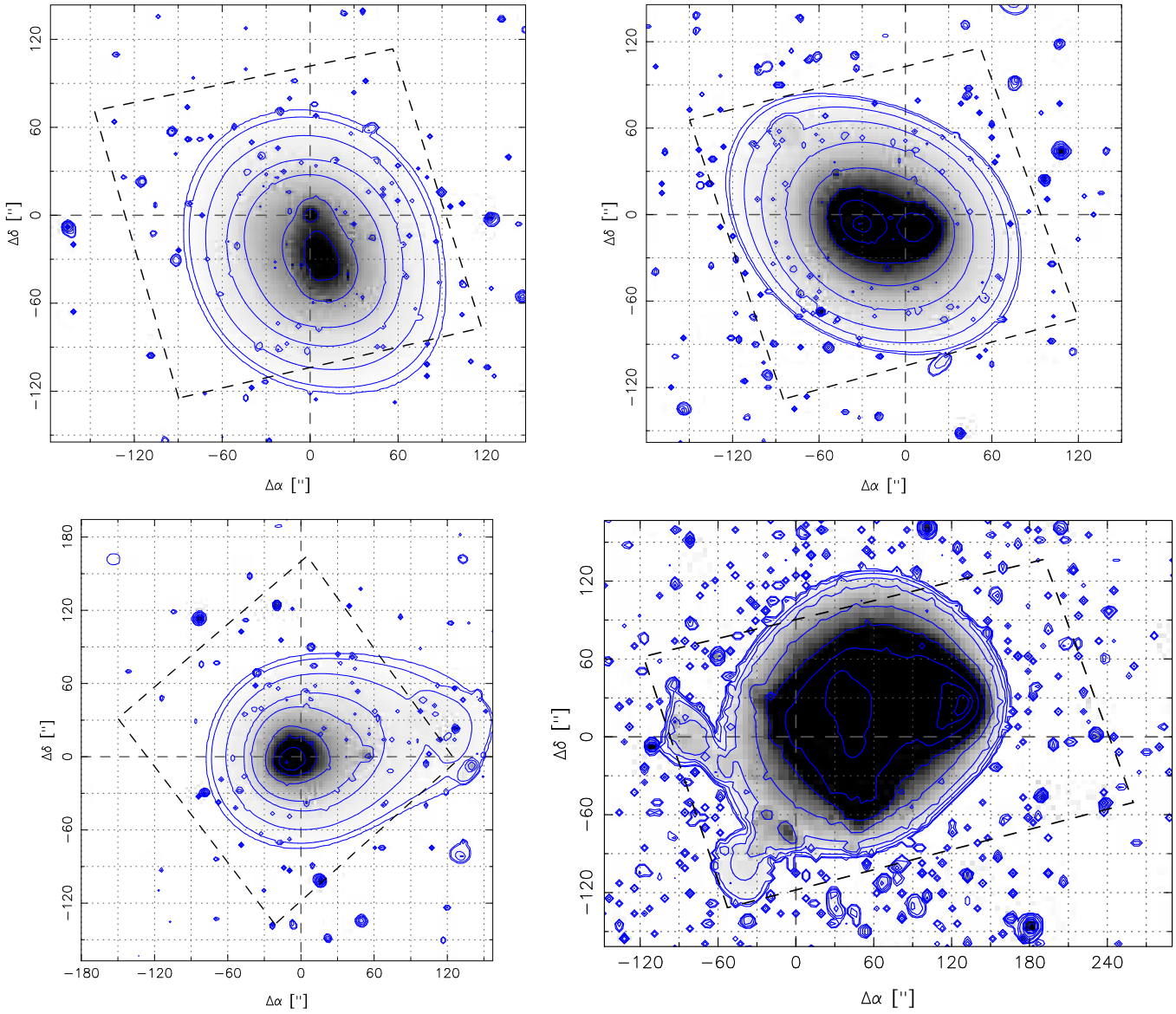

Figure 3.27: From top left, clockwise: $A2183, AS0592, RXJ1000$ and the Bullet Cluster. Contours show X-ray flux in logarithmic steps. These clusters were ultimately identified as multimodal in the lens modelling. The X-ray surface brightness maps for each cluster in the sample can be found in the respective top right panels of the comparison figures in § A.

Table 3.5: Near Infra-Red Cluster Properties

Cluster	$L_k(R < 250kpc)$ $[L_\odot]$	δL_K $[L_\odot]$	$J-K$ Mag	N_{cgal}
A 2813	4.036×10^{12}	4.072×10^{11}	1.2-1.7	52
A 0141	2.820×10^{12}	2.839×10^{11}	1.3-1.6	24
A 2895	3.870×10^{12}	3.893×10^{11}	0.9-1.5	36
RXCJ 0220.9-3829	1.183×10^{12}	1.200×10^{11}	1.1-1.5	12
A 0368	2.463×10^{12}	2.480×10^{11}	1.0-1.6	45
A 3084	3.939×10^{12}	3.956×10^{11}	1.1-1.6	44
A 3088	2.596×10^{12}	2.620×10^{11}	1.3-1.6	33
RXCJ 0331.1-2100	2.302×10^{12}	2.316×10^{11}	1.2-1.4	7
A 3140	2.140×10^{12}	2.151×10^{11}	1.0-1.4	23
A 3192	4.177×10^{12}	4.239×10^{11}	1.0-1.4,1.4-1.8	30,27
A 3292	1.476×10^{12}	1.484×10^{11}	1.0-1.3	10
RXCJ 0528.2-2942	1.293×10^{12}	1.303×10^{11}	1.0-1.3	14
A 3364	2.218×10^{12}	2.226×10^{11}	0.9-1.3	25
AS 0592	4.013×10^{12}	4.032×10^{11}	1.1-1.7	44
1ES0657-558	4.197×10^{12}	4.230×10^{11}	1.4-1.7	72
A 0611	2.313×10^{12}	2.320×10^{11}	1.2-1.7	49
A 0781	2.352×10^{12}	2.381×10^{11}	1.1-1.6	47
Z 2701	1.507×10^{12}	1.509×10^{11}	1.0-1.7	15
RXJ 1000.5+4409	5.832×10^{11}	5.840×10^{10}	0.9-1.4	11
A 2187	2.674×10^{12}	2.685×10^{11}	1.2-1.5	17
A 2537	3.315×10^{12}	3.320×10^{11}	1.2-1.6	36

Table 3.6: Halo positions from K-band luminosity maps.

Cluster	$(\Delta\alpha, \Delta\delta)_0$[1] [″]	$(\Delta\alpha, \Delta\delta)_1$ [″]	$(\Delta\alpha, \Delta\delta)_2$ [″]	$(\Delta\alpha, \Delta\delta)_3$ [″]	$(\Delta\alpha, \Delta\delta)_4$ [″]
A 2813	0.0,0.0	5.3,-40.8	47.5,41.8	-93.7,59.9	-29.0,-24.8
A 0141	0.0,0.0	59.6,-9.8	-79.3,-26.4	-33.6,24.9	-14.0,-54.4
A 2895	0.0,0.0	41.9,10.3	60.3,-13.4	-49.0,18.3	-86.6,-63.9
RXCJ 0220.9-3829	0.0,0.0	-29.6,29.6	88.8,-35.5	-4.0,61.1	
A 0368	0.0,0.0	-57.6,-25.8	21.9,32.1	58.8,30.2	-46.4,73.5
A 3084	0.0,0.0	-26.7,-17.8	-98.0,-20.1	-71.6,-87.9	39.3,-37.0
A 3088	0.0,0.0	-103.1,6.8	-65.9,37.3	32.7,9.6	38.7,-19.1
RXCJ 0331.1-2100	0.0,0.0	-44.8,-44.2			
A 3140	0.0,0.0	-54.5,38.4	-88.9,75.2	36.4,24.1	60.6,-20.0
A 3192	0.0,0.0	80.3,100.8	23.5,-34.4	106.6,5.6	136.0,-121.2
A 3292	0.0,0.0	-75.8,69.7			
RXCJ 0528.2-2942	0.0,0.0	35.1,-101.6	-81.0,31.8	-11.1,52.2	
A 3364	0.0,0.0	-16.7,47.8	15.9,-43.8	-28.1,91.2	24.2,116.4
AS 0592	0.0,0.0	-28.7,-2.0	-113.6,38.4	17.0,-56.6	-87.5,66.9
1ES0657-558	0.0,0.0	-18.4,-26.8	161.2,23.6	-62.3,-97.2	19.0,28.5
A 0611	0.0,0.0	-123.7,63.1	-131.8,-66.5	36.5,-4.2	-44.7,12.8
A 0781	0.0,0.0	-95.0,7.0	-47.6,12.4	-147.7,13.2	-84.2,120.1
Z 2701	0.0,0.0	-112.5,-41.4	17.1,74.6	-45.6,36.2	14.9,-52.2
RXJ 1000.5+4409	0.0,0.0	-109.3,-13.9	62.8,30.2		
A 2187	0.0,0.0	62.6,-80.4	-46.1,-84.7	-78.6,38.5	22.0,-82.8
A 2537	0.0,0.0	-38.7,-33.4	-22.9,0.5	-48.2,-115.7	39.7,20.4

Table 3.7: *CHANDRA* analysis: X-ray Properties and Masses

Cluster	α	$\delta\alpha$	M_h $[M_\odot]$	a [kpc]	$M_p(<250kpc)$ $[M_\odot]$	δM_p $[M_\odot]$
A 2813	-0.342	0.0696	$1.465E\times10^{15}$	782.37	1.512×10^{14}	2.141×10^{13}
A 0141	-0.236	0.0520	9.352×10^{15}	3325.96	1.216×10^{14}	2.730×10^{13}
A 2895	-0.484	0.1292	1.546×10^{15}	876.49	1.383×10^{14}	1.315×10^{13}
RXCJ 0220.9-3829	-0.951	0.0384	9.038×10^{14}	680.18	1.106×10^{14}	8.748×10^{12}
A 0368	-0.920	0.0477	1.107×10^{15}	648.43	1.433×10^{14}	2.940×10^{13}
A 3084	-0.363	0.0457	1.173×10^{15}	726.54	1.326×10^{14}	1.113×10^{13}
A 3088	-0.882	0.0342	1.477×10^{15}	756.38	1.589×10^{14}	2.221×10^{13}
RXCJ 0331.1-2100	-1.202	0.0599	2.257×10^{15}	975.22	1.759×10^{14}	2.352×10^{13}
A 3140	-0.444	0.1136	3.128×10^{15}	1261.90	1.723×10^{14}	2.482×10^{13}
A 3192	—	—	—	—	—	—
A 3292	-0.285	0.0338	1.043×10^{15}	827.71	1.003×10^{14}	1.312×10^{13}
RXCJ 0528.2-2942	-0.273	0.0759	2.518×10^{15}	1647.70	9.512×10^{13}	1.487×10^{13}
A 3364	-0.319	0.030	2.385×10^{15}	1109.60	1.566×10^{14}	1.155×10^{13}
AS 0592	-0.856	0.0403	2.236×10^{15}	917.74	1.886×10^{14}	1.467×10^{13}
1ES0657-558	-0.256	0.0199	2.549×10^{15}	807.81	2.528×10^{14}	1.491×10^{13}
A 0611	-0.701	0.0427	2.957×10^{15}	1059.99	2.064×10^{14}	1.865×10^{13}
A 0781	-0.113	0.0251	2.414×10^{15}	1701.15	8.706×10^{13}	7.836×10^{12}
Z 2701	-0.881	0.1216	3.329×10^{15}	1455.72	1.502×10^{14}	4.114×10^{13}
RXJ 1000.5+4409	-0.946	0.0905	8.727×10^{14}	866.33	7.924×10^{13}	1.002×10^{13}
A 2187	-0.459	0.0945	9.553×10^{14}	666.63	1.197×10^{14}	1.054×10^{13}
A 2537	-0.499	0.0599	9.444×10^{14}	517.30	1.580×10^{14}	1.240×10^{13}

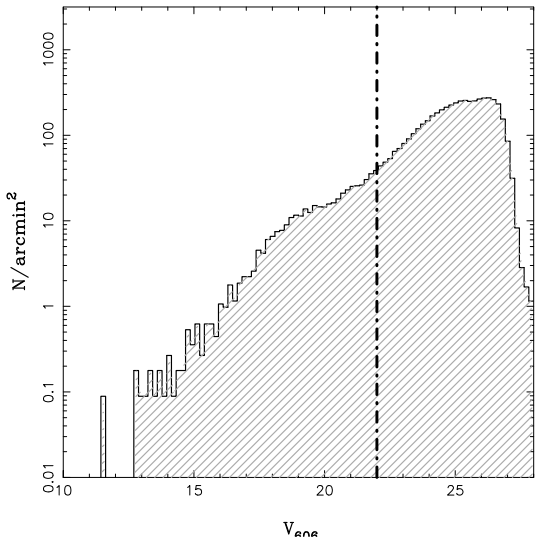

Figure 3.28: Number density of sources versus V_{606}. The dashed line shows the minimum magnitude allowed for faint galaxy selection at V_{606} = 22.

were removed automatically within the analysis pipeline, with a few clusters requiring manual removal of missed diffraction spikes after this. Initial background galaxy catalogues were constructed based on a simple magnitude cut of $V_{606} > 22$, to minimise contamination by cluster members, represented by the bulge in the plot between magnitudes of $V_{606} \sim 16-21$. Finally, detections were removed from the catalogues if they were within $\sim 5''$ of the edge of the field of view, or within $5''$ of the central gap in those drizzled observations from Proposal 9270. After these initial cleaning procedures were carried out, 35447 faint galaxies in total were selected, 1200 – 2000 per cluster (5400 for 1ES0657-558). At this point the selection only depended on the source being fainter then the faint galaxy limit.

3.5.1 Correcting for the PSF

Because the distortion caused by weak lensing on background galaxy images is so small, the blurring of source shapes caused by the PSF can seriously impact the reconstruction of the shear field. IM2SHAPE was used to correct for the PSF and obtain corrected galaxy ellipticity and size measurements. By calculating the residuals of the star ellipticities from a δ-function, it is possible to construct a PSF map, which can then be used with IM2SHAPE to produce PSF corrected

faint galaxy shape information catalogues.

Our PSF correction was performed by using IM2SHAPE to fit a double Gaussian to the stars. The stellar shapes were then compared to a δ-function, and the residuals were smoothed to form a map of the PSF. The smoothing scale was dependent on the number of stars and the width of the field of view. After the initial PSF map construction, the map was used to correct the stellar ellipticities without refitting them. As mentioned in § 2.6.4, the ACS PSF is time dependent, which means it is not possible to stack stars from multiple observations in order to fully sample the PSF over the full field of view, unless those observations are taken within a short time period. As our ACS observations were taken as part of a SNAPSHOT program, and fitted in when there was time and the telescope was facing the correct direction, our clusters were not taken within the same short time period, but observed over a period of several months. As a result, for the majority of the clusters, only the stars detected in that observation was used to construct the PSF map. For those clusters with very few stars, or a poorly sampled field of view, the correction combined with stars from one other cluster was also investigated. Where the correction was improved the final PSF map was made with the augmented star catalogue. IM2SHAPE could then use this map when fitting the a single Gaussian to the shapes of the galaxies, to obtain PSF corrected shear measurements accurate enough to constrain the DM distribution.

Star selection and fitting

The SEXTRACTOR catalogues include information on the stellarity of a source, or how likely it is to be a star. The star selection was performed for each cluster individually, by initially selecting those sources with SEXTRACTOR stellarity > 0.95, signal to noise > 25 and peak flux less than the saturation limit of 84700. These sources where then binned depending on their FWHM value from SEXTRACTOR. The FWHM ranged between $0'' - 10''$ and this range was divided into bins of width $0.1''$. Once the bin with the highest number count, N, had been identified, the FWHM star selection limits were found by iterating up each side of this bin and finding the bin

where the number count was closest to $\frac{1}{2}N$. These values were then scaled by the local slope of the histogram, and by how far the number count of the closest bin was to $\frac{1}{2}$N. The SEXTRACTOR stellarity cut was dropped, and all sources with FWHM within the range found using this method were selected as stars. Fig. 3.29 displays the graph set for one of the Bullet Cluster tiles, in this case resulting in 96 stars being extracted using this algorithm. The red points represent the stars finally selected from the catalogue, and the lines represent the FWHM limits found for this tile. 714 unique sources were selected as stars in this manner.

Each star selected was modelled as a sum of two Gaussians with the following free parameters: $\{x, y, \epsilon, \theta, ab_1, ab_2, A_1, A_2\}$ i.e. the two Gaussians describing each star were forced to have the same position, ellipticity and orientation, their amplitudes and sizes allowed to be different. This allowed us identify point and extended sources. 2000 samples were used. The catalogue of stars was then subjected to further selection criteria based on the IM2SHAPE results- stars satisfying the following criteria were retained: stellar ellipticity $\epsilon < 0.2$, $\delta\epsilon_{1,2} < 0.025$, fitted Gaussian centres within 2 pixels of the SEXTRACTOR original positions, and $ab_i > 0.3$ square pixels. This final selection removed any possible galaxy or cosmic ray contamination.

In total 612 survived theses cuts: 9-90 stars per cluster. Fig. 3.30 summarizes the cluster-to-cluster variation in PSF (e in the plot is equivalent to ϵ in the text). A PSF map was constructed for each cluster on a regular grid of 25×25 points. At each point the average stellar ellipticity and orientation was calculated as the Gaussian weighted mean at that position. The width of the Gaussian used for each cluster was determined by the number of stars from which the respective map was constructed, ranging from $71.6'' - 22.7''$ for maps based on 9 to 96 stars respectively (Fig. 3.31).

As an initial check of the reliability of the PSF maps, they were used to correct the shapes of the stars. For a small subsample of clusters with few stars or a badly sampled PSF, this correction was improved by finding a cluster with a similar map and combining the stellar catalogues

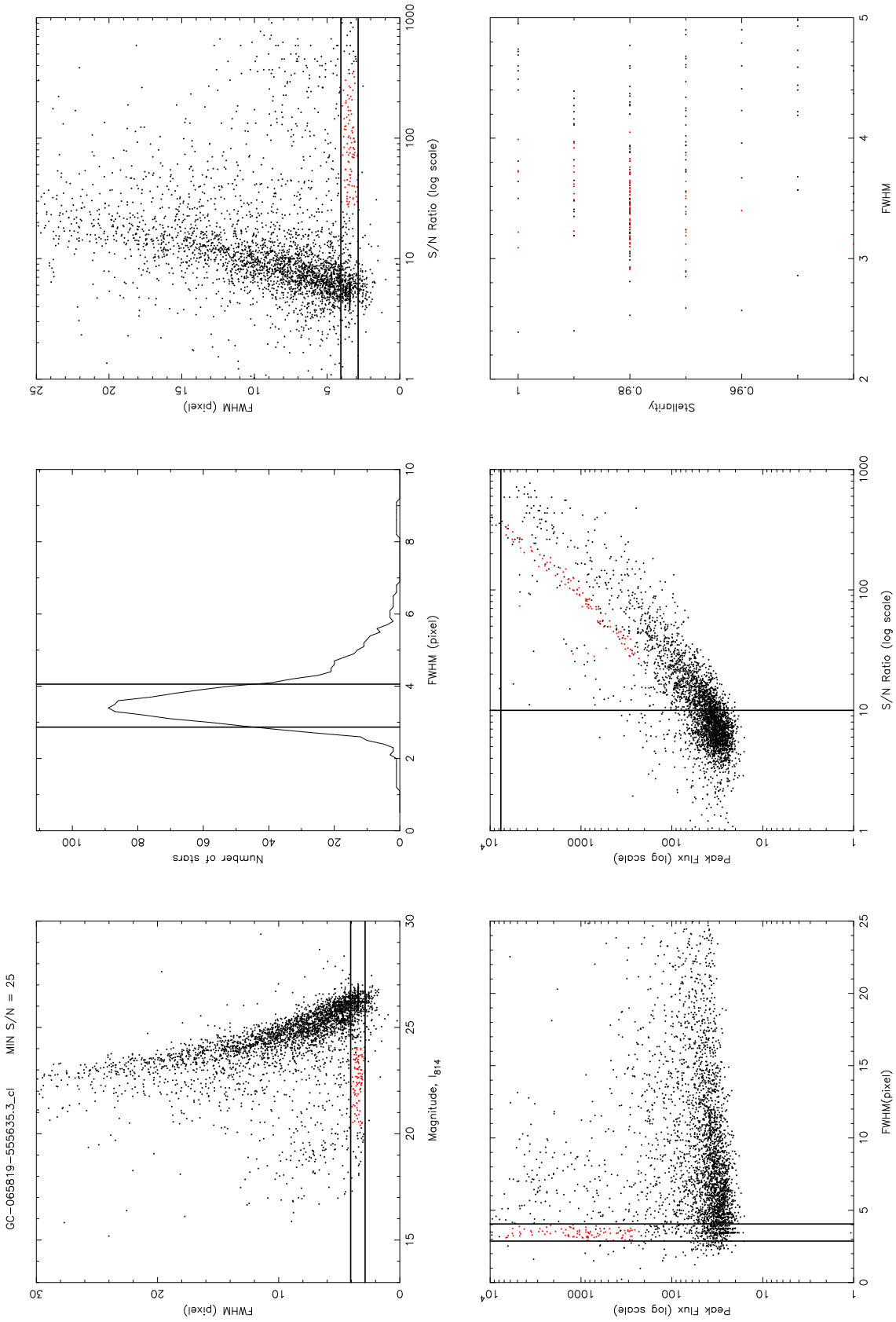

Figure 3.29: Plots showing the selection criteria for stars from the SEXTRACTOR catalogues. The FWHM criteria were calculated individually for each cluster, using the method described in the text. The selected stars are shown in red.

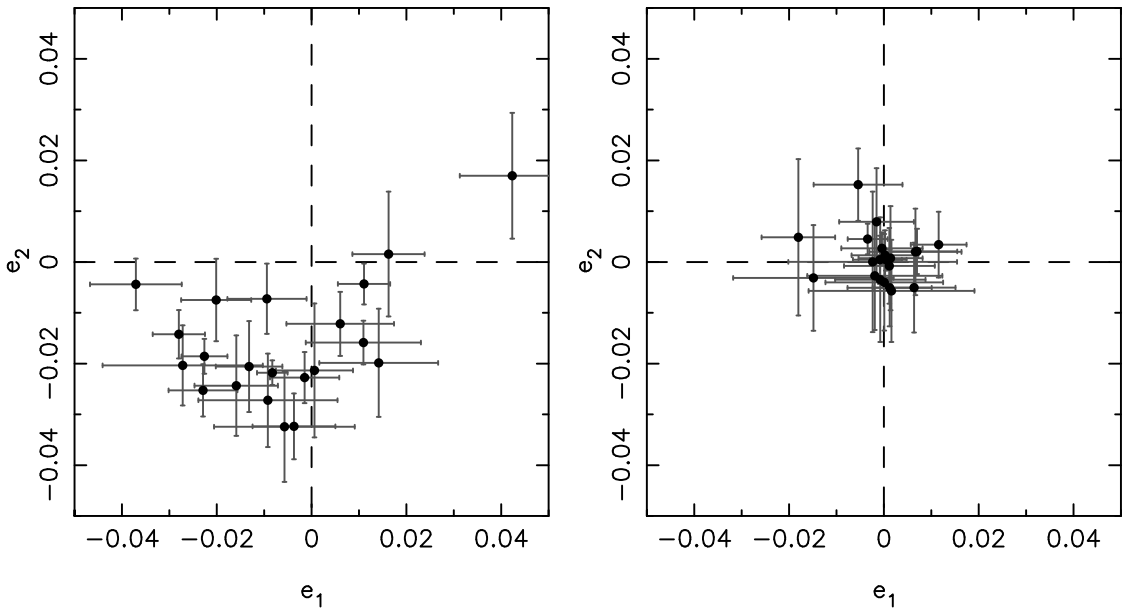

Figure 3.30: Averaged residual ellipticity components of all stars for each cluster, before (left) and after (right) PSF correction.

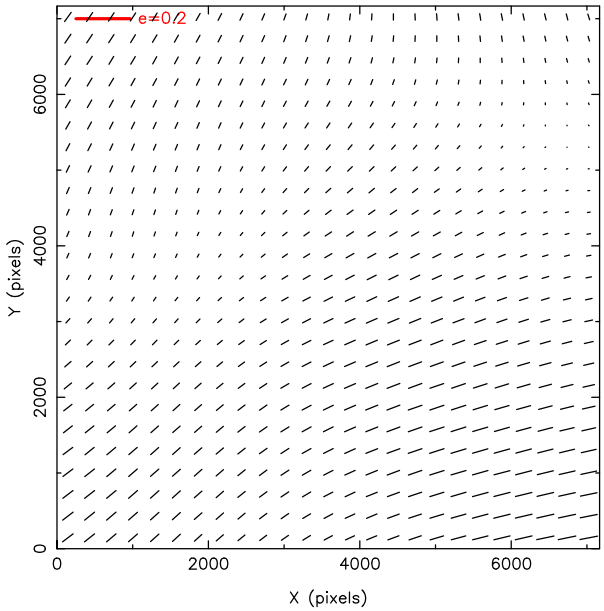

Figure 3.31: The smoothed PSF map for RXCJ0043.3, created using 26 stars and a Gaussian smoothing scale of 42.15″.

from each cluster together two maps together, before creating a joint PSF map. Fig. 3.30 shows the average stellar ellipticities before (left) and after (right) correction. After correction, 17 out of 22 cluster images had both average stellar ellipticity components consistent with zero within one sigma errors.

Faint galaxy shape measurement

The shape of each faint galaxy was measured with IM2SHAPE, once with PSF correction (using the stellar PSF maps) and once without PSF correction. The former was used to obtain galaxy shape measurements, and the latter to obtain galaxy size measurements before PSF correction. In both cases each faint galaxy was modelled as a single Gaussian with the following free parameters: $\{x, y, \epsilon, \theta, ab, A\}$. Previous fits attempted to model the galaxies as a superposition of two Gaussians, one modelling the bulge and the other the disk of the galaxies, but the data were not deep enough to support this level of complexity. Two hundred samples were used to obtain convergence, and in order to check this the IM2SHAPE fitting was repeated. As Figs. 3.32 show, the results lie along a 1-1 relation for all shape characteristics, with divergence only for those very small or extreme sources for which the fit is poor. This follows the reasoning in the STEP program mentioned in § 2.6.4, which mentioned that the ideal number of samples should be checked against the convergence of the fits.

The PSF corrected faint galaxy catalogues and the non PSF corrected faint galaxy catalogues were compared and analysed in order to obtain further systematic cuts of the faint galaxy population. Fig. 3.33 shows a stacked analysis of all sources in the source catalogues.

Based on the IM2SHAPE fits more stringent selection criteria were imposed on the faint galaxy catalogues. The limit on the error in each ellipticity component, $\delta\epsilon_i < 0.15$, was chosen due to the dependence of the shear analysis on accurate ellipticities. The minimum uncorrected

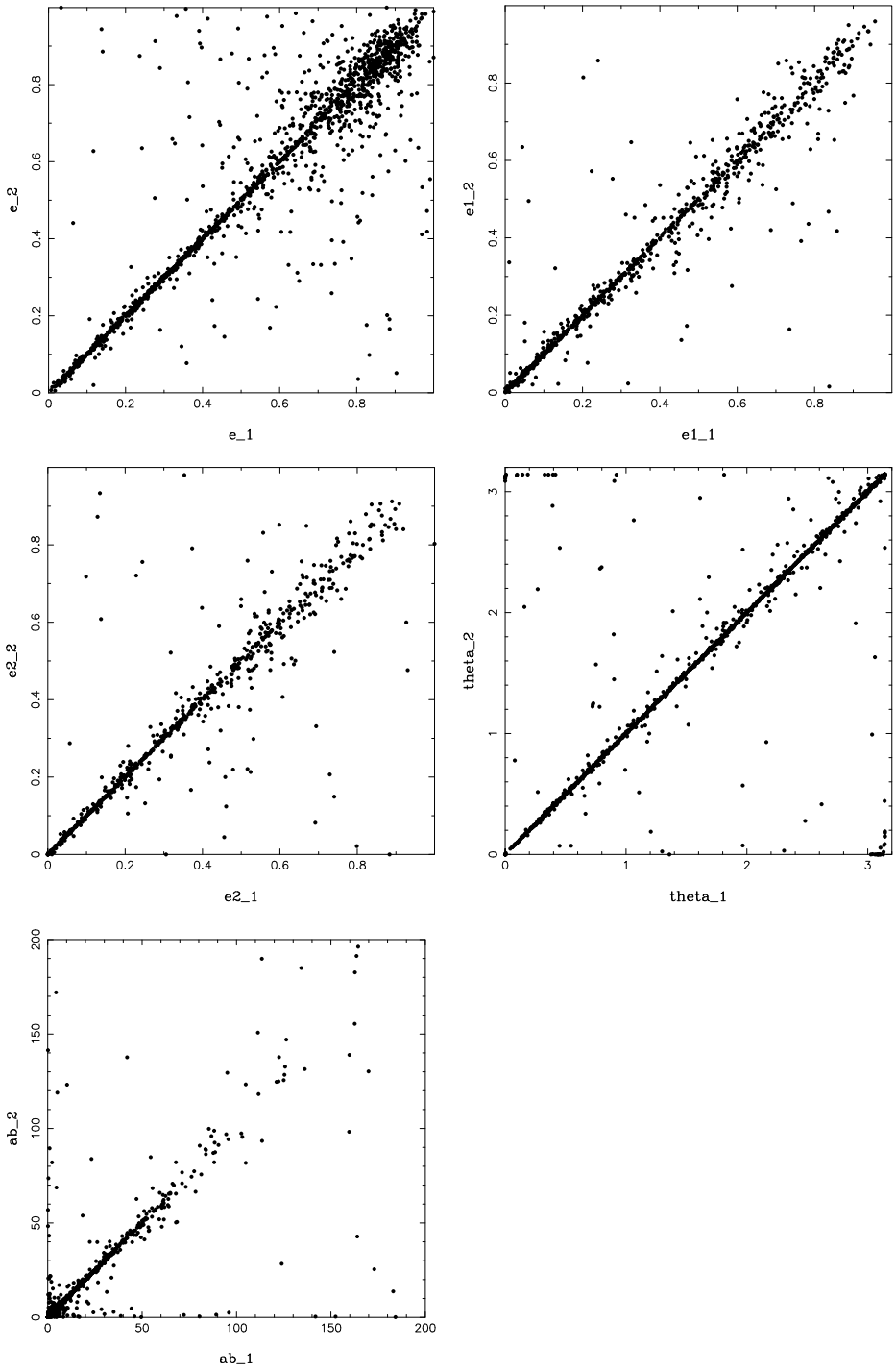

Figure 3.32: A comparison of the fitted quantities for each object in two independent IM2SHAPE runs for *A*2813, the x axis denoting one run, and the y axis denoting the second run. The relation is approximately $1-1$ for most objects, with noisier results where the values are extreme.

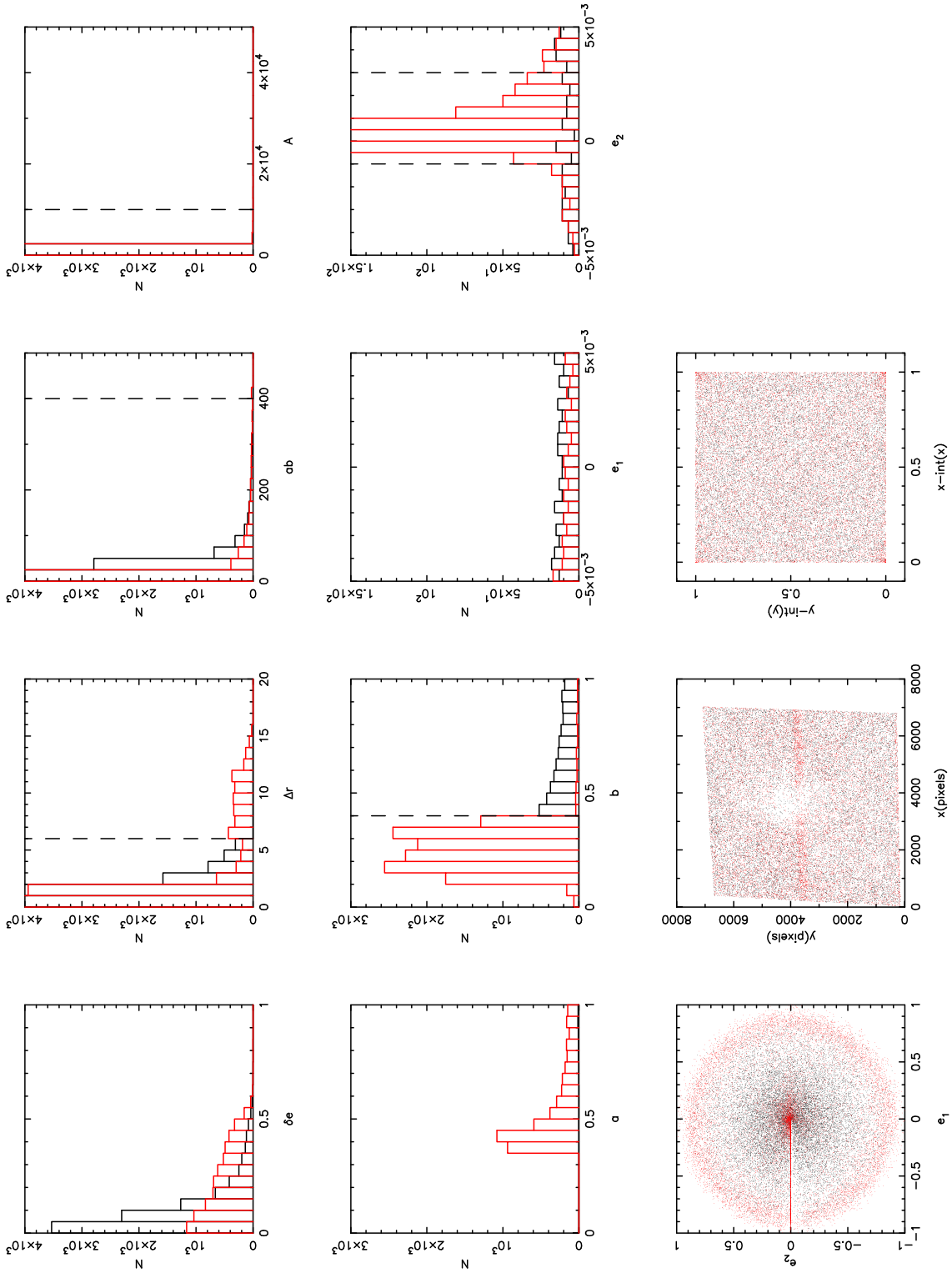

Figure 3.33: Catalogue statistics for all faint objects in all catalogues. The red markers indicate those sources that were rejected. This analysis also shows sources that would be later cut due to their proximity to the low signal to noise areas at the edge of the field of view.

Table 3.8: Catalogue Properties

Cluster	N_{tot}	$N_{gal_{initial}}$	$N_{gal_{final}}$	$N_{gal}/arcmin^2$
A 2813	3317	1636	488	43
A 141	3212	1583	463	41
A 2895	3695	1487	382	34
RXCJ 0220.9-3829	3477	1716	475	42
A 368	3089	1352	344	31
A 3084	3714	1622	427	38
A 3088	3039	1357	386	34
RXCJ 0331.1-2100	3385	1571	408	36
A 3140	3461	1428	324	29
A 3192	3451	1474	473	42
A 3292	3738	1615	365	32
RXCJ 0528.2-2942	3023	1288	305	27
A 3364	3533	1419	316	28
AS 0592	3278	1230	323	29
1ES0657-558	5941	5401	728	38
A 611	2775	1448	447	40
A 781	3397	1437	463	41
Z 2701	2761	1679	541	48
RXJ 1000.5+4409	3818	1876	414	37
A 2187	3401	1461	361	32
A 2537	2609	1367	452	40

area of each fitted Gaussian was required to be twice that of the resolution element, the uncorrected catalogues providing an unbiased estimate of the detection area with respect to the PSF of the camera, the limit given in Eq. 3.3.

$$a * b > 2 \times 4\frac{(1+\epsilon)}{(1-\epsilon)} \tag{3.3}$$

Additional cuts based on IM2SHAPE systematics were also applied to ϵ_1, ϵ_2. This resulted in approximately $30-40$ galaxies per square arcminute, and 8885 faint galaxies selected in total. Finally these catalogues were rotated to align the *x*– and *y*– axes to the WCS. More details on both the faint galaxy selection and PSF correction are listed in Tables. 3.8, 3.9.

Table 3.9: PSF Correction and Star Catalogue Parameters

Cluster	N_{star}	$N_{goodstar}$	Uncorrected Stellar $\bar{\epsilon}$		Corrected Stellar $\bar{\epsilon}$	
			$\bar{\epsilon}_1$	$\bar{\epsilon}_2$	$\bar{\epsilon}_1$	$\bar{\epsilon}_2$
A 2813	28	26	-0.0159 ± 0.0088	-0.0243 ± 0.0099	-0.0016 ± 0.0079	0.0079 ± 0.0106
A 0141	16	13	0.0142 ± 0.0125	-0.0199 ± 0.0107	-0.0019 ± 0.0143	-0.0027 ± 0.0107
A 2895	23	15	-0.0057 ± 0.0148	-0.0324 ± 0.0109	0.0016 ± 0.0175	-0.0057 ± 0.0101
RXCJ 0220.9-3829	12	9	0.0423 ± 0.0111	0.0170 ± 0.0124	-0.0008 ± 0.0095	-0.0035 ± 0.0123
A 0368	22	10	-0.0092 ± 0.0147	-0.0272 ± 0.0092	-0.0024 ± 0.0178	0.0000 ± 0.0138
A 3084	29	19	-0.0272 ± 0.0169	-0.0204 ± 0.0079	-0.0149 ± 0.0169	-0.0031 ± 0.0104
A 3088	25	21	-0.0201 ± 0.0074	-0075 ± 0.0081	0.0066 ± 0.0097	0.0020 ± 0.0085
RXCJ 0331.1-2100	21	18	-0.0229 ± 0.0073	-0.0253 ± 0.0051	0.0012 ± 0.0089	-0.0051 ± 0.0076
A 3140	20	14	-0.0371 ± 0.0097	-0.00440 ± 0.00508	-0.0004 ± 0.0086	0.0027 ± 0.0031
A 3192	21	17	0.0162 ± 0.0076	0.0016 ± 0.0123	-0.0064 ± 0.0087	-0.0051 ± 0.0088
A 3292	37	30	-0.0094 ± 0.0084	-0.0072 ± 0.0069	-0.0054 ± 0.0094	0.0152 ± 0.0071
RXCJ 0528.2-2942	28	24	-0.0037 ± 0.0087	-0.0324 ± 0.0065	0.0012 ± 0.0096	-0.0008 ± 0.0074
A 3364	46	41	-0.0015 ± 0.0073	-0.0228 ± 0.0050	0.0002 ± 0.0070	0.0013 ± 0.0049
AS 0592	63	60	-0.0226 ± 0.0048	-0.0186 ± 0.0034	-0.0035 ± 0.0042	0.0045 ± 0.0030
1ES0657-558	181	169	-0.0083 ± 0.0032	-0.0218 ± 0.0024	0.0004 ± 0.0034	0.0004 ± 0.0021
A 611	28	28	-0.0280 ± 0.0055	-0.0142 ± 0.0048	-0.0009 ± 0.0056	0.0004 ± 0.0047
A 781	26	21	0.0109 ± 0.0121	-0.0159 ± 0.0043	0.0070 ± 0.0085	0.0021 ± 0.0045
Z 2701	9	9	0.0006 ± 0.0081	-0.0214 ± 0.0132	-0.0181 ± 0.0078	0.0049 ± 0.0154
RXJ 1000.5+4409	29	21	0.0060 ± 0.0114	-0.0122 ± 0.0063	0.0001 ± 0.0124	-0.0040 ± 0.0095
A 2187	38	35	0.0111 ± 0.0055	-0.0043 ± 0.0040	0.0116 ± 0.0059	0.0034 ± 0.0065
A 2537	12	12	-0.0132 ± 0.0070	-0.0206 ± 0.0090	0.0014 ± 0.0068	0.0007 ± 0.0103

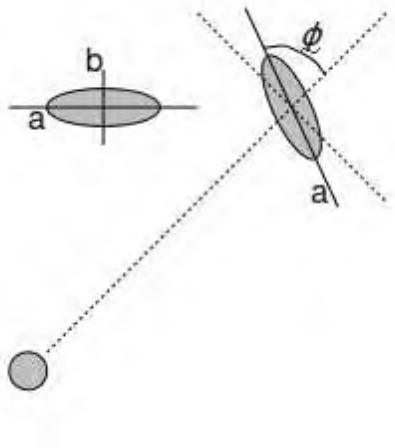

Figure 3.34: A lens galaxy sheared by a potential at 0,0. a and b denote the semi major and minor axes respectively, ϕ the angle of a with respect to the centre of the potential.

3.6 Tangential Shear Analysis

The distortion caused by the potential on a galaxy image can be described by two properties: the tangential and cross components of the shear (Eq. 3.4, Fig. 3.34) with respect to the centre of that potential. The strength of the shear signal at any point is measured by the tangential shear. In the presence of a strong shearing effect the cross component should be consistant with zero. An average of the shear signal over the whole field can give an indication of how massive a cluster is. Substructure in the DM distribution can dilute the shear signal or boost it, depending on the location and size of the substructure, as can the inclusion of faint cluster members in the background galaxy catalogue. The latter effect our results are particular sensitive to as the single filter data is not enough to guarantee exclusion of all cluster members from the faint catalogues: multi colour data is needed to construct a Red Sequence and target the cluster members for removal.

$$\begin{aligned} \gamma_\tau &= -\tau * cos(2\phi) \\ \gamma_X &= \tau * sin(2\phi) \\ \tau &= \frac{(1-(\frac{b}{a})^2)}{2(\frac{b}{a})} \end{aligned} \tag{3.4}$$

The error weighted average of all shear measurements within annuli of $60'' - 150''$ (approximating an ACS field width given a centred BCG) are given in Table 3.10, which also gives the

significance of the tangential signal and by how many σ is the cross component consistant with zero. The ACS pointings were centred on the cluster BCG, thus the brightest and largest galaxy near this position was identified as the BCG and centre of the cluster core. This selection was accurate for all clusters except A 0781, in which observation was believed mispointed and the wrong galaxy identified as the BCG, and A 0141, wherein it is believed the wrong galaxy was identified as the BCG in construction of the LoCuSS cluster catalogue. Fig. 3.35 shows the average cross component versus the tangential component of each cluster for the arcsecond annulus. This annulus was used as it gives a measure of how well the shear signal is determined within the image rather than a mass tracer comparable between clusters. Some of the clusters had surprisingly low γ_τ signal to noise. At least two of these were mispointed: $A0141$ and $A0781$. The image aperture meant the shear of the subclump in the Bullet Cluster interfered with the signal of the BCG centered distribution, causing a low signal to noise for this cluster. The low significances can be due to low mass causing poor constraints, a similar effect caused by poor image quality or substructure on a scale such that the shear field is not sufficiently sampled within the field of view, resulting in the signal being biased low.

This analysis assumes a spherically symmetric cluster centred on the BCG position. However, as will be established in later chapters, some of this clusters are multi modal, while others have mass distributions with centres offset from the BCG. Deviations from these assumptions causes and increase in the cross shears, and reduces the significance of the tangential shear signal. Thus a low shear signal with high cross component could represent not only a low mass cluster with poor constraints, but also a high mass cluster with significant substructure within the shear aperture. Indepth discussion of each cluster result individually in the context of the lens modelling and comparison with multiwavelength data can be found in § 5.1.

Table 3.10: Tangential and Radial shears.

Cluster	γ_τ	$\delta\gamma_\tau$	$S/N(\gamma_{tau})$	γ_X	$\delta\gamma_X$	$N\sigma(\gamma_X cw0)$
A 2813	0.1717	0.0269	6.3915	0.0377	0.0179	3
A 0141	0.0358	0.0230	1.5574	0.0042	0.0196	1
A 2895	0.1107	0.0186	5.9415	0.0613	0.0218	3
RXC J0220.9-3829	0.0767	0.0241	3.1894	0.0481	0.0228	3
A 0368	0.1160	0.0344	3.3734	-0.0320	0.0233	2
A 3084	0.0846	0.0229	3.6977	0.0433	0.0197	3
A 3088	0.1101	0.0265	4.1498	-0.0027	0.0166	1
RXC J0331.1-2100	0.0632	0.0267	2.3686	-0.0546	0.0213	3
A 3140	0.1089	0.0282	3.8629	0.0004	0.0188	1
A 3192	0.1121	0.0208	5.3994	0.0070	0.0176	1
A 3292	0.0862	0.0332	2.5969	-0.0026	0.0259	1
RXC J0528.2-2942	0.1517	0.0246	6.1621	0.0429	0.0258	2
A 3364	0.0941	0.0262	3.5908	0.0168	0.0235	1
AS 0592	0.1257	0.0222	5.6609	-0.0310	0.0163	2
1ES0657-558	0.0454	0.0190	2.3882	-0.0067	0.0135	1
A 0611	0.0869	0.0260	3.3359	0.0147	0.0185	1
A 0781	0.0839	0.0344	2.4382	-0.0520	0.0203	3
Z 2701	0.0235	0.0202	1.1657	0.0035	0.0180	1
RX J1000.5+4409	0.1017	0.0286	3.5541	0.0748	0.0269	3
A 2187	-0.0017	0.0288	-0.0603	0.0090	0.0175	1
A 2537	0.1224	0.0292	4.1958	-0.0100	0.0227	1

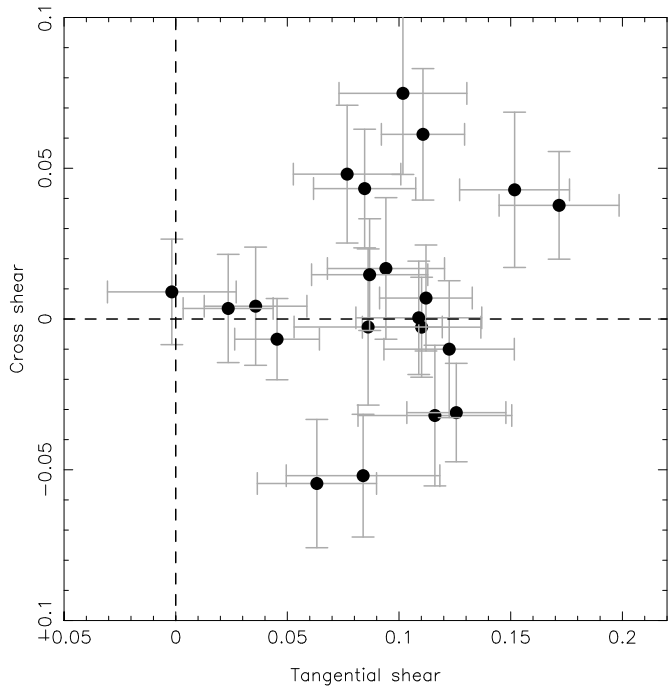

Figure 3.35: Average tangential shear versus cross component of the shear.

3.6.1 Charge Transfer Efficiency

Since the reduction of the ACS SNAPSHOTS and shape measurement of the faint galaxies was performed, Rhodes et al. (2007) (hereafter R07) has published a discussion of the degredation of the Charge Transfer Efficiency (CTE) of the ACS. The charge from each pixel of the CCDS is read out vertically when the data from an observation is stored. The CTE describes how efficiently the charge is transferred from pixel to pixel as it travels towards the read out position. This efficiency has degraded over time, resulting in a charge bleeding effect along the y-axis of the ACS that results in a increase in ellipticity along the y direction, which is most severe towards the centre of the ACS field of view. It impacts faint objects most severely, as the effect is scale independent, and is not removed by PSF correction.

To assess the impact of CTE on our data, the top panel Fig. 3.36 shows the variation of the average e_1 ellipticity component of the faint galaxies against position along the y-axis for A 2813. This component will be reduced if there is shear in the y direction, either from the CTE effect or from the lens field of a cluster. The magnitude of the induced shear by the CTE effect

on faint galaxies in the all the frames in the COSMOS survey, as found by R07, is given in the bottom panel of this plot, which comes from the top panel of Fig. 14 from R07. Both plots show the PSF corrected elliticity. The R07 analysis was performed using observations through filter F814W, however the effects apply to other filters. At its most extreme, the CTE effect induces a shear of ~ 0.04 in the faint galaxies. However, the magnitude of the error on the mean shear of the middle bin, induced by our clusters centred in the middle of the ACS field of view, is 0.08 on average over all clusters. This implies that the variance of the shears in the middle of the range is greater than the magnitude of the CTE effect. Neither this mean shear nor this error on the mean include information about the individual faint galaxy errors, which would act to increase the error on the mean. The average error on this ellipticity component ranges from $0.055-0.068$ for all faint sources in each catalogue. A improved analysis would correct for the CTE, possibly based on the formalisms described in R07, however for this data we conclude the CTE is within the error budget on the shear, and would be difficult to model and remove due to the large measurement error on the shear.

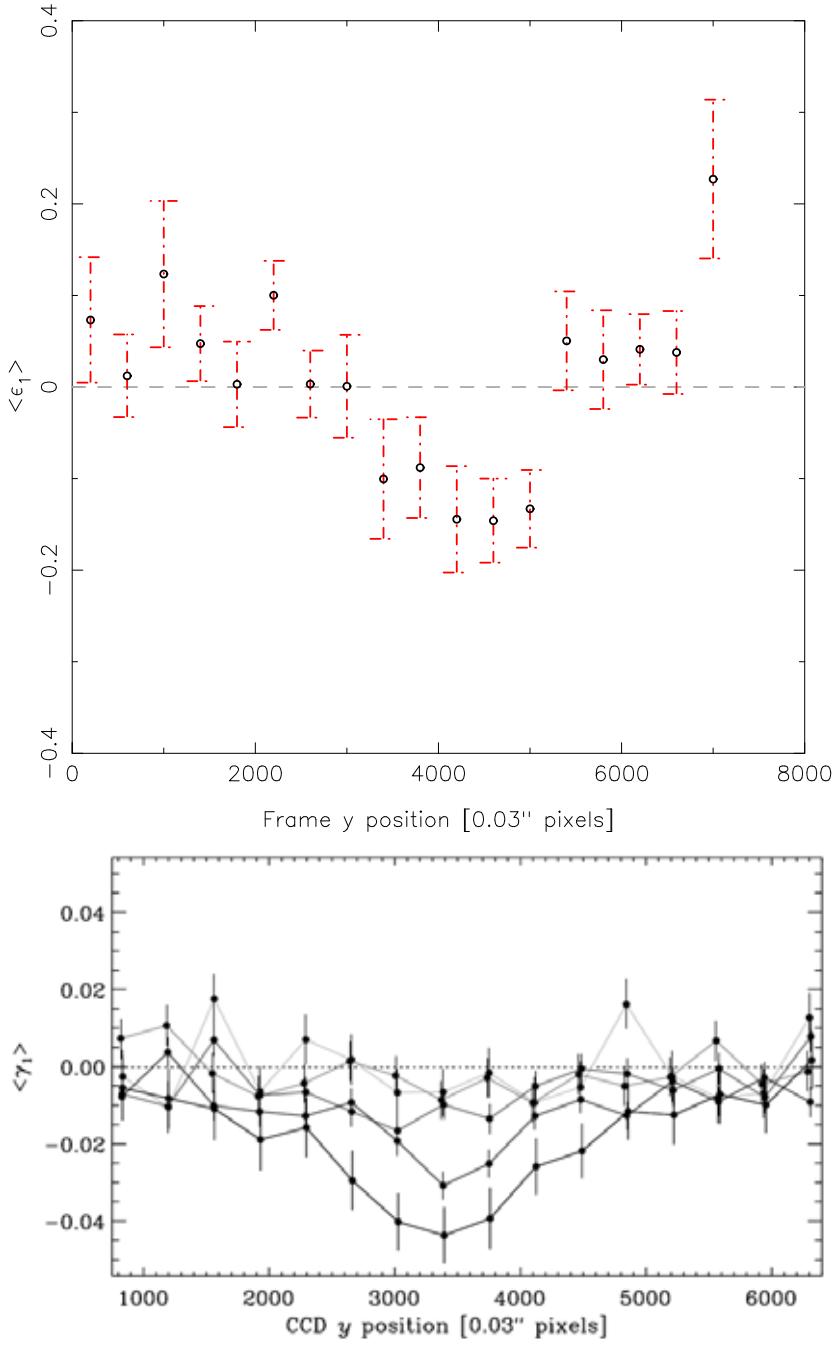

Figure 3.36: Top: average PSF corrected e_1 distribution as a function of position in y for faint galaxies from the observations of A 2813. Error bars denote the error on the mean shear in each bin. The induced shear in this panel is a combination of the shear signal of the cluster and the CTE effect. Bottom: the top panel of Fig. 14 from R07, showing the PSF corrected e_1 distribution as a function of position in y, from all observation frames in the COSMOS survey. The induced shear in this panel is due to the CTE effect only.

Chapter 4

Weak Lens Mass Reconstruction of Cluster Cores

This chapter will cover the parameterized and non-parameterized weak lens analysis of the faint galaxy catalogues obtained in § 3.5. I will start by describing the creation of non-parameterized surface mass density (κ) maps, generated using LENSENT2, and use of these maps to obtain constraints on the mass peak offset from the BCG position. I will describe the parameterized multi halo model fits to unsmoothed and smoothed faint galaxy catalogues using LENSTOOL, the use of IR priors to help constrain the substructure distribution, and discuss the attempts to model and constrain the impact of uncorrected cluster contamination on the ficidual weak masses.

4.1 Non-parameterized mass reconstruction with LENSENT2

LENSENT2 (Bridle et al., 1998; Marshall et al., 2002)[1] was used for the non-parameterized mass reconstruction of the clusters in our sample (§ 2.6.2). Weak lensing analysis usually requires that the shear of several spatially close background galaxies is binned in order to obtain a strong enough signal for model fitting or direct reconstruction. LENSENT2 treats each galaxy shape measurement as a single bin, thus making this method is particularly suited to the single filter, shallow ACS data, with which we cannot afford to lose any resolution via binning. The

[1] LENSENT2 is available from http://www.slac.stanford.edu/ pjm/lensent/

smoothing that would have been applied before hand via shape measurement binning is applied after the reconstruction, characterising the large scale potential of the cluster. The width of this smoothing step can be chosen based on a robust, statistical analysis of the LENSENT2 model properties, rather than arbitrarily choosing a scale if binning the galaxy shear measurements. This allows the data to drive the Bayesian inference of the internal structure of the cluster cores. As lensing is a non local effect, structures outside the faint galaxy observation field of view will impact the shear signal, and thus the mass reconstruction, within the field of view. LENSENT2 accounts for this by buffering the field of view by a factor of $1.5-2$, allowing the opportunity for the reconstruction of mass structure beyond the observed area in some clusters. LENSENT2 is also computationally cheap, which made it ideal for obtaining convergence maps using multiple smoothing scales and resolutions on which to perform our initial analysis.

4.1.1 Maps of the Projected Surface Mass Density

LENSENT2 characterises the large scale potential of the cluster using an Intrinsic Correlation Function (ICF), of Gaussian form, replacing the more common binning of faint galaxy shears before reconstruction. As a result the smoothing that would normally occur through the binning of the faint galaxy shear information is transferred to the reconstruction itself. In this analysis we primarily optimised a physical kpc scale which allowed us to ensure that the minimum spatial scale of reconstructed substructures in the convergence maps was consistent between clusters. While angular smoothing scales are more sensitive to the number density of faint galaxies, as our primary interest is the distribution of substructure within the clusters, the physical smoothing scale allowing us to investigate and compare group scale substructures at all the redshifts in our sample. Also investigated was the impact of changing the reconstruction pixel grid size. For completeness, angular smoothing scales were also investigated, and the most favoured result over the whole sample, $30''$ is consistent with the physical smoothing scale ultimately chosen (100kpc) over the whole sample redshift range (100kpc $\sim (38''-23'')$ for $0.15 < z < 0.3$).

$$Pr(\kappa|\underline{d_0}) = \frac{Pr(\underline{d_0}|\kappa)Pr(\kappa)}{Pr(\underline{d_0})} \tag{4.1}$$

Eq. 4.1 gives Bayes Theorem as applied in LENSENT2. The terms are the likelihood of the shear field given the data, $Pr(\kappa|\underline{d_0})$, the likelihood of the data given the shear field, $Pr(\underline{d_0}|\kappa)$, the prior information on the shear field, $Pr(\kappa)$), and the Bayesian evidence (bottom term).. The Bayesian evidence produced by LENSENT2 can be used to differentiate between different ICF widths. However the profile of the evidence distribution with respect to ICF width for each cluster was not a simple peak. Most clusters had a double peaked evidence distribution, and past a certain width the evidence remained high. The double peak phenomenon was interpreted to be due to the complex structure in the underlying DM distribution. At the position of the first, lower peak in evidence, the ICF width characterises the size of the substructures in the Dark Matter mass distribution. At the second, higher peak in evidence, the larger ICF width has smoothed out any substructures in the map, producing a simpler map that is assigned a better fit, and higher evidence value. After this point the evidence of the fit for a given ICF width rises as the smoothing becomes more extreme and the model even simpler. The ICF width associated with the first peak in the evidence distribution, believed to reflect the scale of substructures in the underlying mass distribution, was initially selected. The lowest width within the error on the evidence was then found, to maximise substructure resolution.

The size of the reconstructed substructures depends on how well the shear field is sampled, and how large their lensing contribution is. There will be a substructure size limit below which the shear contribution will be too small, the faint galaxy sampling too sparse and the measurement error too large to reconstruct that substructure. The higher redshift clusters in our sample are likely to include larger mass clusters due to an X-ray luminosity selection effect: low mass clusters have low X-ray luminosities and are more difficult to detect at higher redshifts. Additionally N_{sub} may be expected to increase with total cluster mass, larger clusters having had a greater number of infall events. So the increasing DM distribution complexity and lower resolution may result in poorer substructure reconstruction of the more distant clusters. This is an

issue which may effect all our analysis, as it depends on how well the shear field is sampled with faint galaxy measurements.

A small physical smoothing scale that produces sensible lower limits on substructure sizes in low redshift maps will allow small, noise dominated substructure detections in the high redshift maps. On the other hand, a physical smoothing scale that is large enough to not be effected by noisy detections in the high redshift maps could be too large for the field of view of the lower redshift maps, and the substructure in the DM distribution would be smoothed out. If the ICF width was at a set arcsecond scale for all clusters, this would allow smaller substructures to be reconstructed in the lower redshift clusters than the higher redshift clusters. This may help with the more distant clusters, as smaller substructures would be smoothed out and only the reliable detections of more massive substructures remain. But this method correlates the lower limit on the size of the reconstructed substructures with redshift, and could result in details in the high redshift maps being smoothed out. In order to systematically quantify cluster mass and substructure and compare the DM distribution complexity between clusters, the physical restrictions must be the same, so applying a physical smoothing scale, and therefore a consistent lower limit on the physical size of the reconstructed substructures, would ensure we are detecting the same range of objects.

The analysis performed on the evidence should produce ICF widths that are large enough to optimise the fit with respect to the difficulties of the high mass clusters, yet small enough so that the detail in the lower redshift cluster maps is not smoothed out. For each cluster the reconstructions were based on 64x64,128x128 or 256x256 pixel grids, centred on the BCG position, with physical ICF widths of $50, 75, 100, 125, 150$kpc and arcsecond ICF widths of $15, 30, 45, 60, 75''$. The scaling nature of the physical ICF width means that at the lower end of our redshift scale ($z = 0.15$) physical apertures above ~ 175kpc will correspond to ($> 70''$), over a third of the width of the field of view, and thus smoothing out most of the structure. The ideal ICF width

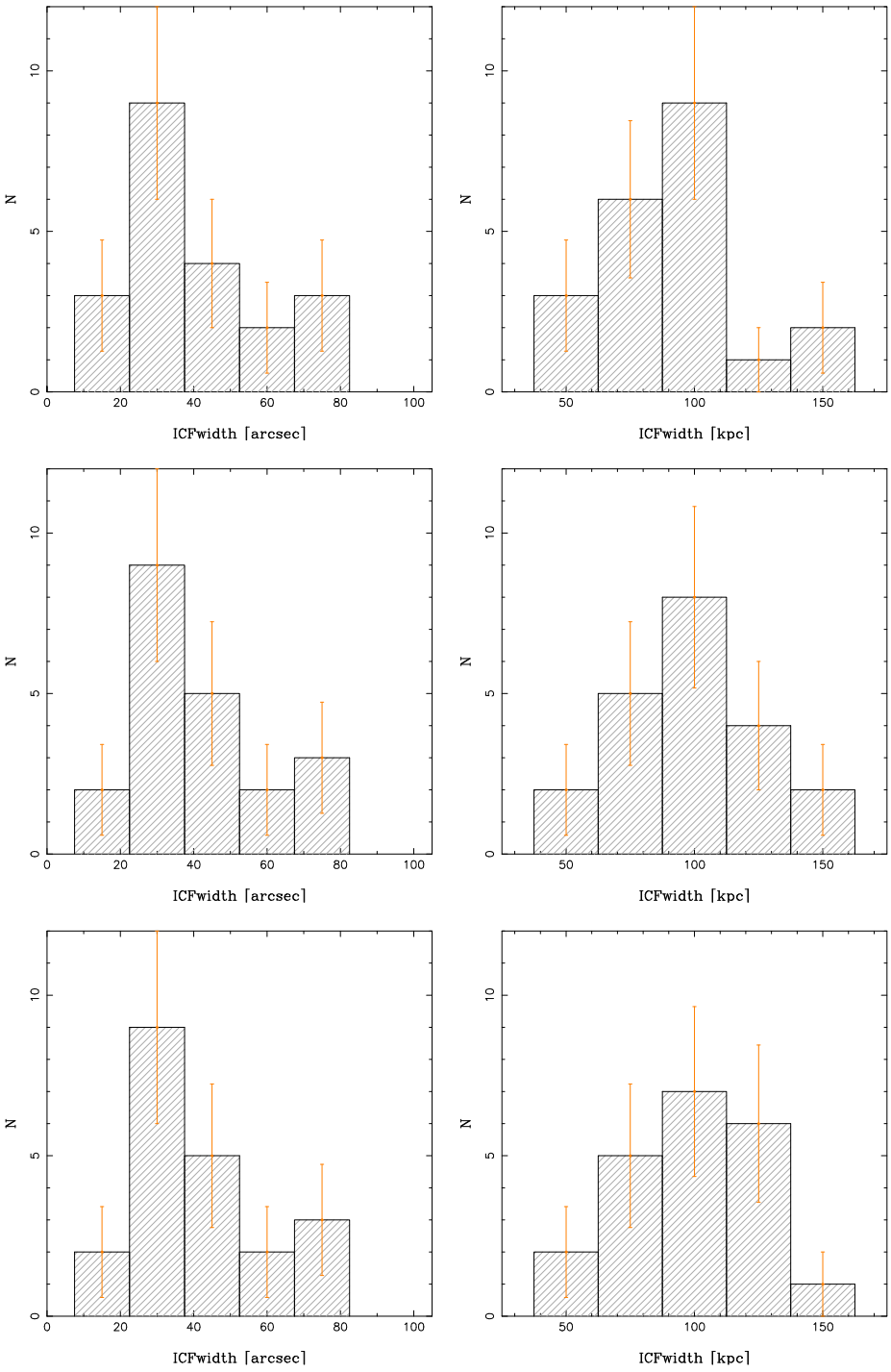

Figure 4.1: The left panel on each row displays the evidence distribution for ICF widths in arcseconds, the right panel the same in kpcs. From top to bottom: 64x64, 128x128 and 256x256 pixel reconstruction grids.

was chosen for each grid resolution and ICF width type for each cluster, following the formalism above. The distribution of widths over all clusters in each model is given in Fig. 4.1. Based on these results, the ICF width was set to 100kpc for all clusters. A smoothing scale of 100kpc translates to $\sim 25''$ at $z = 0.3$, approximately one tenth of the field width, whereas the same scale is equivalent to $\sim 40''$ at $z = 0.15$. The grid size was chosen to be 256x256 pixels, to ease visual comparison with the luminosity and X-ray distribution maps. A comparison of results from different grid sizes at different ends of the redshift scale, using ICF width of 100kpc, are given in Fig. 4.2.

The reconstructions extend the field by a factor of ~ 1.5 to reflect that lensing is a non local effect, and the signal within the field will be influenced by the mass distribution outside it. By comparison with luminosity and X-ray distributions, this could allow investigation into what information can be derived about the mass distribution outside the ACS field of view. The final LENSENT2 mass maps are given in the bottom right panels of Figs. A.1-A.21, and all are shown in Fig. 4.3.

Noise

LENSENT2 produces a map of the noise and finds a signal to noise map by dividing the maximum entropy realisation by the error map. Examples of the κ, noise and signal to noise maps for two clusters are given in Fig. 4.4. Ideally, creating the signal to noise map in this manner should apply errors to both the κ signal and the spatial morphology of structures in the κ map. Any anomalous features in the κ map that are associated with high error in the error map will be given less significance than true features with low associated error. However, any anomalous features in the error map can create false areas of high significance in the signal to noise map.

When the signal to noise maps for all clusters were studied, a strong noise signal was detected that was common to all noise maps generated by LENSENT2. The underlying pattern in

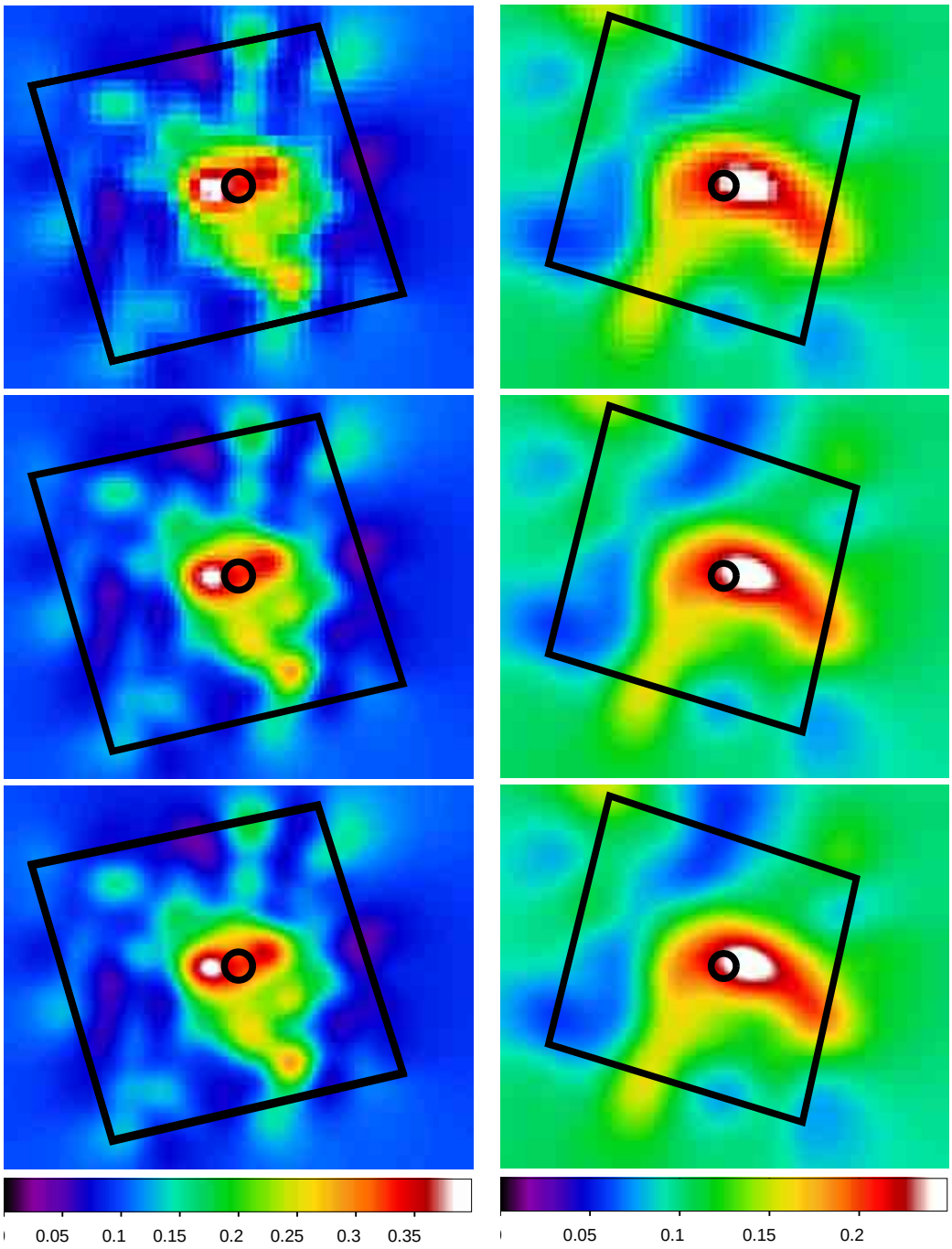

Figure 4.2: Right: A 3292, at z = 0.1501; Left: A 2813, at z = 0.2924. From top to bottom: 64x64, 128x128 and 256x256 pixel maximum entropy pixel reconstruction grids using an ICF width of 100kpc. The black box shows the ACS field of view, and the black circle denotes the BCG position. In both images, North is up and East is left. The colour bar at the bottom shows the κ scale in for each cluster.

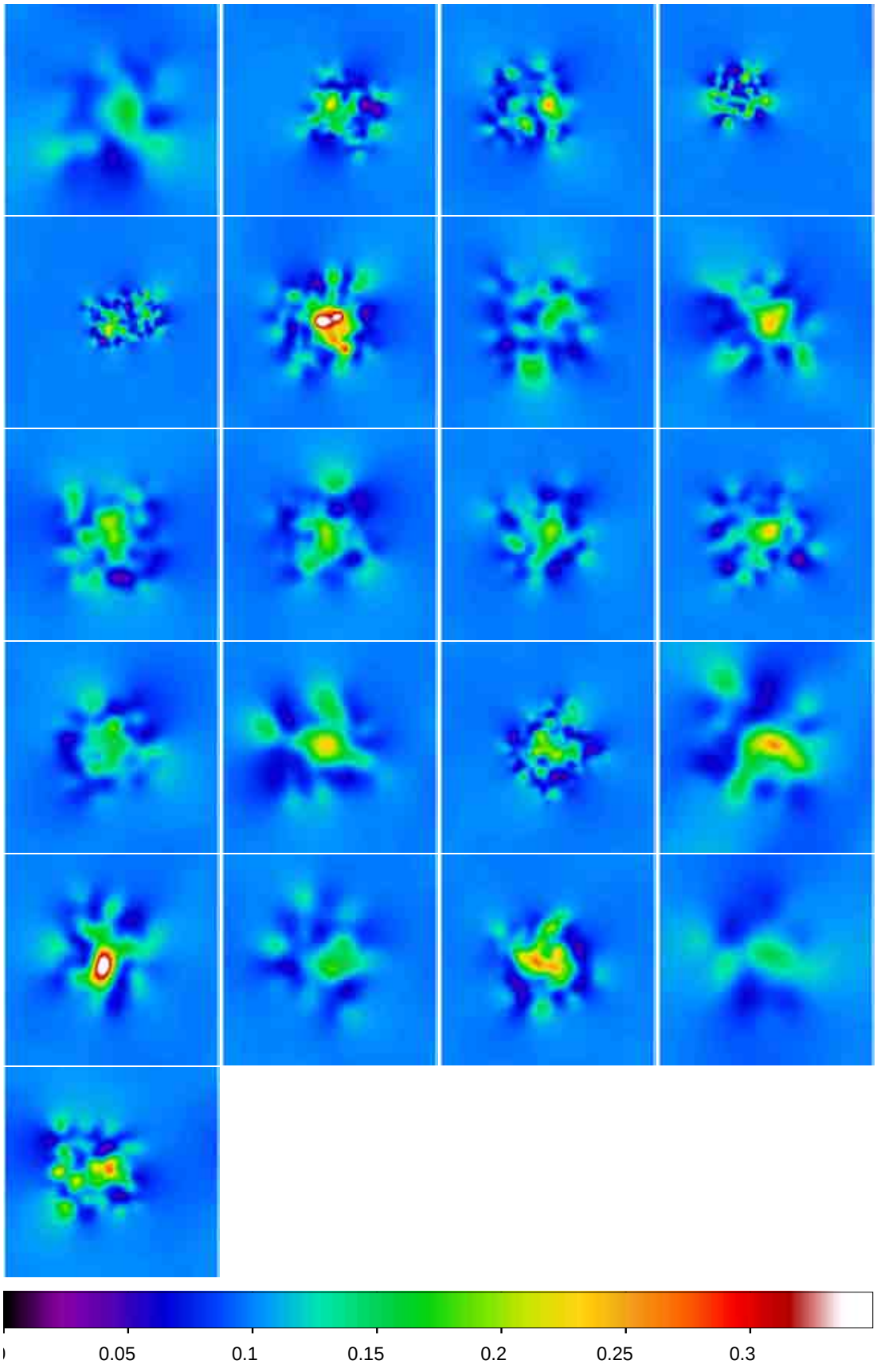

Figure 4.3: Maximum entropy κ maps for all 21 clusters, from left to right, top to bottom: A 2187, A 2537, A 0611, A 0781, IES0657-558, A 2813, A 0141, A 2895, RXC J0220.9, A 0368, A 3084, A 3088, RXC J0331.1, A 3140, A 3192, A 3292, RXC J0528.2, A 3364, AS 0592, RX J1000.5, Z 2701. Each map uses the same colour scaling, given in the colour bar at the bottom. North is up and East is left. The ICF width is 100kpc in all maps except A 2187, where it is 125kpc, and RX J1000.5, where it is 150kpc.

the noise maps created false artefacts when the signal to noise maps were generated, and possibly reduced the signicance of genuine features in the κ maps. Mean noise maps for different smoothing scales are given in Fig. 4.5. Maps reconstructed with a small ICF width are noisier, and this dominates over the underlying noise pattern. However, while maps reconstructed with larger ICF widths have small magnitude noise in the error maps, the underlying pattern is more consistent and of a magnitude to cause significant anomalous structures in the signal to noise map (Fig. 4.4, bottom row, far right panel). Fig. 4.6 shows the same maps but with the colours scaled to the minima and maxima of each image (no colour bars included). The significance and form of the underlying noise pattern compared to the error associated with the mass reconstruction becomes clearer at higher ICF widths.

These artefacts are possibly caused by the random number generator used by LENSENT2 (P. Marshall, priv. comm.) and we decided not to trust the signal to noise map generated by LENSENT2. However the error map does contain valuable information, such as the level of noise in the map and, for those regions where the reconstruction signal dominates over the underlying noise pattern, some information on the positional error. For comparison with multiwavelength data, we wanted to display signal to noise contours on the maps. While the underlying error pattern meant we decided not to directly display the error maps, the average error over the whole error map was used to construct signal to noise levels for contouring and interpreting the κ maps.

In order to investigate the spatial noise on the structures within the reconstructed κ maps, we followed two approaches: a B-mode test, where the reconstruction was repeated with all galaxy observations rotated by 45°, and a bootstrapped MCMC resampling of the faint catalogue to provide constraints on the position of the κ mass peak associated with the BCG.

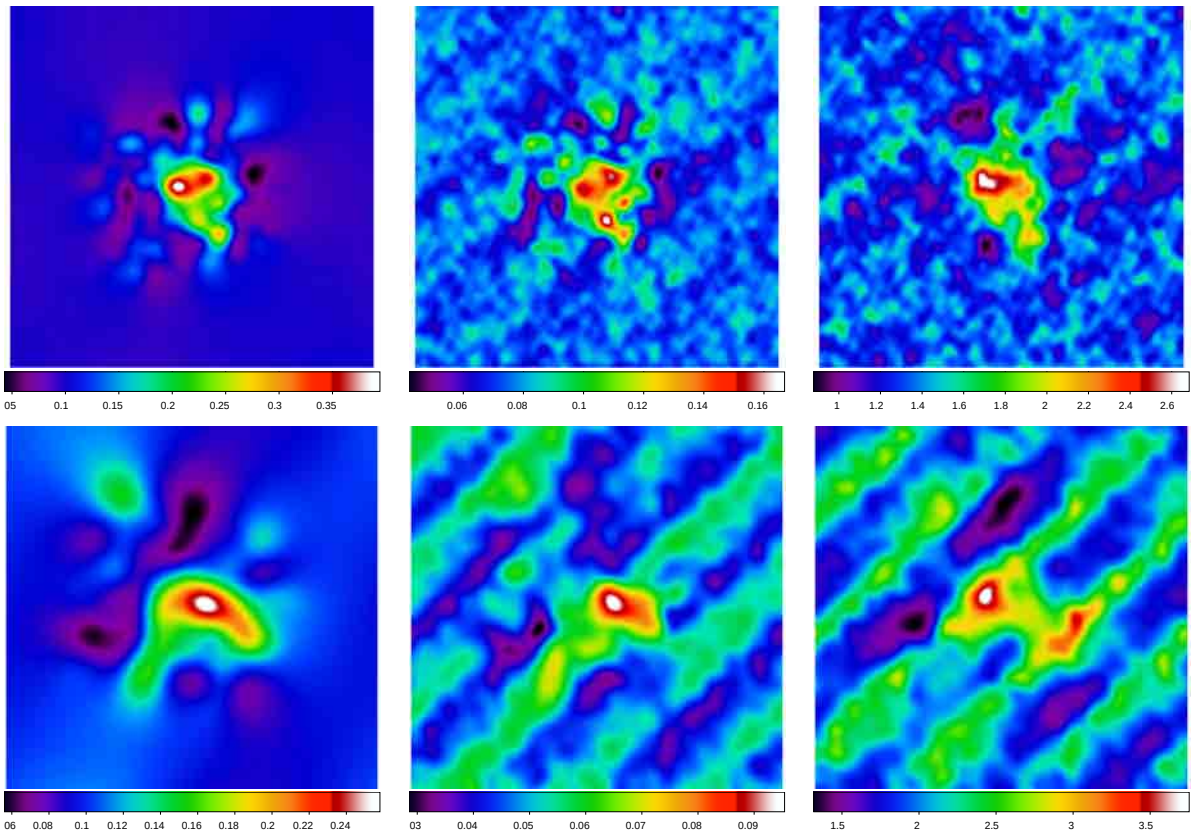

Figure 4.4: Top: maximum entropy, error and signal to noise map for A 2813. This cluster has strong lensing and a very strong shear signal, resulting in a good fit at an ICF width of 100kpc, so the interference from the anomalous noise pattern is less. Bottom: the same again for A 3292, which has a much weaker signal and the map is very much distorted in the signal to noise map due to the underlying noise pattern. In each image, North is up and East is left.

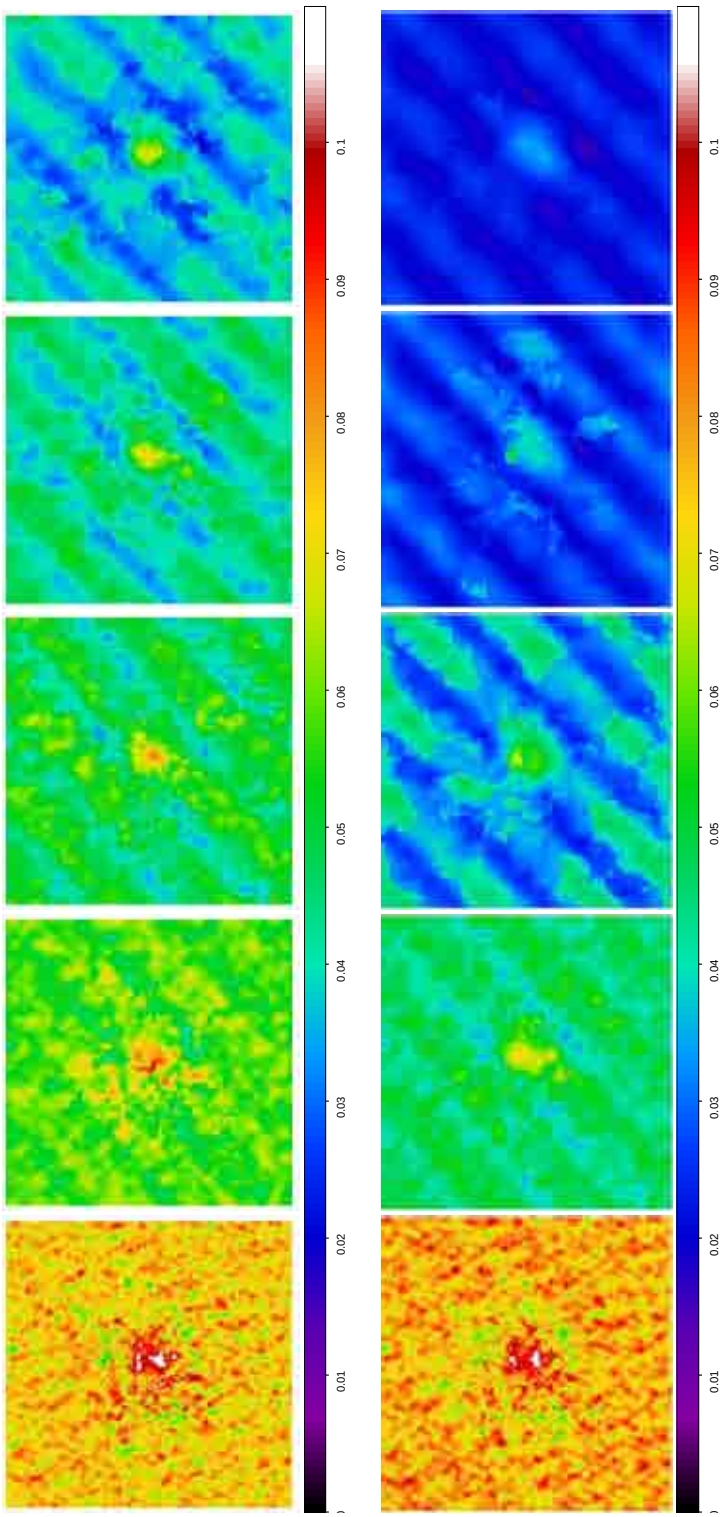

Figure 4.5: Averaged noise maps, rotated so the top of each image is towards the spine: on the left, for ICF widths of $50, 75, 100, 125, 150$ kpc, and on the bottom, for ICF widths of $15, 30, 45, 60, 75''$. The patterns are seen in all averaged noise maps except for those maps where the noise from the poor fit of a small ICF width in each individual cluster map drowns out the underlying pattern.

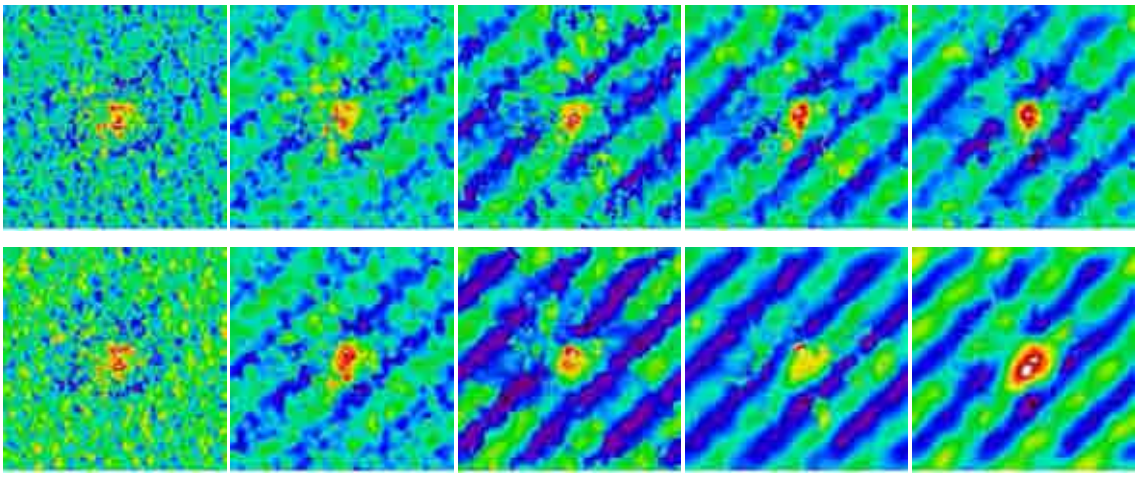

Figure 4.6: Averaged noise maps: on the top, for ICF widths of $50, 75, 100, 125, 150$ kpc, and on the bottom, for ICF widths of $15, 30, 45, 60, 75''$. The colour bars are here scaled to the minima and maxima of each image, to better show the magnitude of the underlying noise pattern against the noise associated with the reconstruction.

4.1.2 B-mode analysis

B-modes measure the amount of noise in the shear measurement, and can be found by adding 45° to the orientation of the faint galaxy image, and repeating the weak shear analysis. The B-mode maps should resemble a noise map: maps with a strong B-mode signal indicate systematic noise in the weak shear measurement that will impact the constraints we can obtain on the DM mass distribution. For all clusters, B-mode maps were found using LENSENT2 with the rotated shear catalogues. At the smoothing scale used for the κ analysis, 100kpc, $8/21$ cluster optimisations failed to converge on a solution. When the κ solution failed to converge, the smoothing scale was increased, in order to increase the size of substructures the would be reconstructed and thus simplify the solution. Increasing the smoothing scale did not work for those B-mode solutions that failed to converge. It was only by decreasing the smoothing scale to 50kpc that $18/21$ were able to converge on a solution. This suggests that for these clusters, the scale of the noisy features in the weak shear data is far less than that of the significant features in the κ map.

Fig. 4.7 shows the κ map and B-mode map for three clusters for which the B-mode map did converge to a solution at the smoothing scale of 100kpc. The top first cluster is A 2813, which

has a strong κ signal, and for which we are able to constrain a multimodal model in the parameterised analysis. The B-mode map, on the left, has a much weaker signal than the κ map, and is largely featureless. The middle cluster is A 3292, for which we saw the underlying noise pattern impacted the signal to noise map in Fig. 4.4. The B-mode map for this cluster is still largely flat and featureless compared to the κ map, but there is more stronger B-mode background noise than for A2 2813. This could mean that the extent to which the underlying noise pattern affects noise map from the LENSENT2 realisation is related to the B-mode signal. The bottom cluster is A 141, for which we obtained a very low shear signal, a high cross shear component and the later parameterised weak lens analysis failed to reconstruct a significant DM halo, and we shall find conclude later that this cluster has a mispointed HST:ACS observation. The B-mode map is almost as strong as the κ map, indicative of the very low shear signal and noise in the shear catalogue. We concluded that the B-mode maps were consistent with the shear signal and cross component analysis, but as they did not all converge at the same smoothing scale as the κ maps, could not be used to determine uncertainties on the spatial properties of different features.

4.1.3 Constraints on the Peak of the Mass Distribution

The offset between the BCG position, X-ray peak and DM distribution peak is an important indicator of dynamical state and can provide insight into the interaction physics between baryons and DM. Thus we wanted to assess the constraints on the positions of structures observed in the LENSENT2 convergence maps.

To obtain constraints on the position of the mass peak associated with the BCG, we created 100 bootstrapped MC LENSENT realizations for each cluster, and analysed the statistical properties of the results. The simulated faint galaxy catalogues were created by randomly, and with replacement, selecting galaxies from the original faint galaxy catalogues, with the number of objects in the simulated catalogue matching the number of objects in original faint galaxy catalogue. LENSENT2 generated maximum entropy maps using these simulated catalogues,

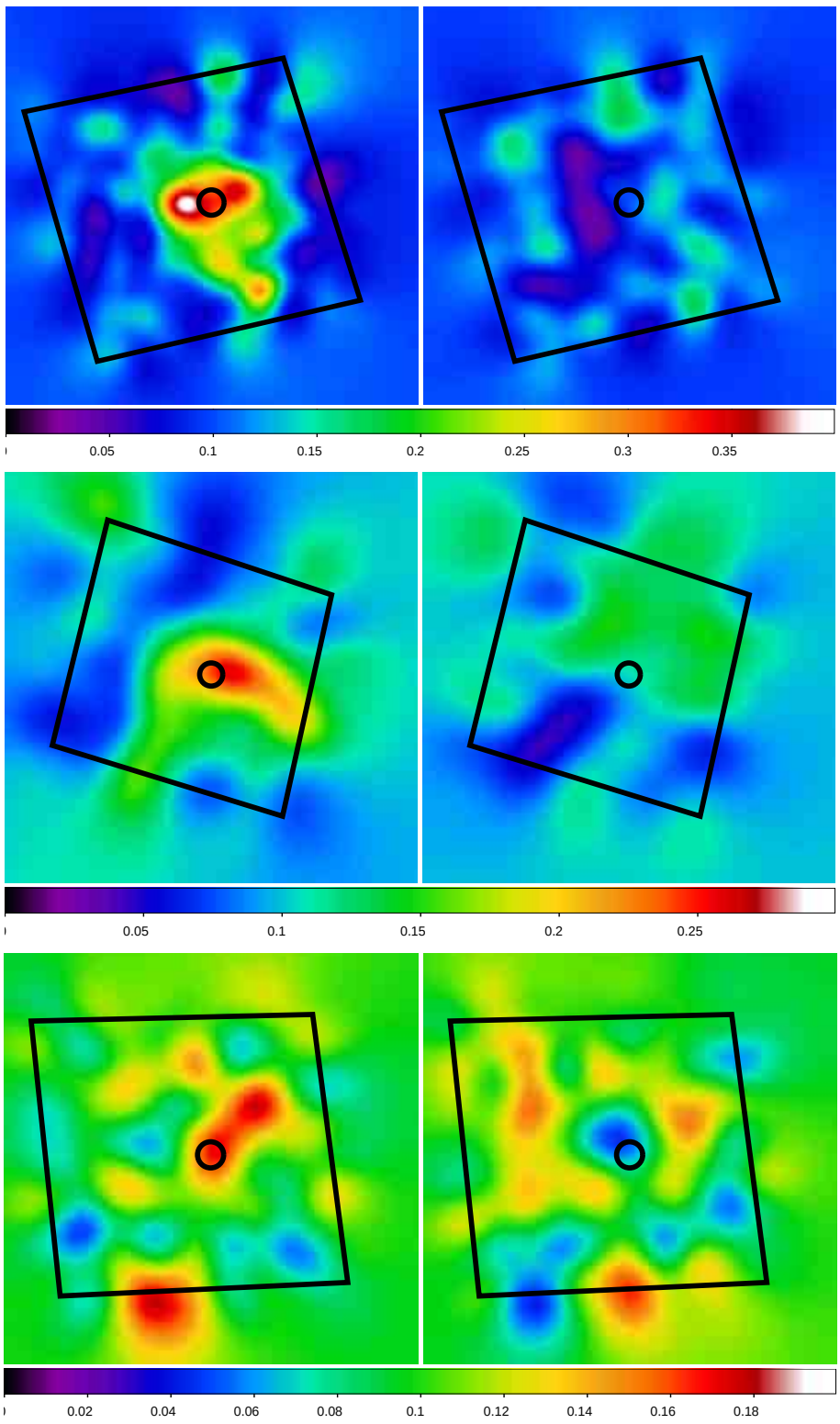

Figure 4.7: From top to bottom, κ (left) and B-mode (right)LENSENT2 realisations for A 2813, A 3292 and A 0141. The black box denotes the ACS field of view, and the black circle the analysis BCG position. North is up and E is west.

using a FWHM of 100kpc, and the peaks in the maximum entropy maps were identified and fitted using IRAF function *phot*. The standard deviation on the 2σ-clipped average of all these positions was then calculated. A similar process identified the peak in the maximum entropy map created using the original faint galaxy catalogues. It should be noted that with the original catalogues, RX J1000.5+4409 and A 2187 do not successfully reconstruct at 100kpc, and so the DM peak positions and constraints on these positions, for these maps were found using 150kpc and 125kpc reconstructions respectively.

The distribution of the samples is plotted for each cluster in Figs. 4.8- 4.10. The green, red and black contours represent the approximate $99\%, 95\%$ and 68% limits. The mass peak positions, offsets from the BCG and interpretation are discussed as part of the Results chapter in § 5.4 (Fig. 5.4, Table. 5.1, 5.2).

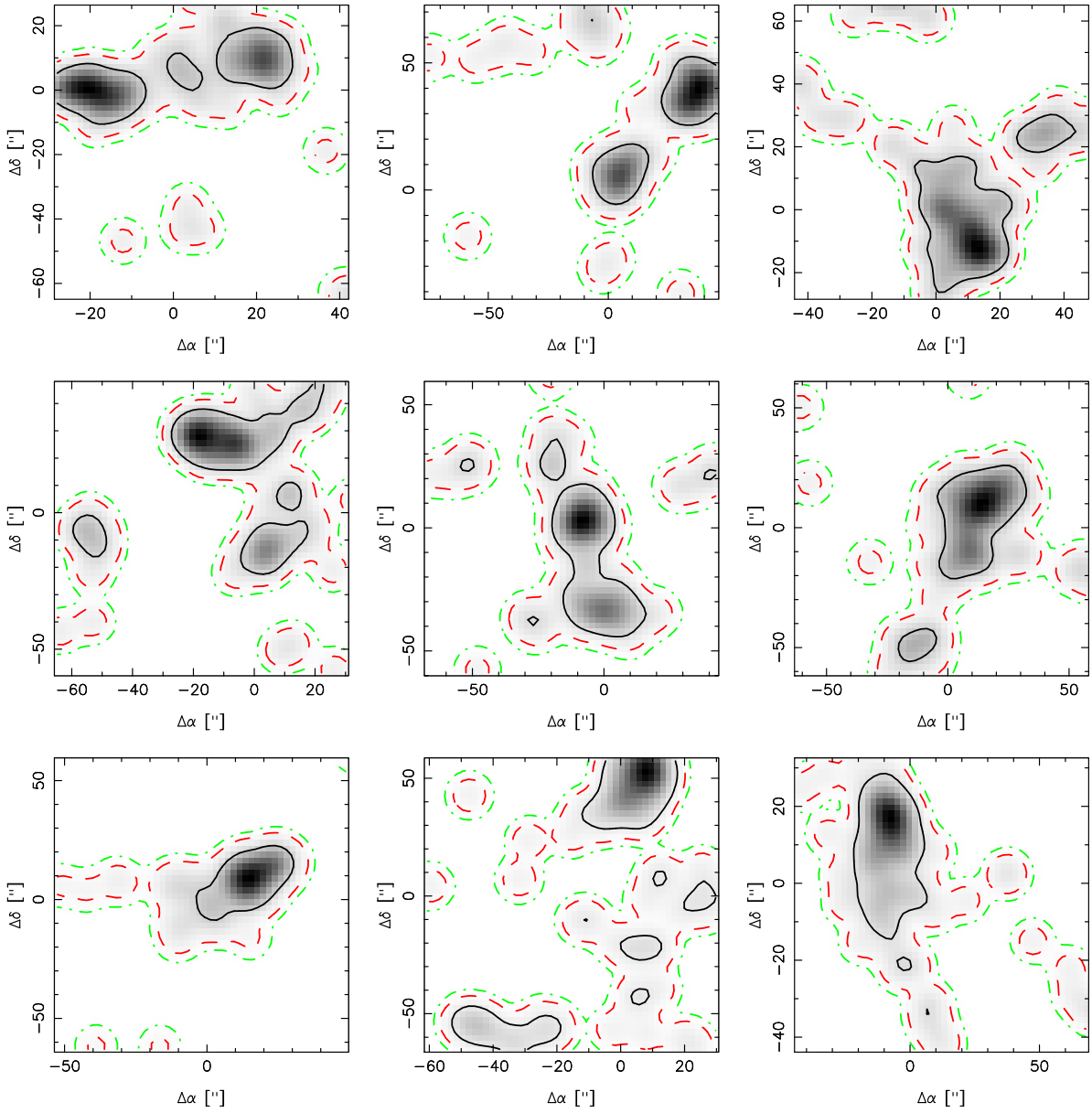

Figure 4.8: X,Y sample distributions from LENSENT2 MC runs, in arcseconds. From left to right, A 2183, A 0141, A 2895, RXCJ 0220.9-3829, A 0368, A 3084, A 3088, RXCJ 0331.1-2100 and A 3140.

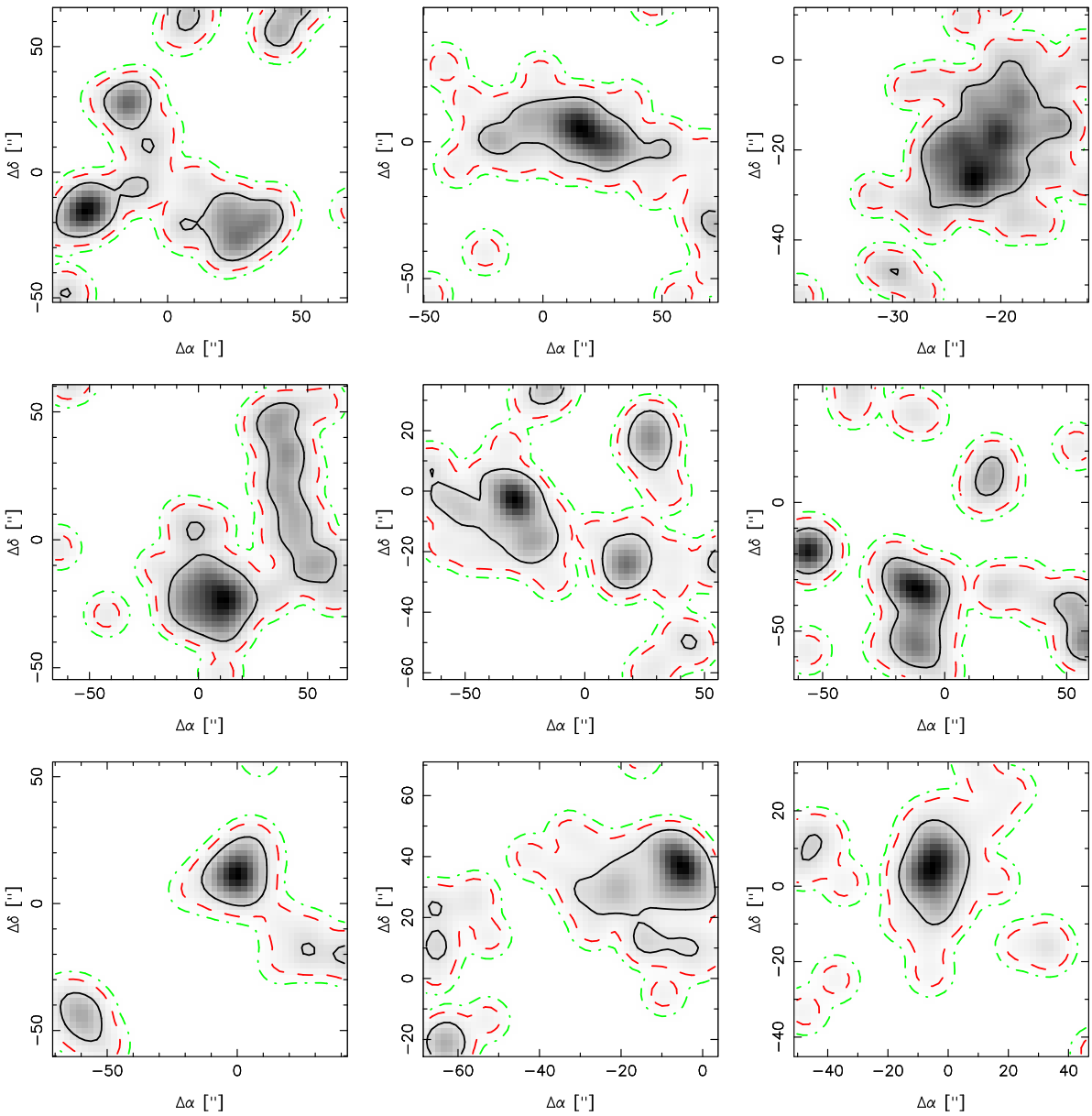

Figure 4.9: X,Y sample distributions from LENSENT2 MC runs, in arcseconds. From left to right, A 3192, A 3292, RXCJ 0528.2-2942, A 3364, AS 0592, 1ES0657-558, A 0611, A 0781 and Z 2701

4.2 Parameterised Modelling with LENSTOOL

The primary aims of the parameterised model fitting was to constrain the cluster total mass, complexity and mass substructure fraction, in order to probe the internal structure and thus the recent assembly history of these clusters. However, it was unknown at the start of the analysis

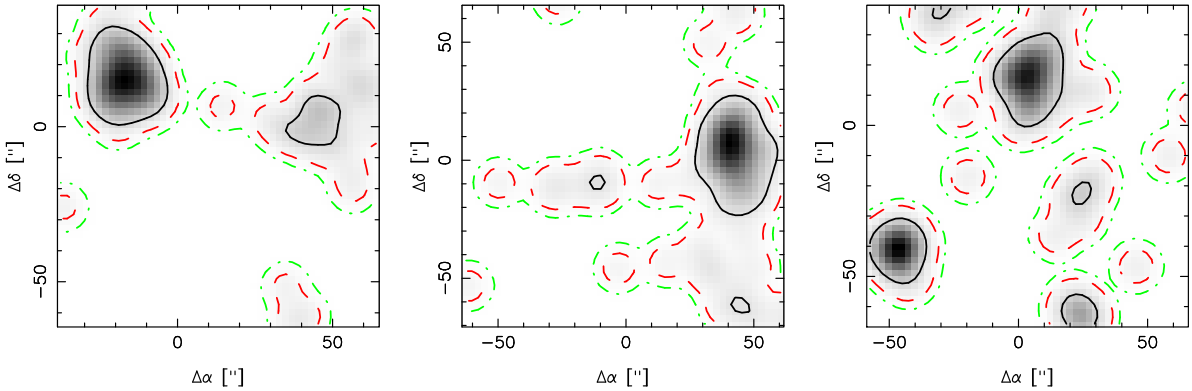

Figure 4.10: X,Y sample distributions from LENSENT2 MC runs, in arcseconds. From left to right, RX J1000.5+4409, A 2187 and A 2537.

how far the shallow data could constrain the models. Thus a large portion of this analysis involved testing different types of models and evaluating the constraints obtained on the mass and structure of the clusters.

4.2.1 Model freedom and the use of priors.

The models that were optimised included N_h cluster scale PIEMD potentials and additional galaxy scale PIEMD potentials based on an input catalogue of cluster galaxies, scaled by the galaxy magnitudes. Throughout this analysis, only the properties of the cluster scale DM potentials were optimised, the cluster galaxies included to provide a mass and position prior on the optimisation.

Our source plane was fixed at a redshift of 1: for clusters between redshifts of $0.15-0.3$, small variation in the redshift plane of 1 has an impact that is consistent within the systematic errors on the fitted σ_0. This is because the shear effect depends on the ratio between the angular diameter distances between the source, the observer, and the lens. For variation of 0.2 around the source redshift of 1.0, this ratio does not significantly vary for clusters within redshifts of $0.15-0.3$. The variance is greater for clusters at higher redshift: we tested varying the source

redshift for $A3192$, which was found to lie at $z = 0.42$. The variation in σ_0 induced by remodelling the cluster with source redshifts of $z = 0.8, 1.2$ was still consistent within 1σ errors with the σ_0 found with source redshift of 1.0. Thus we concluded that placing all our sources in the same lens plane would not severely impacted the cluster mass reconstruction.

The cluster scale DM haloes were parameterised with PIEMDs (described in § 2.6.3). The models initially consisted of $n \in \{1, ..., 5\}$ cluster scale haloes with the velocity dispersion, σ_0, and halo position optimised using LENSTOOL. These models were fitted to catalogues of individual faint galaxy shapes. The halo positions were constrained by an approximation of ACS field of view, restricted by the limitations on the shape of the x,y prior in LENSTOOL. In order to determine model complexity we sought to use the Bayesian evidence mentioned in Eq. 4.1. If model A is more likely than model B, the evidence for A will be higher than the evidence for B. If A is significantly more likely, $ln(E_A) - ln(E_B) > 1$. This is equivalent to saying a multimodal model will be chosen over a simpler model if $P(N_h = N)/P(N_h = 1) > e^1$. The evidence values produced by different model complexities were so similar that the difference between two models was usually < 1. These models had too much freedom, and the constraints from the individual galaxy shapes were not enough to provide robust conclusions on both the model complexity and halo position. It was decided that the models needed further simplification via prior information.

The IR data was used to constrain the LENSTOOL models in two ways. Cluster galaxy catalogues, extracted from the IR data by finding the Red Sequence of galaxies (see § 3.4.1 for construction of the cluster galaxy catalogues and K-band luminosity density maps), were assigned truncated PIEMDs based on their K-band magnitudes, and added to the LENSTOOL models. The smoothed K-band luminosity density maps were analysed using SEXTRACTOR to obtain positions of significant substructures in the light distribution, with the assumption that the light traced the underlying DM mass distribution. For each cluster, the subpeak positions were added, in order of luminosity, to a model containing at first just a single cluster scale peak

fixed on the BCG position. In these optimisations, the only free parameter was the velocity dispersion.

Despite fixing the positions of the possible DM haloes based on luminosity peaks, and only fitting the velocity dispersion of the cluster scale DM haloes, the models were still unable to reliably constrain the complexity of the DM distribution via the Bayesian evidence. For a subset of the clusters, the geometry of the halo positions and poor constraints resulted in unphysical models. The only part of the modelling process that was left to simplify were the faint galaxy catalogues themselves.

4.2.2 Fitting Complex Models to Smoothed Faint Galaxy Catalogues

The final step in the search for reliable models and well constrained masses was to consider smoothing the faint galaxy catalogues before fitting the models constructed using the IR prior. Gaussian smoothing was used on the faint galaxy catalogues in order to suppress non-random contributions to the shape noise, which were believed responsible for the poor statistical discrimination between models of differing complexity. These could be caused by small scale local SL strength signals, and uncorrected observational noise. A truncated 2D gaussian filter (Eqn. 4.2), was applied at each point on a 15x15 grid, covering the ACS field of view. The contribution from each galaxy observation within the truncation radius was further weighted by the error on the ellipticity, allowing us to incorporate the observed error into our faint galaxy catalogues, something not previously possible when using the individual galaxy shape measurements as constraints. The truncation was performed to prevent the gaussian smoothed shear at each point being diluted by the perpendicular shear on the other side of the potential. The truncation radius would have to be small enough that the perpendicular shear terms wouldn't impact the signal, but large enough so that the non random noise terms were correctly removed by the smoothing. The optimisation of both the truncation radius and smoothing scales are described below.

The 2D gaussian filter is given by Eqn. 4.2,

$$\omega_i = \frac{1}{\sigma^2 2\pi} \exp\left(-\frac{r_i^2}{2\sigma^2}\right) \tag{4.2}$$

where r_i is the distance from each faint galaxy observation within the truncation radius to the grid point. Using this method the weighted contributions from all faint galaxy observations were summed and averaged at each grid point. As the weak lensing regime only applies up to $\sim 60''$ from the centre of the lensing mass distribution, no contributions from faint galaxies within that region were counted, and no grid points from within that region were added to the final catalogues. Examples of the shear pattern of a selection of the smoothed catalogues are given in Fig. 4.11.

When the truncation radius is low compared to the smoothing scale, the Bayesian evidence associated with the model can be affected. As we wanted to choice of the most probable model to be impacted only by the cluster complexity, we wanted to find the lowest truncation width for which the evidence was stable. Thus we were not interested in the evidence for each truncation radius, but the impact that the truncation radius had on evidence as it decreased. For each cluster, truncation widths of $\{180, 200, 220, 240, ..., 500\}$kpc were considered for two smoothing widths, 50kpc and 100kpc. The likelihood of a higher truncation radius against a lower truncation radius, and the reduced χ^2 for each truncation radius, is given in Fig. 4.12.

When the truncation radius is too small, the faint galaxy catalogue is not well sampled and the non random error terms still dominate. The evidence of the fitted model fluctuates, as does the goodness of fit parameter. When these truncation radii are implemented the evidence obtained for different smoothing scales or model complexity is not a reliable value with which to optimise either. The evidence stabilised at for larger truncation radii given a smoothing scale of 100kpc, than for a smoothing scale of 50kpc. As for the smaller smoothing scale there was little negative impact on the reduced χ^2 when the truncation radius was increased, the truncation width was optimised for the larger smoothing scale.

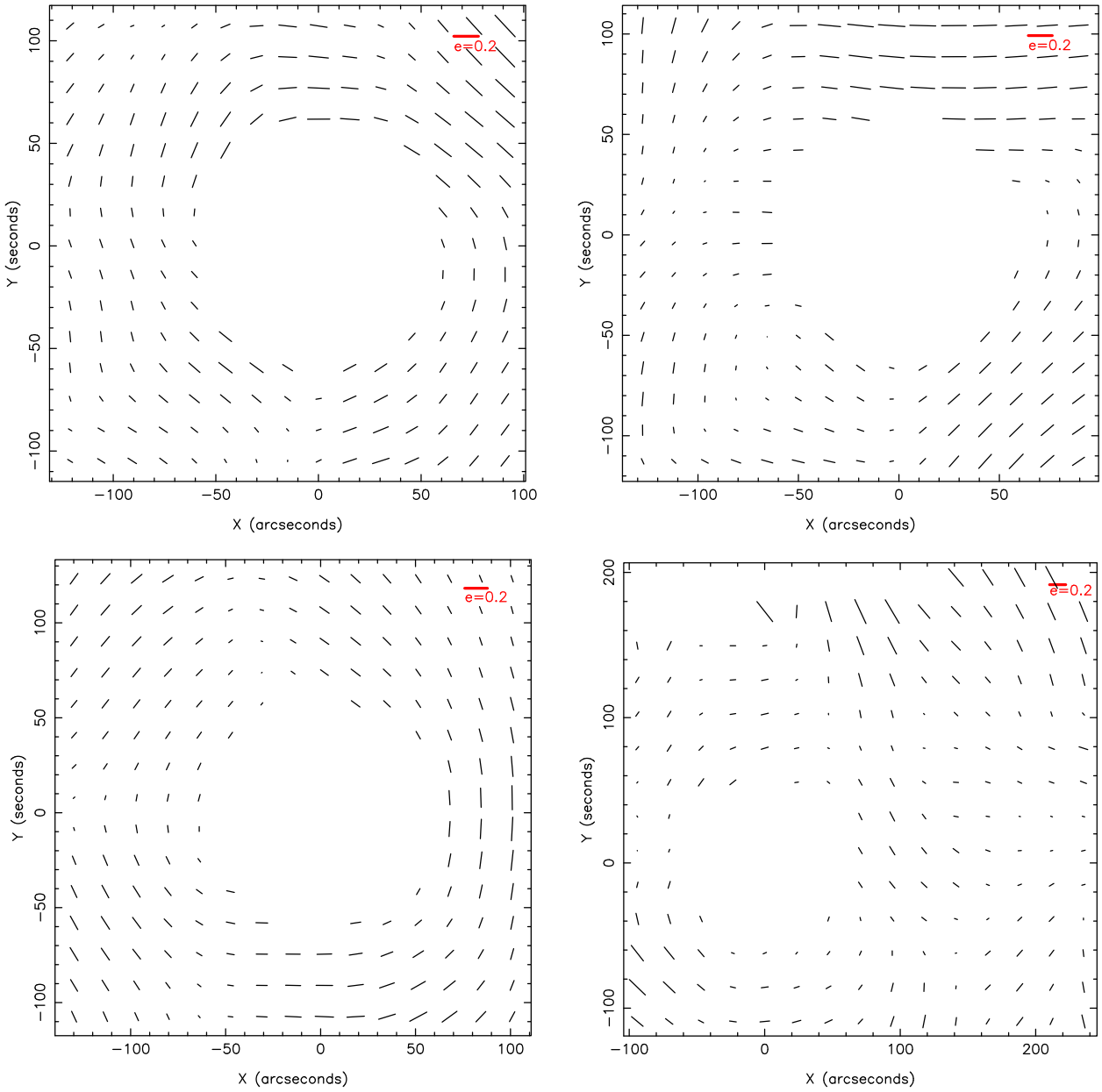

Figure 4.11: The smooth catalogues represented as stick plots for (clockwise from top left) $A2813$, $A0368$, the Bullet cluster, and $AS0592$. The final fitted models have 2 haloes, 1 halo, 2 haloes and 3 haloes respectively. The scale of each stick is given on each plot. The smoothing scale used was 90kpc.

Importantly, the optimum truncation radius for each cluster chosen in this manner was found to be independent of the complexity of the model used. A truncation radius of 380kpc was chosen for all clusters, to maintain the smallest truncation radius possible, while ensuring that the evidence of any smoothing scale or model complexity optimisation was not impacted by the truncation radius. It should be noted here that the evidence for both A 3192 and the Bullet Cluster never stabilised, likely due to their extended and complex mass substructure.

After the truncation radius was optimised, a range of smoothing scales were investigated. These were in physical units, following the justification of the LENSENT2 analysis. Each model was constructed using the subpeak positions from the luminosity density maps, created with the cluster galaxy catalogues. Haloes were added to the model in order of luminosity, starting with the position associated with the BCG, to a maximum of 5 haloes. Each cluster was run with smoothing scales of $\sigma_g = \{30, 40, 50, 60, 70, 80, 90, 100, 110, 120\}$kpc, approximating a range of FWHMs from $\sim \{75-280\}$kpc. The optimum smoothing scale was then found for each model complexity (Fig. 4.13). As with the truncation radius, the optimum smoothing scale was found to be independent of the choice of model complexity. The modal σ_g result for this analysis, 50kpc, was consistent with the optimum result from the LENSENT2 analysis. The models using the modal smoothing scale and the individual smoothing scale were then analysed to determine the most probable model complexity in each case (Tables 4.1, 4.2).

The complexity of the models could be determined using the likelihood of a multihalo model over a simpler model. The tables include more than one model where a more complex model is clearly favoured over a simpler model, or where the differences in evidence are not significant enough to strongly differentiate between models. In these cases, Occam's razor applies, and the simplest model should be chosen.

In order to check that the evidence for a model with a probable halo position added after

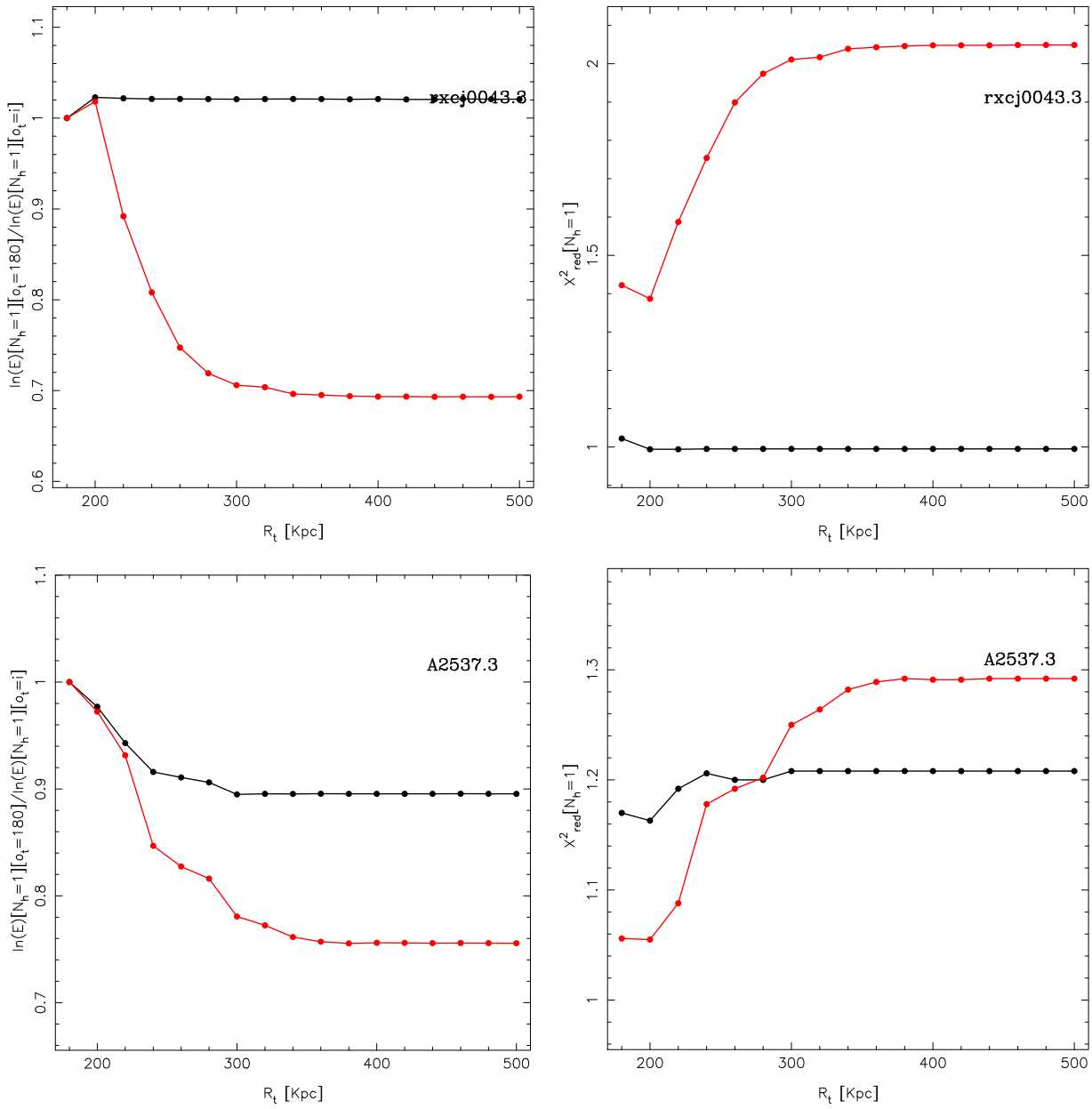

Figure 4.12: The left plots show the change in evidence with respect to the truncation radius, the right plots the impact on the reduced χ^2. The black line is for σ_g = 50kpc, the red line for σ_g = 100kpc. Top: $A2813$; bottom: $A2537$.

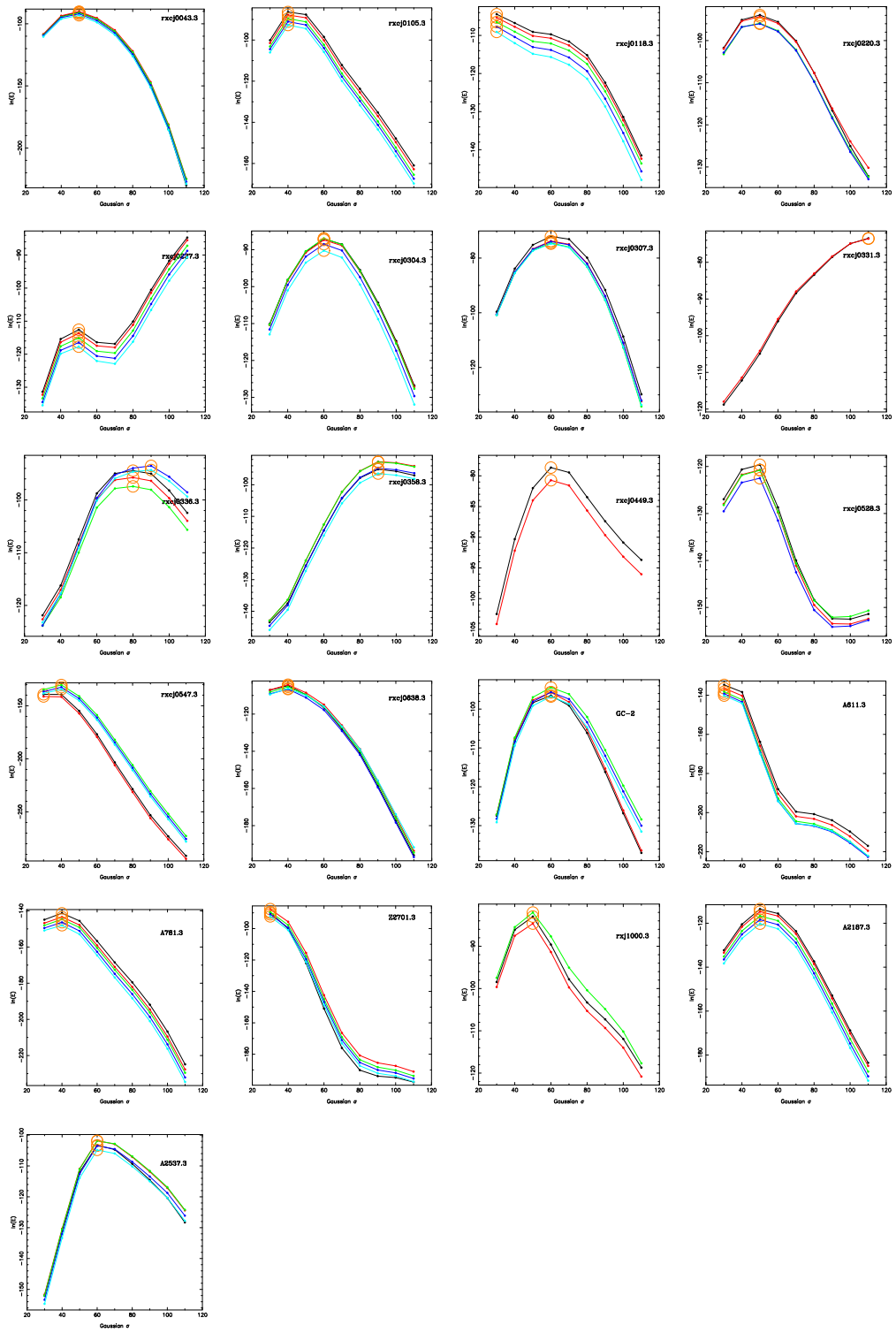

Figure 4.13: σ_g versus evidence for each cluster. From top to bottom, left to right: A 2813, A 141, A 2895, RXC J0220.9, A 0368, A 3084, A 3088, RXC J0331.1, A 3140, A 3192, A 3292, RXC J0528.2, A 3364, AS 0592, 1ES0657, A 0611, A 0781, Z 2701, RX J1000.5, A 2187, A 2537. On each plot: black denotes one halo model,red denotes two halo model, green the three halo model, blue the four halo model and light blue a five halo model. Orange circles identify peaks in the evidence distributions for each model complexity. Where this choice differs between models, the optimum σ_g associated with the most likely model based on the evidence, is chosen. Final σ_g choices are shown in Tables. 4.1, 4.2.

several unlikely halo positions were included was not biased low, new models were constructed that included those haloes with significant group scale ($300 kms^{-1}$) or larger velocity dispersions, even if the evidence of the original model suggested it was less likely than a simpler model. The likelihood of these models was then compared with the most probable models from the initial optimisations and the final models selected.

However, despite evidence for multi modal structure in models with larger smoothing scales, and in the luminosity density and X-ray maps, the evidence differences for some clusters were not significant to support complex models, as was the case for the non smoothed faint galaxy catalogues. It was found by comparison with smoothing optimisations that did not include the cluster galaxy PIEMDs, that including the cluster galaxies in the model motivates the evidence to favour small smoothing scales and thus reconstruction of smaller scale mass structures. While cluster galaxy catalogues are essential for providing position and mass priors on the models, during smoothing scale optimisation they resulted in small smoothing scales that were insufficiently large to remove the non random error terms from the faint galaxy measurements. It was decided not to include the cluster galaxies when optimising the smoothing scale in order to tune σ_g to the uncertainties in the faint galaxy catalogues only. This resulted in a modal optimum smoothing scale of 90kpc. The distribution of evidence for each smoothing scale, for unimodal and bimodal models, is shown in Fig. 4.14.

From the previous smoothing scale analysis, $A3364$ was noted to strongly prefer all mass to be place on the third brightest peak in the luminosity density map. In the σ_g optimisation plot above, the black line represents a single halo model with the halo positioned on this third light subpeak, and the red line represents a two halo model with the haloes centred on the two brightest peaks in the lightmap, which includes the BCG. As with the other clusters, the optimisation of a single halo on the BCG position agrees with the two halo result. When the haloes do not include the true mass centre, as indicated by all previous models, a larger smoothing scale is preferred, likely trying to compensate for the shift in mass distribution centre. When the mass is

Table 4.1: LENSTOOL Modelling Results (σ_g optimised with cluster galaxies included in the models)

Cluster	Optimum σ_g	N_h	$ln(E)$	$P(N_h)/P(1)$	χ^2_{red}	Modal σ_g	N_h	$ln(E)$	P(N_h)/P(1)	χ^2_{red}	Halo IR ID[a]
A 2813	50	1	-91.94	1.00	1.01	—	—	—	—	—	0
		2	-91.28	1.93	1.00		—	—	—	—	0 1
		3	-92.18	0.79	1.00		—	—	—	—	0 1 3
A 0141	40	1	-86.34	1.00	1.01	50	1	-87.64	1.00	1.03	0
A 2895	30	1	-104.43	1.00	1.19	50	1	-109.07	1.00	1.24	0
RXCJ 0220.9	50	1	-93.93	1.00	1.06	—	—	—	—	—	0
		2	-94.30	0.69	1.06		—	—	—	—	0 1
		2b	-93.62	1.36	1.05		—	—	—	—	0 3
A 0368	50	1	-112.59	1.00	1.25	—	—	—	—	—	0
A 3084	60	1	-87.07	1.00	0.91	50	1	-90.57	1.00	0.95	0
		2	-87.35	0.76	0.92		2	-90.78	0.81	0.95	0 1
		2b	-86.22	2.34	0.89		2b	-89.77	2.23	0.93	0 2
A 3088	60	1	-73.42	1.00	0.80	50	1	-76.20	1.00	0.84	0
		2	-74.07	0.52	0.81		2	-76.57	0.69	0.84	0 2
		2b	-73.32	1.11	0.80		2b	-76.30	0.90	0.84	0 3
		3	-73.55	0.88	0.80		3	-75.22	2.66	0.83	0 2 3
RXCJ 0331.1	110	1	-73.46	1.00	0.77	50	1	-104.40	1.00	1.12	0
		2	-73.57	0.90	0.77		2	-104.13	1.31	1.10	0 1
A 3140	80	1	-94.44	1.00	1.05	50	1	-107.48	1.00	1.20	0
		2	-91.54	18.17	1.01		2	-106.67	2.25	1.18	0 3
		3	-92.31	8.41	1.01		3	-107.48	1.00	1.19	0 3 4
A 3192	90	1	-95.12	1.00	1.03	50	1	-125.55	1.00	1.37	0
		2	-92.70	11.25	0.99		2	-123.99	4.76	1.35	0 1
		2b	-95.39	0.76	1.03		2b	-125.58	0.97	1.37	0 2
		3	-92.81	10.07	0.99		3	-123.93	5.05	1.35	0 1 2
A 3292	60	1	-78.66	1.00	0.88	50	1	-82.00	1.00	0.91	0

[a]Halo identification number from Table 3.6

Table 4.2: LENSTOOL Modelling Results (σ_g optimised with cluster galaxies included in the models)

Cluster	Optimum σ_g	N_h	$ln(E)$	$P(N_h)/P(1)$	χ^2_{red}	Modal σ_g	N_h	$ln(E)$	P(N_h)/P(1)	χ^2_{red}	Halo IR ID
RXCJ 0528.2	50	1	-119.62	1.00	1.27	—	—	—	—	—	0
		2	-119.95	0.72	1.27		—	—	—	—	0 2
A 3364	40	1	-139.38	1.00	1.47	50	1	-154.84	1.00	1.64	0
		1b	-126.60	3.55E5	1.33		1b	-136.95	5.88E7	1.44	2
AS 0592	40	1	-104.69	1.00	1.13	50	1	-109.58	1.00	1.18	0
		2	-104.19	1.65	1.13		2	-108.52	2.89	1.17	0 1
		3	-103.74	2.59	1.11		3	-107.09	12.06	1.14	0 1 4
1ES0657	60	1	-96.52	1.00	1.09	50	1	-98.37	1.00	1.11	0
		2	-95.34	3.25	1.07		2	-97.71	1.93	1.10	0 2
		1b	-95.34	3.25	1.07		1b	-97.24	3.10	1.10	1
		2b	-93.91	13.60	1.05		2b	-96.51	6.42	1.08	1 2
A 611	30	1	-134.71	1.00	1.60	50	1	-163.83	1.00	1.94	0
A 781	40	1	-141.29	1.00	1.35	50	1	-145.57	1.00	1.39	0
Z 2701	30	1	-89.95	1.00	1.08	50	1	-122.04	1.00	1.47	0
		2	-87.60	10.49	1.04		2	-115.51	685.40	1.38	0 1
RXJ 1000.5	50	1	-82.98	1.00	0.87	—	—	—	—	—	0
		2	-80.82	8.67	0.84		—	—	—	—	0 2
A 2187	50	1	-113.57	1.00	1.32	—	—	—	—	—	0
A 2537	60	1	-103.25	1.00	1.11	50	1	-112.02	1.00	1.21	0
		2	-101.82	4.18	1.09		2	-110.91	3.03	1.20	0 1
		3	-101.86	4.01	1.10		3	-111.04	2.66	1.20	0 1 2

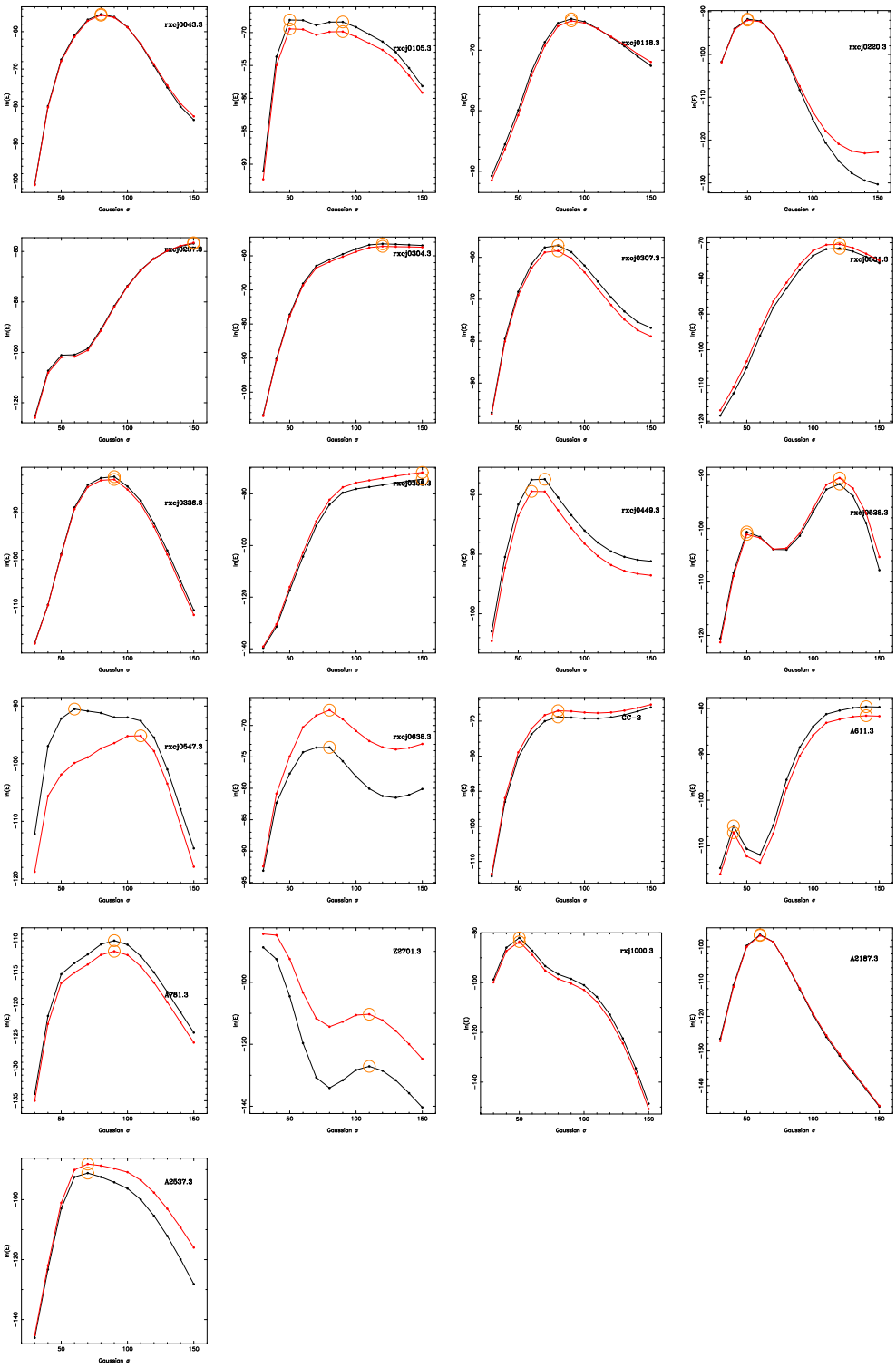

Figure 4.14: σ_g versus evidence for each cluster. From top to bottom, left to right: A 2813, A 141, A 2895, RXC J0220.9, A 0368, A 3084, A 3088, RXC J0331.1, A 3140, A 3192, A 3292, RXC J0528.2, A 3364, AS 0592, 1ES0657, A 0611, A 0781, Z 2701, RX J1000.5, A 2187, A 2537. On each plot: the black line denotes the results for a single halo model and the red line denotes the result for a bimodal model. Orange circles identify peaks in the evidence distributions for each model complexity. Where this choice differs between models, the optimum σ_g associated with the most likely model based on the evidence, is chosen. For some clusters, the actual smoothing scale chosen was taken from where the slope of the evidence distribution suddenly changed. Final σ_g choices are shown in Tables. 4.3, 4.4.

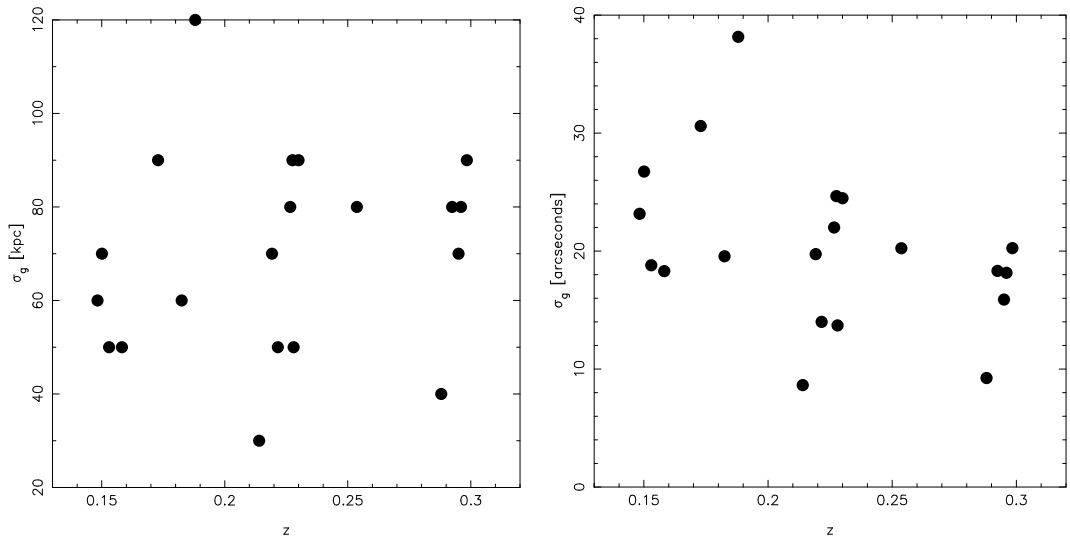

Figure 4.15: Left: Optimal σ_g versus cluster redshift. Right: The same σ_g converted into arcseconds versus cluster redshift.

centered on the third light peak position, the non linear errors are optimally removed at a lower smoothing scale. This implies that there are fewer errors in the optimisation associated with this position, and provides more evidence that *A*3364 has a significant offset between the Dark Matter, X-ray and luminosity distributions. *A*3364 is covered in greater detail in § 6.1.

To test whether the choice of smoothing scale is redshift-dependent, and therefore whether we can trust structural measurements across the sample, we plot smoothing scale versus redshift (Fig. 4.15). Despite large cluster-to-cluster scatter the lack of dependence of physical scale on redshift suggests that the chosen smoothing scales reflect the properties of the clusters and not their redshift distribution.

Once the smoothing scale was tuned to the uncertainties in the faint galaxy catalogues, the cluster galaxies were added as individual PIEMDS, scaled by their K-band magnitudes, and the models optimised under LENSTOOL (Tables 4.3, 4.4). This time the evidence was no longer impacted by non linear error terms in the faint galaxy measurements, and was able to provide clear constraints on model complexity for the majority of the clusters. As stated previously, a

multimodal model, A, was chosen over a simpler model, B, if $P(A)/P(B) > 2.7$. Out of 21 clusters, 8 were mutimodal and 13 were unimodal, ie $38.1^{+13.3}_{-12.0}$% of the clusters had more than one halo in the most probable parameterized model. The final models are summarised in Table 4.5.

4.2.3 Weak Lens Masses

Once the ficidual models were decided on, LENSTOOL was used to generate mass and error maps, by entering the best fit dispersions as the parameters for the cluster scale components, and adding in the cluster galaxy scale potentials. LENSTOOL could then be set to generate an intergrated 2D mass map that could be compared with the spatial maps of the X-ray flux and luminosity, or the LENSENT2 κ maps, or from which masses could be extracted by summing the pixel contributions within a set aperture (Tables 4.6, 4.7). The aperture in which the mass was found was chosen to be 250kpc, to aid comparison with Richard et al. (2010), where the SL in 20 clusters cores were analysed to constrain the masses. At this point A 3192 was removed from the main sample, as it was discovered to lie outside the redshift range that we wished to investigate.

The weak lens masses ranged from $2-15\times10^{13}M_{\odot}$. Within the aperture of 250kpc, we expected the masses to be larger than 1×10^{44} for clusters in this luminosity range. Thus we concluded that the masses from the models were biased low. In order to determine the extent of the low mass bias, we compared the weak lens masses from the 90kpc smoothed results to the projected X-ray masses found in § 3.4.2, in Fig. 4.16.

The average weak lens mass to X-ray mass ratio, for the sample that did not include A 0781, A 0141 (both removed for being miscentred and as a result poorly reconstructed) and A 3192, was M_{WL}/M_X = 0.57, with a standard deviation of 0.19. The average M_X/M_{WL} for the same sample was 1.95 with a standard deviation of 0.68. Assuming that the X-ray mass is a reliable indicator of the truth, and that the $M_{WL}-M_X$ discrepancy is very small within such a small

Table 4.3: LENSTOOL: Modelling Results (σ_g optimised without cluster galaxies)

Cluster	Optimum σ_g	N_h	$ln(E)$	$P(N_h)/P(1)$	χ^2_{red}	Modal σ_g	N_h	$ln(E)$	P(N_h)/P(1)	χ^2_{red}	$Halo_{ID}$
A 2813	80	1	-126.23	1.00	1.39	90	1	-152.69	1.00	1.69	0
		2	-124.23	7.39	1.36		2	-149.78	18.36	1.65	0 1
		3	-125.46	2.16	1.37		3	-150.97	5.58	1.66	0 1 2
A 0141	90	1	-135.20	1.00	1.59	—	—	—	—	—	0
A 2895	90	1	-122.39	1.00	1.39	—	—	—	—	—	0
RXCJ 0220.9-3829	50	1	-93.93	1.00	1.06	90	1	-116.58	1.00	1.32	0
		2	-94.3	0.69	1.06		2	-116.11	1.60	1.40	0 1
		2b	-93.62	1.36	1.05		2b	-115.86	2.05	1.30	0 3
		—	—	—	—		3	-116.38	1.22	1.31	0 1 3
A 0368	50	1	-112.59	1.00	1.25	90	1	-100.511	1.00	1.11	0
A 3084	70	1	-88.54	1.00	0.93	90	1	-104.38	1.00	1.09	0
		2	-88.90	0.70	0.93		2	-104.82	0.64	1.10	0 1
		2b	-87.79	2.12	0.91		2b	-103.96	1.52	1.09	0 2
A 3088	80	1	-82.015	1.00	0.90	90	1	-94.41	1.00	1.04	0
		2b	-81.41	1.83	0.89		2b	-93.52	2.44	1.02	0 3
RXCJ 0331.1-2100	120	1	-73.54	1.00	0.77	90	1	-78.56	1.00	0.83	0
		2	-73.81	0.76	0.77		2	-78.38	1.20	0.81	0 1
A 3140	90	1	-95.01	1.00	1.05	—	—	—	—	—	0
		2	-91.18	46.06	1.00		—	—	—	—	0 3
		3	-91.93	21.76	1.01		—	—	—	—	0 1 3
A 3192	90	1	-95.12	1.00	1.03	—	—	—	—	—	0
		2	-92.70	11.25	0.99		—	—	—	—	0 1
		2b	-95.39	0.76	1.03		—	—	—	—	0 2
		3	-92.81	10.07	0.99		—	—	—	—	0 1 2
A 3292	70	1	-79.46	1.00	0.88	90	1	-87.40	1.00	0.97	0

Table 4.4: LENSTOOL: Modelling Results (σ_g optimised without cluster galaxies)

Cluster	Optimum σ_g	N_h	$ln(E)$	$P(N_h)/P(1)$	χ^2_{red}	Modal σ_g	N_h	$ln(E)$	P(N_h)/P(1)	χ^2_{red}	$Halo_{ID}$
RXCJ 0528.2-2942	50	1	-119.62	1.00	1.27	90	1	-152.39	1.00	1.61	0
		2	-119.95	0.72	1.27		2	-151.73	1.93	1.60	0 2
A 3364	60	1	-176.93	1.00	1.87	90	1	-253.16	1.00	2.68	0
		1b	-154.57	5.14E9	1.63		1b	-225.63	9.04E11	2.39	2
AS 0592	80	1	-140.97	1.00	1.52	90	1	-158.57	1.00	1.72	0
		2	-138.72	9.49	1.50		2	-156.15	11.25	1.69	0 1
		3	-135.09	357.81	1.44		3	-151.75	915.99	1.63	0 1 4
1ES0657-558	80	1	-106.15	1.00	1.20	90	1	-116.17	1.00	1.31	0
		2	-103.07	21.76	1.15		2	-111.64	92.76	1.25	0 2
		1b	-104.65	4.48	1.18		1b	-114.68	4.44	1.29	1
		2b	-101.35	121.51	1.13		2b	-109.86	550.04	1.23	1 2
A 611	40	1	-138.38	1.00	1.64	90	1	-203.89	1.00	2.42	0
		—	—	—	—		2b	-203.87	1.02	2.41	3 4
		—	—	—	—		3	-204.42	0.59	2.43	0 3 4
A 781	90	1	-191.90	1.00	1.83	—	—	—	—	—	0
Z 2701	30	1	-89.95	1.00	1.08	90	1	-193.95	1.00	2.35	0
		2	-87.60	10.49	1.04		2	-185.48	4769.52	2.24	0 1
RXJ 1000.5+4409	50	1	-82.98	1.00	0.87	90	1	-107.29	1.00	1.12	0
		2	-80.82	8.67	0.84		2	-103.33	52.46	1.07	0 2
A 2187	60	1	-115.60	1.00	1.34	90	1	-152.89	1.00	1.78	0
A 2537	70	1	-104.70	1.00	1.13	90	1	-114.56	1.00	1.23	0
		2	-102.92	5.93	1.10		2	-111.86	14.88	1.20	0 1
		3	-102.84	6.42	1.11		3	-111.60	19.30	1.20	0 1 2

Table 4.5: LENSTOOL: Ficidual Model Properties

Cluster	N_h	$\delta(\alpha,\delta)''$	σ_g	P(N_h)/P(1)	χ^2_{red}	Modal σ_g	P(N_h)/P(1)	χ^2_{red}
A 2813	2	0,0	80	7.39	1.36	90	18.36	1.65
		5,–41						
A 0141	1	0,0	90	1.00	1.59	—	—	—
A 2895	1	0,0	90	1.00	1.39	—	—	—
RXCJ 0220.9	1	0,0	50	1.00	1.06	90	1.00	1.32
A 0368	1	0,0	50	1.00	1.25	90	1.00	1.11
A 3084	1	0,0	70	1.00	0.93	90	1.00	1.09
A 3088	1	0,0	80	1.00	0.90	90	1.00	1.04
RXCJ 0331.1	1	0,0	120	1.00	0.77	90	1.00	0.83
A 3140	2	0,0	90	46.06	1.00	—	—	—
		36,24						
A 3192	2	0,0	90	11.25	0.99	—	—	—
		80,101						
A 3292	1	0,0	70	1.00	0.88	90	1.00	0.97
RXCJ 0528.2	1	0,0	50	1.00	1.27	90	1.00	1.61
A 3364	1	16,–44	60	5.14E9	1.63	90	9.04E11	2.39
AS 0592	3	0,0	80	357.81	1.44	90	915.99	1.63
		–29,–2						
		–88,67						
1ES0657	2	–18,–27	80	121.51	1.13	90	550.04	1.23
		161,24						
A 611	1	0,0	40	1.00	1.64	90	1.00	2.42
A 781	1	0,0	90	1.00	1.83	—	—	—
Z 2701	2	0,0	30	10.49	1.04	90	4769.52	2.24
		–113,–41						
RXJ 1000.5	2	0,0	50	8.67	0.84	90	52.46	1.07
		63,–40						
A 2187	1	0,0	60	1.00	1.34	90	1.00	1.78
A 2537	2	0,0	70	5.93	1.10	90	14.88	1.20
		–39,–33						

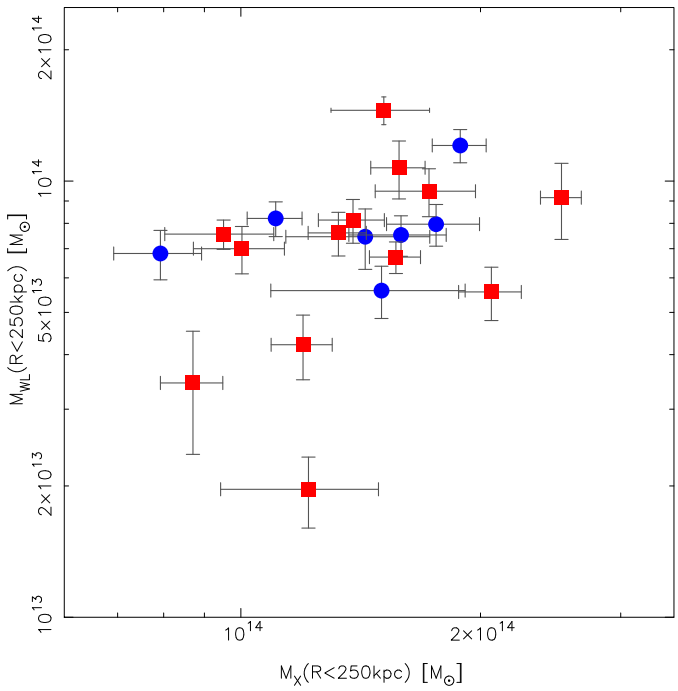

Figure 4.16: $M_{WL}-M_X$ relation obtained using the models fitted to gaussian smoothed data, with common smoothing scale 90kpc. The same key as in Fig. 4.18 applies.

aperture, then there is some systematic bias in the reduction or modelling that is affecting the strength of the shear signal, and thus producing lower σ_0 than expected. I explored two possible causes: cluster galaxy contamination of the faint galaxy shear catalogues, and the smoothing method used during the LENSTOOL modelling.

Cluster contamination

Cluster contamination refers to the inclusion of faint cluster galaxies in the faint galaxy catalogues. The overall effect is to dilute the shear signal, resulting in a lower average tangential shear for the cluster and an underestimated mass measurement. (see § 2.6.4 for more details). Because the faint galaxy catalogues were constructed using only a magnitude cut, and not multi-filter colour information, the analysis is likely to have been impacted by such contamination.

In order to try and quantify the errors introduced by cluster contamination on our models, we created adjusted catalogues, where we assume the shear values are affected by a degree of

cluster contamination $(10, 20, 30, 40, 50\%)$, and boost the shear signal to imitate the 'true' catalogues. In our simple analysis we boost the unsmoothed shear signal by $100/(100-X\%)$, where X is the contamination percentage of the total catalogue, and then smoothed using a scale of 90kpc and the same truncation width as our previous analysis, 380kpc. Because the analysis is being performed on cluster cores, with a very small field of view, we assume the cluster galaxy contamination to be constant across the field. The 10σ cluster galaxy catalogues for $A2813$ and $A3088$ were used in this analysis. We then fitted single halo models to each boosted catalogue for each cluster, and obtained the best fit velocity dispersion and errors. On average, the fitted σ_0 is boosted by a factor of 1.28 between the 0% and 50% contamination correction models. 20/21 clusters had corrected σ_0 consistent with the uncorrected σ_0, when correcting for 20% contamination, this falls to 17/21 when correcting for 30% contamination. In the 50% case only 4/21 clusters had corrected σ_0 consistent with the uncorrected value.

Fig. 4.17 shows the increase in fitted velocity dispersion for each cluster, assuming $0, 10, 30, 50\%$ (grey,blue,green,red) contamination correction. In earlier analysis on unsmoothed faint galaxy catalogues, the distributions suggested that the impact of even in the most extreme case of cluster contamination that we modelled, 50%, the difference in σ_0 was comparable to the systematic error in the fit. The resulting improvement in $\delta\sigma_0$ once the faint galaxy catalogues were smoothed meant the fitted σ_0 were accurate enough to be impacted by cluster contamination. However, this simple method only modelled the removal of the low mass bias of cluster contamination by boosting the shear. Faint cluster galaxies would be among the brightest of the faint galaxy catalogue, and would likely have well constrained shape measurements. As the error on ellipticity is also used to weight the faint objects when the catalogues are smoothed, this means the signal from these objects would be favoured over the majority of the real background galaxies in the uncorrected model. In these models the error on ellipticity is scaled as the ellipticity to maintain fractional errors and the weighting distribution, which uses the standard deviation of the ellipticity distribution. However, when cluster members were removed, there would be fewer objects as well constrained, increasing the standard deviation of the ellipticity

distribution and likely increasing the associated error on σ_0 in the corrected results compared to our model. The galaxy number counts were also not altered in the corrected catalogues: in the 50% contamination correction, 50% of the faint objects would be removed in a truly corrected catalogue, which would increase the error on the corrected σ_0.

For the smoothed data, low levels of contamination are consistent within the systematic error of the true σ_0 value, however multi-filter data would greatly enhance the accuracy of our analysis, especially for clusters at high redshift where there would be a considerable magnitude overlap between the faint cluster member population and the brighter faint galaxy population.

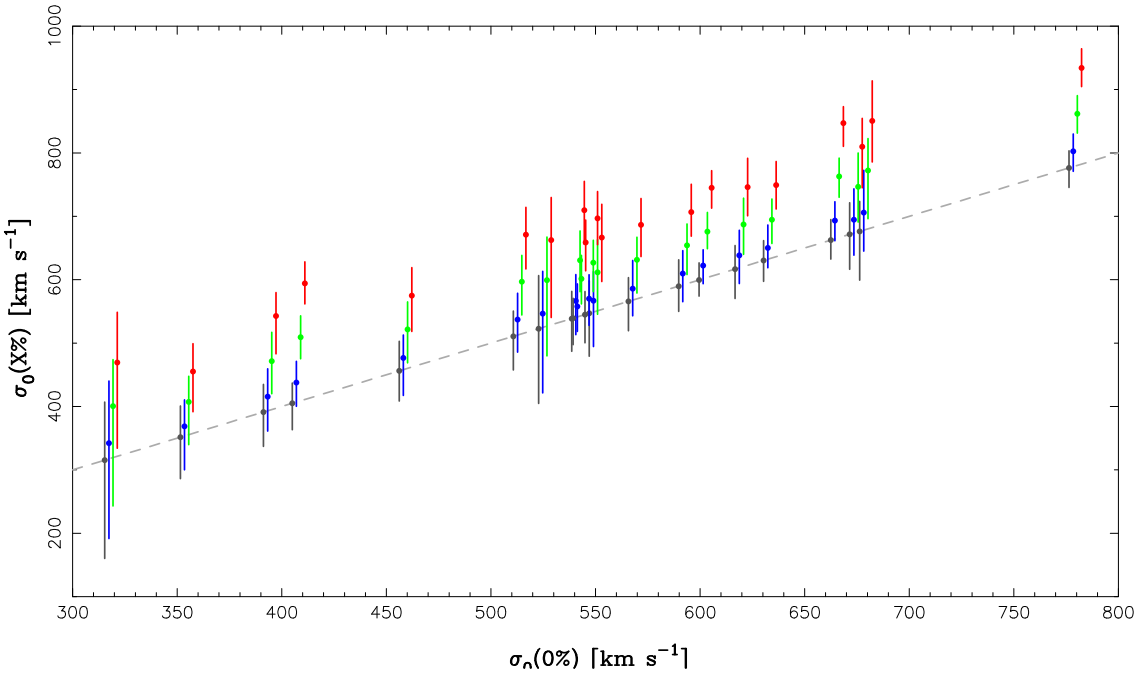

Figure 4.17: For each cluster the fitted σ_v for the uncorrected catalogues is grey, for corrected catalogues assuming 10% contamination, the fitted σ_v is coloured blue, for 30% assumed contamination, green, and for the extreme case of correction for 50% contamination, red.

Impact of Smoothing Method

The Gaussian smoothing of the faint galaxy catalogues was truncated to avoid perpendicular shear contributions from faint galaxies on the other side of the centre of the mass distribution diluting the signal at each grid point. Similarly, the faint galaxy shear contributions to each point

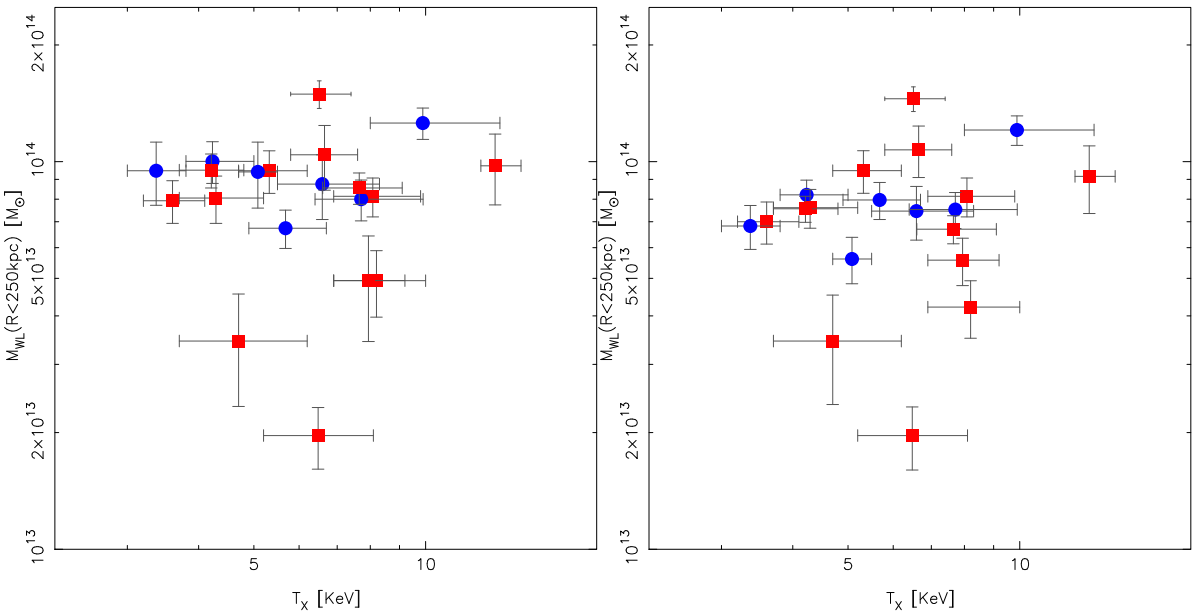

Figure 4.18: Left: $M_{WL} - T_X$ obtained using the models fitted to gaussian smoothed data, with individually optimised smoothing scales, and Right: the same using models fitted to data smoothed with common scale 90kpc. The blue circles denote cool core clusters, and the red squares denote non cool core clusters.

were weighted by their ellipticity errors, to prevent poorly constrain measurements impacting the smoothed shear. However, it was possible that the smoothing method was still contributing to the low mass bias. In order to investigate the manner in which the smoothing impacted the LENSTOOL model results, we compared the masses from models with individually optimised smoothing scales, and models using the modal smoothing scale 90kpc. These are plotted against X-ray temperature in Fig. 4.18.

The left hand plot in Fig. 4.18 gives the masses from models with individually optimised smoothing scales. The clusters with the lowest X-ray temperatures have weak lensing masses that are relatively high (albeit still less than expected) compared to the clusters with higher X-ray temperatures, for example RXC J0220.9-3829, RXC J0528.2-2942 and RX J1000.5+4409. These three clusters all had σ_g = 50kpc. Oversmoothing can bias the weak lens masses low. Thus other clusters, with larger smoothing scales, may have a greater degree of low bias in their masses in comparison with this sub sample, despite the truncation of the gaussian filter. However there are other clusters with very low smoothing scales, with no adverse impact, or, as in

the case of A 0611, the opposite effect. In addition, RXC J0220.9-3829 and RXC J0528.2-2942 show some indication of DM substructure, but the evidence was not strong enough to support the complexity at this smoothing scale. Fitting a single halo to a possible multimodal shear signal may have resulted in an overly massive halo to compensate for the complexities in the shear data. The lowest lensing masses in this figure belong to (lowest first) A 0141, A 0781, and A 2187. A 0141 and A 0781 were both miscentred on the ACS field of view, while A 2187 is associated with a negligible tangential shear result, and has possibly not been reconstructed successfully with this method. It is apparent that the weak lensing masses for those models with individually optimised smoothing scales suffered different degrees of a low bias.

The right side of Fig. 4.18 gives the same plot with the weak lens masses from the models fitted to data smoothed with the common smoothing scale, 90kpc. There is still alot of scatter in the weak lens mass measurements, however, ignoring the most extreme low mass clusters, the bias now appeared to be more consistent in this plot across the whole sample. This implies that the apparent systematic bias is related to the truncated gaussian smoothing filter used on the faint galaxy catalogues. There appears to be a positive relation between X-ray temperature and weak lens mass for the majority of the clusters, again ignoring the most extreme low mass clusters. This suggests that the low mass bias may act on all models equally when the same smoothing scale is used. Such an effect would only impact normalisation in the mass-observable scaling relations, and not the slope.

In order to explore structural segregation in the mass-observable scaling relations, I wanted to assess sources of bias in the weak lens mass measurement and determine whether these mass estimates can be trusted. Assuming the most extreme case of the faint galaxy shear catalogues suffering 50% cluster contamination, the corrected M_{WL} would be increased by a factor of 1.64. The more likely case of less extreme cluster galaxy contamination would require a smaller correction. When I looked at the impact of smoothing scale on the mass estimates, I found evidence that the low mass bias was dependent on the smoothing scale used, and may be consistent across

the whole sample when a global smoothing scale is applied.

The cause of the low bias is likely a combination of the uncorrected cluster contamination of the faint galaxy catalogue, inadequate removal of the non random noise terms in the faint galaxy shear measurements, and the truncation radius failing to prevent perpendicular shear terms diluting the average shear at each bin point, with systematics related to the smoothing of the faint galaxy catalogue responsible for the majority of the bias. Future application of this pipeline would involve investigation of the truncation width and filtering method, while an improved analysis would use multi-filter observations to produce uncontaminated faint galaxy catalogues. For this thesis, motivated by the right hand panel of Fig. 4.18, we assume that the smoothing and truncating of the shear catalogues is the dominant effect, and for the common smoothing scale 90kpc the impact of the smoothing method is consistent across all the cluster in the sample. This means it will primarily impact the normalisation of the mass-observable scaling relations and not the underlying physical trends.

4.3 Summary

In this chapter I described the non-parametrised and parametrised weak lens mass reconstruction of the cluster cores, using Bayesian statistics to robustly constrain substructure complexity and the spatial mass distribution.

LENSENT2 was used to reconstruct maps of the projected surface mass distribution, κ, which will be used to interpret the assembly history of the cluster by comparison with maps of X-ray and luminosity density, and to efficiently obtain an initial guide to the level of structural mass complexity that could be expected from the WL analysis of each cluster. By bootstrapped re-sampling of the original shear catalogues, constraints were obtained on the offset between the BCG and the peak of the mass distribution, which can be used as an indicator of cluster dynamics and recent merger and infall activity.

Table 4.6: LENSTOOL: Weak Lensing Masses

Cluster	N_h	σ_g^{opt} [kpc]	$(\alpha,\delta)_{aper}$ [″],[″]	$M_{WL}(<650\text{kpc})$ $[10^{14}M_\odot]$	$M_{WL}(<250\text{kpc})$ $[10^{13}M_\odot]$	σ_g^{modal}	$M_{WL}(<650\text{kpc})$ $[10^{14}M_\odot]$	$M_{WL}(<250\text{kpc})$ $[10^{13}M_\odot]$	$Halo_{ID}$
A 2813	2	80	0,0	3.8 ± 0.3	14.9 ± 1.2	90	3.7 ± 0.3	14.5 ± 1.1	0 1
A 0141	1	90	0,0	0.3 ± 0.09	2.0 ± 0.4	—	—	—	0
A 2895	1	90	0,0	1.8 ± 0.2	8.1 ± 0.9	—	—	—	0
RXCJ 0220.9-3829	1	50	0,0	2.4 ± 0.3	10.0 ± 1.2	90	2.0 ± 0.2	8.2 ± 0.8	0
A 0368	1	50	0,0	2.1 ± 0.4	8.8 ± 1.7	90	1.8 ± 0.3	7.5 ± 1.2	0
A 3084	1	70	0,0	1.8 ± 0.3	8.1 ± 1.1	90	1.7 ± 0.2	7.6 ± 0.9	0
A 3088	1	80	0,0	1.9 ± 0.2	8.0 ± 1.0	90	1.8 ± 0.2	7.5 ± 0.8	0
RXCJ 0331.1-2100	1	120	0,0	1.5 ± 0.2	6.7 ± 0.8	90	1.8 ± 0.2	8.0 ± 0.9	0
A 3140	2	90	0,0	2.3 ± 0.3	9.5 ± 1.2	—	—	—	0 3
A 3192[a]	1	90	0,0	2.6 ± 0.4	10.8 ± 1.5	—	—	—	0
	2b		0,0	2.7 ± 0.5	10.6 ± 1.9	—	—	—	0 2
	2(fg)		80,101	—	3.1 ± 2.4	—	—	—	1
	2(bg)		0,0	2.7 ± 0.5	11.3 ± 1.6	—	—	—	0
	3(fg)		80,101	—	3.2 ± 2.4	—	—	—	1
	3(bg)		0,0	2.8 ± 0.6	11.0 ± 1.9	—	—	—	0 2
A 3292	1	70	0,0	1.8 ± 0.2	7.9 ± 1.0	90	1.6 ± 0.2	7.0 ± 0.9	0

[a]These masses were calculated by scaling the foreground group velocity dispersion w.r.t. the correct redshift, and placing the aperture on the group position. The error map was generated during the optimisation at the cluster redshift. $M(r_{aper}=650)$ is unavailable for the foreground group due to the insufficient size of the error map. The error on the cluster mass at this radius will be boosted by contribution from error in the map associated with the foreground cluster, and thus will be an overestimate.

Table 4.7: LENSTOOL: Weak Lensing Masses

Cluster	N_h	σ_g^{opt} [kpc]	$(\alpha,\delta)_{aper}$ [″],[″]	$M_{WL}(<650\text{kpc})$ $[10^{14}M_\odot]$	$M_{WL}(<250\text{kpc})$ $[10^{13}M_\odot]$	σ_g^{modal}	$M_{WL}(<650\text{kpc})$ $[10^{14}M_\odot]$	$M_{WL}(<250\text{kpc})$ $[10^{13}M_\odot]$	$Halo_{ID}$
RXCJ 0528.2	1	50	0,0	2.3 ± 0.2	9.5 ± 1.0	90	1.9 ± 0.1	7.6 ± 0.6	0
A 3364	1	60	16,–44	2.1 ± 0.2	8.6 ± 0.8	90	1.6 ± 0.1	6.7 ± 0.6	2
AS 0592	3	80	0,0	3.3 ± 0.4	12.6 ± 1.2		3.2 ± 0.3	12.1 ± 1.1	0 1 4
1ES0657	2	80	–18,–27	2.7 ± 0.5	9.8 ± 2.0		2.6 ± 0.5	9.2 ± 1.8	1 2
A 0611	1	40	0,0	1.2 ± 0.4	4.9 ± 1.5	90	1.4 ± 0.2	5.6 ± 0.8	0
A 0781	1	90	0,0	1.0 ± 0.3	3.4 ± 1.1	—	—	—	0
Z 2701	2	30	0,0	2.8 ± 0.6	9.4 ± 1.8		1.7 ± 0.3	5.6 ± 0.8	0 1
RXJ 1000.5	2	50	0,0	2.5 ± 0.5	9.5 ± 1.8		1.8 ± 0.2	6.8 ± 0.9	0 2
A 2187	1	50	0,0	1.0 ± 0.2	4.9 ± 1.0	90	0.9 ± 0.2	4.2 ± 0.7	0
A 2537	2	70	0,0	2.8 ± 0.5	10.4 ± 2.0		2.9 ± 0.4	1.1 ± 1.6	0 1

LENSTOOL was used to constrain the complexity of parameterised models of the mass distribution, using PIEMD haloes to model cluster and galaxy scale structures. IR priors on the halo positions and removal of non random error terms in the shear measurements via smoothing of the faint galaxy catalogues provided the simplification of the model necessary to obtain statistically sound conclusions on the number and spatial distribution of cluster scale DM haloes within the cluster cores. Out of 21 clusters, $8/21$ ($38.1^{+13.3}_{-12.0}$%) of the most probable mass models contained more than one cluster scale halo.

The reconstructed lens masses from LENSTOOL were biased low due a combination of uncorrected cluster contamination effects and systematics in the smoothing method, however the mass-observable scaling relation suggest this bias is broadly consistent across the cluster sample when the same smoothing scale is used. In conclusion, when discussing the mass assembly histories of clusters via comparison with between 2D maps of mass, X-ray and luminosity density, the optimum model based on the Bayesian statistics should be used, and when discussing global sample properties in the mass-observable scaling relations, a common smoothing scale should be applied to the shear catalogues so the low mass bias only impacts the normalisation of the scaling relations.

Using the models I have constructed in this chapter I will now discuss an indepth analysis of individual clusters, and the sample as a whole, in § 5.

Chapter 5

Multi Wavelength Properties of Cluster Cores

In this chapter I present the main results of the thesis on the structure of X-ray luminous galaxy cluster cores. I begin with discussions on individual clusters in § 5.1, then I discuss the mass-observable scaling relations, the DM substructure distribution and offsets between the mass, the BCG and the X-ray centroids.

5.1 Individual Clusters

In Appendix A are figures showing the 2D K-band luminosity density, X-ray surface brightness, LENSENT2 κ and LENSTOOL mass maps, which are compared and discussed in this section. The caption on Fig. A.1 applies to all clusters. Cluster properties such as LENSTOOL model complexity, subhalo positions, X-ray luminosity and temperature, cool core (CC) status and mass/X-ray BCG offsets are summarised in Table 5.1, 5.2. The DM substructure fractions were calculated as the fraction of mass in the LENSTOOL model not included in the BCG PIEMD and DM cluster scale halo closest to the BCG position. Clusters were classed as having cool cores if the logarithmic slope of the gas density profile at $0.04r_{500}$, α, was < -0.85, and disturbed if the X-ray centroid was offset more than $15kpc$ from the BCG (Sanderson et al., 2009).

The clusters are discussed assuming that DM is collisionless and that mass follows light, as we assumed when invoking the K-band position prior to help constrain the parameterised LENSTOOL models. Therefore where the mass distribution suggests a significant peak without a corresponding structure in the luminosity density distribution, the mass peak will be treated with skepticism, and possible explanations for such a peak considered.

5.1.1 A 2813

The core structure of A 2813 is bimodal in the luminosity, X-ray and LENSTOOL mass maps (Fig. A.1). The LENSENT κ map implies the mass distribution is bimodal aligned E-R around the BCG position, with weaker support for the N-S bimodal structure. In this case, it is possible that the K-band position prior used in the LENSTOOL MODELLING compensated for a noisy shear signal, allowing for a more accurate reconstruction of the mass distribution, as there is no evidence the the κ map BCG associated E-W bimodallity structure in either the luminosity or X-ray maps. The DM mass is most strongly associated with the BCG position in the parameterised and non-parameterised mass distributions from the lensing analysis, but the X-ray map is associated with the luminosity subpeak 40″ S of the BCG. The X-ray and mass distribution, in combination with the lack of a cool core, may imply that the subpeak in the luminosity distribution has passed through the core, resulting the disturbed X-ray morphology and disrupting the cool core. The offset of the bulk of the X-ray emission from the BCG and DM peak could suggest a bullet-like morphology. The interpretation of this cluster's formation history would benefit from deeper X-ray observations to determine whether there is an X-ray shock feature in the gas distribution, and to constrain the structure associated with the non parameterised reconstruction of the mass around the BCG. This cluster is thus an example of a possible 'extreme' cluster identified for future study using the methods in this thesis.

Table 5.1: Cluster Properties

Cluster	N_h	(α,δ) ["]	L_X $(10^{44} ergs\,s^{-1})$	T_X keV	α	$\Delta(BCG,X)$ $[kpc]$	$\Delta(BCG,DM)$ $[kpc]$	$f_{sub}(250kpc)^a$	CC?	Disturbed?
A 2813	2	0,0 5,–41	8.8 ± 1.4	$6.5^{+0.9}_{-0.7}$	-0.34 ± 0.07	116.4 ± 2.2	80.8 ± 81.7	0.39 ± 0.03	no	yes
A 0141	1	0,0	6.7 ± 1.1	$6.5^{+1.6}_{-1.3}$	-0.24 ± 0.05	623.4 ± 1.8	175.8 ± 66.8	0.73 ± 0.13	no	yes
A 2895	1	0,0	6.4 ± 0.9	$8.1^{+1.7}_{-1.2}$	-0.48 ± 0.13	45.1 ± 1.8	43.4 ± 42.8	0.23 ± 0.03	no	yes
RXCJ 0220	1	0,0	5.8 ± 0.7	$4.2^{+0.8}_{-0.4}$	-0.95 ± 0.04	5.0 ± 1.8	94.5 ± 70.0	0.05 ± 0.01	yes	no
A 0368	1	0,0	4.9 ± 0.7	$6.6^{+1.7}_{-1.1}$	-0.92 ± 0.05	7.7 ± 1.8	35.2 ± 17.6	0.20 ± 0.03	yes	no
A 3084	1	0,0	4.7 ± 0.8	$4.3^{+0.9}_{-0.6}$	-0.36 ± 0.05	46.1 ± 1.8	39.2 ± 37.2	0.23 ± 0.03	no	yes
A 3088	1	0,0	8.0 ± 1.4	$7.7^{+2.2}_{-1.3}$	-0.88 ± 0.03	14.6 ± 2.0	46.1 ± 18.8	0.18 ± 0.02	yes	no
RXCJ 0331	1	0,0	5.0 ± 1.3	$5.7^{+1.0}_{-0.8}$	-1.20 ± 0.06	5.4 ± 1.6	140.9 ± 136.2	0.06 ± 0.01	yes	no
A 3140	2	0,0 36,24	4.3 ± 0.65	$5.3^{+0.9}_{-0.6}$	-0.44 ± 0.11	13.1 ± 1.5	29.7 ± 11.2	0.62 ± 0.08	no	yes
A 3192[b]	2	0,0 80,101	2.7 ± 0.4	—	—	—	181.7 ± 139.7	0.15 ± 0.02	—	—
A 3292	1	0,0	3.3 ± 0.5	$3.6^{+0.5}_{-0.4}$	-0.29 ± 0.03	5.4 ± 1.3	45.4 ± 22.3	0.06 ± 0.01	no	no

[a] The substructure fractions were calculated from models using smoothing scale of 90kpc

[b] The second position listed for A 3192 is included in the most probable model for this cluster, but is associated with a foreground group outside the field of view. The substructure fraction listed for the cluster is from the single halo model.

Table 5.2: Cluster Properties

Cluster	N_h	(α,δ) [″]	L_X $(10^{44} ergs\, s^{-1})$	T_X keV	α	$\Delta(BCG,X)$ $[kpc]$	$\Delta(BCG,DM)$ $[kpc]$	$f_{sub}(250kpc)^a$	CC?	Disturbed?
RXCJ 0528	1	0, 0	2.9 ± 1.1	$4.2^{+0.6}_{-0.5}$	-0.27 ± 0.08	30.1 ± 1.4	82.3 ± 16.8	0.04 ± 0.003	no	yes
A 3364	1	16, −44	4.7 ± 0.4	$7.7^{+1.4}_{-1.1}$	-0.32 ± 0.03	40.9 ± 1.3	64.8 ± 20.0	0.14 ± 0.01	no	yes
AS 0592	3	0, 0 −29, −2 −88, 67	12.3 ± 1.0	$9.9^{+3.6}_{-1.9}$	-0.86 ± 0.04	102.2 ± 1.8	111.8 ± 106.2	0.50 ± 0.04	yes	yes
1ES0657	2	−18, −27 161, 24	26.6 ± 2.1	$13.2^{+1.5}_{-0.7}$	-0.26 ± 0.02	200.2 ± 2.2	189.2 ± 78.8	0.26 ± 0.05	no	yes
A 611	1	0, 0	8.1 ± 0.5	$7.9^{+1.3}_{-1.0}$	-0.70 ± 0.04	1.4 ± 2.2	32.9 ± 16.8	0.17 ± 0.02	no	no
A 781	1	0, 0	10.2 ± 0.8	$4.7^{+1.5}_{1.0}$	-0.11 ± 0.03	81.3 ± 2.2	144.9 ± 26.9	0.25 ± 0.08	no	yes
Z 2701	2	0, 0 −113, −41	6.3 ± 0.5	$5.1^{+0.4}_{-0.4}$	-0.88 ± 0.12	3.9 ± 1.7	27.6 ± 11.9	0.26 ± 0.04	yes	no
RXJ 1000	2	0, 0 63, 30	1.8 ± 0.1	$3.4^{+0.4}_{-0.4}$	-0.95 ± 0.09	14.8 ± 1.3	26.2 ± 30.3	0.40 ± 0.05	yes	yes
A 2187	1	0, 0	3.1 ± 0.2	$8.2^{+1.8}_{-1.3}$	-0.46 ± 0.10	1.4 ± 1.5	114.8 ± 18.9	0.26 ± 0.04	no	no
A 2537	2	0, 0 −39, −33	11.8 ± 1.7	$6.7^{+0.9}_{-0.9}$	-0.50 ± 0.06	25.1 ± 2.2	54.3 ± 140.5	0.48 ± 0.07	no	yes

[a] The substructure fractions were calculated from models using smoothing scale of 90kpc

5.1.2 A 0141

The SNAPSHOT observation of A 0141 was mispointed to a prominent light peak south of the cluster core. The X-ray image in Fig. A.2 shows comparatively weaker emission in this region compared to the X-ray surface brightness structure to the North, and the LENSENT2 and LENSTOOL analysis both struggled to constrain the mass distribution. The DM structure reconstruction of this cluster is counted as failing due to the mispointed observation.

5.1.3 A 2895

The luminosity, X-ray and LENSENT2 κ 2D distributions for A 2895 all show some substructure $\sim 100''$ SE of the BCG, with further evidence for smaller NE and NW extensions in the core, on $30''-60''$ scales (Fig. A.3). However the SE substructure has low significance (2σ) in the κ map, and is not supported by the evidence in the LENSTOOL model. It may be a foreground collection of galaxies, or even a valid substructure of the cluster core that is not massive enough to induce a shear signal strong enough for this analysis to detect it. The X-ray peak is N of the BCG and also offset from the X-ray centroid. The unusual X-ray surface brightness edges in the central square arcminute could possibly be related to the luminosity subpeaks to the immediate NE and NW of the BCG position, and similar $3-4\sigma$ extensions in the κ map. The LENSTOOL mass map consists of a single halo fixed on the BCG position, and the LENSTOOL modelling shows no significant support for any substructure in the core. This cluster lacks a cool core and in combination with the X-ray offset in the core and possible features in the central arcminute in both the luminosity, X-ray and κ maps, this cluster could be undergoing dynamical unrest in the core that has disrupted the cooling flows. Deeper lensing observations would be necessary to determine constrain the mass and shear contribution of the SE subpeak in the luminosity map, and try to obtain greater constraints on the structure around the BCG.

5.1.4 RXC J0220.9-3829

The map of the X-ray emission suggests a slight N-S elongation, while the luminosity distribution shows some structure to the NE (Fig. A.4). The LENSENT2 κ map supports both of these features, while the LENSTOOL comprises of a single cluster scale halo fixed on the BCG position. This cluster has a cool core, and appears undisturbed.

5.1.5 A 0368

The X-ray emission and luminosity density maps in Fig A.5 both show mild elongation along the E-W axis. The X-ray contours appear undisturbed, and there is no evidence for substructure in the emission. The κ map is very noisy, with the 3σ detection in the core suggesting a possible N-S elongation in the mass. When the IR prior is invoked, the LENSTOOL evidence only supports a unimodal model with the mass centred on the BCG. This comparison, in combination with a cool core and small X-ray centroid offset, suggests this cluster is likely unimodal and undisturbed.

5.1.6 A 3084

The 2D luminosity density in the core of *A*3084 is concentrated on the BCG position, with substructures of dimmer cluster members to the SW and SE (Fig. A.6). The X-ray emission is slightly extended from the BCG to the SW, albeit not as far as the cluster galaxy distribution. The κ map is noisy, with most of the mass centred on the BCG and a 3σ subpeak to the ESE and 3σ extension to the SSE, consistent with the light subpeaks at $\sim -100'', -15''$ and $\sim -75'', -90''$. Neither of these positions are supported by most probable LENSTOOL mass map, which has a single halo fixed on the BCG position, with no significant evidence for substructure. It is possible that the luminosity subpeaks to the SE do not have the mass necessary to produce a strong signal that the LENSTOOL model can account for when the position of the mass peaks is fixed on

the K-band prior positions. If we assume the luminous substructure to the SW is connected and not a projection effect, this structure may have recently passed through the core. This cluster has no cool core, which may support this explanation, if the infall perturbed the cool core. However, if this is the correct explanation of what happened, the weak lens analysis of the shallow ACS data is unable to support it. Deeper weak lens observations could improve constraints on the mass distribution, while cluster galaxy redshifts and velocity dispersion would help determine the 3D luminosity structure of the cluster core.

5.1.7 A 3088

A 3088 has a cool core, and the X-ray and luminosity distributions show little evidence of substructure, with the X-ray emission peak just NW of the BCG (Fig. A.7). The κ map also places the mass NW of the BCG, with an extended structure to the SE, and one to the E that may be related to some cluster galaxies near the eastern edge of the ACS field of view. The evidence supported mass map is unimodal and centred on the BCG, consistent with the very small offset seen in the X-ray. This cluster appears undisturbed.

5.1.8 RXC J0331.1-2100

The mass distribution in the LENSENT κ map is very flat, with some evidence for the subpeak in the luminosity map, to the SE of the BCG (Fig. A.8). The most probable LENSTOOL model is unimodal, with the DM cluster halo centred on the BCG position, in good agreement with the undisturbed X-ray distribution. RXC J0331.1-2100 has a cool core, simple luminosity distribution and appears undisturbed. The flat κ map, is possibly related to the high cross component of the shear, which was inconsistent with zero within 3σ, in combination with a low average tangential shear (Table. 3.10, indicating high levels of noise in the faint galaxy catalogue.

5.1.9 A 3140

A 3140 has clear indications of a turbulent recent history by the related extensions evident in the X-ray and luminosity distributions, NE of the BCG (Fig. A.9). Given the obvious structure in the light and X-ray it might be expected that the DM distribution would be similar perturbed. The LENSENT2 κ distribution appears offset to the E, with an extension to the SW. There is also some indication of mass substructure to the N. The LENSTOOL massmap is even more interesting with the mass concentrated on the BCG and a luminosity peak (resolved in the 75kpc smoothed light map that the IR prior was generated from) just to the NW, at $\sim (30, 20)''$ from the BCG position. The placement of mass NW of the BCG may be related to the X-ray emission centred W of the BCG and the dim cluster galaxy population W of the BCG. With its lack of cool core *A*3140 is likely post merger, with the infalling structure having passed NE through the core, leaving the feature in the X-ray, and mass distribution ending up offset from the cluster core. Deeper weak lens and X-ray observations would be required to better understand the structural discrepancies in this cluster core.

5.1.10 A 3192

This cluster is associated with RXC J0358.8–2955 and listed at $z = 0.168$ by Böhringer et al. (2004b). However, RXCJ0358 (on which our data are centered) has recently been identified as lying at $z = 0.425$ (Ebeling et al., 2010). We discuss the properties of the optically detected system A 3192 in § 6.2.

5.1.11 A 3292

The X-ray map has an interesting extension immediately W of the BCG but with no related luminous substructure (Fig. A.11). By comparison, the luminosity density is centered on the

BCG. The most probable LENSTOOL modal is unimodal, with all mass assigned to a halo centred on the BCG position. However the peak of the κ map is also offset to the W, in agreement with the X-ray emission. This could indicate that the cluster galaxy selection has omitted some members in this region. A 3292 doesn't have a cool core, which in combination with the disturbance in the X-ray surface brightness suggests this cluster is disturbed.

5.1.12 RXC J0528.2-2942

The luminosity distribution for RXC J0528.2-2942 has a subpeak sW of the BCG in the corner of the ACS field of view, and a WSW of the BCG and just outside the ACS field of view, that may be related to the extension in the X-ray contours towards this direction (Fig. A.12). This structure is not reflected in the κ map, which is centre SE of the BCG with extensions to the N and W. The LENSTOOL model has a single DM halo centred on the BCG position, consistent with the mostly central luminosity distribution, although the region below the BCG had no position prior and wasn't modelled. The X-ray emission is offset below the BCG, in possible agreement with the κ results. This non coolcore cluster is disturbed, with offset luminosity, DM and X-ray distributions: the The strong κ detection and difference between the spatial maps suggests the interpretation of this cluster would require deeper weak lens data to improve the constraints on the mass distribution, and a spectroscopically selected cluster galaxy catalogue to ensure completeness in the luminosity density map. This cluster is another example of thie method identifying interesting clusters for indepth study.

5.1.13 A 3364

The luminosity and X-ray distributions strongly suggest a disturbed cluster with interaction between the BCG and a galaxy to the immediate North, with extended emission N and S of the BCG (Fig. A.13). In contrast the most probably LENSTOOL models very strongly prefer to position all mass on the SW subpeak at $\sim (15, -40)''$, in agreement with the κ distribution,

which peaks between the BCG and the SW luminous subpeak. A 3364 lacks a cool core, and appears strongly disturbed, with large offsets between the X-ray, light and mass centres. It is likely the result of a complex and possibly trimodal merger, and ideal for studying the interaction between baryons and DM. The large offset between the luminosity, X-ray and mass distributions, and the constraints on the weak lens mass modelling is discussed in depth in § 6.1.

5.1.14 AS 0592

The X-ray emission, luminosity density, κ and LENSTOOL mass maps all imply that AS 0592 is a multimodal cluster with interesting core structure. The κ map closely reflects the bimodal core structure of the X-ray emission, with the larger mass peak associated with the larger X-ray peak, which itself is associated with the subpeak in the luminosity distribution. The LENSTOOL mass map places the majority of the mass on the BCG position. Both the κ and mass map have structures coincident with the luminosity subpeaks in the NE of the ACS field of view, and the LENSTOOL supported peak is coincident with a distortion in the X-ray contours. The κ map also shows further support for the extended light structure to the NW of the BCG, although there was no support for this position in the LENSTOOL fixed halo model or in the X-ray emission. Surprisingly this complex and disturbed cluster has a cool core. Given the bimodal X-ray distribution, this could indicate a pre merger system, with the mass subpeak and X-ray contour distortion in the NE remnants of an earlier infall event. The derivation of the structure distribution of this cluster has been very successful, and while the mass was not well constrained, the results for this cluster demonstrates the potential of this method to efficiently determine cluster complexity and identify extreme clusters for detailed study.

5.1.15 1ES0657-558

The Bullet Cluster is famous for its shock fronted X-ray emission and complex structure. By including it in this analysis, it provided a way of testing the systematics in the results from the

lens analysis pipeline. The X-ray emission, luminosity density, κ and mass maps can be seen in Fig. A.15. The most probable LENSTOOL model is not a bimodal model with one halo fixed on the BCG position, but a bimodal model with one halo on the subpeak in the luminosity map, and the main cluster DM halo at $\sim (-20, -30)''$, the brighter peak SE of the BCG in the luminosity map. The κ is in agreement with the mass map that the peak of the DM distribution closest to the BCG is strongly offset from the BCG position, while the position of the subpeak from LENSENT is in agreement with the position from the IR prior. Both lensing structures maps support that the Bullet Cluster is a non cool core merger in the plane of the sky, with the main cluster DM component offset from the BCG position. A more detailed look of the systematics in the spatial constraints is given in § 6.1.

5.1.16 A 0611

The bright peak in the NE corner of the luminosity map, matched by X-ray emission, is not in agreement with the κ map distribution (Fig. A.16): this feature is possibly a result of projection, or otherwise unrelated to the cluster. The κ map instead shows more evidence for a DM subpeak $30''$ immediate SE of the BCG, possibly related to a luminous subpeak just W of this position. The LENSTOOL model contains a single DM halo fixed on the BCG position. This is a non cool core cluster, but the logarithmic slope of the gas density profile, α = –0.70 is still quite steep, suggesting that a cool core could be forming. The cluster appears spatially undisturbed, with DM substructure near the core. One possible interpretation is that the cluster is recovering its cool core after a distant past merger.

5.1.17 A 0781

There is almost no evidence for any structure in the κ map and LENSTOOL assigned negligible mass to this position every time it was included. The actual position of the BCG is not in the

centre of the ACS field of view, which, in combination with the complex structure of this cluster, is likely responsible for the failure to constrain this model, similar to issues encountered with A 0141. Another contributing factor may be related to the cross component of the shear, which was not consistent with zero within 3σ.

5.1.18 Z 2701

The luminosity density map has two significant subpeaks to the N and SE (Fig. A.18). The κ map has a lot of substructure, with one prominent peak coincident with the SE subpeak in the luminosity distribution. This position is supported the most probable LENSTOOL model, which is bimodal and includes this position and the BCG position. This subpeak may be related to the NE-SE aligned of the X-ray emission, which may also be related to the northern subpeak in the luminosity map. Z 2701 is a cool core cluster, and the small offsets between the X-ray centroid, mass peak BCG suggest it is undisturbed.

5.1.19 RX J1000.5+4409

The mass, κ, luminosity density and X-ray emission 2D distributions are given in Fig. A.19. Comparison of all the maps suggests RX J1000.5+4409 is a bimodal cluster. The κ map shows structure from the far E side of the field of view to the W, supported by galaxy distribution in the E, but the alignment of the western structure to the SW, is at odds with the alignment in the luminosity and X-ray maps, to the NW: the κ distribution is also rather flat and has a high background: the contours in this map begin at 3σ. The most probably LENSTOOL model is bimodal, the subpeak in the NW agreeing with the X-ray map. It could be that the use of the IR prior compensates for noisy shear measurements and helps constrain the model, but alternatively this prior, which not only restraints the position of possible cluster scale DM haloes, but also adds a mass prior by way of the PIEMD potentials of the cluster galaxies, could remove information on an offset of the subpeak centre of mass from the luminosity subpeak position. This cluster

has the lowest X-ray luminosity in the sample and a cool core, both indicators that the cluster is undisturbed, however the offset between the X-ray centroid and BCG suggests it is disturbed. Assuming this is the case, and assuming that the NW feature in the X-ray map is related to the NW substructure in the LENSTOOL mass map, it could be that this substructure has passed by the core in projection.

5.1.20 A 2187

A 2187 appears has a strong NW distortion in the luminosity distribution (Fig. A.20), but the X-ray emission is extended WSW. The morphology of the X-ray emission, X-ray structure in the core and the lack of a cool core suggests this cluster is disturbed. The κ map is noisy, but the offset of the centre of the most significant feature, associated with the BCG, to the W, may be related to the disturbance in the X-ray contours. However the most probable LENSTOOL model has a very low mass halo fixed on the BCG position. The lensing constraints on this cluster are not very strong, and the tangential shear for this cluster is negligable. It could be that the disturbed nature of this cluster has resulted in a shear signal morphology too complex to be constrain by this analysis of the shallow HST data. The analysis of this cluster would likely benefit from deeper observations to better constrain the WL shear signal, and from a more robust cluster galaxy selection method.

5.1.21 A 2537

The luminosity distribution is multiimodal near the BCG, a configuration supported by the LENSTOOL model, weakly indicated in the κ map but not supported by the X-ray distribution. The X-ray distribution appears undisturbed and smooth, however this cluster does not have a cool core, and the X-ray centroid is offset from the BCG position. The substructure in the lensing mass and luminosity maps and the lack of a cool core may be due to previous infall history: if this was along, or at a shallow angle to the line of sight, then the X-ray contours may appear

undisturbed.

5.1.22 Summary

The cluster conclusions drawn above motivated A 3140 and RX J1000 being classed as disturbed despite having offsets just short of the criterion of $> 15kpc$ set by (Sanderson et al., 2009). Based on comparing the multi-wavelength structure maps, A 0781 and A 0141 were removed from the sample, while A 3192 was removed for being outside the redshift range established during the LoCuSS sample selection. This left 18 clusters in the final sample. Of these, 7/18 ($38.9\%^{+14.5}_{-13.1}$) had cool cores and 11/18 ($61.1^{+13.1}_{-14.5}$) were classed as non cool core. 10/18 ($55.6\%^{+13.6}_{-14.4}$) were classed as disturbed, and 8/18 ($44.4\%^{+14.4}_{-13.6}$) as undisturbed. Clusters are considered multimodal in the DM distribution if the best fit LENSTOOL model had more than one cluster scale potential, with 7/18 clusters being multimodal.

Of the 7 cool core clusters, 5/7 were classed as undisturbed, while of the 11 clusters lacking a cool core, only 3/11 were classed as undisturbed. 6/10 disturbed clusters had multimodal mass models, compared to 1/8 of the undisturbed clusters, possibly suggesting dynamical status is related to the existence of significant mass substructure in the core.

If both cool core status, and DM core substructure are related to dynamical state, it may be expected that the non cool clusters are more likely to be multimodal. However, when we look at the segregation in most probable LENSTOOL model complexity between cool core and non cool core clusters, 3 out of 7 ($42.9\%^{+24.8}_{-22.3}$) of the most probable LENSTOOL mass models for cool core clusters were multimodal, compared to 4/11 ($26.7\%^{+16.2}_{-12.3}$) of the non cool core clusters. Two of the cool core clusters were classed as disturbed based on the offset between the X-ray distribution and the BCG position, and these also had multimodal LENSTOOL models. Thus cool core status may not be a perfect indicator of dynamical state if the cool core hasn't been perturbed by infalling substructures, or has since restablished itself. This result could also imply that in

this analysis substructure in cool core clusters is easier to constrain. If non cool core status suggests a disturbed morphology and recent infall, then the mass substructure distribution may be too complex too constrain with the shallow SNAPSHOT observations. A disturbed cluster with a cool core could result if enough time has passed such that the cool core has re-established itself after a merger, possibly resulting in a simpler DM morphology that is easier to constrain. Similary, if the substructure has not fallen through the core, then the cool core may have not been disturbed yet, and the DM substructure may be more distinct from the underlying cluster halo and easier to constrain.

5.2 Scaling Relations and Observable Quantities

The clusters in this sample were primarily chosen using their X-ray luminosity, and were not chosen based on their mass or evidence of SL effects. The aim was to obtain a sample representative of the entire cluster population, in order to probe global relationships between cluster properties. We examined to look at three scaling relations, $M_{WL}-T_X$, $M_{WL}-L_X$ and $M_{WL}-L_K$, to investigate whether the cool core status of a cluster impacted the slope or scatter of this relations. Although the weak lens cluster mass estimates were biased low, by using a common smoothing scale we hoped to maintain a common low mass bias across the sample and show that this bias only impacted the normalisation of any mass based scaling relations, and not the slope.

5.2.1 Theoretical Model

Their rarity means clusters can be treated as isolated systems, and can be considered in be virialised: as the time it takes a galaxy to cross a cluster (assuming a virial radius of $\sim 1.5-2$Mpc) is much less than the age of the Universe, so we assume the cluster is in Virial Equilibrium, ie the kinetic energy is half that of the gravitational energy. Then we can apply this Virial Theorem

to determine the relation between the X-ray temperature and the virial mass, $T_X \propto M_{vir}/R_{vir}$. As the virial mass is proportional to the cube of the virial radius, where the average density of the cluster is 200 times the critical density of the universe, then for masses within radii of fixed overdensities,

$$T \propto \frac{M}{R} \propto M^{\frac{2}{3}} \tag{5.1}$$

For masses found within fixed radii, R does not scale with M, and thus,

$$T \propto \frac{M}{R} \propto M \tag{5.2}$$

The X-ray luminosity is related to the gas density and X-ray temperature (Eq. 5.3). Using a similar reasoning the relationship between L_X and M at fixed radii can deduced,

$$L_X \propto \rho_g^2 T^{\frac{1}{2}} R^3 \tag{5.3}$$

The gas density, ρ_g, can be related to the cluster mass using the gas mass fraction, $f_g = M_g/M = (\rho_g * R^3)/M$, to give,

$$L_X \propto (\frac{f_g M}{R^3})^2 T^{\frac{1}{2}} R^3 \propto \frac{f_g^2 M^2}{R^3} T^{\frac{1}{2}} \tag{5.4}$$

As before, at fixed radii R does not scale with M, and Eq. 5.4 becomes,

$$L_X \propto f_g^2 M^2 T^{\frac{1}{2}} \tag{5.5}$$

And as for masses at fixed radii, $M \propto T_X$,

$$L_X \propto f_g^2 M^{5/2} \tag{5.6}$$

This can be rearrange to get $M \propto L_X^{0.4}$. So the slope of the logged $M_{WL} - T_X$ and $M_{WL} - L_X$ relations, using masses at fixed radii, is expected to be 1.0 and 0.4 respectively.

If we assume that a massive cluster with a deep potential well has a bright X-ray luminosity because it has accumulated a lot of X-ray gas, then we may conclude that it has experienced significant mass infall to create the potential well in the past. More massive clusters are expected to have formed earlier, to allow for the accretion of their mass. Thus we would expect

the core to be dominated by large, old, red elliptical galaxies. This infall and environment could also quench star formation, resulting in fewer young stars, making the galaxies in the core even redder. Based on this scenario, we may expect the K-band luminosity, which reflects the amount of 'red' light emitted from the cluster, to also trend with mass. Thus we also assume a slope of 0.4 for the logged $M_{WL} - L_K$ relation, to test whether X-ray and IR luminosity scale similarly with the weak lensing mass, which could imply a link between the increase in X-ray emitting gas and SF quenching in galaxy cluster cores.

5.2.2 Results

Fig. 5.1 shows the weak lens masses found using the best fit parameters from the optimum LENSTOOL models for each cluster, against K-band luminosity, L_K, X-ray temperature, T_X, and X-ray luminosity, L_X. The log-log relation between the properties was fit as a straight line, with $log_{10}M_{WL} = B + A \times X$, where $X = log_{10}T_X, L_X, L_K$. This fitting was done using a weighted orthogonal distance regression algorithm, called ODRPACK (Boggs et al., 1989), where the orthogonal distance from each measured data point is minimised. ODRPACK takes account of the error associated with each data point by weighting each point by $1/\sigma^2$. As part of the fitting process, ODRPACK returns the predicted error on each measurement, assuming that the best fit relation is true. This error is an estimate of the measurement error and the intrinsic scatter combined. The average of these errors is given at the top of each plot, colour coded by subsample type. Assuming that, on average, the clusters have similar measurement errors, then these mean errors indicate the relative differences in intrinsic scatter between each subsample.

The theory outlined above predicts that for the mass-temperature relation we would expect A to equal 1.0, and for the mass-luminosity relation $A = 0.4$. The best fit results for A and B are given in Table. 5.3. In agreement with the derivation above, $M_{WL} \propto T_X$ for the whole sample, with cool core clusters having a shallower slope and non cool core a steeper slope. The scatter in the fit to the cool core clusters is less than that to the whole sample, or the non cool core

Table 5.3: Best fit relation for $M_{WL} - T_X, L_X, L_K$ for 18 clusters.

X	All Clusters		Cool Core Clusters		Non Cool Core Clusters	
	A	B	A	B	A	B
T_X	0.86 ± 0.32	13.25 ± 0.25	0.51 ± 0.24	13.51 ± 0.18	1.02 ± 0.54	13.12 ± 0.44
T_X	[1.0]	13.14 ± 0.04	[1.0]	13.15 ± 0.05	[1.0]	13.13 ± 0.06
L_X	0.42 ± 0.11	13.58 ± 0.09	0.31 ± 0.14	13.67 ± 0.12	0.51 ± 0.18	13.51 ± 0.15
L_X	[0.4]	13.60 ± 0.03	[0.4]	13.60 ± 0.03	[0.4]	13.60 ± 0.04
L_K	0.36 ± 0.12	13.79 ± 0.05	0.27 ± 0.13	13.84 ± 0.05	0.54 ± 0.23	13.70 ± 0.10
L_K	[0.4]	13.78 ± 0.03	[0.4]	13.80 ± 0.03	[0.4]	13.76 ± 0.04

Table 5.4: Best fit relation for $M_{WL} - T_X, L_X, L_K$ when outlier A 2187 is excluded.

X	All Clusters		Cool Core Clusters		Non Cool Core Clusters	
	A	B	A	B	A	B
T_X	0.78 ± 0.27	13.32 ± 0.21	0.51 ± 0.24	13.51 ± 0.18	0.85 ± 0.43	13.28 ± 0.34
L_X	0.39 ± 0.11	13.62 ± 0.09	0.31 ± 0.14	13.67 ± 0.12	0.45 ± 0.18	13.57 ± 0.16
L_K	0.37 ± 0.10	13.80 ± 0.05	0.27 ± 0.13	13.84 ± 0.05	0.51 ± 0.20	13.73 ± 0.09

clusters. When the slope is fixed to 1.0, the normalisation is consistant between the cool core and non cool core subsamples.

The $M_{WL} - L_X$ is also in agreement with the derived relation of 0.4. As with the mass-temperature relation, the cool core clusters have a shallower slope and smaller scatter than the full or non cool core cluster samples. When the slope is fixed to 0.4, the normalisations are all consistant with each other between the subsamples. The $M_{WL} - L_K$ relation for the complete sample is also consistant with 0.4. Again, the cool core cluster subsample has a shallower slope and smaller scatter. Removing the cluster with the lowest mass, A 2187, as an outlier, makes little difference to the results, and all properties are consistent with the results from the original sample within the errors (Table. 5.4) The main result from these relations is that L_K and L_X trend with mass in the same way.

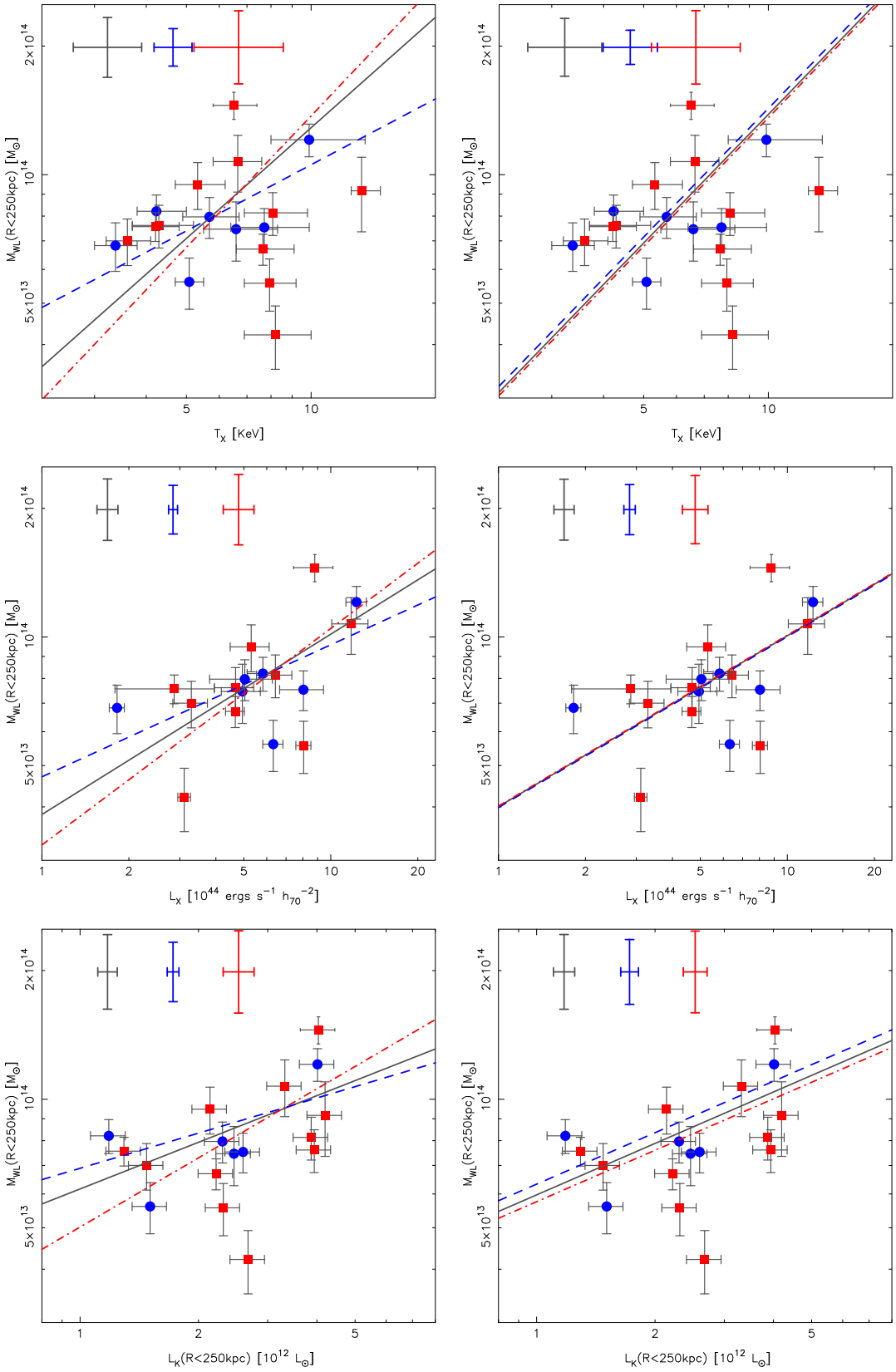

Figure 5.1: Top:$M_{WL}(< 250kpc)$ versus T_X with a free fitted slope (left) and slope fixed to 1 (right). Blue circles denote clusters with cool cores, red squares denote clusters without cool cores. The solid black line gives the fit to whole sample, blue dashed line to the cool core clusters, red dot-dash line to the non cool core clusters. The intrinsic scatter is given as error bars on each fitted relation. Middle: $M_{WL}(< 250kpc)$ versus L_X, same as before. Bottom: $M_{WL}(< 250kpc)$ versus L_K, same as before.

5.3 Substructure Fraction Distribution

The substructure fraction is defined as the amount of mass not included in the BCG or in the cluster scale DM halo associated with the BCG position, and has been related to formation history and dynamical state. We compared our results with those from Richard et al. (2010) (hereafter JR10), in order to determine whether cluster selection based on X-ray luminosity probes the same underlying cluster population as cluster selection based on SL features. Of the 20 JR10 clusters, and 18 clusters discussed here, only 2 are coincident, $Z\,2701$ and $A\,0611$.

The substructure fractions from our analysis are given in Table. 5.1, 5.2, and were generated using the best fit LENSTOOL model parameters: the mass of the cluster within 250kpc was first found using only the BCG magnitude scaled PIEMD and the cluster scale DM halo associated with the BCG position, and then this quantity was used with the total cluster mass to determine what fraction of the cluster mass was associated with substructures such as large scale DM haloes in the multimodal models and the cluster galaxies (Eq. 5.7),

$$f_{sub} = \frac{M_{tot}(< 250kpc) - M_{BCG+DM_0}(< 250kpc)}{M_{tot}(< 250kpc)} \tag{5.7}$$

The substructure fractions from our analysis where compared with those from JR10 in Fig. 5.2, in the form of the substructure fraction distribution (left) and cumulative distribution (right). The maximum offset between the two samples in the cumulative distribution is $D = 0.3722$. Using the two sample Kolmogorov-Smirnov test, the probability that these samples were drawn from the same underlying cluster population is $P = 0.110$, implying that we can't reject this hypothesis with any significance. Thus the L_X selected sample is drawn from the same underlying cluster population than the cluster sample selected based on SL features. However, while global properties are consistent between the two samples, the results for the two common clusters, A 0611 and Z 2701, are in conflict. Our analysis suggests unimodal and bimodal DM structures, with substructure fractions of 0.17 ± 0.02 and 0.26 ± 0.04, for A 0611 and Z 2701 respectively, where as JR10 finds substructure fractions of 0.10 ± 0.01 and 0.04 ± 0.02. The low mass bias in our analysis could cause the substructure fraction to be mildly boosted, but

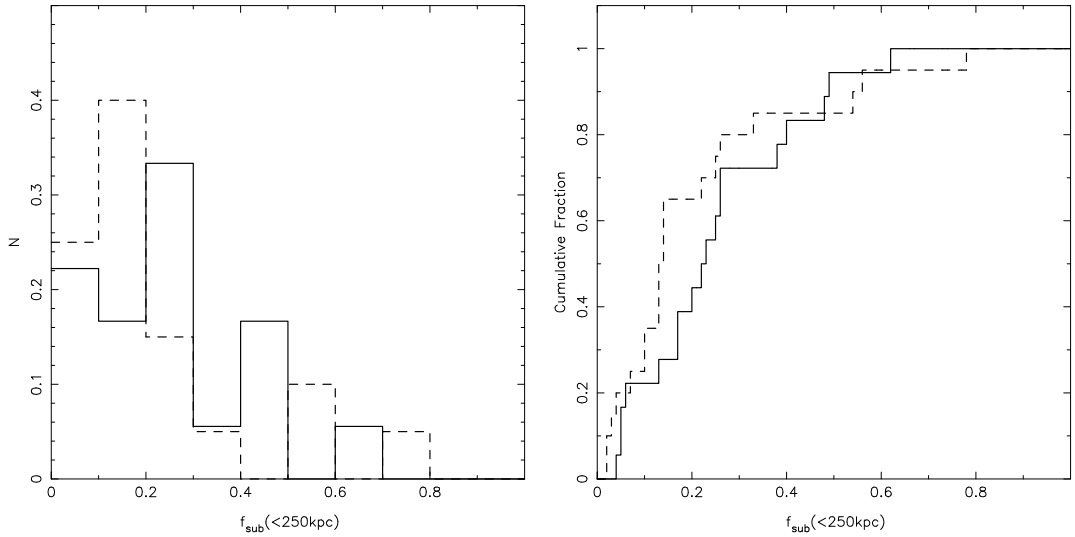

Figure 5.2: Left: f_{sub} distribution, with this analysis given by the solid histogram, and the results from JR10 given by the dashed histogram. Right: Cumulative distribution of f_{sub}, with the same key as before.

the main source of contamination would be an increase in the contribution of the cluster galaxies, particularly the BCG. The result for Z 2701, however, is considerably different. A possible explanation is that these substructure fractions were found from SL masses, and require the observation of strongly lensed background galaxies to constrain the cluster mass. While 4 images were used to constrain the model for A 611, only 2 images were used to constrain the model for Z 2701. The subhalo detected in the WL analysis we performed had no associated SL in the JR10 analysis. As our substructure fraction is impacted by the inclusion of this subhalo in the model, this highlights the importance of weak lens analysis for those clusters and substructures in clusters that do not have SL images of galaxies.//

As in JR10, we sought to investigate the relationship between the substructure fraction, defined as the the fraction of mass not included in the BCG or main cluster scale DM haloes, and the slope of the gas profile, α. The comparison with α is in Fig. 5.3. The best fit slope and normalisation for the relation $log_{10}(f_{sub}) = A + B\alpha$, $B = 1.28 \pm 0.53$ and $A = 0.19 \pm 0.43$ are consistant with JR10, who obtained $B = 1.15 \pm 0.22$ and $A = 0.09 \pm 0.12$. Like JR10, our results suggest α and f_{sub} from WL are positively correlated, although the significance from this analysis is only 2σ. This suggests that clusters without cool cores have higher substructure fractions,

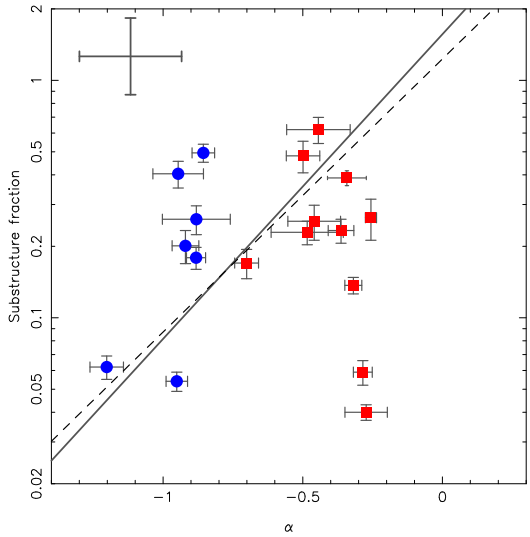

Figure 5.3: α versus f_{sub} within an aperture of $250kpc$. Blue circles denote cool core clusters, and red squares denote non cool core clusters. The relation fit to this analysis is given by the solid black line, and the result from JR10 by the dashed black line.

suggesting recent infall and merging history resulting in a high core substructure fraction disrupts the cool core.

5.4 Offsets between Mass Peaks and BCG Centroids

The LENSENT2 Maximum Entropy results provide a map of the surface mass density, κ, which does not depend on a prior supplied by the IR light, as the LENSTOOL optimisations did. This means we can use the peak of the mass distribution in these maps to constrain BCG-Mass offsets. The full derivation of the peak positions and their 2σ clipped σ_{stdv} is given in § 4.1.3. The mass peak offsets from the BCG and errors are summarised in Table. 5.1, 5.2. Fig. 5.4 shows the DM peak position relative to the cluster BCG position, with the error bars showing σ_{stdv}. Those with red error bars have positions consistant with the BCG position of $(0, 0)$.

The clusters with mass peaks consistant with the BCG position are A 2813, A 3084, AS 0592, A 2537 and RXJ 1000.5. Only A 3084 was modelled with a single DM halo fixed on the BCG position during the LENSTOOL analysis. The other four are bimodal, with a subhalo near the

cluster core, and a halo on the BCG position. This bimodality is present, or indicated, in the κ map in all four clusters, and is in agreement with the IR prior. Other bimodal clusters, such as Z 2701 and the Bullet cluster, did not have peak positions consistant with the BCG position. The placement of the multimodal clusters with mass peak positions consistent with the BCG position, discussed above, in this disturbed subset and on the possible relation, suggests a more appropriate comparison may be between the mass centroid offset, where the centre of the mass is found as the average centre of the κ realisation, rather than the κ peak position.

The clusters that had significant offsets between the peak of the non parameterised projected mass distribution and the BCG position included most of those clusters that were modelled by a single halo fixed on the BCG position during the parameterised LENSTOOL modelling, would could imply that the use of an IR prior, and assuming light so closely follows mass, may limit the information on the DM distribution in the parameterised modelling. However, this included clusters that, when the structure maps from the two lensing analysis, X-ray and luminosity data were compared, appeared undisturbed, so these large offsets may be due to large uncertainties in the non parameterised maps. The constraints from this analysis are not strong enough to optimise the position as well as the velocity dispersion of the cluster scale DM haloes in the parameterised analysis, so a deeper WL dataset may be required to study this fully.

The right panel of Fig. 5.4, plots the mass peak offset from the BCG against the offset between the X-ray centroid. Beyond an X-ray offset of $10-15kpc$, there appears to be a positive correlation between the two offsets, although the large errors on the peak positions suggest it would have a large scatter. It is also beyond this offset that the clusters are classed as disturbed. It should be noted that while the magnitude of the mass and X-ray peak offsets from the BCG position may be correlated, they may not be in the same direction. If the X-ray offset is large and indicates the cluster is dynamically disturbed, then the infall into the core may result in the BCG moving about the centre of the DM potential well, resulting in an offset between the BCG and the peak of the DM mass distribution. While indicative of such an interesting result, the

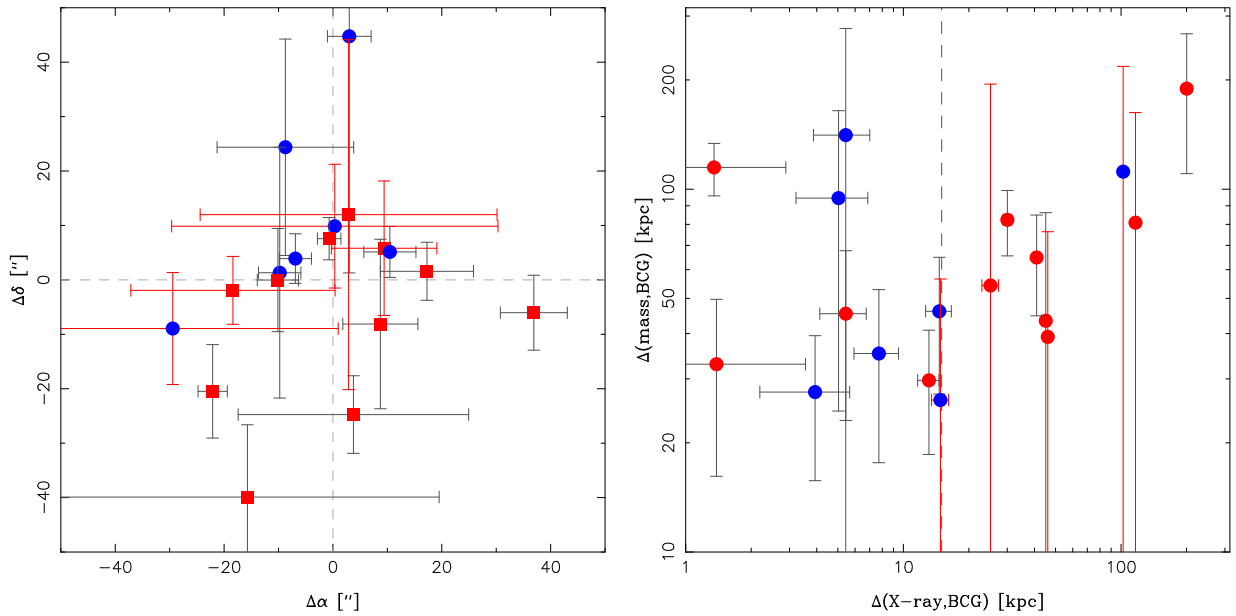

Figure 5.4: Left: Averaged peak positions for each cluster with respect the BCG position $(0,0)$, with errors generated from bootstrapped MC runs. The error bars are red when the mass peak position is consistant with the BCG position. Right: Mass peak to BCG offset against X-ray centroid to BCG offset, with offsets in *kpc*. Again, those clusters with mass peak positions consistant with zero have red error bars. In both figures blue circles denote cool core clusters, red squares denote non cool core clusters. The vertical dashed line at $15kpc$ gives the disturbed cluster X-ray offset cut.

constraints from this analysis are not strong enough to draw significant conclusions.

5.5 Summary

We performed a standardised and robust weak lens analysis on 21 X-ray luminous cluster cores at redshifts between 0.15 and 0.3. This involved a non-parameterised analysis LENSENT2, which provided initial mass maps and mass peak offsets from the BCG. We then used IR data to construct a cluster galaxy based prior on the spatial distribution of the mass, and used these to obtain the most probable parameterised models form LENSTOOL. We then compared the 2D mass distributions from both WL methods with 2D maps of the X-ray surface brightness and K-band luminosity density.

Comparisons of the maps for each cluster suggested the most probable models for cool core

clusters were more commonly multimodal than the models for non cool core clusters. This either suggests that cool core clusters are more likely to have significant substructure, or substructures in cool core clusters are more likely to be reconstructed via the parameterised and non parameterised methods used in this analysis, than the substructure in the non cool core clusters. The latter conclusion suggests that multimodal cool core clusters may have simpler substructure morphologies than non cool core clusters. However the small sample size means that $3/7 = 42.9\%^{+24.8}_{-22.3}$), and $4/11 = 36.4\%^{+19.5}_{-16.5}$), giving 1σ errors. The difference between the two subsamples is not significant, and would require a much larger sample size to constrain the statistical errors.

Several clusters were identified not only as multimodal, but also as highly disturbed, with interesting substructure in all maps, highlighting this analysis' efficiency at identifying 'extreme' clusters for future, indepth analysis.

We also investigated the mass-observable scaling relations. Both $M_{WL}-T_X$, $M_{WL}-L_X$ followed the relations predicted by theory, and the weak lens mass trends with K-band luminosity in the same way as with X-ray luminosity. In all relations, cool core clusters appeared to follow a shallower relation than non cool core clusters, although the slopes and normalisations between the subsamples were consistent within the error.

The substructure fraction distribution matched that found in JR10, and suggested that the SL selected clusters in JR10 were drawn from the same underlying cluster population as the luminosity selected clusters in this sample. There was a weak, positive correlation between α and f_{sub}, another result consistent with JR10, suggesting a link between significantly clumpy DM structure and the lack of a cool core in clusters.

The mass peak offset from the BCG was found using the LENSENT2 κ maps. Of the 18 clusters, 4 clusters with peak positions consistent with the BCG position were bimodal in most

of the multi-wavlength maps, with the substructure modelled in both the κ and mass maps. The mass peak offset from the BCG was also compared to the X-ray centroid offset. This comparison was suggestive of a positive correlation, with the scatter noticeably decreasing for X-ray offsets $> 10-15kpc$. However the large errors on the mass peak offsets mean this would difficult to constrain with this dataset.

Chapter 6

Individual Cluster Studies: A 3364 and A 3192

This chapter describes the focussed analysis of two clusters, A 3364 and A 3192. The first, A 3364, appears to have a large offset between the only halo in the LENSTOOL parameterised model, and the BCG position. In order to constrain the error on this offset and investigate the reliability of the parameterised and non-parameterised result, constraints from the literature on the position of the mass subpeak in the Bullet Cluster is compared to the analysis of the same peak, as described in this thesis, in order to determine the systematic error. It is concluded that, in the case of A 3364, the non-parameterised mass peak position is consistant with the BCG position, but when the underlying K-band luminosity distribution is used as a prior for the parameterised models, the constraints strongly prefer this offset position.

The second cluster, A 3192, was found to have a redshift of 0.42, which lay outside the redshift range probed by LoCuSS. In studying this cluster apart from the main sample, it was discovered that the likelihood cause of the confusion over the redshift of A 3192, previous thought to be 0.1687, was due to a foreground galaxy group just outside the field of view. The weak lens signal of this group is detectable in both the parameterised and non-parameterised analysis of this cluster. The paper describing this discovery and the analysis is included in its submitted form, and it is under peer review by Astrophysical Journal Letters.

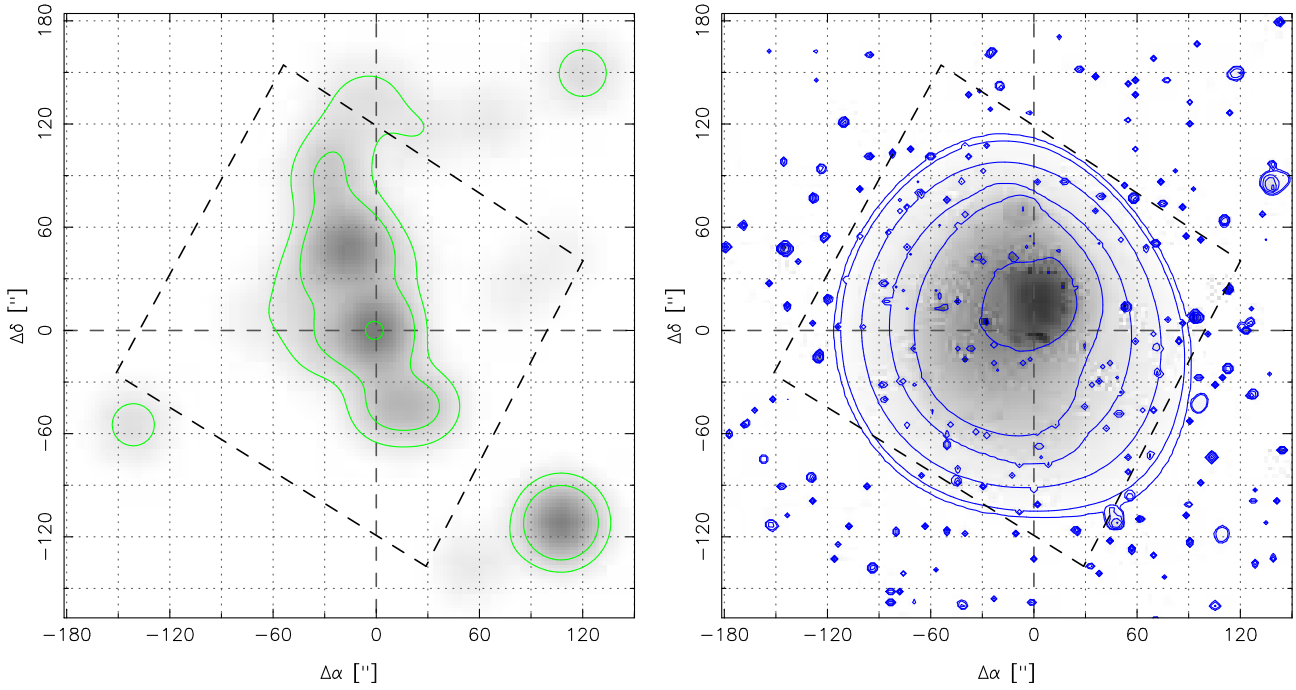

Figure 6.1: A 3364: left, luminosity density map, centred on the BCG position, with contours of $1, 2, 5 \times 10^{13}, 1 \times 10^{14} L_{\odot} Mpc^{-2}$, and right, the smoothed X-ray emission, with logarithmically stepped contours.

6.1 A 3364: A New Cosmic Trainwreck?

A 3364 is a moderately X-ray bright (T_X = 7.65keV) galaxy cluster at z = 0.1483, at the very lower redshift limit of our sample. The maps of luminosity density and X-ray emission indicate a bimodal cluster with some merger activity between the two main luminosity components, the BCG and a bright subpeak to the NE (Fig. 6.1). A third major, dimmer, luminous subpeak can be seen $\sim 40''$ SW of the BCG, with dim X-ray emission extended in this direction. From the distribution of the light and X-ray emitting gasses, it would be expected that the majority of the Dark Matter signal would be associated with the BCG and Northern luminosity peak. This follows from assuming that mass follows light, and that the DM, like the galaxies, acts as collisionless particles during mergers. This conclusion is supported by observations of a very famous merger, the Bullet Cluster (Clowe et al., 2004b) where a pass through of a galaxy group through a cluster has resulted in the X-ray gas being shocked between two clumps consisting of light and DM.

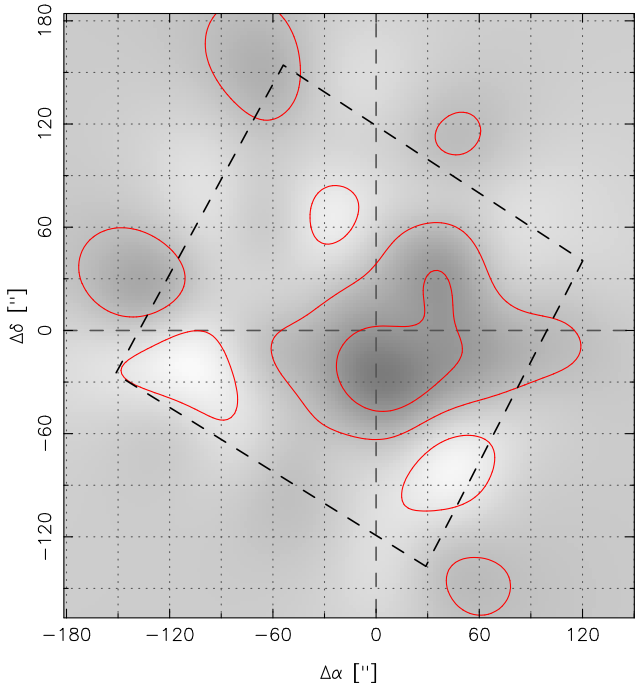

Figure 6.2: A 3364: the LENSENT2 κ reconstruction, the contours denoting 2σ and 3σ levels

However, the analysis of the weak shear signal with LENSENT2 and LENSTOOL suggests this is not the case (Fig. 6.2). The maximum entropy reconstruction from LENSENT2, representing the κ distribution, places the majority of the DM between the BCG and the dimmer luminosity peak to the SW. The Bayesian statistics from the LENSTOOL analysis strongly supported all mass being assigned to the subpeak SW of the BCG, with $P(SW)/P(BCG) = 5.1 \times 10^9$. Models solely featuring, or including, haloes on the BCG and Northern subpeak positions were soundly rejected. If accurate, such a large offset between the peak of the DM mass and the main X-ray and luminosity distributions may reflect a very complex cluster merger history, with possible implications on the interplay between DM and baryons, and may imply that the DM is not fully collisionless. To determine whether this result is reliable, I needed to obtain a reliable estimate of the systematic error on the measurement of the DM peak.

The Bullet Cluster(1ES0657-558) is a famous example of the difference in behaviours of the three major cluster components (gas, galaxies and DM) when a merger occurs. The X-ray emitting gas interacts with itself and a shock front can clearly be seen in the X-ray emission map.

The galaxies and DM act collisionless, remaining in their cluster and group concentrations. Since discovery in 2002 (Markevitch et al., 2002), the Bullet Cluster has been studied in many wavelengths. In 2004, Clowe et al. (2004b) (hereafter C04) performed a weak lensing analysis. Utilising the Seitz & Schneider (1995) variant of the Kaiser and Squires method, C04 produced non parameterised maps of the DM distribution and explored the constraints obtainable on the subpeak position. In order to constrain the systematics in my method, I compared the best fit positions and associated errors for the subpeak position, from LENSTOOL and LENSENT2, to the result in C04. The decision to model the subpeak was motivated by two reason: as constraints on the subpeak, these systematics would be a conservative estimate of the systematics affecting the fitted position of the main cluster halo, as in A 3364, and the C04 paper only produced detailed position results for the subpeak, preventing me from exploring their constraints on the BCG.

This chapter will summarise the results from the analysis of the Bullet Cluster and A 3364, and then explore the constraints that can be obtained on the positions of peaks in the DM distribution from both LENSENT2 and LENSTOOL. After comparison with C04 I will draw conclusions on the impact of systematics on the DM position measurements, and discuss the interesting structure in A 3364.

6.1.1 Modelling

Fig. 6.3 shows the luminosity density, X-ray emission, LENSENT2 κ and LENSTOOL mass maps for the Bullet Cluster, from § A. The bimodal configuration is clear in the light and weak lensing reconstructions, while the X-ray emission is drawn out between the two peaks, with the shock front (the 'bullet') associated with the subpeak. The bimodal LENSTOOL model, with main peak centre associated with the light peak SE of the BCG position, is more probable than a single halo model by a factor of $P(2)/P(1) = 121.5$, and more probable than a bimodal model with the main cluster component fixed on the BCG position by a factor of $P(2)/P(BCG, 2) = 5.6$.

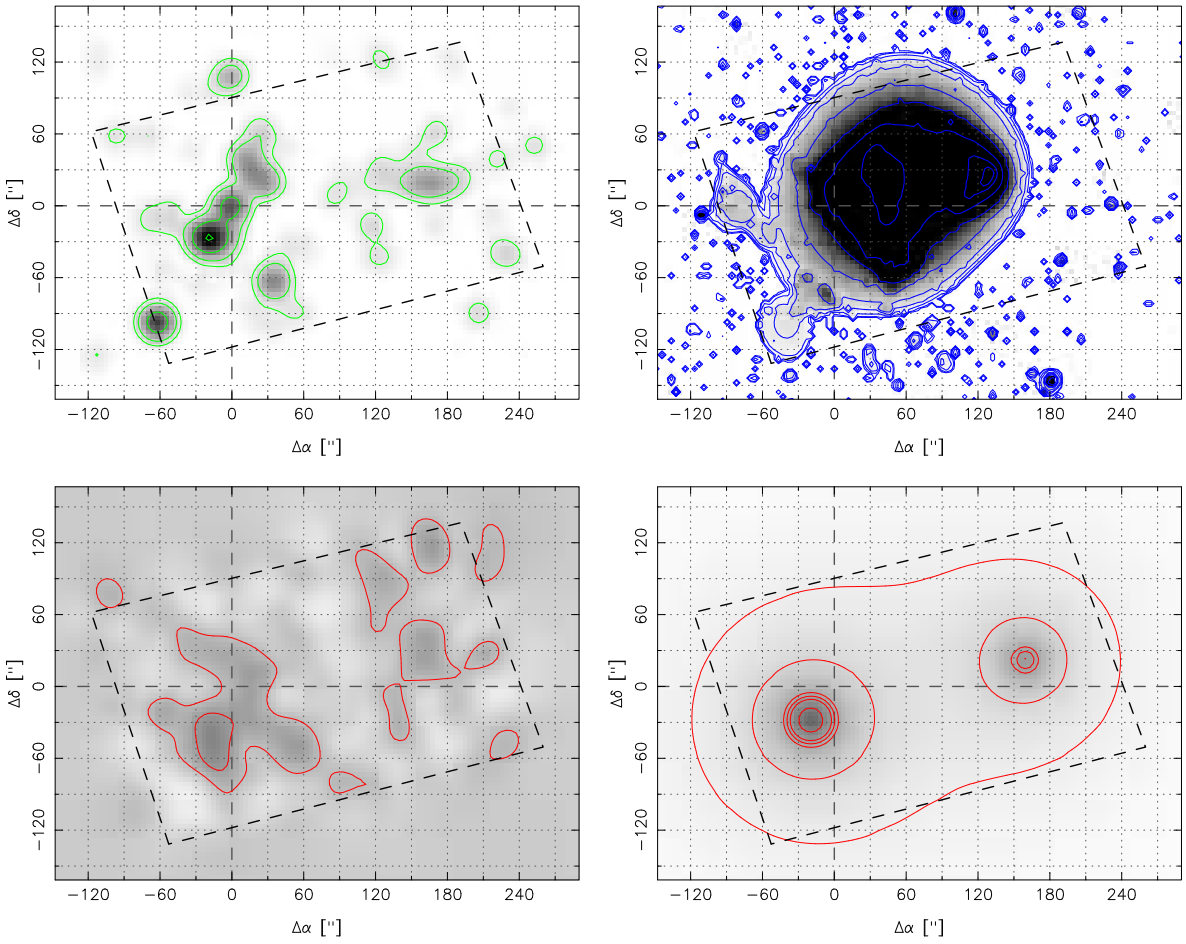

Figure 6.3: Bullet Cluster: Top: left, luminosity density map, centred on the BCG position, with contours of $1,2,5\times10^{13},1\times10^{14}L_{\odot}Mpc^{-2}$, and right, the smoothed X-ray emission, with logarithmically stepped contours. Bottom: left, the LENSENT2 κ reconstruction, the contours denoting $2\sigma,3\sigma$ levels, and right, the LENSTOOL mass density model favoured by the Bayesian evidence, contours at (0.001, 0.002, 0.005, 0.01 ... 1)$\times10^{12}M_{\odot}Mpc^{-2}$.

The pipeline is capable of constraining the spatial distribution of DM. To quantify the offset constraints, I need to optimise the peak position of the Dark Matter using my weak lensing data, and compare it to a weak lensing result from the literature.

In C04, constraints on the peak position of the subpeak were found by simulating the faint galaxy catalogues by random resampling of the original catalogue, and obtaining the peak position from each KS93 variant realisation. These positions were plotted to form a 2D map of the sample distribution (see Figure 2. of C04), from which we obtained a subpeak position of $06:58:16.75,-55:56:35$, or $(156.59,22.10)''$ with respect to the BCG position (Table 6.1).

The offset between this position and the best fit position from LENSENT and LENSTOOL, compared to the 1σ error on the peak position, is used as an estimate of the systematic error in my analysis.

The DM subpeak position in the LENSENT2 κ reconstruction was chosen to be the pixel with the highest κ value, restricted to a $60'' \times 60''$ box centred on the luminosity subpeak position, and then this position refitted with the IRAF function PHOT. Constraints on this position were found using a method analogous to C04. The faint galaxy catalogue was bootstrap resampled 1000 times and LENSENT used to reconstruct the κ map for each realisation of the catalog. The DM subpeak position was found in the same way as the real DM subpeak position was found in the original reconstruction. The sample distribution of peak positions around the luminosity subpeak position (green point in plot) is given in Fig. 6.4. The subpeak and position from LENSENT2 is listed in Table 6.1. This is offset by $(4.50, 8.45)''$ compared to the result from C04. The offset compared to the 1σ error, $\frac{4.50}{12.00} = 0.38$, $\frac{8.45}{20.51} = 0.41$ suggests the systematic error in the analysis of the subpeak position is $\sim 40\%$ of the statistical error. Thus we concluded that the systematic error in the same analysis on the position of the main cluster DM peak position of A 3364 would be, at most, 40% of the statistical error, assuming the constraints on the position of a massive primary cluster component stronger than those on a subpeak.

An independent analysis using parameterized models was performed using LENSTOOL. A bimodal model was fitted to data smoothed with the modal smoothing scale from the fixed position analysis, $\sigma_g = 90$kpc. The positions from the Bayesian sample file, ~ 55 thousand samples, are plotted in Fig. 6.5. The peak position chosen was the optimum output, based on the χ^2_{red} value of the sample, and is given in Table 6.1. These constraints were much poorer than those from LENSENT2, possibly due to the parameterised nature of the LENSTOOL model, which would have had to take into account the artefacts seen in the LENSENT map. However, within the 1σ confidence limits, the two results are consistant with each other. When compared to the CL04 constraints, the LENSTOOL result falls just short of being consistant within 1σ errors.

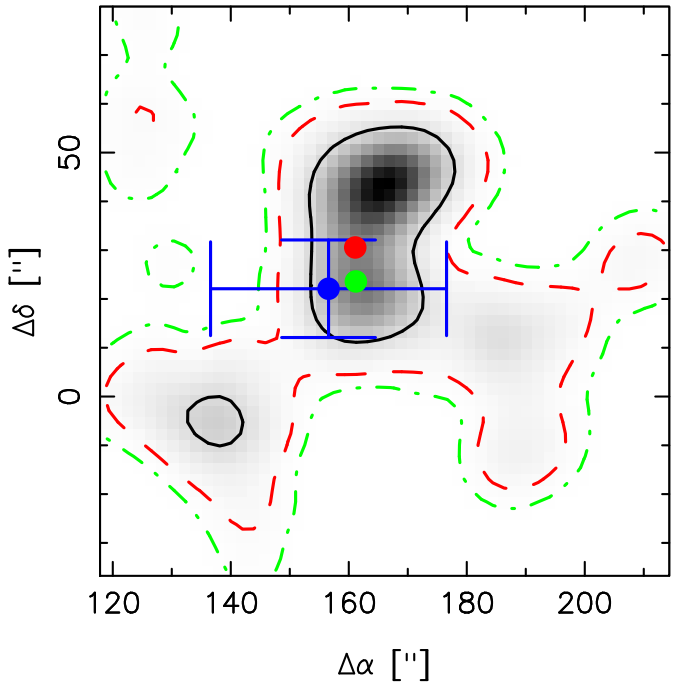

Figure 6.4: Bullet Cluster: Peak positions from 1000 bootstrapped LENSENT realisations. The green point denotes the position of the luminous subpeak, the blue point denotes the C04 subpeak position with errors, and the red point gives the LENSENT2 peak position in the κ map generated using the original catalogue. The 68%, 95% and 98% confidence limits are given by the solid black, dashed red and dot dashed green contours respectively.

A similar analysis was performed for A 3364. The weak shear analysis suggested a unimodal model was preferred, with the centre of the mass distribution strongly offset from the BCG position. The LENSENT2 results are recorded in Table 6.2, and the sample distribution is given in Fig. 6.6. Assuming systematic errors of 40% of the statistical error, $\pm(19.93, 17.65)''_{stat} \pm (7.97, 7.06)''_{syst}$. Within the combined 1σ statistical and systematic error, this result is consistant

Table 6.1: *BulletCluster*: subpeak positions and errors

Source	Subpeak Position		68% limits	
	α [$''$]	δ [$''$]	α [$''$]	δ [$''$]
Clowe	156.59	22.10	$\pm$20	$\pm$10
LENSENT2	161.09	30.55	+7.99,–9.47	+20.19,–19.47
LENSTOOL	161.39	56.79	+25.38,–31.01	+21.64,–22.64

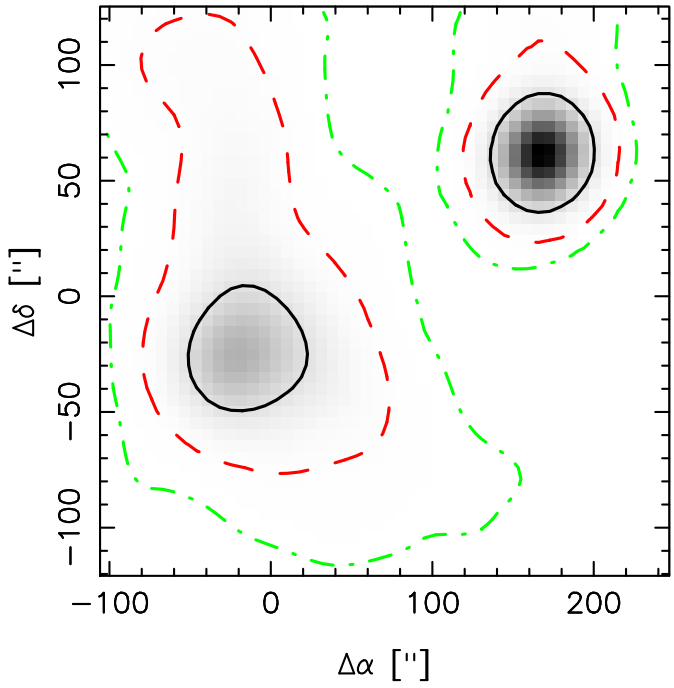

Figure 6.5: *BulletCluster*: distribution of x-y samples from the bimodal LENSTOOL position and σ_0 optimisation, with σ_{gauss} = 90kpc. The 68%, 95% and 98% confidence limits are given by the solid black, dashed red and dot dashed green contours respectively.

with the BCG position at $(0,0)$ at the very edge of the 68% limits, although the κ map clearly favours placing the majority of the DM distribution south of the BCG position.

The LENSTOOL position analysis also places the majority of the mass south of the BCG position (Table 6.2). The tighter constraints in this LENSTOOL fit, compared to the constraints on the Bullet Cluster subpeak position, is likely due to the position being fitted being that of the main mass component of the cluster. The LENSENT2 map suggested the mass distribution was rather flat. In order to test the implications of a flatter distribution, the models with fixed halo positions and the 90kpc unimodal position optimisation were both rerun with the core radius doubled, r_{core} = 75kpc to r_{core} = 150kpc, however changing the core radius did not change the spatial configuration of the mass distribution: the results from r_{core} = 75kpc and r_{core} = 150kpc are consistant with each other, and neither are consistant with the BCG position.

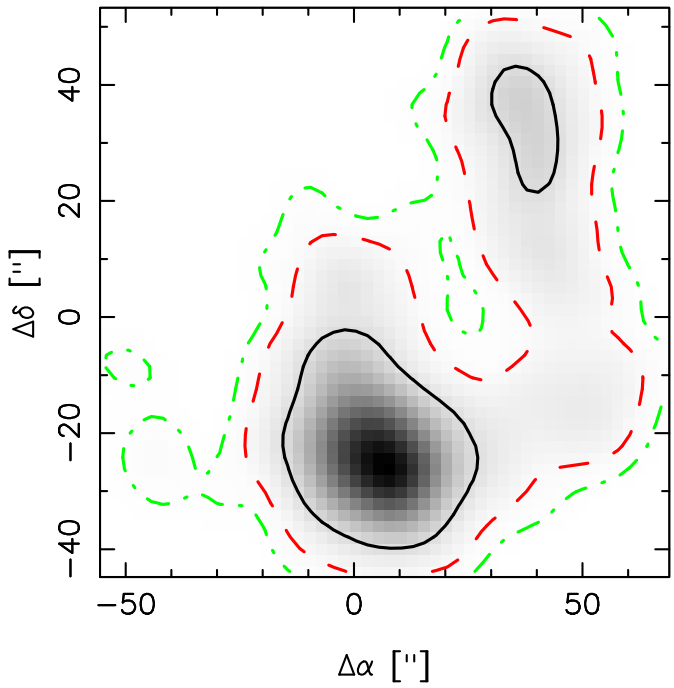

Figure 6.6: *A*3364: Peak positions from 1000 bootstrapped LENSENT realisations, $FWHM$ = 100kpc. The 68%, 95% and 98% confidence limits are given by the solid black, dashed red and dot dashed green contours respectively.

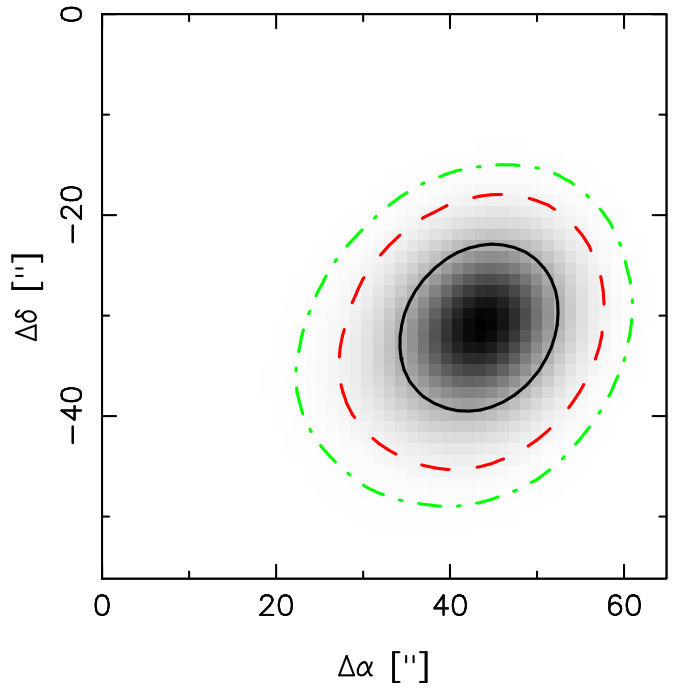

Figure 6.7: A 3364: distribution of x-y samples from the unimodal LENSTOOL position and σ_0 optimisation, with σ_{gauss} = 90kpc. The 68%, 95% and 98% confidence limits are given by the solid black, dashed red and dot dashed green contours respectively.

Table 6.2: *A*3364: peak positions and errors

Source	Subpeak Position		68% limits	
	α [″]	δ [″]	α [″]	δ [″]
LENSENT2	3.77	−24.75	+19.13, −20.73	+20.17, −15.13
LENSTOOL	42.66	−32.06	+7.29, −9.58	+7.91, −7.82

6.1.2 Summary and Discussion

A 3364 is a non cool core cluster (Table. 5.1, 5.2) with three prominent luminous components on a NE-SW axis, with the BCG in the middle. The X-ray emission is centred between the NE peak and the BCG, and has extended, faint emission encompassing the lower, dimmer luminous peak. The WL mass reconstructions, both parameterised and unparameterised, suggest the bulk of the DM mass is associated with the SW luminous subpeak, and not with the brighter BCG and NE luminous subpeak.

By comparison of the results for the subpeak of the Bullet Cluster with a similar analysis in CL04, systematics in the DM peak position from LENSENT were estimated to be 40% of the statistical error. This is a conservative estimate, as the peak constraints on the BCG would be stronger than those on a subpeak. A 3364 appears to have a well constrained faint galaxy shear catalogue, with a $> 3\sigma$ tangential shear signal and cross components consistent with zero within 1σ. The Bullet Cluster also has a well constrained cross shear component, although the shear signal within the annulus chosen is just 2.4σ due to shear signal interference from the mass subpeak. Both clusters have average stellar residual ellipticities consistent with zero, suggesting the PSF correction was successful for both clusters. A 3364 lies at the lower edge of the redshift range of this study, whereas the Bullet Cluster is one of the more distant clusters in the study, however, the comparable PSF correction and low systematics in the shear signal suggests we can use the result on the subpeak of the Bullet Cluster as a conservative indicator of the position systematics in our analysis. Taking into account this systematic error the DM peak position

from LENSENT2 for $A3364$ is just consistent with the BCG position. However, the probability of this position from the LENSTOOL modelling, $P(SW)/P(BCG) = 5.1 \times 10^9$ suggests that even though the data is not good enough to distinguish between a halo centred on the BCG or not in flexible models such as the unparameterised analysis, when alternative priors are invoked based on NIR data, and the model is parameterised with physically motivated haloes, the data strongly supports the SW position.

The mass to light ratios within 50kpc for the BCG, NE subpeak and SW subpeak positions are 11.22 ± 3.19, 8.70 ± 2.14 and 20.36 ± 6.19 respectively at the optimum smoothing scale, 60kpc and 9.55 ± 2.46, 7.88 ± 1.71, 16.49 ± 4.70 at the common smoothing scale 90kpc. Based on the average $M_{WL}/M_X = 0.5$ for the final sample at the common smoothing scale, and assuming M_{WL} should be equal to M_X, a corrected set of mass to light ratios becomes 19.10 ± 4.92,15.76 ± 3.42 and 32.98 ± 9.40 respectively. The M_{WL}/L_K ratio of the SW peak is consistant with (Kneib et al., 2003), however the BCG subpeak and SW subpeak M_{WL}/L_K are undermassive at $\sim 4\sigma$.

A 3364 has also been observed with XMM-Newton, from which we present the T_X map (Fig. 6.8 (priv.comm.Y.Zhang). In this map we note two arc like structures adjacent to the NE and SW subpeaks in the K-band luminosity density map. The feature in the N is cold, $kT = 5.88 \pm 0.19$, with regions above and below of 6.6 ± 0.28 and $6.02 \pm 0.2 - 6.5 \pm 0.24$ respectively. The feature in the SW is hot, $kT = 7.58 \pm 0.32$, and is significantly hotter compared to the regions immediately above ($kT = 6.54 \pm 0.24$) and below ($kT = 6.27 \pm 0.23$). This could represent sloshing, as the dynamical activity in the cluster core seen in the T_X map is on a similar scale to that seen at other wavelengths. However it is hard to constrain the presence of a possible shock in the SW and a cold front in the N with *XMM* resolution and shallow *Chandra* data.

Underluminous 'dark haloes' are a rising topic of interest in studies of complex mergers (Mahdavi et al., 2007; Merten et al., 2011). Given the likelihood that the offset in this cluster

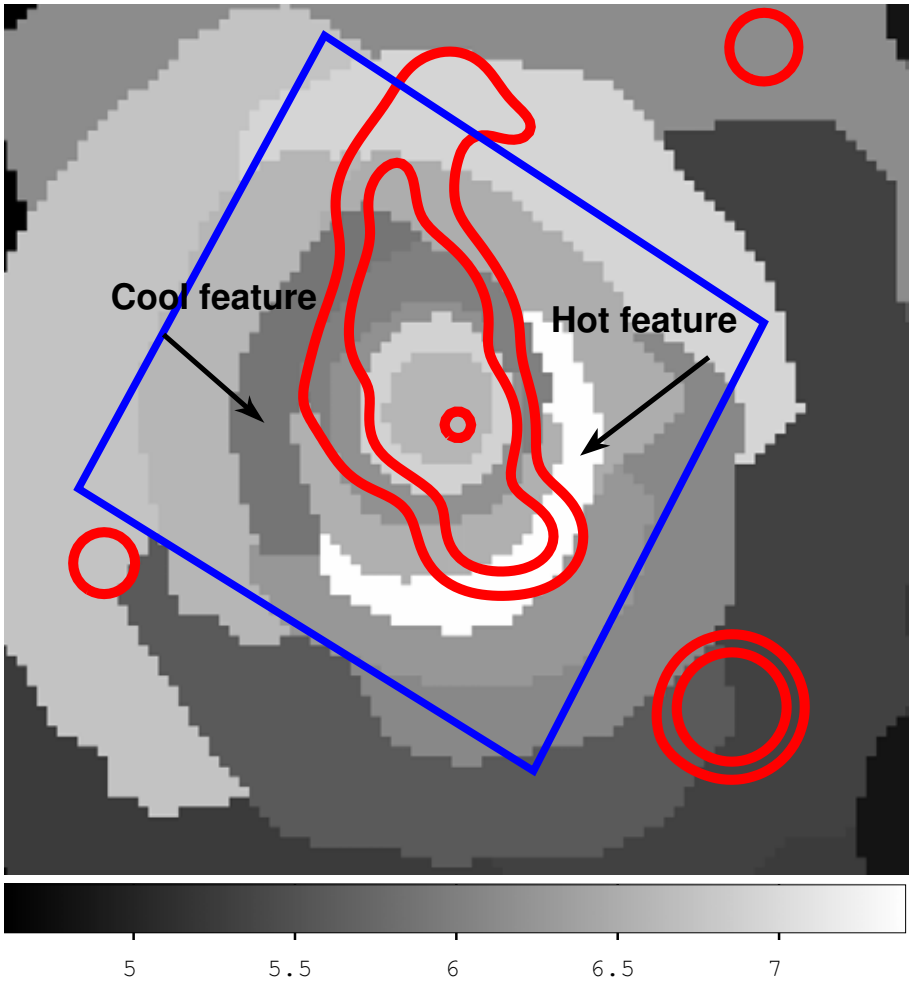

Figure 6.8: A 3364: Temperature map, kT, from XMM-Newton observations. The lighter regions correspond to higher temperatures. The luminosity density is overlaid in red contours. The ACS field of view is overlaid in blue.

significant, deeper optical data with multiple filters could greatly contribute to providing better constrained maps of the DM structure. Deeper X-ray observations are also required to study the disturbed ICM and the relationship of the hot and cold features with the underlying mass and luminosity distributions. *A* 3364 is an example of an 'extrema' cluster cheaply identified by this lensing pipeline using *HST* SNAPSHOT data, the weak lens analysis necessary to identify the anomalously offset and overmassive subpeak to the SW. The later indepth study of this cluster, and clusters like it, has the potential to improve our understanding of the interplay between baryons and DM.

6.2 Disentangling A 3192 from RXC J0358

6.2.1 Introduction

Early[1] galaxy cluster searches identified clusters as over-densities of galaxies on photographic plates (Abell, 1958; Abell et al., 1989), and have stimulated a rich legacy of cosmological and astrophysical research. The reliability of these catalogs is limited by the projection of multiple galaxy systems along the line-of-sight (Lucey, 1983, see also Ebeling et al. 1995). The importance of enhanced cluster discovery methods is therefore now well-established. Such methods include color-selection of the red-sequence of early-type galaxies (e.g. Gladders & Yee, 2000) and large-scale X-ray surveys (e.g. Ebeling et al., 1998, 2000; Böhringer et al., 2004a; Lloyd-Davies et al., 2010), both of which help to overcome projection effects.

The redshift of clusters at $z \gtrsim 0.3$ can be under-estimated due to the greater availability of spectroscopic identifications of galaxies at lower redshifts, and the absence of all-sky optical/near-infrared photometry of sufficient depth. For example, MACS J1149.5+2223 at z = 0.54 (Ebeling et al., 2007; Smith et al., 2009) was originally identified at z = 0.176 (Böhringer et al., 2000). Such misidentifications raise the question of whether the low redshift "interloper"

[1]The following section has been submitted as a letter to Astrophysical Journal Letters, and is undergoing peer review.

galaxies are isolated, or reside in a galaxy group or cluster. In the latter case, the rich multi-wavelength datasets available on galaxy clusters, including weak-lensing observations, creates the possibility of obtaining new and unexpected constraints on the masses of galaxy groups.

Reliable mass measurements of galaxy groups are of great interest because they would help to test the reliability of mass-observable scaling relations down to $\lesssim 10^{13} M_{\odot}$. However such measurements are challenging due to the relatively low contrast of galaxy groups over the local density field. Previous gravitational lensing studies of groups have therefore measured the mean group properties based on stacked analysis (Hoekstra et al., 2003; Mandelbaum et al., 2006; Leauthaud et al., 2010). However, Limousin et al. (2009) successfully detected a weak-lensing signal from 6 strong-lensing-selected groups, encouraging renewed effort to measure the mass of individual groups.

In this letter we present a joint weak-lensing/near-infrared study of Abell 3192 (hereafter A 3192). This optically-selected cluster (Abell et al., 1989) has been associated with galaxies spectroscopically identified at $z = 0.168$ (Way et al., 2005), and with RXC J0358.8–2955 (hereafter RXC J0358), an X-ray luminous cluster 2 arcmin East of the optical position (Böhringer et al., 2004a). Most recently, RXC J0358 has been added to the MACS cluster sample at $z = 0.425$ (Ebeling et al., 2010). The interpretation of Abell et al.'s original optical cluster identification is therefore ambiguous. Specifically, what are the relative contributions of the galaxy systems at $z = 0.168$ and $z = 0.425$ to the total mass and luminosity along this line-of-sight? We combine *Hubble Space Telescope (HST)* and ground-based near-infrared observations to answer this question.

In §2 we describe the observations and initial data analysis; §3 details the structural analysis and results, including gravitational lens models; our results are summarized in §4. We assume $H_0 = 70\,\mathrm{km\,s^{-1}\,Mpc^{-1}}$, $\Omega_{\mathrm{M}} = 0.3$ and $\Omega_{\Lambda} = 0.7$; in this cosmology $1''$ corresponds to 2.87kpc and 5.57kpc at $z = 0.168$ and $z = 0.425$ respectively. Galactic extinction towards A 3192 is negligible

(Schlegel et al., 1998). All magnitudes are calibrated to Vega.

6.2.2 Observations and Analysis

Optical Data

A 3192 was observed as part of the Local Cluster Substructure Survey (LoCuSS[2]) through the F606W filter (hereafter V_{606}) with the Advanced Camera for Surveys (ACS) on-board *HST*[3] on December 19, 2006 (PID:10881; PI: G. P. Smith). The observation was centered on a bright galaxy at $03^h58^m54^s$, $-29°55'31''$ (J2000), i.e. $54''$ East of the X-ray position of RXC J0358 (Böhringer et al., 2004a), and $3.4'$ South East of the optical position of A 3192 (Abell et al., 1989). The total observation of 1.2 ksec was split into three with a shift of $0.3''$ between each exposure. The data were reduced in a standard manner using MULTIDRIZZLE (Koekemoer et al., 2002) onto a final pixel scale of $0.03''$/pixel. Visual inspection of the reduced data (Fig. 6.9) reveals that the bright galaxy at the center of the frame is surrounded by a diffuse envelope of light and is coincident with the peak of the X-ray emission from RXC J0358 (see Figure 6 of Ebeling et al., 2010). We therefore interpret this galaxy as the brightest cluster galaxy (BCG) of RXC J0358. A pair of bright elliptical galaxies lie $41''$ South West of the BCG, suggesting that the cluster core may have a bi-modal structure. This is supported by the identification of two candidate triply-imaged background galaxies between the BCG and this galaxy pair – A1 and A2 in Fig. 6.9. This interpretation is based on the mirror symmetry in the morphology of both A1.1/A1.2 and A2.1/A2.2. Confirmation of our identification of A1.3 and A2.3 will require spectroscopy and/or detailed strong-lens modeling, both of which are beyond the scope of this study.

[2]http://www.sr.bham.ac.uk/locuss

[3]Based in part on observations with the NASA/ESA *Hubble Space Telescope* obtained at the Space Telescope Science Institute, which is operated by the Association of Universities for Research in Astronomy, Inc., under NASA contract NAS5-26555.

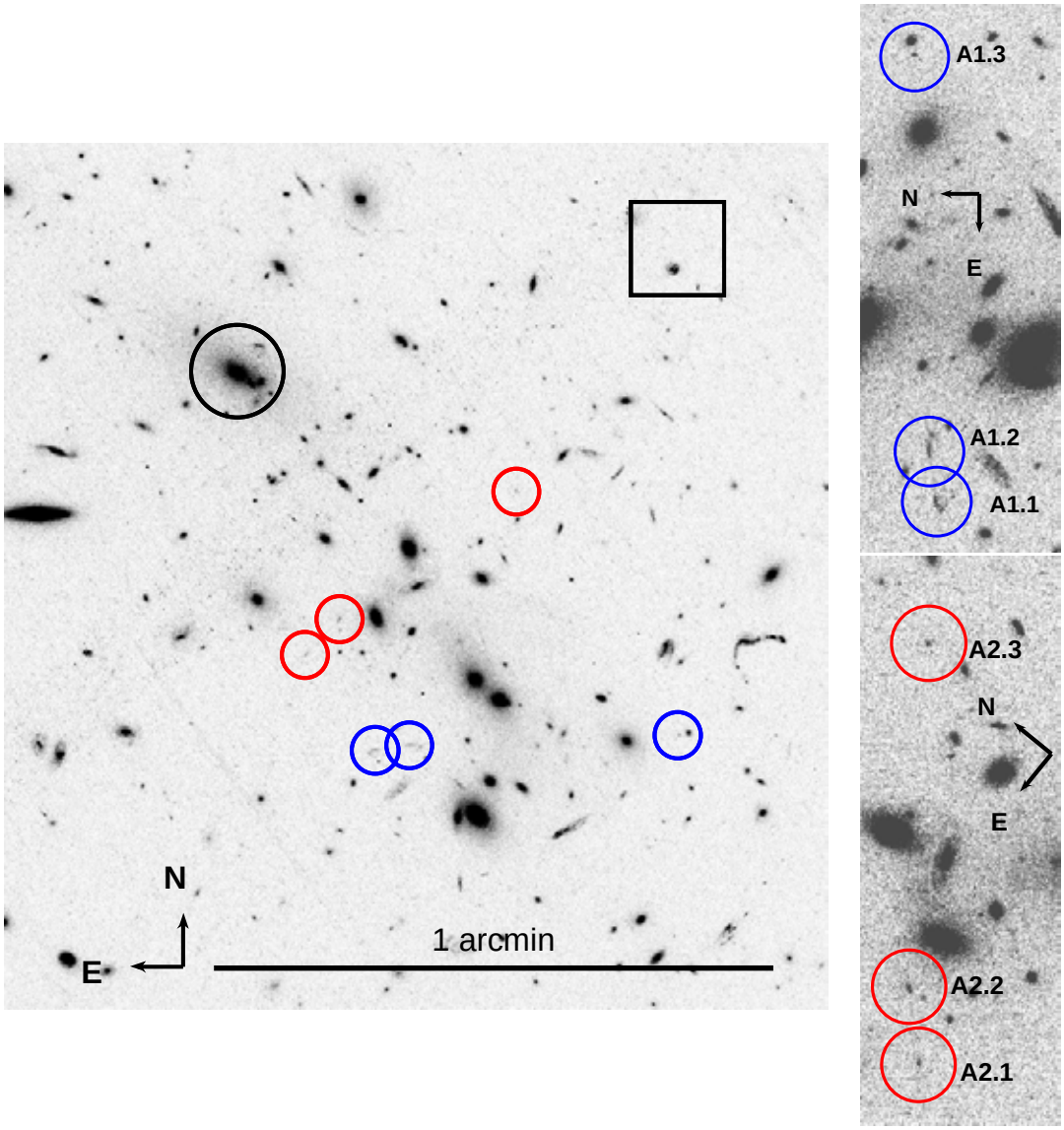

Figure 6.9: LEFT – *HST*/ACS V_{606} observation centered on the BCG of RXC J0358 (black circle) 54″ East of the X-ray position from Böhringer et al. (2004a, black square). Two candidate triply-imaged galaxies are marked by blue and red circles. North is up and East is left. RIGHT – Zooms into the candidate triply-imaged background galaxies identified at left.

The reduced ACS frame was analyzed with SEXTRACTOR (Bertin & Arnouts, 1996), extracting sources subtending > 5 contiguous pixels at 1.5σ/pixel above the local background, corresponding to $\mu_{606} = 23.0\,\mathrm{mag/arcsec^2}$. After removing objects within $5''$ of the edge of the frame, and adjacent to bright stars and their diffraction spikes, a total of 2630 sources remained. This sample is complete down to $V_{606} \simeq 26.5$. We then used IM2SHAPE[4] (Bridle et al., 2002) to fit a double Gaussian model to 21 bright, isolated, and unsaturated stars drawn from this photometric catalog. The results of these fits were used to construct a map of the spatial variation of the ACS point spread function (PSF) across the observed field of view. The average residual stellar ellipticity after subtraction of the PSF model were consistent with zero: $\langle\epsilon_1\rangle = (6.4 \pm 8.7) \times 10^{-3}$, $\langle\epsilon_2\rangle = (-5.1 \pm 8.8) \times 10^{-3}$. We also selected a sample of 1474 faint ($V_{606} > 22$) background galaxies, and fitted a single Gaussian model convolved with the PSF map to each of these galaxies. Galaxies with well-defined shape measurements ($\delta\epsilon < 0.15$) that subtend a minimum of two resolution elements were then retained for the weak-lensing analysis. The final sample comprised 473 galaxies, equating to a number density of $42\mathrm{arcmin}^{-2}$, the faintest galaxies at $V_{606} = 27.2$.

This faint galaxy sample is well-matched to similar samples used to constrain the mass distribution in galaxy clusters at $z \simeq 0.2$ (e.g. Okabe et al., 2010b). In the lens models described in §6.2.3 we therefore place the faint galaxies in a plane at $z_S = 1$. Experiments with $z_S = 0.8$ and $z_S = 1.2$ confirmed that these redshift uncertainties are not a dominant source of error in our results – they propagate to fractional uncertainties on best-fit model parameters of $\sim 3-9\%$ in §6.2.3. We also anticipate uncertainties in our weak-lensing analysis from the selection of background galaxies solely on apparent magnitude, which likely causes contamination by faint cluster galaxies, and thus dilution of the weak-lensing signal (Broadhurst et al., 2005). Indeed, the mass of X-ray luminous cluster cores may be under-estimated by a factor of ~ 2 if this dilution is left uncorrected (Okabe et al., 2010b). Resolution of this issue requires multi-filter weak-lensing observations. In the absence of such data we simply note that the projected masses calculated in §6.2.3 may be under-estimated by a factor of 2. Our conclusions are insensitive to

[4]http://www.sarahbridle.net/im2shape/

this uncertainty.

Near-infrared Data

A 3192 was also observed with ISPI on the CTIO Blanco 4-m telescope at Cerro Tololo Inter-American Observatory[5], in Febuary 2007 for 1020 seconds each in the J- and K-bands. The data were reduced using an automated pipeline of IRAF tasks to dark subtract, flat-field, align and co-add the individual frames. The astrometric and photometric calibration of the reduced frames are good to root mean square precisions of $0.1''$ and 0.1mags respectively, based on 2MASS[6] catalogs (Skrutskie et al., 2006). The reduced frames reach depths of $J(3\sigma) = 21.8$ and $K(3\sigma) = 20.3$, measured in apertures of diameter twice the full width half maximum (FWHM) of point sources: FWHM = $0.9''$ and $1.0''$ in the J- and K-bands respectively. These frames were analyzed individually with SEXTRACTOR, extracting sources subtending > 4 contiguous pixels above 1.5σ/pixel; each pixel subtends $0.3''$. The merged near-infrared photometric catalog comprises 468 extended sources down to $K = K^{\star}(z = 0.425) + 2 = 18.54$, all of which are detected in the J-band, and 149 of which are brighter than $K = K^{\star}(z = 0.168) + 2 = 16.75$, where $K^{\star}(z)$ is derived from Lin et al. (2006).

6.2.3 Results

Near-infrared Luminosity Density

The $(J-K)$ colors reveal two prominent "cluster red sequences" (Fig. 6.10), the colors of which are consistent with early-type galaxies at $z = 0.168$ and $z = 0.425$ (King & Ellis, 1985). Hereafter we refer to galaxies with colors of $1 < (J-K) < 1.4$ and $1.4 < (J-K) < 1.8$ as blue and

[5]Based in part on observations at the Cerro Tololo Inter-American Observatory, National Optical Astronomy Observatory, which are operated by the Association of Universities for Research in Astronomy, under contract with the National Science Foundation.

[6]This publication makes use of data products from the Two Micron All Sky Survey, which is a joint project of the University of Massachusetts and the Infrared Processing and Analysis Center/California Institute of Technology, funded by the National Aeronautics and Space Administration and the National Science Foundation.

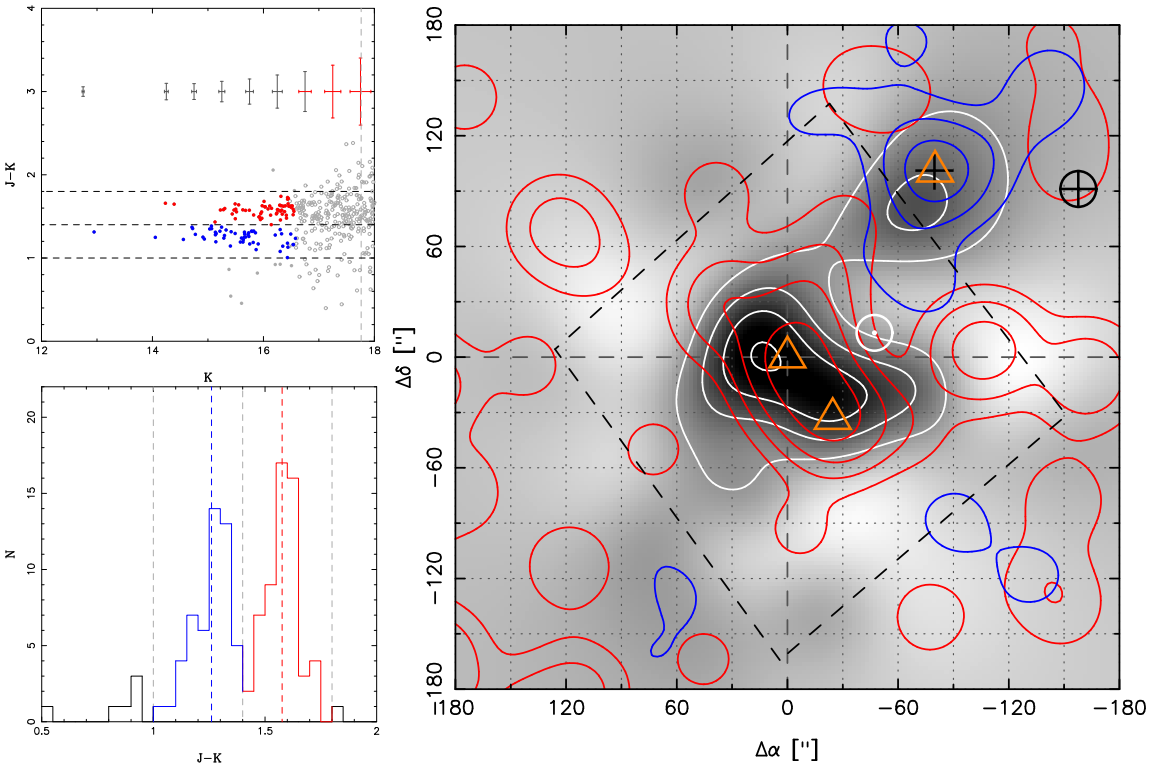

Figure 6.10: LEFT, TOP: $(J-K)/K$ color-magnitude diagram for extended sources detected in the CTIO/ISPI data. The red and blue points denote sources selected as lying in the red and blue peaks respectively in the histogram below. The error bars show the mean photometric uncertainty as a function of K-band magnitude, turning red at $\delta K > 0.1$ or $\delta(J-K) > 0.3$. LEFT, BOTTOM: Distribution of $(J-K)$ colors of galaxies detected at a signal-to-noise of $\sigma \geq 10$. The blue and red portions of the histogram are defined at $1 < (J-K) < 1.4$ and $1.4 < (J-K) < 1.8$ respectively. RIGHT: Multi-wavelength view of the $6' \times 6'$ field centered on the BCG of RXC J0358, showing as red and blue contours the K-band luminosity density of the red and blue galaxy populations selected from the panels at left. The projected total mass distribution reconstructed from the weak-lensing signal measured in the *HST*/ACS data is shown as the greyscale with white contours starting at 3σ significance, and spaced at 1σ). Black crosses mark the positions of galaxies with measured redshifts within 1000 km s^{-1} of $z = 0.168$. Orange triangles mark the positions of the three group/cluster-scale dark matter halos included in the LENSTOOL model of this cluster (§6.2.3). White and black circles mark the X-ray and optical positions of RXC J0358 and A 3192 respectively Böhringer et al. (2000); Abell et al. (1989)

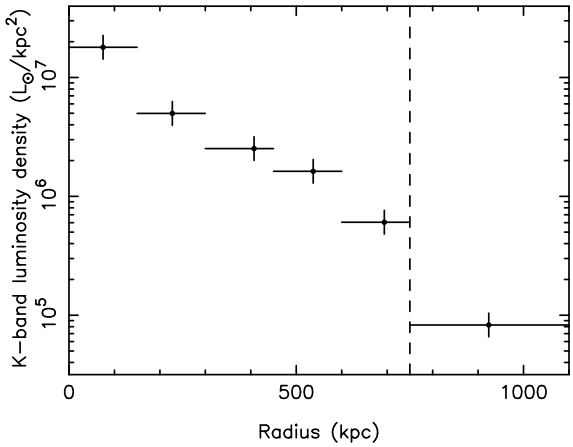

Figure 6.11: K-band luminosity density profile of galaxies on the red sequence at $z = 0.168$ – i.e. blue galaxies defined as $1 < (J-K) < 1.4$ in §6.2.3, down to $K < K^{\star}+2 = 16.75$. The profile is centered on the luminosity density peak of the blue galaxies. The vertical dashed line marks the outer edge of the outermost bin that has full coverage in our CTIO/ISPI data; the outermost bin has not been corrected for incomplete areal coverage. The data points are plotted at the mean radius of the galaxies in each bin, and the horizontal error bars show the width of the bins.

red galaxies respectively. Note that the near-infrared colors of galaxies at these redshifts are relatively insensitive to spectral type, with Sdm galaxies being just ~ 0.3 magnitudes bluer than E/S0 galaxies. Contamination of the blue (lower-redshift) galaxy sample by late-type galaxies at $z = 0.425$ is therefore negligible.

The luminosity density of red galaxies is centered on the BCG and bright elliptical galaxies in the core of RXC J0358. In contrast, the luminosity density of blue galaxies peaks on a bright $K = 12.91 \pm 0.02$ (equivalent to $5.5L_K^{\star}$) galaxy known to be at $z = 0.168$. The total K-band luminosity of the blue galaxies down to $K^{\star}+2$ at $z = 0.168$ within an aperture of radius 250kpc centered on this galaxy is $L_K = (2.0 \pm 0.2) \times 10^{12} L_{\odot}$. To correct statistically for contamination by non-members we applied the same selection function to randomly placed 250kpc apertures in the UKIDSS/DXS observations of the SWIRE ELAIS N1 field (Lawrence et al., 2007; Hambly et al., 2008), obtaining a corrected luminosity of $L_K = (1.9 \pm 0.3) \times 10^{12} L_{\odot}$. Following a similar procedure we also estimate the background corrected K-band luminosity of the central $R < 250$kpc of RXC J0358 to be $L_K = (6.6 \pm 1.0) \times 10^{12} L_{\odot}$. Finally, we note that the luminosity density of blue galaxies declines monotonically with projected distance from the brightest galaxy, confirming that this is an extended galaxy system and not an approximately uniform

sheet of galaxies (Fig. 6.11).

Abell et al. (1989) placed A 3192 in richness class 3. This classification requires revision in the light of our results. We therefore use our near-infrared photometry to estimate the richness of of the foreground group and RXC J0358 within the limits imposed by the solid-angle probed by the CTIO/ISPI data, and correcting statistically for contamination as discussed above. The resulting richness estimates of $R(< 750$ kpc) = 35 ± 8 and $R(< 1.5$ Mpc) = 63 ± 15 place the foreground group and RXC J0358 in richness classes 0 and 1 respectively.

Gravitational Lens Modeling

We now investigate the total mass distribution along the line-of-sight through A 3192. First, we reconstructed the projected mass density distribution using LENSENT2[7] – we refer the reader to Bridle et al. (1998) and Marshall et al. (2002) for details of this algorithm. In brief, the mass distribution was reconstructed onto a 256×256 grid of pixels spanning twice the *HST*/ACS field of view. The values of these pixels were constrained by the shapes of the background galaxies selected in §6.2.2, with a Gaussian intrinsic correlation function (ICF) of FWHM= $40''$. This ICF width (effectively the resolution of the resulting density map) yielded the highest Bayesian evidence, and therefore the most appropriate representation of the mass distribution given the data and choice of reconstruction grid. The resulting mass map is in excellent agreement with the optical/near-infrared results (§§6.2.2 & 6.2.3), i.e. the mass distribution is elongated along the axis that joins the BCG of RXC J0358 and the bright pair of elliptical galaxies to the South West, and a second density peak coincides with the blue luminosity density peak to the North-West, despite this peak lying outside the field of view of the *HST*/ACS observation (Fig. 6.10). These two structures are detected at peak signal-to-noise ratios of 6.2 and 4.4 respectively.

Encouraged by these detections, we used LENSTOOL[8] (Jullo et al., 2007) to fit models that

[7] http://www.slac.stanford.edu/ pjm/lensent/
[8] http://www.oamp.fr/cosmology/lenstool/

Table 6.3: Gravitational lens models

ID	N_h	$\frac{Pr(N_h)}{Pr(N_h=1)}$	χ^2_{red}	$\Delta\alpha$	$\Delta\delta$	Redshift	σ_0 (km/s)	M_{WL} [a] ($10^{14}M_\odot$)
A	1	1.0	0.9	$0''$	$0''$	0.425	810 ± 50	1.2 ± 0.1
B	2	1.5	0.9	$0''$	$0''$	0.425	710 ± 90	1.2 ± 0.2
				$-24''$	$-33''$	0.425	430 ± 150	
C	2	10.2	0.9	$0''$	$0''$	0.425	820 ± 50	1.2 ± 0.1
				$-80''$	$101''$	0.168	400 ± 90	0.3 ± 0.2
D	3	18.2	0.9	$0''$	$0''$	0.425	720 ± 80	1.2 ± 0.2
				$-24''$	$-33''$	0.425	450 ± 150	
				$-80''$	$101''$	0.168	400 ± 90	0.3 ± 0.2

[a] All masses are measured within an aperture of physical radius 250kpc, which corresponds to $87''$ and $45''$ when placed at $z = 0.168$ and $z = 0.425$ respectively. The mass of RXC J0358 is measured within an aperture centered on the BCG, and the mass of A 3192 is measured within an aperture centered on the peak of the luminosity density map of blue galaxies in Fig. 6.10. These apertures do not overlap.

describe the mass distribution as a superposition of parametrized dark matter halos, aiming to estimate the mass of each system. The first model comprises a single cluster-scale halo centered on the BCG of RXC J0358 at $z = 0.425$. This halo (and all other halos discussed below) is parameterized as a smoothly truncated pseudo isothermal elliptical mass distributions (PIEMD) following Kneib et al. (1996), with core radius and truncation radius fixed at 75kpc and 1000kpc respectively. This single-halo model fits the data well, with a best-fit central velocity dispersion of $\sigma_0 \simeq 800\mathrm{km/s}$ (Model A in Table 6.3). We then added a second halo in the core of RXC J0358, centered on the pair of elliptical galaxies $40''$ South West of the BCG. This model (Model B in Table 6.3) is statistically indistinguishable from Model A. However, if the second halo is centered on the blue luminosity density peak at $z = 0.168$, then the Bayesian evidence of a 2-halo model is $10\times$ greater than for the single halo model (Model C in Table 6.3). Interestingly, in this model, the foreground (blue) galaxy system has a central velocity dispersion of $\sigma_0 \simeq 400\mathrm{km/s}$ and a total projected mass of $M_{WL}(< 250\mathrm{kpc}) \simeq 3 \times 10^{13} M_\odot$ – i.e. a mass comparable with galaxy groups. Model D includes all three of the halos discussed above, in an attempt to describe both the bi-modal structure of RXC J0358 and the foreground galaxy group. Among the models tried, this model maximizes the probability of the data (Table 6.3).

We also added the candidate triply-imaged background galaxies, A1 and A2, as constraints on Models A-D, with the redshifts of these galaxies as free parameters, with a prior of $0.4 < z < 5$ on both. In this case, the probability of Model D exceeded that of all simpler models by at least a factor of 10^{14}. However, this model has $\chi^2_{red} = 2.4$ and the redshifts of the triply-imaged galaxies are not well-constrained: $z_{\rm A1} = 3.6 \pm 0.4$ and $z_{\rm A2}(2\sigma) \gtrsim 4.5$. We therefore do not explore the joint strong/weak-lensing constrained models further, except to say that they are qualitatively consistent with the weak-lensing models. Spectroscopic confirmation of A1 and A2 is essential to progress on these joint models.

In summary, the projected mass of the foreground galaxy group and RXC J0358 are estimated to be $M_{WL}(< 250{\rm kpc}) \sim (3^{+4}_{-2}) \times 10^{13} M_\odot$ and $M_{\rm WL}(< 250{\rm kpc}) = (1.2^{+1.2}_{-0.2}) \times 10^{14} M_\odot$ respectively, where the positive error bar includes both statistical (this section) and systematic (§6.2.2) errors. Combining these with the K-band luminosities from §6.2.3, we obtain total mass-to-light ratios of $M_{\rm WL}/L_K(< 250{\rm kpc}) = (16^{+21}_{-11}) M_\odot/L_\odot$ and $(17^{+17}_{-3}) M_\odot/L_\odot$ respectively. We also note that the mass of RXC J0358 is consistent with the typical mass of a strong-lensing cluster core (Richard et al., 2010).

Cross-check with archival *Chandra* data

We use the REXCESS mass-L_X relation (Pratt et al., 2009) to estimate the bolometric X-ray luminosity of the foreground galaxy group, obtaining $L_X \sim 6 \times 10^{42}$ erg s^{-1}. This is consistent with an independent estimate of $L_X \sim 10^{42} - 10^{43}$ erg s^{-1} derived from our richness estimate (§6.2.3) and Ledlow et al.'s (2003) richness-L_X relation. These luminosities imply an X-ray flux of $\sim 10^{-14} - 10^{-13}$ erg s^{-1} cm^{-2} at $z = 0.168$. A short (10ksec) observation of A 3192 is available in the *Chandra* archive (ObsID: 11719). We therefore use our flux estimate to predict the count rate in the $0.5 - 7.0$ keV band from the foreground group using WebPIMMS[9], obtaining $\lesssim 6 \times 10^{-3}$cts sec^{-1}, assuming an APEC model with a temperature in the range $1 - 3.4$ keV and

[9] http://heasarc.nasa.gov/Tools/w3pimms.html

an abundance of 0.4 solar. The predicted signal in the archival data is therefore $\lesssim 60$ counts – i.e. faint, and difficult to detect, especially against the background of the X-ray bright cluster RXC J0358. Nevertheless, we processed the *Chandra* data using CIAO v4.3, with CALDB v4.3, following the methods described in Sanderson et al. (2009). There is no obvious extended X-ray emission centered on the foreground group in these data. We therefore conclude that the archival *Chandra* data are consistent with our interpretation of the foreground system as a galaxy group at $z = 0.168$.

6.2.4 Summary

We have combined a *HST*/ACS snapshot observation with shallow near-infrared observations from the Blanco 4-m telescope to disassemble the original optical identification of A 3192 into the X-ray luminous cluster RXC J0358.8–2955 at $z = 0.425$ and a foreground galaxy group at $z = 0.168$. We detect two red sequences of early-type galaxies within a $10' \times 10'$ field of view centered on RXC J0358. The galaxies associated with the redder of the two sequences are co-located with RXC J0358, their color being consistent with the cluster redshift of $z = 0.425$. In contrast, the galaxies associated with the bluer of the two sequences are co-located with the original optical position of A 3192, their color being consistent with the redshift of $z = 0.168$ that was originally assigned to both A 3192 and RXC J0358. We therefore conclude that the original Abell cluster is comprised of two galaxy systems in projection, one at $z = 0.168$, and the other at $z = 0.425$ – i.e. RXC J0358.

We detect these two galaxy systems at 4.4σ and 6.2σ significance respectively in our weak-lensing analysis of the ACS snapshot data. The former detection is particularly striking, as the luminosity and mass peaks of the blue foreground system lie outside the field of view observed with ACS. The Bayesian evidence of weak-lensing-constrained mass models that include cluster/group-scale dark matter halos centered on both mass peaks exceed that of simpler models by a factor ≥ 10. We also estimate the mass of these two systems within projected radii of

250 kpc, obtaining $M_{WL}(z = 0.168) \simeq 3 \times 10^{13} M_{\odot}$ and $M_{WL}(z = 0.425) \simeq 1.2 \times 10^{14} M_{\odot}$. Combining these estimates with our near-infrared photometry, we estimate that the mass-to-light ratio of both is $M_{WL}/L_K \simeq 20 M_{\odot}/L_{\odot}$, consistent with previous measurements in groups and clusters (Kneib et al., 2003; Lin et al., 2006).

More broadly, our results highlight the important contributions that follow-up near-infrared and weak-lensing observations can make to the interpretation of cluster surveys. It is well-known that the n_e^2 dependence of the X-ray emissivity of intracluster gas gives X-ray surveys an important advantage in the discovery of massive clusters. Joint analysis of red sequences detected in near-infrared photometry and the mass density structure revealed by gravitational lensing observations is, however, critical to assigning galaxy systems projected along the same line-of-sight the correct redshifts and masses. These issues will be highly relevant to future cluster surveys including *eROSITA*.

Chapter 7

Summary

Galaxy clusters are unique laboratories for the study of the interplay between baryons and DM, and for constraining DM physics. Through the comparison of multiwavelength observations, it is possible to relate the dynamics of the gas, galaxies and Dark Matter, and explore the evolutionary history of structure formation in our Universe. However, each mass tracer, be it X-ray temperature or total cluster luminosity, relies on simplifying assumptions, such as hydrostatic equilibrium in X-ray analysis, or assuming mass follows light when using cluster luminosity. Using the impact of the gravitional potential of the cluster on images of background galaxies to measure the DM mass relies on gravitational physics, and avoids assumptions on the dynamical state of the cluster. However, the DM mass is sensitive to projection effects, and different modelling approaches require assumptions on the complexity of the underlying DM mass distribution, or external mass estimates to break the mass sheet degeneracy. In order to constrain cluster physics, these assumptions must be tested, and various degeneracies broken, by combining multiwavelength observations.

Scaling relations can be used to determine cluster masses from observables such as X-ray temperature and luminosity. Clusters lying on the same scaling relation can be assumed to have similar formation histories, and dynamical state can be seen in the structural segregation of scaling relations. Comparing different mass estimates from multiwavelength data can help normalise these relations and compensate for the impact of the assumptions used to generate the masses from different observables. Constraining scatter in scaling relations is also important for cluster cosmology, as the cluster mass function can be used to derive cosmological parameters such as ω and σ_8. Any scatter in the scaling relation used to obtain the cluster mass will translate

into uncertainty on the fitted parameters.

Studies on individual, 'extreme', clusters, are particular useful for determining how baryonic and DM interact. During cluster mergers, the differing behaviours of the galaxies, gas and DM are more obvious, as the gas undergoes shocks and heating, while the galaxies and DM act as collisionless particles. Mergers in the plane of the sky are particularly useful, as the offsets between each component is simpler to constrain, and can be used to determine the collisional cross section of the DM. On the other hand, some clusters undergoing multiple mergers appear to have subhaloes that have been stripped of their DM or galaxies, suggesting DM is not as collisionless as previously thought. These clusters provide a unique insight into the conflicting behaviours of the cluster components, differences that may not be apparant in the undisturbed distributions of relaxed clusters. However, these clusters are by their nature are very rare, and usually only discovered serendipitously.

The best prospects for assembling large samples of 'extreme' type clusters, obtaining rigorous statistics on structural segregation in scaling relations and obtaining constraints on cosmological parameters from clusters lies in large scale surveys. Studying the clustering of galaxies (baryonic acoustic oscillations, BAOs) and using weak lensing to constrain the DM structure of the Universe are among the goals of several future surveys. PANSTARRS (Kaiser et al., 2010), although aimed at detection and tracking of potential near earth hazards, will be repeatedly surveying large parts of the sky in multiple colour bands, lending itself to the study of Dark Energy via galaxy cluster WL. Both the Large Synoptic Survey Telescope (Ivezic et al., 2008) and the Dark Energy Survey (DES) (Flaugher, 2005; Sánchez & the Des collaboration, 2010) camera aim to survey thousands of square degrees of the southern sky, and among other goals use visible and near Infra-Red imaging to study Dark Energy, again via a combination of BAO and weak lens tomography. DES expects to image around 300 million galaxies, and provides constraints on the geometry of the Universe. EUCLID (Laureijs et al., 2010) is a proposed ESA space telescope, to perform a large scale survey of galaxies and clusters up to $z \sim 2$. The 20,000 square

degree wide field survey would allow for the study of the evolution of cosmic structures and Dark Energy. This telescope has been specifically optimised for weak lensing and BAO probes of DE. These future surveys are going to provide immense data volumes that will require years of analysis and processing time. Thus it is necessary to develop analysis pipelines capable of quickly processing and catagorising galaxy and cluster observations in order to generate subsamples for indepth study, and identify extrema that will impact any constraints obtained on Dark Energy.

This thesis aimed to explore the above goals by reconstructing the 2D spatial mass distributions of 19/21 cluster cores using weak lens analysis of *HST:ACS* SNAPSHOT observations, providing a quick and efficient method of obtaining initial science products from large cluster samples. The analysis involved reduction of the observations, correction of the PSF, construction of faint galaxy catalogues, analysis of the IR data and construction of cluster galaxy catalogues and a prior for the DM halo position, modelling using parameterised and non parameterised methods, and generation of projected WL masses and 2D maps of the projected mass distribution, X-ray surface brightness and IR luminosity density. The 2D spatial distributions and properties of the luminosity, gas and DM components of each cluster were then compared to determine the dynamical state and recent infall history of each cluster.

In § 4 we obtained constraints on the DM substructure complexity and spatial distribution using parameterised and non parameterised WL reconstruction methods. These included constraints on the offset between the peak of the mass distribution and the BCG, and mass substructure fractions, both indicators of assembly history in clusters. The analysis was more successful at constraining the spatial distribution of mass in the cluster core than the total mass itself. When the weak lens mass from the most likely LENSTOOL model, with individually optimised faint galaxy catalogue smoothing scales, was compared to the X-ray mass and X-ray temperature, there appeared to be a varying low mass bias across the sample. This bias appeared to become more consistent when the faint galaxy catalogues for each cluster were smoothed with the

same scale, indicating that the bias was due to the smoothing method. Models of cluster galaxy contamination of the faint galaxy catalogue were used to assess the possible impact of only selection faint galaxies using the magnitude in a single filter. Even in the most extreme model of the shear signal being diluted by a factor of a half, it was concluded that possible cluster galaxy contamination could not account for the entirety of the low mass bias. Thus the bias in the weak lens masses obtained in this analysis is believed to primarily an artifact of the smoothing of the faint galaxy shear catalogues. Assuming that by using a constant smoothing scale, the bias impacts each faint galaxy catalogue in the same way, we further assumed that this would only impact the normalisation of trends in the mass-observable scaling relations. This has allowed us to use these masses to explore segregation in such relations between cool core and non cool core clusters. However, these assumptions have yet to be tested with more rigorous analysis, something that would be applied in future refinements of the weak lens reconstruction pipeline, and thus the conclusions drawn from the scaling relation analysis should be treated with caution.

Comparison of multi-wavelength results for each the cluster individually in § 5 suggested that substructure in cool core clusters was more likely to be detected and constrained by the WL methods than substructure in the non cool core clusters, possibly due to cool core cluster substructure having simpler morphologies. The majority of the clusters in this sample are disturbed, based on their X-ray centroid-BCG offsets, and this analysis identified several 'extreme' clusters that could provide constraints on DM physics should they be studied with deeper X-ray and optical observations. Such identifications are necessary for larger scale surveys where populations of severly disturbed clusters, with properties strongly divergent from the expected scaling relations, could impact the generalised results obtained on the nature of Dark Energy.

The slope of the $M_{WL} - T_X$ and $M_{WL} - T_X$ relations are consistent with theory, while the WL mass appears to trend with K-band luminosity as it does with the X-ray luminosity. The cool core clusters appeared to follow a shallower relation with less scatter in each case, although the segregation in the mass-observable scaling relations is not significant. Comparison of the

substructure fraction distribution with JR10 suggests that the X-ray luminosity selected cluster sample is drawn from the same underlying cluster population as the SL selected cluster sample. Our fit to the positive correlation between the logged slope of the gas density, α, and mass substructure fraction, is consistent with the result in JR10, albeit at a lower significance of 2σ. Finally, we discussed the offset between the mass distribution and the BCG, and found that beyond an X-ray centroid to BCG offset $10-15$kpc there was a positive correlation between the mass and X-ray offsets, however the large errors on the peak position of the DM mass distribution from LENSENT means that such a relation could not be constrained using the results of this analysis, 4/5 of clusters with mass peak positions consistent with the BCG position had bimodal mass distributions in their cores, suggesting a better comparison would use the mass centroid position. We conclude that the constraints on position from LENSENT and on the weak lens mass from LENSTOOL are not very strong, and would benefit from improvements not only to the analysis pipeline, such as reviewing the shear catalogue smoothing, but also to the underlying data set, as colour data would allow for the construction of an uncontaminated weak shear catalogue.

Two clusters were selected for in depth analysis. The mass distribution for A 3364, which exhibited a disturbed X-ray morphology focused on the BCG and a bright peak in the luminosity to the NE, was found to be primarily associated with a dimmer galaxy subpeak in the SW, a result conclusively supported by the Bayesian statistics of the IR prior motivated models (§ 6.1). Comparison of constraints on the Bullet Cluster mass subpeak position with the literature conservatively suggested that the non parameterised analysis of A 3364 was not able to significantly confirm such an offset. However when alternative priors are invoked based on NIR or X-ray data, the data strongly supports the SW position, demonstrating the important of the inclusion of multi-wavelength data in this analysis. In A 3192, a foreground group outside the ACS field of view is detected via both LENSENT2 and LENSTOOL WL analysis (§ 6.2). The analysis of the shear signal in this observation demonstrated the ability of the WL pipeline to reconstruct the DM distribution on a large range of mass scales. Both of these clusters will be the subjects of short papers, with the paper on A 3192 already submitted for review.

7.1 Future Prospects

The work in this thesis has great potential for future refinement and improvement. Within the pipeline itself, the IR priors on DM halo positions would benefit from an automated cluster galaxy Red Sequence fitting and extraction, possibly with the addition of cluster galaxy redshifts from spectroscopy, while aperture mass densitometry could be used to provide a weak lens prior for the parameterised modelling. Multi-filter SNAPSHOT observations would reduce the impact of cluster contamination in the faint galaxy shear catalogues, resulting in tighter constraints on the weak lens masses, while the PSF models and CTE corrections of Rhodes et al. (2007) could reduce the instrument induced error in the shear. The smoothing algorithm used to prepare the faint galaxy catalogues for the parameterised modelling is clearly biasing the mass low, and future work will be performed to identify the cause of this and remove this systematic error. Finally, the interpretation of cluster structure formation history from the galaxy, gas and DM map comparison would benefit from other multiwavelength data, such as spectroscopy to better interpret the dynamics in projection, and better references to the literature.

Additionally, this analysis has focussed on obtaining a significant shear signal for weak lens analysis from shallow, noisy data. Such an approach is ideally placed to take advantage of the masses of archival data from not only the Hubble Space Telescope, but also imaging data from ground based telescopes, which can also achieve the $20-40$ galaxies per square arcminute of the SNAPSHOT data. A large scale analysis of archival data would allow for the identification of cluster samples suited to probing different science goals, such as mergers or cooling flows in relaxed systems. As the Hubble Space Telescope comes to the end of it's operating life, and with financial concerns over the future of the James Webb Telescope, such streamlined samples would have an advantage in proposals competing for ever more valuable telescope time.

This thesis has the described the multi-wavelength analysis of 21 cluster cores, and the

efforts to constrain the DM distribution using a combination of lensing methods and multi-wavelength priors. We have successfully modelled the spatial structure for 19 of these clusters, and drawn conclusions on their thermal assembly histories. Despite a low mass bias in the reconstructed WL masses we have explored segregation in the mass-observable scaling relations, and confirmed that our results agree with the theoretical models. We have found that mass structural properties such as substructure are correlated to X-ray profile and distribution offset. In depth studies have demonstrated the ability of this thesis work to constrain the spatial mass distribution of cluster to group scale structures, efficiently identify 'extreme' clusters for future study that can provide insight into the physics of DM. Finally, the work described here has potential applications to the analysis of large scale survey products, in order to quickly catagorise clusters for subsample studies and aid in the research to constrain the geometry of our Universe, Dark Matter and Dark Energy.

References

Abell, G. O. 1958, ApJS, 3, 211

Abell, G. O., Corwin, Jr., H. G., & Olowin, R. P. 1989, ApJS, 70, 1

Allen, S. 2002, in HST Proposal, 9270–+

Allen, S. W. 1998, MNRAS, 296, 392

Bahcall, N. A. 1999, in Formation of Structure in the Universe, ed. A. Dekel & J. P. Ostriker, 135–+

Bartelmann, M. 2010, Reviews of Modern Physics, 82, 331

Bartelmann, M., Narayan, R., Seitz, S., & Schneider, P. 1996, ApJ, 464, L115+

Bartelmann, M. & Schneider, P. 2001, Phys. Rep., 340, 291

Bennett, C. L., Bay, M., Halpern, M., Hinshaw, G., Jackson, C., Jarosik, N., Kogut, A., Limon, M., Meyer, S. S., Page, L., Spergel, D. N., Tucker, G. S., Wilkinson, D. T., Wollack, E., & Wright, E. L. 2003a, ApJ, 583, 1

Bennett, C. L., Halpern, M., Hinshaw, G., Jarosik, N., Kogut, A., Limon, M., Meyer, S. S., Page, L., Spergel, D. N., Tucker, G. S., Wollack, E., Wright, E. L., Barnes, C., Greason, M. R., Hill, R. S., Komatsu, E., Nolta, M. R., Odegard, N., Peiris, H. V., Verde, L., & Weiland, J. L. 2003b, ApJS, 148, 1

Bertin, E. & Arnouts, S. 1996, A&AS, 117, 393

Boggs, P. T., Donaldson, J. R., Byrd, R. h., & Schnabel, R. B. 1989, ACM Trans. Math. Softw., 15, 348

Böhringer, H., Schuecker, P., Guzzo, L., Collins, C. A., Voges, W., Cruddace, R. G., Ortiz-Gil, A., Chincarini, G., De Grandi, S., Edge, A. C., MacGillivray, H. T., Neumann, D. M., Schindler, S., & Shaver, P. 2004a, A&A, 425, 367

—. 2004b, A&A, 425, 367

Böhringer, H., Voges, W., Huchra, J. P., McLean, B., Giacconi, R., Rosati, P., Burg, R., Mader, J., Schuecker, P., Simiç, D., Komossa, S., Reiprich, T. H., Retzlaff, J., & Trümper, J. 2000, ApJS, 129, 435

Borgani, S., Murante, G., Springel, V., Diaferio, A., Dolag, K., Moscardini, L., Tormen, G., Tornatore, L., & Tozzi, P. 2004, MNRAS, 348, 1078

Bouwens, R. J., Illingworth, G. D., Labbe, I., Oesch, P. A., Trenti, M., Carollo, C. M., van Dokkum, P. G., Franx, M., Stiavelli, M., González, V., Magee, D., & Bradley, L. 2011, Nature, 469, 504

Bradač, M. 2004, in Baryons in Dark Matter Halos, ed. R. Dettmar, U. Klein, & P. Salucci

Bradač, M., Allen, S. W., Treu, T., Ebeling, H., Massey, R., Morris, R. G., von der Linden, A., & Applegate, D. 2008, ApJ, 687, 959

Bradač, M., Clowe, D., Gonzalez, A. H., Marshall, P., Forman, W., Jones, C., Markevitch, M., Randall, S., Schrabback, T., & Zaritsky, D. 2006, ApJ, 652, 937

Bradač, M., Lombardi, M., & Schneider, P. 2004a, A&A, 424, 13

Bradač, M., Schneider, P., Lombardi, M., & Erben, T. 2004b, ArXiv Astrophysics e-prints

Bridle, S., Kneib, J.-P., Bardeau, S., & Gull, S. 2002, in The shapes of galaxies and their dark halos, Proceedings of the Yale Cosmology Workshop ”The Shapes of Galaxies and Their Dark Matter Halos”, New Haven, Connecticut, USA, 28-30 May 2001. Edited by Priyamvada Natarajan. Singapore: World Scientific, 2002, ISBN 9810248482, p.38, ed. P. Natarajan, 38–+

Bridle, S. L., Hobson, M. P., Lasenby, A. N., & Saunders, R. 1998, MNRAS, 299, 895

Broadhurst, T., Takada, M., Umetsu, K., Kong, X., Arimoto, N., Chiba, M., & Futamase, T. 2005, ApJ, 619, L143

Brodwin, M., Stern, D., Vikhlinin, A., Stanford, S. A., Gonzalez, A. H., Eisenhardt, P. R., Ashby, M. L. N., Bautz, M., Dey, A., Forman, W. R., Gettings, D., Hickox, R. C., Jannuzi, B. T., Jones, C., Mancone, C., Miller, E. D., Moustakas, L. A., Ruel, J., Snyder, G., & Zeimann, G. 2011, ApJ, 732, 33

Cacciato, M., Bartelmann, M., Meneghetti, M., & Moscardini, L. 2006, A&A, 458, 349

Clowe, D., Bradač, M., Gonzalez, A. H., Markevitch, M., Randall, S. W., Jones, C., & Zaritsky, D. 2006, ApJ, 648, L109

Clowe, D., De Lucia, G., & King, L. 2004a, MNRAS, 350, 1038

Clowe, D., Gonzalez, A., & Markevitch, M. 2004b, ApJ, 604, 596

Clowe, D., Luppino, G. A., Kaiser, N., Henry, J. P., & Gioia, I. M. 1998, ApJ, 497, L61+

Corless, V. L. & King, L. J. 2007, MNRAS, 380, 149

Czoske, O., Kneib, J.-P., Soucail, G., Bridges, T. J., Mellier, Y., & Cuillandre, J.-C. 2001, A&A, 372, 391

Czoske, O., Moore, B., Kneib, J., & Soucail, G. 2002, A&A, 386, 31

Demarco, R., Wilson, G., Muzzin, A., Lacy, M., Surace, J., Yee, H. K. C., Hoekstra, H., Blindert, K., & Gilbank, D. 2010, ApJ, 711, 1185

Dressler, A., Oemler, A. J., Couch, W. J., Smail, I., Ellis, R. S., Barger, A., Butcher, H., Poggianti, B. M., & Sharples, R. M. 1997, ApJ, 490, 577

Ebeling, H., Barrett, E., Donovan, D., Ma, C.-J., Edge, A. C., & van Speybroeck, L. 2007, ApJ, 661, L33

Ebeling, H., Edge, A. C., Allen, S. W., Crawford, C. S., Fabian, A. C., & Huchra, J. P. 2000, MNRAS, 318, 333

Ebeling, H., Edge, A. C., Böhringer, H., Allen, S. W., Crawford, C. S., Fabian, A. C., Voges, W., & Huchra, J. P. 1998, MNRAS, 301, 881

Ebeling, H., Edge, A. C., Mantz, A., Barrett, E., Henry, J. P., Ma, C. J., & van Speybroeck, L. 2010, MNRAS, 407, 83

Ebeling, H., Mendes de Oliveira, C., & White, D. A. 1995, MNRAS, 277, 1006

Eisenstein, D. J., Zehavi, I., Hogg, D. W., Scoccimarro, R., Blanton, M. R., Nichol, R. C., Scranton, R., Seo, H.-J., Tegmark, M., Zheng, Z., Anderson, S. F., Annis, J., Bahcall, N., Brinkmann, J., Burles, S., Castander, F. J., Connolly, A., Csabai, I., Doi, M., Fukugita, M., Frieman, J. A., Glazebrook, K., Gunn, J. E., Hendry, J. S., Hennessy, G., Ivezić, Z., Kent, S., Knapp, G. R., Lin, H., Loh, Y.-S., Lupton, R. H., Margon, B., McKay, T. A., Meiksin, A., Munn, J. A., Pope, A., Richmond, M. W., Schlegel, D., Schneider, D. P., Shimasaku, K., Stoughton, C., Strauss, M. A., SubbaRao, M., Szalay, A. S., Szapudi, I., Tucker, D. L., Yanny, B., & York, D. G. 2005, ApJ, 633, 560

Evrard, A. E., Metzler, C. A., & Navarro, J. F. 1996, ApJ, 469, 494

Evrard, A. E., Mohr, J. J., Fabricant, D. G., & Geller, M. J. 1993, ApJ, 419, L9+

Fabian, A. C. 1994, ARA&A, 32, 277

Fahlman, G., Kaiser, N., Squires, G., & Woods, D. 1994, ApJ, 437, 56

Falco, E. E., Gorenstein, M. V., & Shapiro, I. I. 1985, ApJ, 289, L1

Finoguenov, A., Reiprich, T. H., & Böhringer, H. 2001, A&A, 368, 749

Flaugher, B. 2005, International Journal of Modern Physics A, 20, 3121

Forman, W., Kellogg, E., Gursky, H., Tananbaum, H., & Giacconi, R. 1972, ApJ, 178, 309

Freedman, W. L., Madore, B. F., Gibson, B. K., Ferrarese, L., Kelson, D. D., Sakai, S., Mould, J. R., Kennicutt, Jr., R. C., Ford, H. C., Graham, J. A., Huchra, J. P., Hughes, S. M. G., Illingworth, G. D., Macri, L. M., & Stetson, P. B. 2001, ApJ, 553, 47

Friedman, A. 1922, Zeitschrift fÃijr Physik A Hadrons and Nuclei, 10, 377, 10.1007/BF01332580

Friedmann, A. 1924, Zeitschrift fur Physik, 21, 326

Gavazzi, R. 2005, A&A, 443, 793

Gilbank, D. G., Gladders, M. D., Yee, H. K. C., & Hsieh, B. C. 2011, AJ, 141, 94

Gladders, M. D. 2004, in Clusters of Galaxies: Probes of Cosmological Structure and Galaxy Evolution, ed. J. S. Mulchaey, A. Dressler, & A. Oemler, 89–+

Gladders, M. D. & Yee, H. K. C. 2000, AJ, 120, 2148

—. 2005, ApJS, 157, 1

Gursky, H., Solinger, A., Kellogg, E. M., Murray, S., Tananbaum, H., Giacconi, R., & Cavaliere, A. 1972, ApJ, 173, L99+

Haines, C. P., Smith, G. P., Egami, E., Ellis, R. S., Moran, S. M., Sanderson, A. J. R., Merluzzi, P., Busarello, G., & Smith, R. J. 2009, ApJ, 704, 126

Haines, C. P., Smith, G. P., Pereira, M. J., Egami, E., Moran, S. M., Hardegree-Ullman, E., Rawle, T. D., & Rex, M. 2010, A&A, 518, L19+

Hambly, N. C., Collins, R. S., Cross, N. J. G., Mann, R. G., Read, M. A., Sutorius, E. T. W., Bond, I., Bryant, J., Emerson, J. P., Lawrence, A., Rimoldini, L., Stewart, J. M., Williams, P. M., Adamson, A., Hirst, P., Dye, S., & Warren, S. J. 2008, MNRAS, 384, 637

Hernquist, L. 1990, ApJ, 356, 359

Heymans, C., Van Waerbeke, L., Bacon, D., Berge, J., Bernstein, G., Bertin, E., Bridle, S., Brown, M. L., Clowe, D., Dahle, H., Erben, T., Gray, M., Hetterscheidt, M., Hoekstra, H., Hudelot, P., Jarvis, M., Kuijken, K., Margoniner, V., Massey, R., Mellier, Y., Nakajima, R., Refregier, A., Rhodes, J., Schrabback, T., & Wittman, D. 2006, MNRAS, 368, 1323

Hinshaw, G., Nolta, M. R., Bennett, C. L., Bean, R., Doré, O., Greason, M. R., Halpern, M., Hill, R. S., Jarosik, N., Kogut, A., Komatsu, E., Limon, M., Odegard, N., Meyer, S. S., Page, L., Peiris, H. V., Spergel, D. N., Tucker, G. S., Verde, L., Weiland, J. L., Wollack, E., & Wright, E. L. 2007, ApJS, 170, 288

Hinshaw, G., Weiland, J. L., Hill, R. S., Odegard, N., Larson, D., Bennett, C. L., Dunkley, J., Gold, B., Greason, M. R., Jarosik, N., Komatsu, E., Nolta, M. R., Page, L., Spergel, D. N., Wollack, E., Halpern, M., Kogut, A., Limon, M., Meyer, S. S., Tucker, G. S., & Wright, E. L. 2009, ApJS, 180, 225

Hoekstra, H. 2003, MNRAS, 339, 1155

Hoekstra, H., Franx, M., Kuijken, K., Carlberg, R. G., & Yee, H. K. C. 2003, MNRAS, 340, 609

Hoekstra, H., Franx, M., Kuijken, K., Carlberg, R. G., Yee, H. K. C., Lin, H., Morris, S. L., Hall, P. B., Patton, D. R., Sawicki, M., & Wirth, G. D. 2001, ApJ, 548, L5

Hoekstra, H., Yee, H. K. C., & Gladders, M. D. 2004, ApJ, 606, 67

Hubble, E. 1929, Proceedings of the National Academy of Science, 15, 168

Ivezic, Z., Tyson, J. A., Acosta, E., Allsman, R., Anderson, S. F., Andrew, J., Angel, R., Axelrod, T., Barr, J. D., Becker, A. C., Becla, J., Beldica, C., Blandford, R. D., Bloom, J. S., Borne, K., Brandt, W. N., Brown, M. E., Bullock, J. S., Burke, D. L., Chandrasekharan, S., Chesley, S., Claver, C. F., Connolly, A., Cook, K. H., Cooray, A., Covey, K. R., Cribbs, C., Cutri, R., Daues, G., Delgado, F., Ferguson, H., Gawiser, E., Geary, J. C., Gee, P., Geha, M., Gibson, R. R., Gilmore, D. K., Gressler, W. J., Hogan, C., Huffer, M. E., Jacoby, S. H., Jain,

B., Jernigan, J. G., Jones, R. L., Juric, M., Kahn, S. M., Kalirai, J. S., Kantor, J. P., Kessler, R., Kirkby, D., Knox, L., Krabbendam, V. L., Krughoff, S., Kulkarni, S., Lambert, R., Levine, D., Liang, M., Lim, K., Lupton, R. H., Marshall, P., Marshall, S., May, M., Miller, M., Mills, D. J., Monet, D. G., Neill, D. R., Nordby, M., O'Connor, P., Oliver, J., Olivier, S. S., Olsen, K., Owen, R. E., Peterson, J. R., Petry, C. E., Pierfederici, F., Pietrowicz, S., Pike, R., Pinto, P. A., Plante, R., Radeka, V., Rasmussen, A., Ridgway, S. T., Rosing, W., Saha, A., Schalk, T. L., Schindler, R. H., Schneider, D. P., Schumacher, G., Sebag, J., Seppala, L. G., Shipsey, I., Silvestri, N., Smith, J. A., Smith, R. C., Strauss, M. A., Stubbs, C. W., Sweeney, D., Szalay, A., Thaler, J. J., Vanden Berk, D., Walkowicz, L., Warner, M., Willman, B., Wittman, D., Wolff, S. C., Wood-Vasey, W. M., Yoachim, P., Zhan, H., & for the LSST Collaboration. 2008, ArXiv e-prints

Jain, B., Jarvis, M., & Bernstein, G. 2006, Journal of Cosmology and Astro-Particle Physics, 2, 1

Jarvis, M., Bernstein, G., & Jain, B. 2004, MNRAS, 352, 338

Jarvis, M. & Jain, B. 2004, ArXiv Astrophysics e-prints

Jee, M. J., Rosati, P., Ford, H. C., Dawson, K. S., Lidman, C., Perlmutter, S., Demarco, R., Strazzullo, V., Mullis, C., Böhringer, H., & Fassbender, R. 2009, ApJ, 704, 672

Jeffreys, H. 1961, Theory of probability / by Harold Jeffreys, 3rd edn. (Clarendon Press, Oxford :), viii, 447 p. :

Jing, Y. P. & Suto, Y. 2000, ApJ, 529, L69

Jones, C. 2004, in HST Proposal, 10200–+

Jullo, E., Kneib, J.-P., Limousin, M., Elíasdóttir, Á., Marshall, P. J., & Verdugo, T. 2007, New Journal of Physics, 9, 447

Kaiser, N. 1986, MNRAS, 222, 323

—. 1995, ApJ, 439, L1

Kaiser, N., Burgett, W., Chambers, K., Denneau, L., Heasley, J., Jedicke, R., Magnier, E., Morgan, J., Onaka, P., & Tonry, J. 2010, in Society of Photo-Optical Instrumentation Engineers (SPIE) Conference Series, Vol. 7733, Society of Photo-Optical Instrumentation Engineers (SPIE) Conference Series

Kaiser, N. & Squires, G. 1993, ApJ, 404, 441

Kassiola, A. & Kovner, I. 1993, ApJ, 417, 450

Kauffmann, G., Heckman, T. M., White, S. D. M., Charlot, S., Tremonti, C., Peng, E. W., Seibert, M., Brinkmann, J., Nichol, R. C., SubbaRao, M., & York, D. 2003, MNRAS, 341, 54

King, C. R. & Ellis, R. S. 1985, ApJ, 288, 456

King, L. J., Clowe, D. I., & Schneider, P. 2002, A&A, 383, 118

King, L. J., Schneider, P., & Springel, V. 2001, A&A, 378, 748

Kneib, J.-P., Ellis, R. S., Santos, M. R., & Richard, J. 2004, ApJ, 607, 697

Kneib, J.-P., Ellis, R. S., Smail, I., Couch, W. J., & Sharples, R. M. 1996, ApJ, 471, 643

Kneib, J.-P., Hudelot, P., Ellis, R. S., Treu, T., Smith, G. P., Marshall, P., Czoske, O., Smail, I., & Natarajan, P. 2003, ApJ, 598, 804

Kochanek, C. S. 1990, MNRAS, 247, 135

—. 2004, ArXiv Astrophysics e-prints

Koekemoer, A. M., Fruchter, A. S., Hook, R. N., & Hack, W. 2002, in The 2002 HST Calibration Workshop : Hubble after the Installation of the ACS and the NICMOS Cooling System, Proceedings of a Work shop held at the Space Telescope Science Institute, Baltimore, Maryland, October 17 and 18, 2002. Edited by Santiago Arribas, Anton Koekemoer , and Brad Whitmore. Baltimore, MD: Space Telescope Science Institute, 2002., p.337, ed. S. Arribas, A. Koekemoer, & B. Whitmore, 337–+

Komatsu, E., Dunkley, J., Nolta, M. R., Bennett, C. L., Gold, B., Hinshaw, G., Jarosik, N., Larson, D., Limon, M., Page, L., Spergel, D. N., Halpern, M., Hill, R. S., Kogut, A., Meyer, S. S., Tucker, G. S., Weiland, J. L., Wollack, E., & Wright, E. L. 2009, ApJS, 180, 330

Kormann, R., Schneider, P., & Bartelmann, M. 1994, A&A, 284, 285

Laureijs, R. J., Duvet, L., Escudero Sanz, I., Gondoin, P., Lumb, D. H., Oosterbroek, T., & Saavedra Criado, G. 2010, in Society of Photo-Optical Instrumentation Engineers (SPIE) Conference Series, Vol. 7731, Society of Photo-Optical Instrumentation Engineers (SPIE) Conference Series

Lawrence, A., Warren, S. J., Almaini, O., Edge, A. C., Hambly, N. C., Jameson, R. F., Lucas, P., Casali, M., Adamson, A., Dye, S., Emerson, J. P., Foucaud, S., Hewett, P., Hirst, P., Hodgkin, S. T. ., Irwin, M. J., Lodieu, N., McMahon, R. G., Simpson, C., Smail, I., Mortlock, D., & Folger, M. 2007, MNRAS, 379, 1599

Leauthaud, A., Finoguenov, A., Kneib, J., Taylor, J. E., Massey, R., Rhodes, J., Ilbert, O., Bundy, K., Tinker, J., George, M. R., Capak, P., Koekemoer, A. M., Johnston, D. E., Zhang, Y., Cappelluti, N., Ellis, R. S., Elvis, M., Giodini, S., Heymans, C., Le Fèvre, O., Lilly, S., McCracken, H. J., Mellier, Y., Réfrégier, A., Salvato, M., Scoville, N., Smoot, G., Tanaka, M., Van Waerbeke, L., & Wolk, M. 2010, ApJ, 709, 97

Ledlow, M. J., Voges, W., Owen, F. N., & Burns, J. O. 2003, AJ, 126, 2740

Limousin, M., Cabanac, R., Gavazzi, R., Kneib, J., Motta, V., Richard, J., Thanjavur, K., Foex, G., Pello, R., Crampton, D., Faure, C., Fort, B., Jullo, E., Marshall, P., Mellier, Y., More, A., Soucail, G., Suyu, S., Swinbank, M., Sygnet, J., Tu, H., Valls-Gabaud, D., Verdugo, T., & Willis, J. 2009, A&A, 502, 445

Limousin, M., Kneib, J., & Natarajan, P. 2005, MNRAS, 356, 309

Limousin, M., Kneib, J. P., Bardeau, S., Natarajan, P., Czoske, O., Smail, I., Ebeling, H., & Smith, G. P. 2007a, A&A, 461, 881

Limousin, M., Richard, J., Jullo, E., Kneib, J.-P., Fort, B., Soucail, G., Elíasdóttir, Á., Natarajan, P., Ellis, R. S., Smail, I., Czoske, O., Smith, G. P., Hudelot, P., Bardeau, S., Ebeling, H., Egami, E., & Knudsen, K. K. 2007b, ApJ, 668, 643

Lin, Y.-T. & Mohr, J. J. 2004, ApJ, 617, 879

Lin, Y.-T., Mohr, J. J., Gonzalez, A. H., & Stanford, S. A. 2006, ApJ, 650, L99

Lin, Y.-T., Mohr, J. J., & Stanford, S. A. 2003, ApJ, 591, 749

—. 2004, ApJ, 610, 745

Lloyd-Davies, E. J., Romer, A. K., Hosmer, M., Mehrtens, N., Davidson, M., Sabirli, K., Mann, R. G., Hilton, M., Liddle, A. R., Viana, P. T. P., Campbell, H. C., Collins, C. A., Dubois, E. N., Freeman, P., Hoyle, B., Kay, S. T., Kuwertz, E., Miller, C. J., Nichol, R. C., Sahlen, M., Stanford, S. A., & Stot t, J. P. 2010, ArXiv e-prints

Lombardi, M. & Bertin, G. 1999a, A&A, 348, 38

—. 1999b, A&A, 342, 337

Lucey, J. R. 1983, MNRAS, 204, 33

Mahdavi, A., Hoekstra, H., Babul, A., Balam, D. D., & Capak, P. L. 2007, ApJ, 668, 806

Mahdavi, A., Hoekstra, H., Babul, A., & Henry, J. P. 2008, MNRAS, 384, 1567

Mandelbaum, R., Seljak, U., Cool, R. J., Blanton, M., Hirata, C. M., & Brinkmann, J. 2006, MNRAS, 372, 758

Markevitch, M., Gonzalez, A. H., Clowe, D., Vikhlinin, A., Forman, W., Jones, C., Murray, S., & Tucker, W. 2004, ApJ, 606, 819

Markevitch, M., Gonzalez, A. H., David, L., Vikhlinin, A., Murray, S., Forman, W., Jones, C., & Tucker, W. 2002, ApJ, 567, L27

Marrone, D. P., Smith, G. P., Richard, J., Joy, M., Bonamente, M., Hasler, N., Hamilton-Morris, V., Kneib, J., Culverhouse, T., Carlstrom, J. E., Greer, C., Hawkins, D., Hennessy, R., Lamb, J. W., Leitch, E. M., Loh, M., Miller, A., Mroczkowski, T., Muchovej, S., Pryke, C., Sharp, M. K., & Woody, D. 2009, ApJ, 701, L114

Marshall, P. J. 2001, in Clusters of Galaxies and the High Redshift Universe Observed in X-rays, ed. D. M. Neumann & J. T. V. Tran

Marshall, P. J., Hobson, M. P., Gull, S. F., & Bridle, S. L. 2002, MNRAS, 335, 1037

Massey, R., Heymans, C., Bergé, J., Bernstein, G., Bridle, S., Clowe, D., Dahle, H., Ellis, R., Erben, T., Hetterscheidt, M., High, F. W., Hirata, C., Hoekstra, H., Hudelot, P., Jarvis, M., Johnston, D., Kuijken, K., Margoniner, V., Mandelbaum, R., Mellier, Y., Nakajima, R., Paulin-Henriksson, S., Peeples, M., Roat, C., Refregier, A., Rhodes, J., Schrabback, T., Schirmer, M., Seljak, U., Semboloni, E., & van Waerbeke, L. 2007, MNRAS, 376, 13

Massey, R., Kitching, T., & Nagai, D. 2011, MNRAS, 223

Massey, R., Kitching, T., & Richard, J. 2010, Reports on Progress in Physics, 73, 086901

Medezinski, E., Broadhurst, T., Umetsu, K., Coe, D., Benítez, N., Ford, H., Rephaeli, Y., Arimoto, N., & Kong, X. 2007, ApJ, 663, 717

Medezinski, E., Broadhurst, T., Umetsu, K., Oguri, M., Rephaeli, Y., & Benítez, N. 2010, MNRAS, 405, 257

Mellier, Y. 1999, ARA&A, 37, 127

Meneghetti, M., Rasia, E., Merten, J., Bellagamba, F., Ettori, S., Mazzotta, P., Dolag, K., & Marri, S. 2010, A&A, 514, A93+

Merten, J., Coe, D., Dupke, R., Massey, R., Zitrin, A., Cypriano, E. S., Okabe, N., Frye, B., Braglia, F., Jimenez-Teja, Y., Benitez, N., Broadhurst, T., Rhodes, J., Meneghetti, M., Moustakas, L. A., Sodre, Jr., L., Krick, J., & Bregman, J. N. 2011, ArXiv e-prints

Meylan, G., Jetzer, P., North, P., Schneider, P., Kochanek, C. S., & Wambsganss, J., eds. 2006, Gravitational Lensing: Strong, Weak and Micro, ed. G. Meylan, P. Jetzer, P. North, P. Schneider, C. S. Kochanek, & J. Wambsganss

Miller, A. D., Caldwell, R., Devlin, M. J., Dorwart, W. B., Herbig, T., Nolta, M. R., Page, L. A., Puchalla, J., Torbet, E., & Tran, H. T. 1999, ApJ, 524, L1

Miralda-Escude, J. 1991, ApJ, 370, 1

Miralda-Escude, J. & Babul, A. 1995, ApJ, 449, 18

Mushotzky, R. F. 2004, in Clusters of Galaxies: Probes of Cosmological Structure and Galaxy Evolution, ed. J. S. Mulchaey, A. Dressler, & A. Oemler, 123–+

Nagai, D., Vikhlinin, A., & Kravtsov, A. V. 2007, ApJ, 655, 98

Narayan, R. & Bartelmann, M. 1996, ArXiv Astrophysics e-prints

Natarajan, P., De Lucia, G., & Springel, V. 2007, MNRAS, 376, 180

Natarajan, P., Kneib, J., Smail, I., Treu, T., Ellis, R., Moran, S., Limousin, M., & Czoske, O. 2009, ApJ, 693, 970

Natarajan, P., Kneib, J.-P., & Smail, I. 2002, ApJ, 580, L11

Navarro, J. F., Frenk, C. S., & White, S. D. M. 1997, ApJ, 490, 493

Navarro, J. F., Hayashi, E., Power, C., Jenkins, A. R., Frenk, C. S., White, S. D. M., Springel, V., Stadel, J., & Quinn, T. R. 2004, MNRAS, 349, 1039

Navarro, J. F., Ludlow, A., Springel, V., Wang, J., Vogelsberger, M., White, S. D. M., Jenkins, A., Frenk, C. S., & Helmi, A. 2010, MNRAS, 402, 21

Norris, J. R. 2007, Markov Chains, 1st edn. (Cambridge University Press), 237 S.

Okabe, N., Okura, Y., & Futamase, T. 2010a, ApJ, 713, 291

Okabe, N., Takada, M., Umetsu, K., Futamase, T., & Smith, G. P. 2010b, PASJ, 62, 811

Okabe, N., Zhang, Y.-Y., Finoguenov, A., Takada, M., Smith, G. P., Umetsu, K., & Futamase, T. 2010c, ApJ, 721, 875

Owers, M. S., Randall, S. W., Nulsen, P. E. J., Couch, W. J., David, L. P., & Kempner, J. C. 2011, ApJ, 728, 27

Penzias, A. A. & Wilson, R. W. 1965, ApJ, 142, 419

Pereira, M. J., Haines, C. P., Smith, G. P., Egami, E., Moran, S. M., Finoguenov, A., Hardegree-Ullman, E., Okabe, N., Rawle, T., & Rex, M. 2010, A&A, 518, L40+

Petters, A. O., Levine, H., & Wambsganss, J. 2001, Singularity theory and gravitational lensing (Singularity theory and gravitational lensing / Arlie O. Petters, Harold Levine, Joachim Wambsganss. Boston : Birkhäuser, c2001. (Progress in mathematical physics ; v. 21))

Poole, G. B., Fardal, M. A., Babul, A., McCarthy, I. G., Quinn, T., & Wadsley, J. 2006, MNRAS, 373, 881

Pratt, G. W., Croston, J. H., Arnaud, M., & Böhringer, H. 2009, A&A, 498, 361

Press, W. H. & Schechter, P. 1974, ApJ, 187, 425

Randall, S. W., Markevitch, M., Clowe, D., Gonzalez, A. H., & Bradač, M. 2008, ApJ, 679, 1173

Rasia, E., Ettori, S., Moscardini, L., Mazzotta, P., Borgani, S., Dolag, K., Tormen, G., Cheng, L. M., & Diaferio, A. 2006, MNRAS, 369, 2013

Rhodes, J. D., Massey, R. J., Albert, J., Collins, N., Ellis, R. S., Heymans, C., Gardner, J. P., Kneib, J.-P., Koekemoer, A., Leauthaud, A., Mellier, Y., Refregier, A., Taylor, J. E., & Van Waerbeke, L. 2007, ApJS, 172, 203

Richard, J., Kneib, J.-P., Ebeling, H., Stark, D. P., Egami, E., & Fiedler, A. K. 2011, MNRAS, 414, L31

Richard, J., Kneib, J.-P., Jullo, E., Covone, G., Limousin, M., Ellis, R., Stark, D., Bundy, K., Czoske, O., Ebeling, H., & Soucail, G. 2007, ApJ, 662, 781

Richard, J., Smith, G. P., Kneib, J., Ellis, R. S., Sanderson, A. J. R., Pei, L., Targett, T. A., Sand, D. J., Swinbank, A. M., Dannerbauer, H., Mazzotta, P., Limousin, M., Egami, E., Jullo, E., Hamilton-Morris, V., & Moran, S. M. 2010, MNRAS, 404, 325

Robertson, H. P. 1935, ApJ, 82, 284

Rubin, V. C. & Ford, Jr., W. K. 1970, ApJ, 159, 379

Rubin, V. C., Ford, W. K. J., & . Thonnard, N. 1980, ApJ, 238, 471

Sánchez, E. & the Des collaboration. 2010, Journal of Physics Conference Series, 259, 012080

Sand, D. J., Treu, T., & Ellis, R. S. 2002, ApJ, 574, L129

Sand, D. J., Treu, T., Ellis, R. S., Smith, G. P., & Kneib, J.-P. 2008, ApJ, 674, 711

Sand, D. J., Treu, T., Smith, G. P., & Ellis, R. S. 2004, ApJ, 604, 88

Sanderson, A. J. R., Edge, A. C., & Smith, G. P. 2009, MNRAS, 398, 1698

Sanderson, A. J. R. & Ponman, T. J. 2010, MNRAS, 402, 65

Sanderson, A. J. R., Ponman, T. J., & O'Sullivan, E. 2006, MNRAS, 372, 1496

Santos, J. S., Fassbender, R., Nastasi, A., Böhringer, H., Rosati, P., Šuhada, R., Pierini, D., Nonino, M., Mühlegger, M., Quintana, H., Schwope, A. D., Lamer, G., de Hoon, A., & Strazzullo, V. 2011, A&A, 531, L15+

Sarazin, C. L. 1988, X-ray emission from clusters of galaxies (Cambridge University Press)

Schaeffer, R., Maurogordato, S., Cappi, A., & Bernardeau, F. 1993, MNRAS, 263, L21+

Schlegel, D. J., Finkbeiner, D. P., & Davis, M. 1998, ApJ, 500, 525

Schneider, P. 1996, MNRAS, 283, 837

—. 2006a, Extragalactic Astronomy and Cosmology (Extragalactic Astronomy and Cosmology, by Peter Schneider. Berlin: Springer, 2006.)

Schneider, P. 2006b, in Saas-Fee Advanced Course 33: Gravitational Lensing: Strong, Weak and Micro, ed. G. Meylan, P. Jetzer, P. North, P. Schneider, C. S. Kochanek, & J. Wambsganss, 1–89

Schneider, P. 2006c, in Saas-Fee Advanced Course 33: Gravitational Lensing: Strong, Weak and Micro, ed. G. Meylan, P. Jetzer, P. North, P. Schneider, C. S. Kochanek, & J. Wambsganss, 269–451

Schneider, P., King, L., & Erben, T. 2000, A&A, 353, 41

Schneider, P. & Seitz, C. 1995, A&A, 294, 411

Schneider, P., van Waerbeke, L., Mellier, Y., Jain, B., Seitz, S., & Fort, B. 1998, A&A, 333, 767

Seitz, C. & Schneider, P. 1995, A&A, 297, 287

Seitz, S. & Schneider, P. 1996, A&A, 305, 383

—. 2001, A&A, 374, 740

Seitz, S., Schneider, P., & Bartelmann, M. 1998, A&A, 337, 325

Shaw, L. D., Weller, J., Ostriker, J. P., & Bode, P. 2006, ApJ, 646, 815

Sivia, D. S. with Skilling, J. 2008, Data Analysis: A Bayesian Tutorial, Second Edition, 2nd edn. (Oxford University Press)

Skrutskie, M. F., Cutri, R. M., Stiening, R., Weinberg, M. D., Schneider, S., Carpenter, J. M., Beichman, C., Capps, R., Chester, T., Elias, J., Huchra, J., Liebert, J., Lonsdale, C., Monet, D. G., Price, S., Seitzer, P., Jarrett, T., Kirkpatrick, J. D., Gizis, J. E., Howard, E., Evans, T., Fowler, J. a nd Fullmer, L., Hurt, R., Light, R., Kopan, E. L., Marsh, K. A., McCallon, H. L., Tam, R., Van Dyk, S., & Wheelock, S. 2006, AJ, 131, 1163

Smail, I. 2004, in Clusters of Galaxies: Probes of Cosmological Structure and Galaxy Evolution, ed. J. S. Mulchaey, A. Dressler, & A. Oemler, 108–+

Smail, I., Ellis, R. S., Aragon-Salamanca, A., Soucail, G., Mellier, Y., & Giraud, E. 1993, MNRAS, 263, 628

Smith, G. 2006, in HST Proposal, 10881–+

Smith, G. P., Ebeling, H., Limousin, M., Kneib, J.-P., Swinbank, A. M., Ma, C.-J., Jauzac, M., Richard, J., Jullo, E., Sand, D. J., Edge, A. C., & Smail, I. 2009, ApJ, 707, L163

Smith, G. P., Edge, A. C., Eke, V. R., Nichol, R. C., Smail, I., & Kneib, J.-P. 2003, ApJ, 590, L79

Smith, G. P., Kneib, J.-P., Ebeling, H., Czoske, O., & Smail, I. 2001, ApJ, 552, 493

Smith, G. P., Kneib, J.-P., Smail, I., Mazzotta, P., Ebeling, H., & Czoske, O. 2005, MNRAS, 359, 417

Smith, G. P., Smail, I., Kneib, J.-P., Czoske, O., Ebeling, H., Edge, A. C., Pelló, R., Ivison, R. J., Packham, C., & Le Borgne, J.-F. 2002a, MNRAS, 330, 1

Smith, G. P., Smail, I., Kneib, J.-P., Davis, C. J., Takamiya, M., Ebeling, H., & Czoske, O. 2002b, MNRAS, 333, L16

Smith, G. P. & Taylor, J. E. 2008, ApJ, 682, L73

Soucail, G., Mellier, Y., Fort, B., Mathez, G., & Cailloux, M. 1988, A&A, 191, L19

Spergel, D. N., Verde, L., Peiris, H. V., Komatsu, E., Nolta, M. R., Bennett, C. L., Halpern, M., Hinshaw, G., Jarosik, N., Kogut, A., Limon, M., Meyer, S. S., Page, L., Tucker, G. S., Weiland, J. L., Wollack, E., & Wright, E. L. 2003, ApJS, 148, 175

Springel, V., White, S. D. M., Jenkins, A., Frenk, C. S., Yoshida, N., Gao, L., Navarro, J., Thacker, R., Croton, D., Helly, J., Peacock, J. A., Cole, S., Thomas, P., Couchman, H., Evrard, A., Colberg, J., & Pearce, F. 2005, Nature, 435, 629

Squires, G. & Kaiser, N. 1996, ApJ, 473, 65

Squires, G., Kaiser, N., Babul, A., Fahlman, G., Woods, D., Neumann, D. M., & Böhringer, H. 1996, ApJ, 461, 572

Squires, G., Neumann, D. M., Kaiser, N., Arnaud, M., Babul, A., Böhringer, H., Fahlman, G., & Woods, D. 1997, ApJ, 482, 648

Targett, T. A., Dunlop, J. S., McLure, R. J., Best, P. N., Cirasuolo, M., & Almaini, O. 2011, MNRAS, 4

Tyson, J. A., Wenk, R. A., & Valdes, F. 1990, ApJ, 349, L1

Umetsu, K. & Broadhurst, T. 2008, ApJ, 684, 177

Umetsu, K., Medezinski, E., Broadhurst, T., Zitrin, A., Okabe, N., Hsieh, B., & Molnar, S. M. 2010, ApJ, 714, 1470

Viana, P. T. P., Kay, S. T., Liddle, A. R., Muanwong, O., & Thomas, P. A. 2003, MNRAS, 346, 319

Vikhlinin, A., Kravtsov, A., Forman, W., Jones, C., Markevitch, M., Murray, S. S., & Van Speybroeck, L. 2006, ApJ, 640, 691

Vikhlinin, A., Kravtsov, A. V., Burenin, R. A., Ebeling, H., Forman, W. R., Hornstrup, A., Jones, C., Murray, S. S., Nagai, D., Quintana, H., & Voevodkin, A. 2009, ApJ, 692, 1060

Vikhlinin, A., McNamara, B. R., Forman, W., Jones, C., Quintana, H., & Hornstrup, A. 1998, ApJ, 502, 558

Voit, G. M. 2005, Reviews of Modern Physics, 77, 207

Walker, A. G. 1935, MNRAS, 95, 263

Way, M. J., Quintana, H., Infante, L., Lambas, D. G., & Muriel, H. 2005, AJ, 130, 2012

Zhang, Y., Finoguenov, A., Böhringer, H., Kneib, J., Smith, G. P., Kneissl, R., Okabe, N., & Dahle, H. 2008, A&A, 482, 451

Zhang, Y., Okabe, N., Finoguenov, A., Smith, G. P., Piffaretti, R., Valdarnini, R., Babul, A., Evrard, A. E., Mazzotta, P., Sanderson, A. J. R., & Marrone, D. P. 2010, ApJ, 711, 1033

Zwicky, F. 1933, Helvetica Physica Acta, 6, 110

—. 1937a, Phys. Rev. Lett., 51, 290

—. 1937b, ApJ, 86, 217

—. 1937c, Phys. Rev. Lett., 51, 679

Appendix A

Multiwavelength Structure Maps

The figures in this Appendix compare the spatial distributions of the K-band luminosity (top left), X-ray surface brightness (top right), non parameterised κ reconstruction (bottom right) and parameterised weak lens mass model (bottom right), and are the result of the analysis described in § 3.4.1, § 3.4.2, § 4.1 and § 4.2.

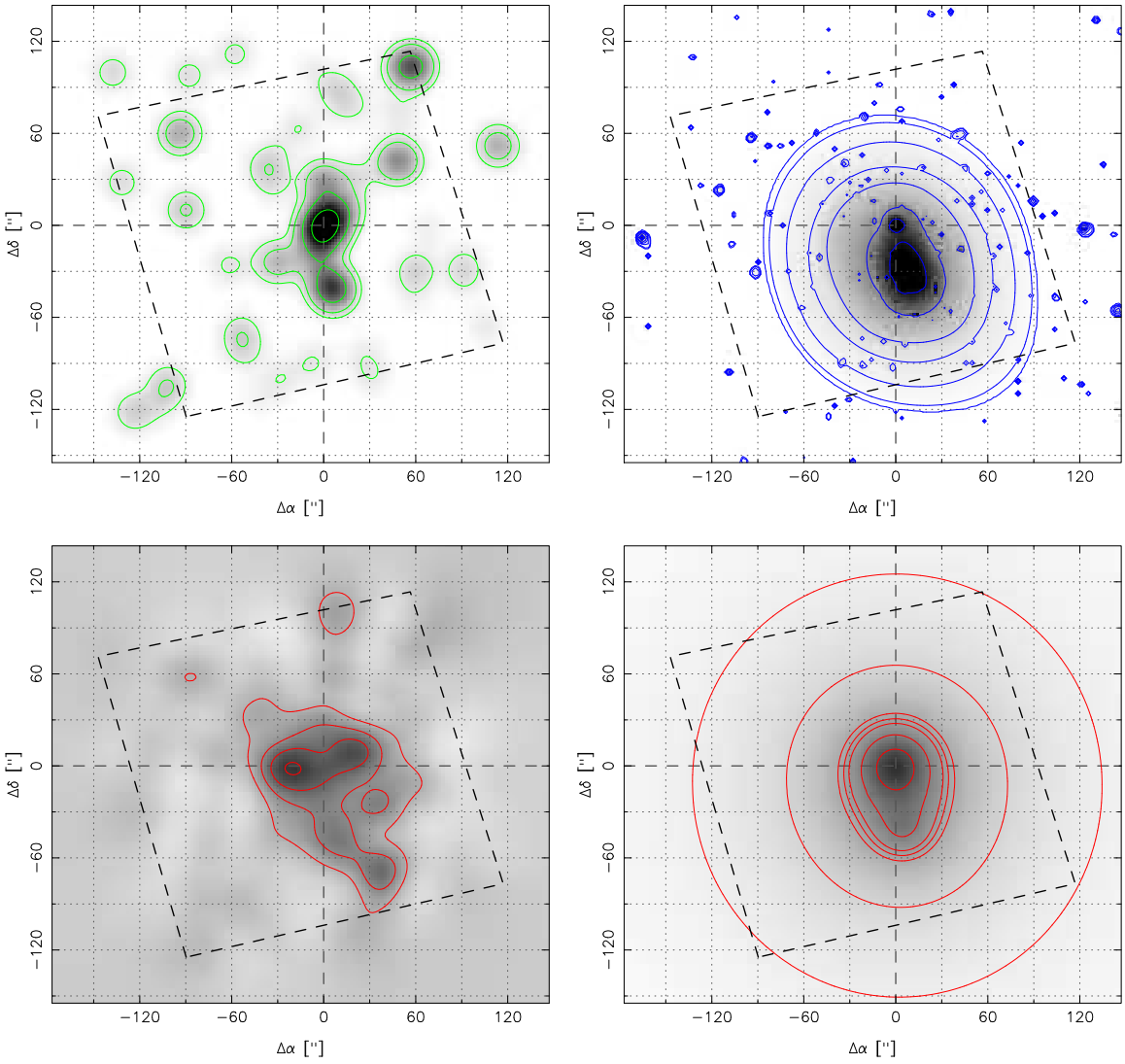

Figure A.1: *A*2813: Top: left, K-band luminosity density map, centred on the BCG position, with contours of $1,2,5\times10^{13}$, $1\times10^{14}L_{\odot}Mpc^{-2}$, and right, the smoothed X-ray emission, with logarithmically stepped contours at surface brightnesses of $0.001,0.002,0.005,0.01,0.02,0.05$ and so on, to highlight the structure in the map. Bottom: left, the LENSENT2 κ reconstruction, the contours denoting $2\sigma,3\sigma,4\sigma...$ levels, and right, the LENSTOOL mass density model favoured by the Bayesian evidence, contours at (0.001, 0.002, 0.005, 0.01...1) $\times10^{12}M_{\odot}Mpc^{-2}$. North is up the page, and East to the left. These details apply to all cluster plots in this section.

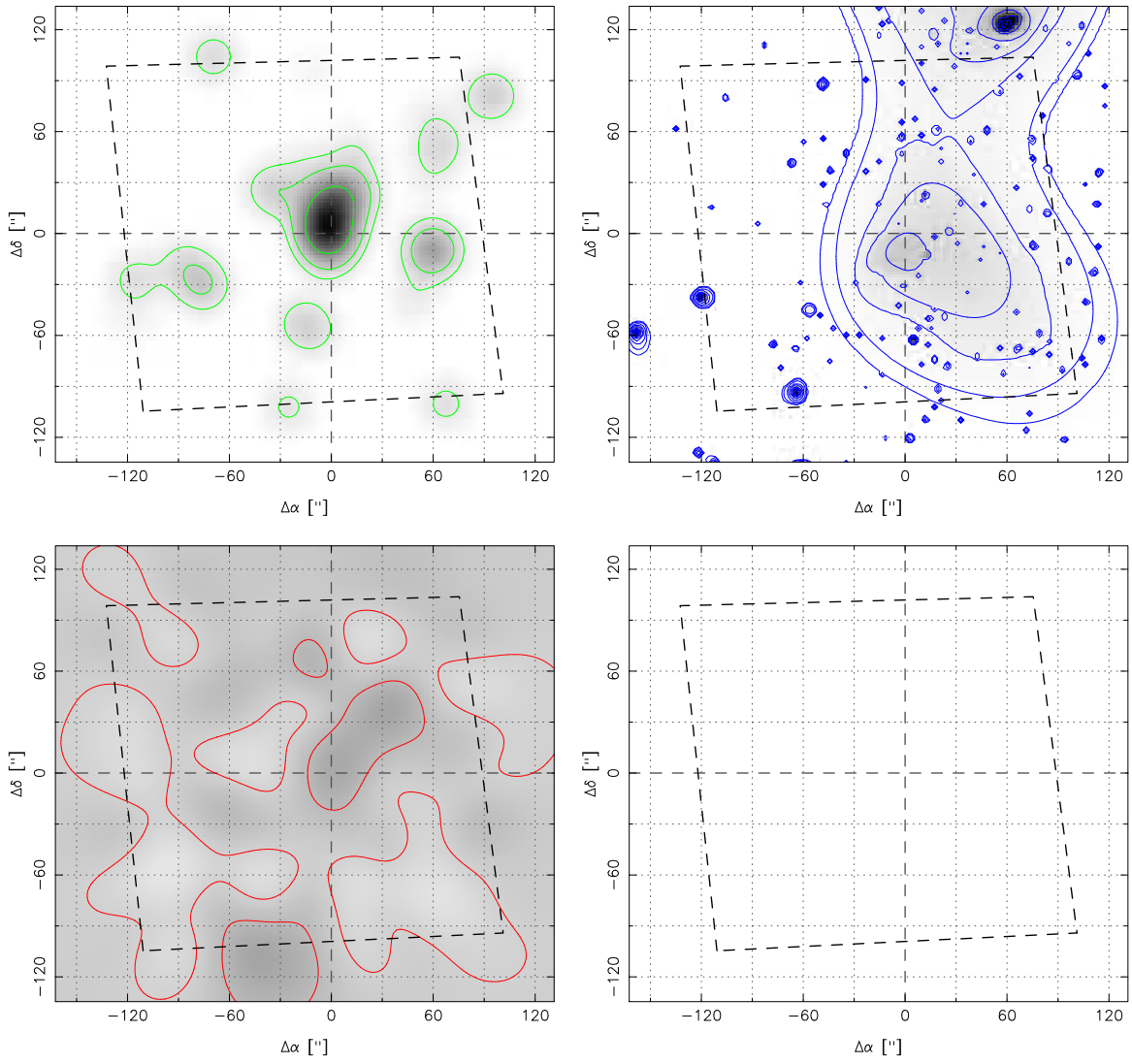

Figure A.2: *A*0141: as for *A*2813. The bottom left map of the LENSTOOL reconstructed mass is blank as the model failed to support any significant mass distributions in this region.

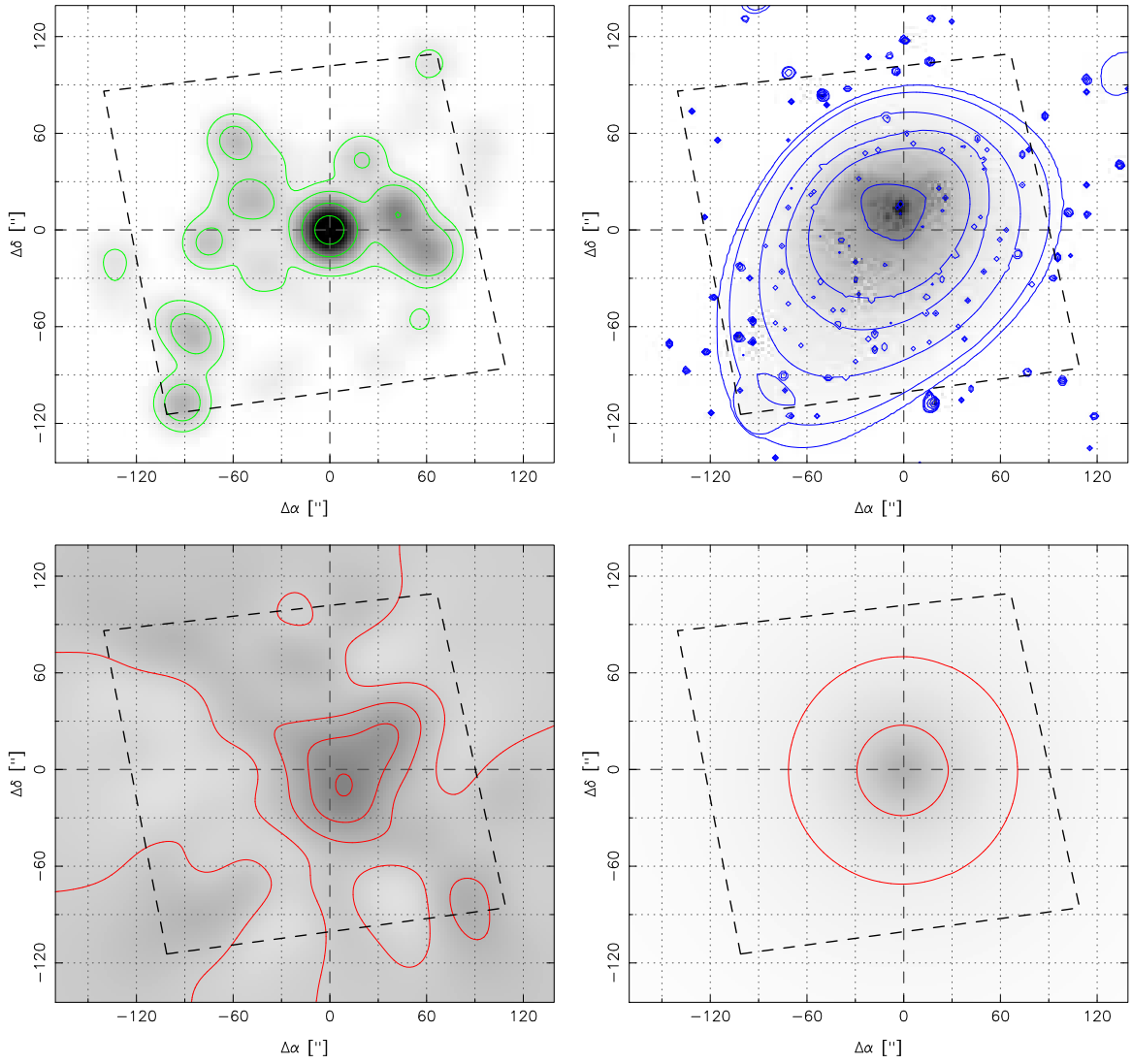

Figure A.3: *A*2895

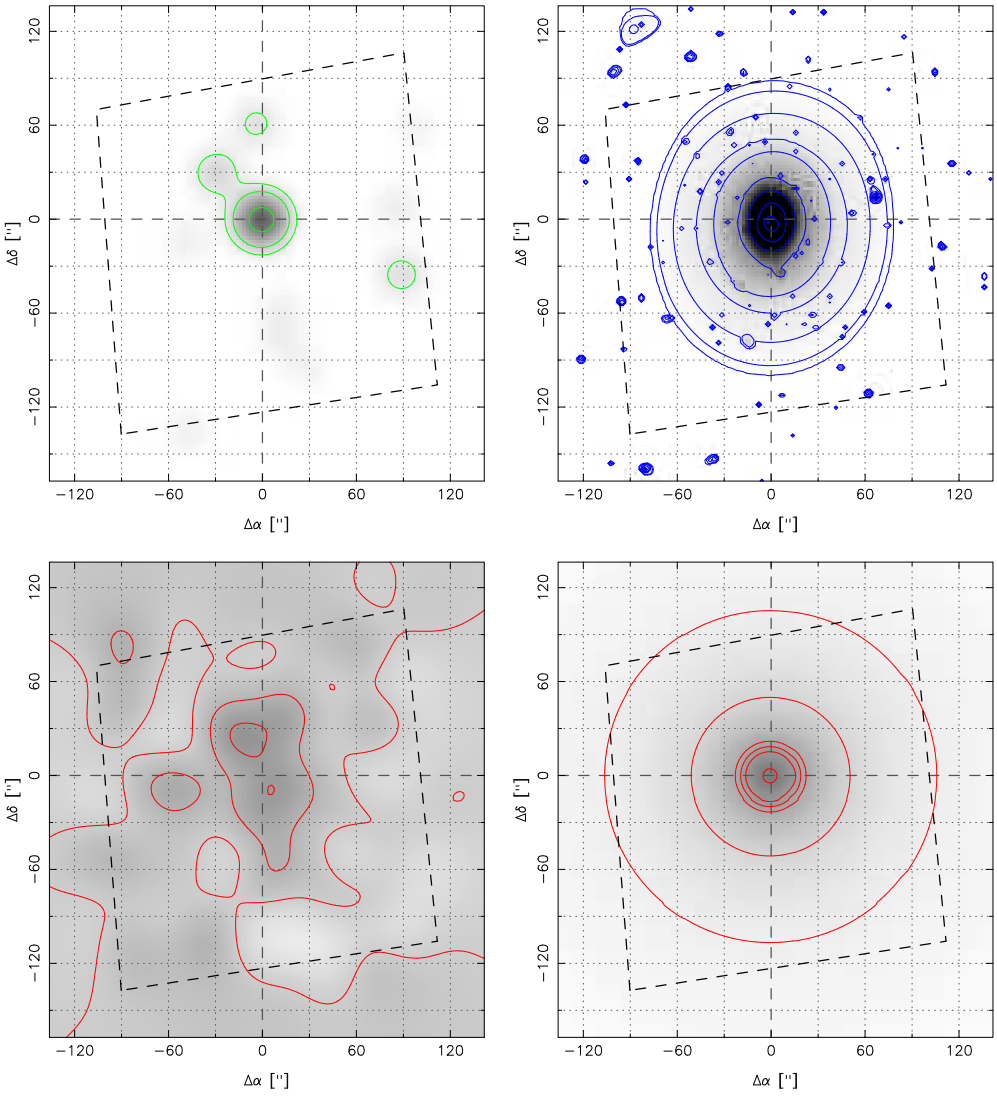

Figure A.4: *RXCJ* 0220.9 − 3829

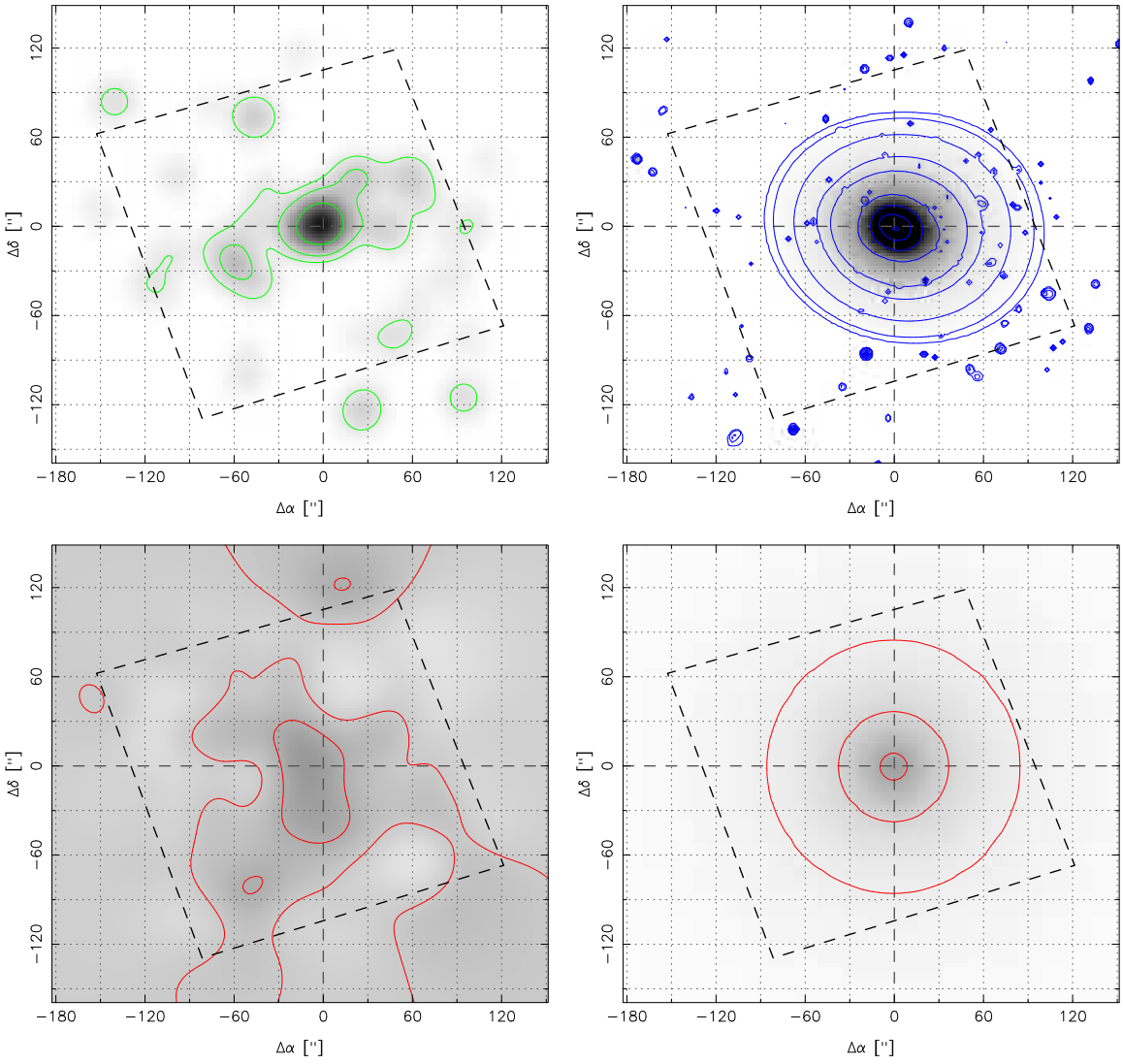

Figure A.5: *A*0368

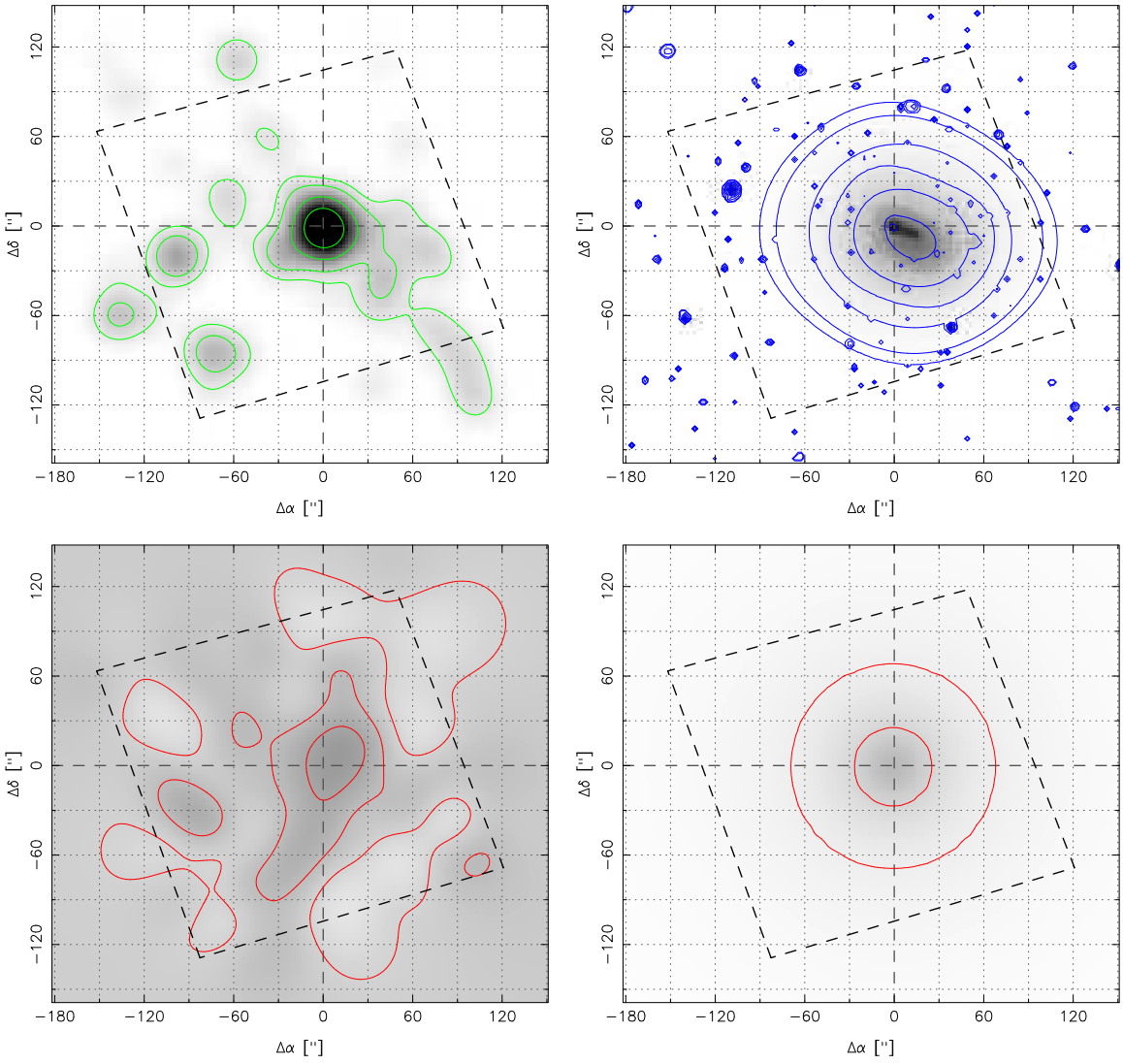

Figure A.6: *A*3084

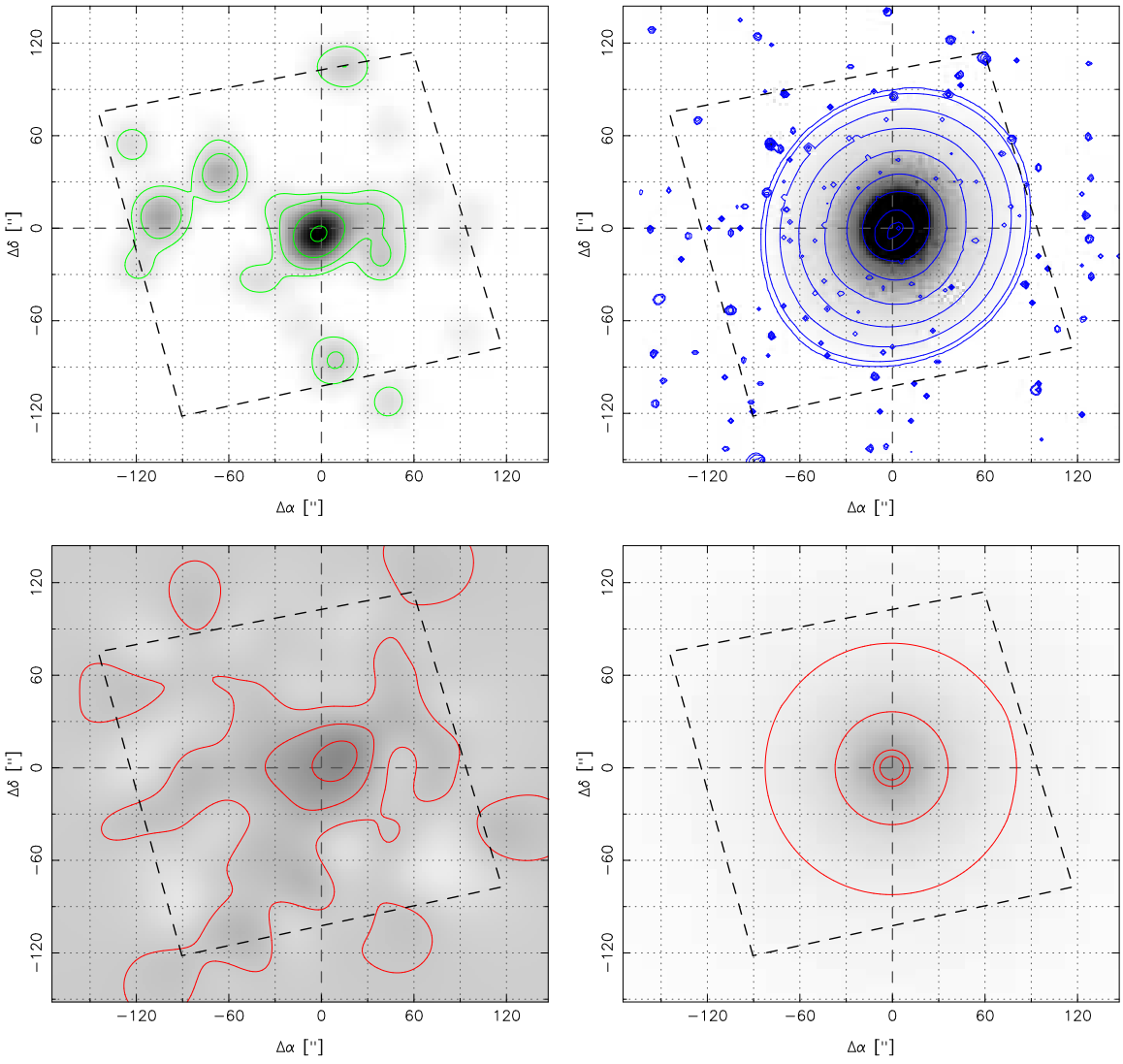

Figure A.7: *A*3088

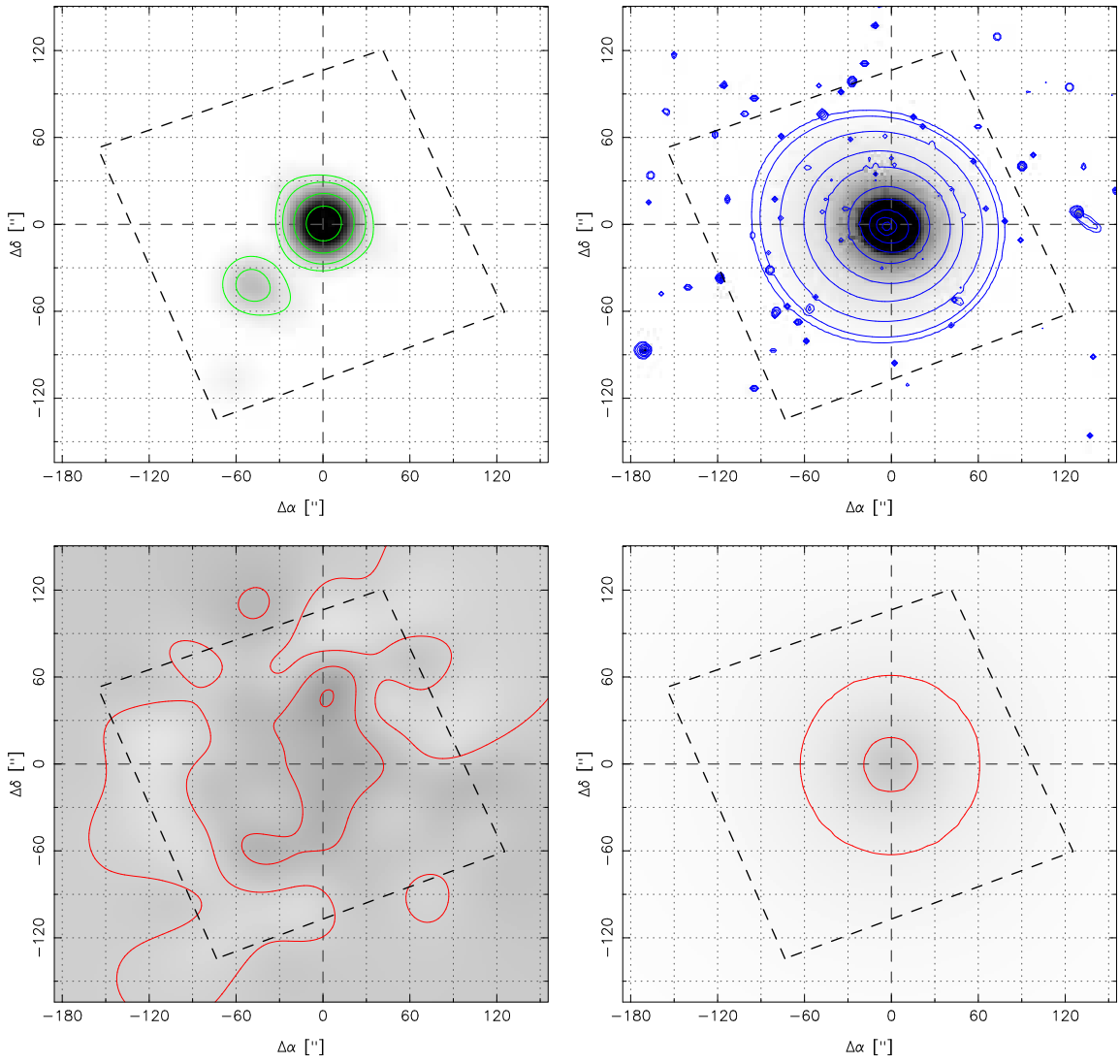

Figure A.8: *RXCJ* 0331.1−2100

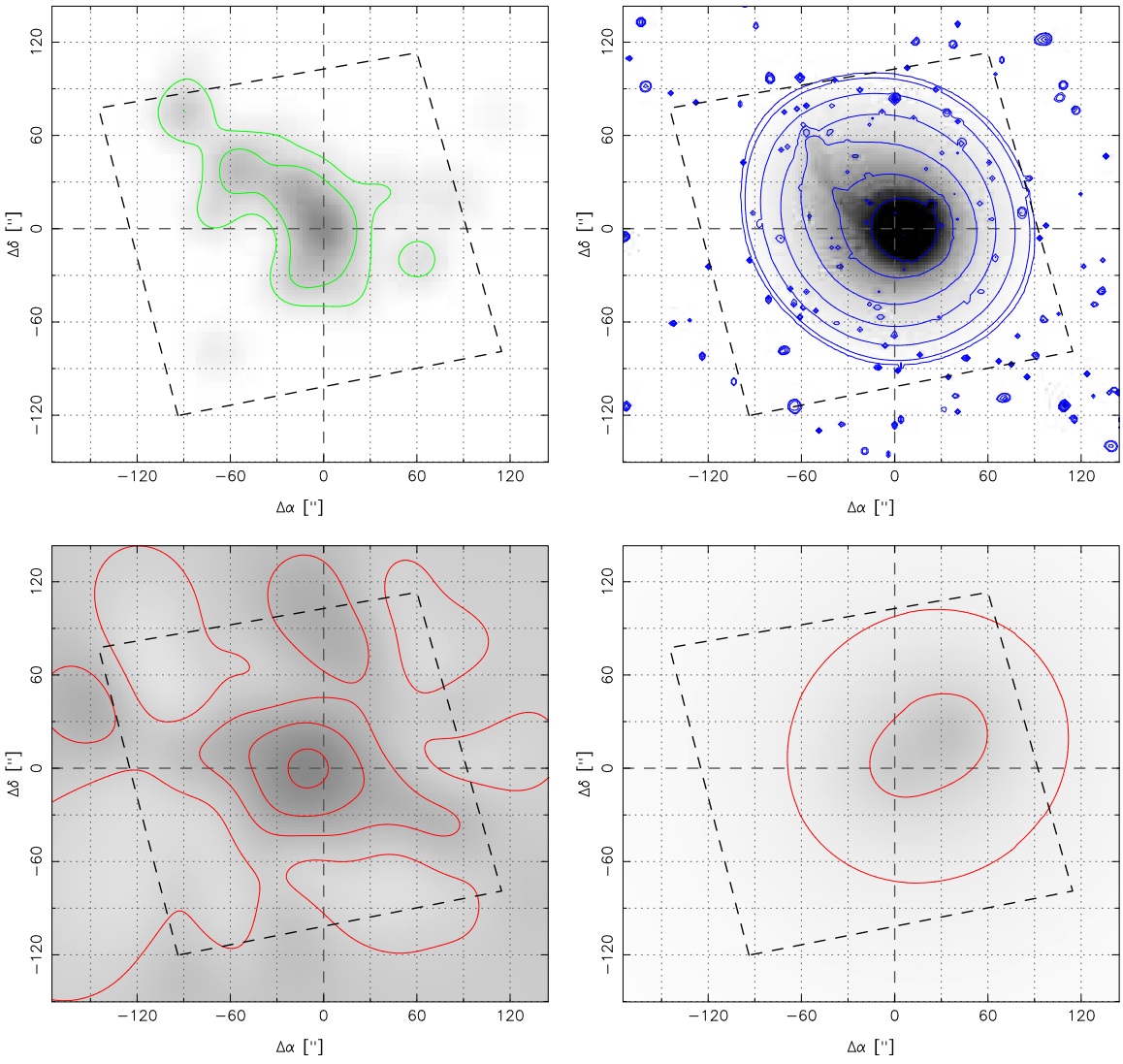

Figure A.9: *A*3140

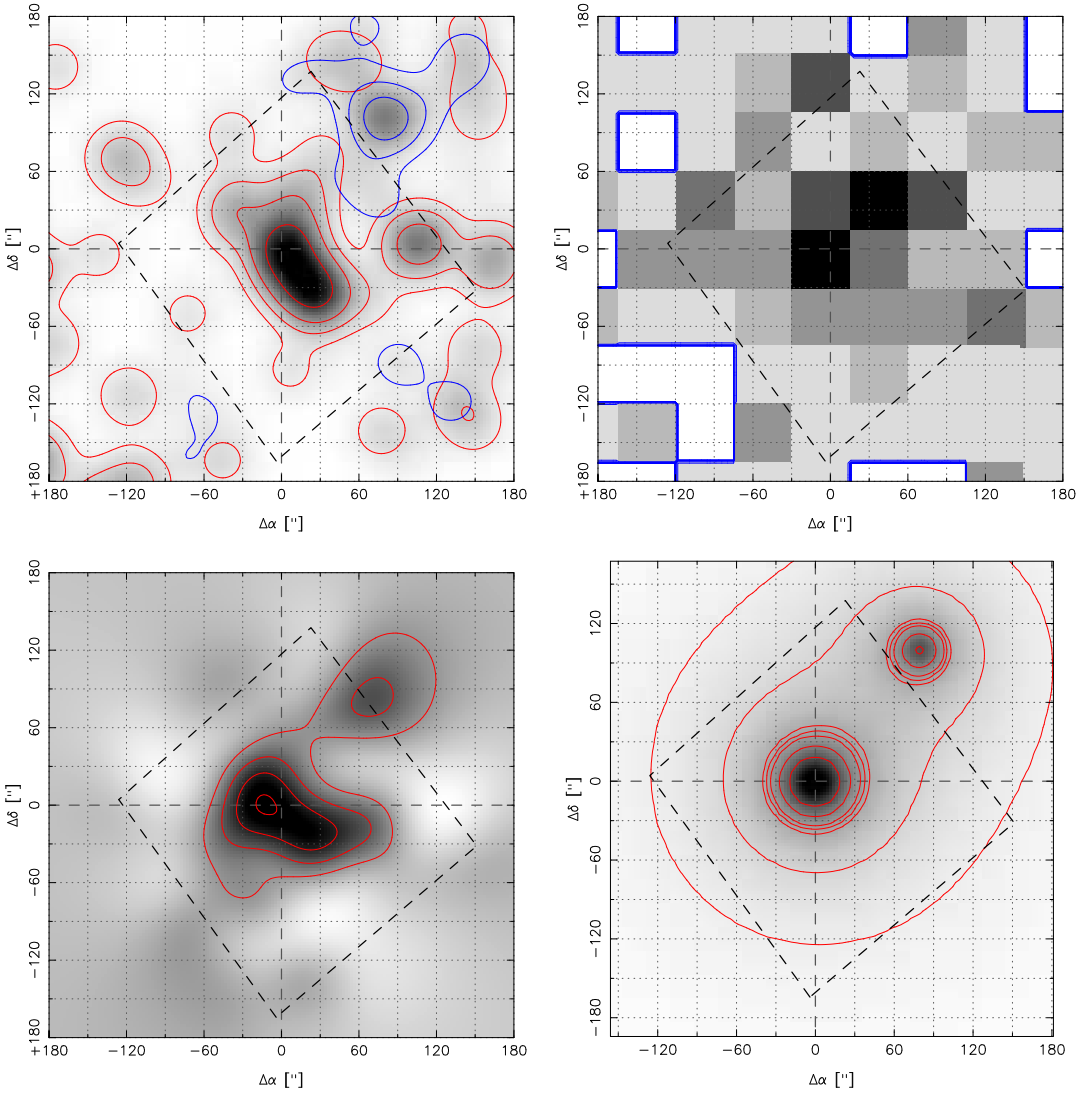

Figure A.10: $A3192$: X-ray, κ and lenstool as for $A2813$, however in the luminosity map, blue and red contours represent $(0.2, 0.5, 1, 2, 5)\times10^{13}$ and 1×10^{14} solar luminosities for the foreground group and background cluster galaxy populations respectively. The X-ray map for this cluster is a ROSAT archival image.

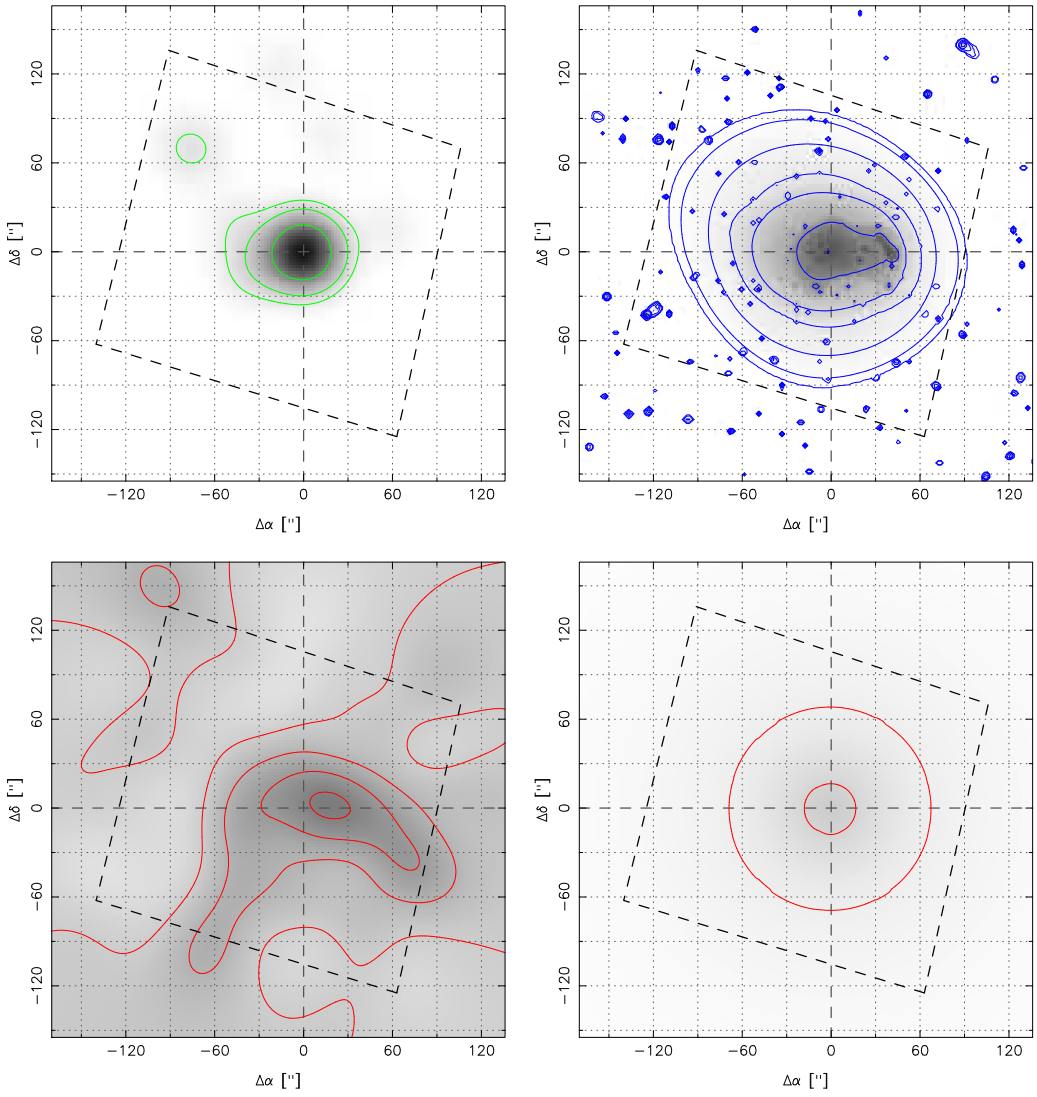

Figure A.11: *A*3292

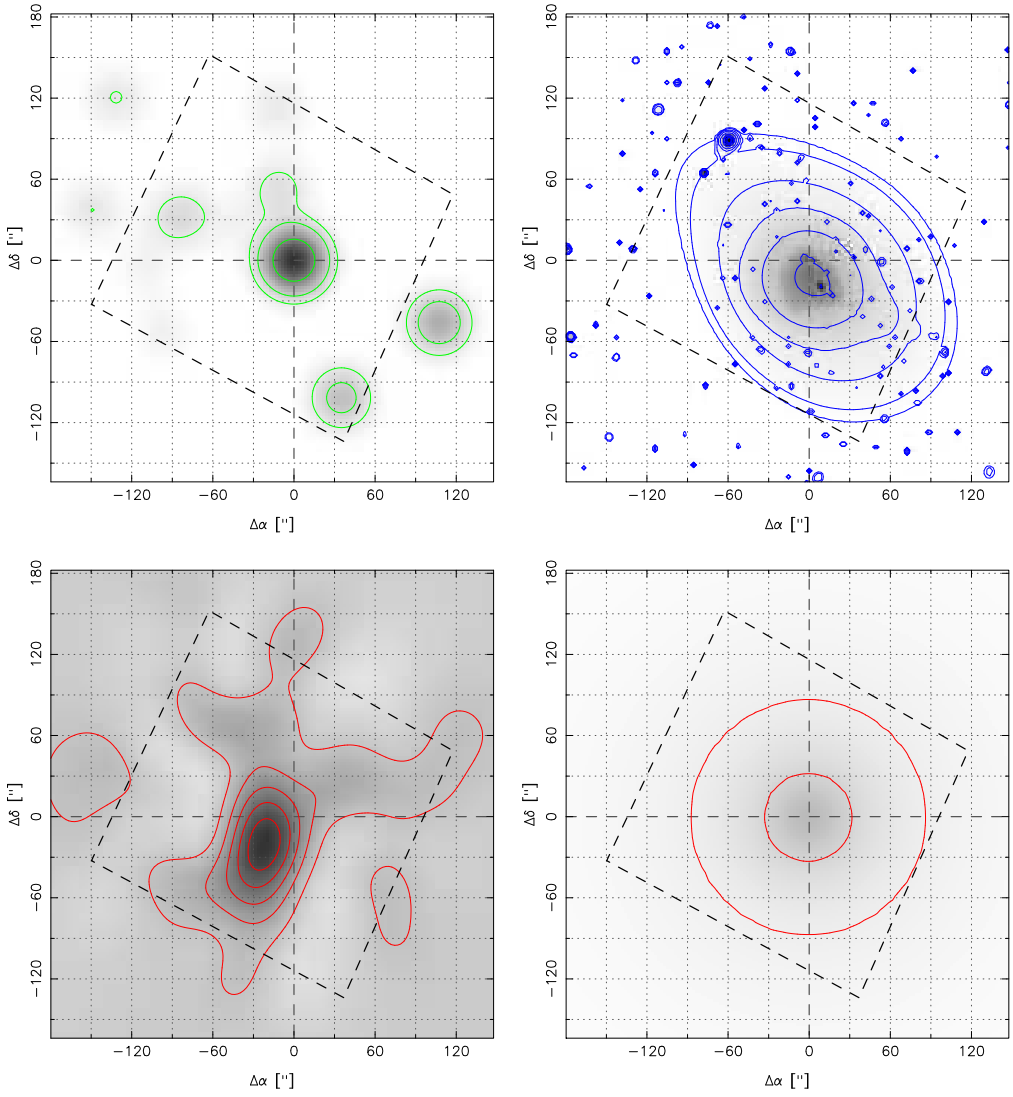

Figure A.12: *RXCJ* 0528.2 − 2942

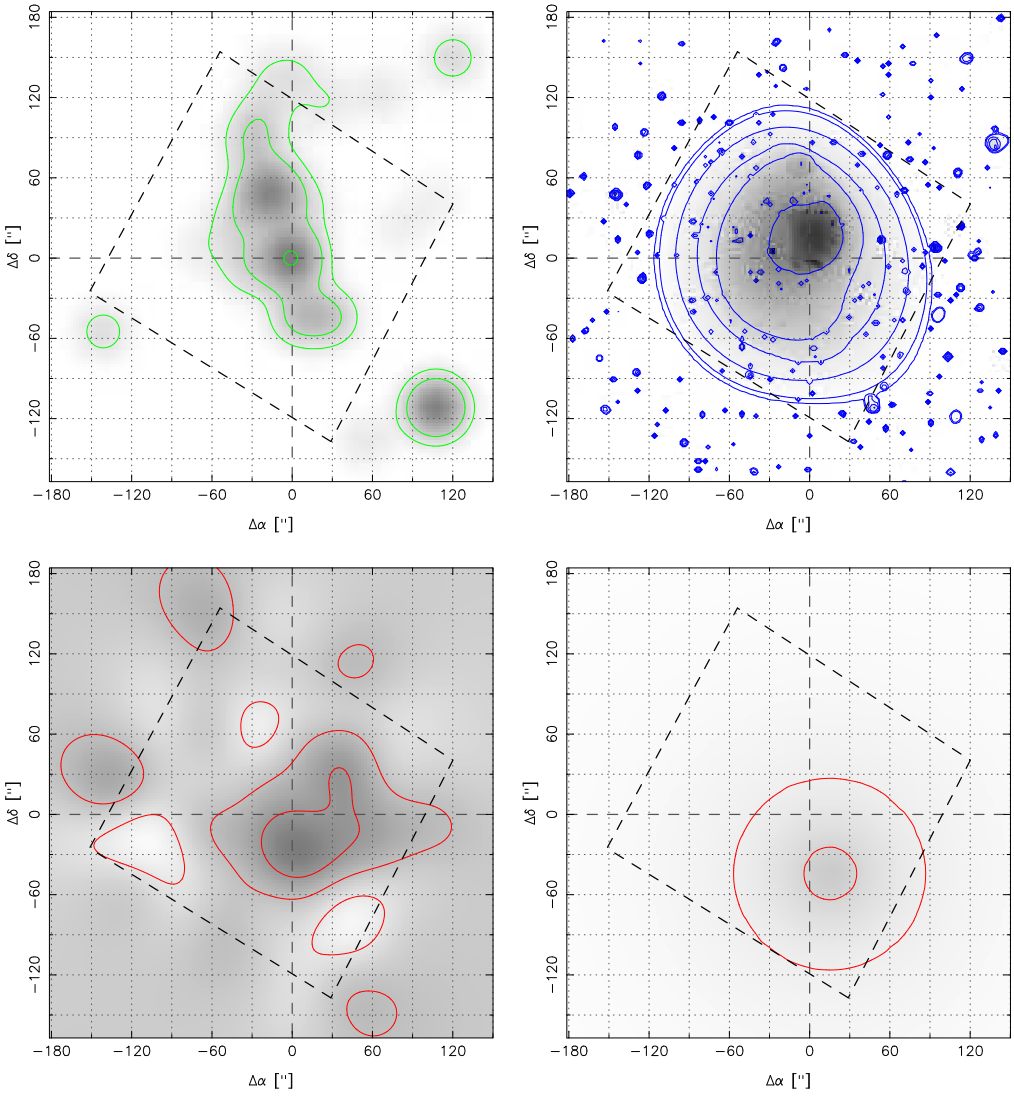

Figure A.13: *A*3364

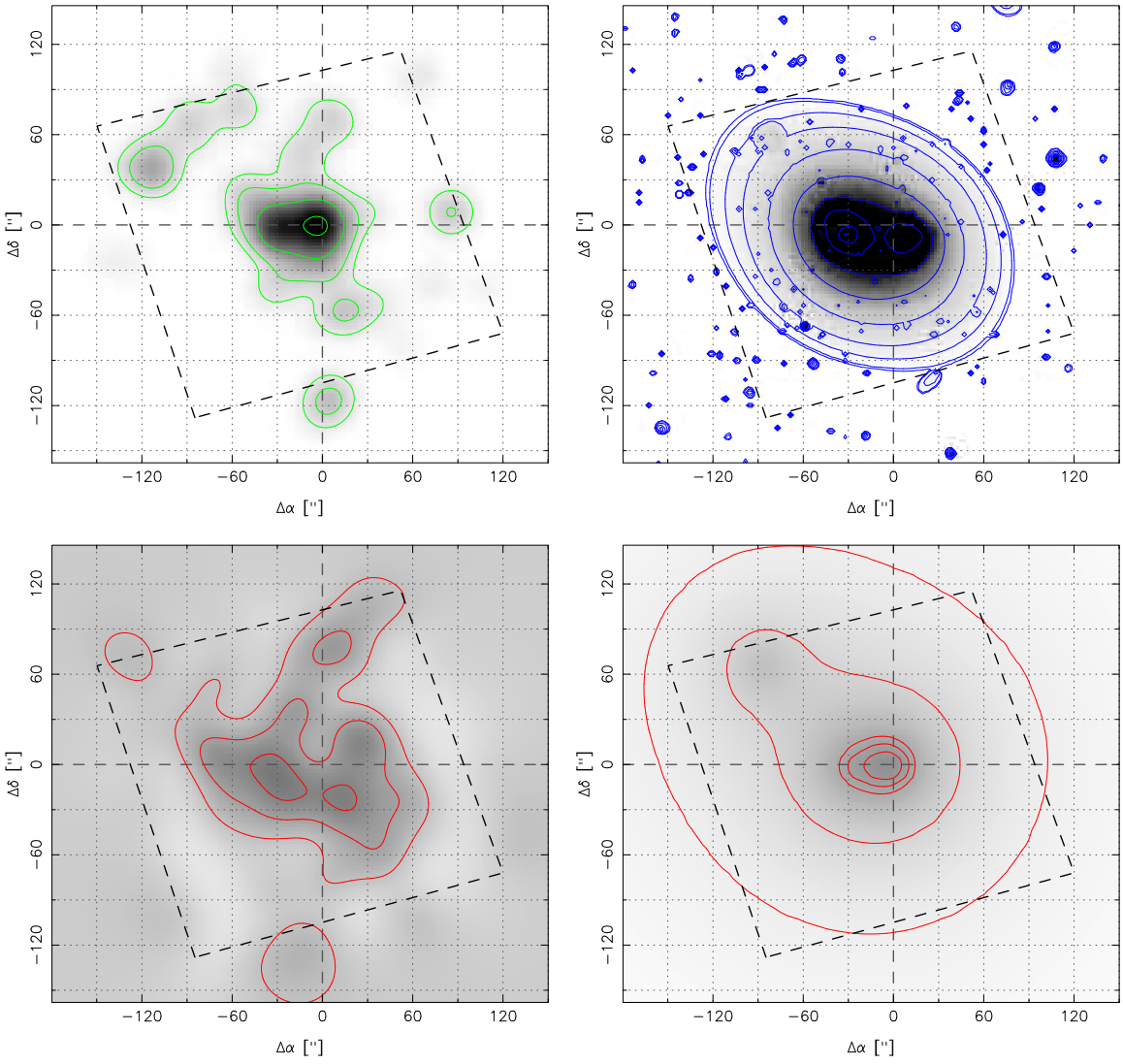

Figure A.14: *AS*0592

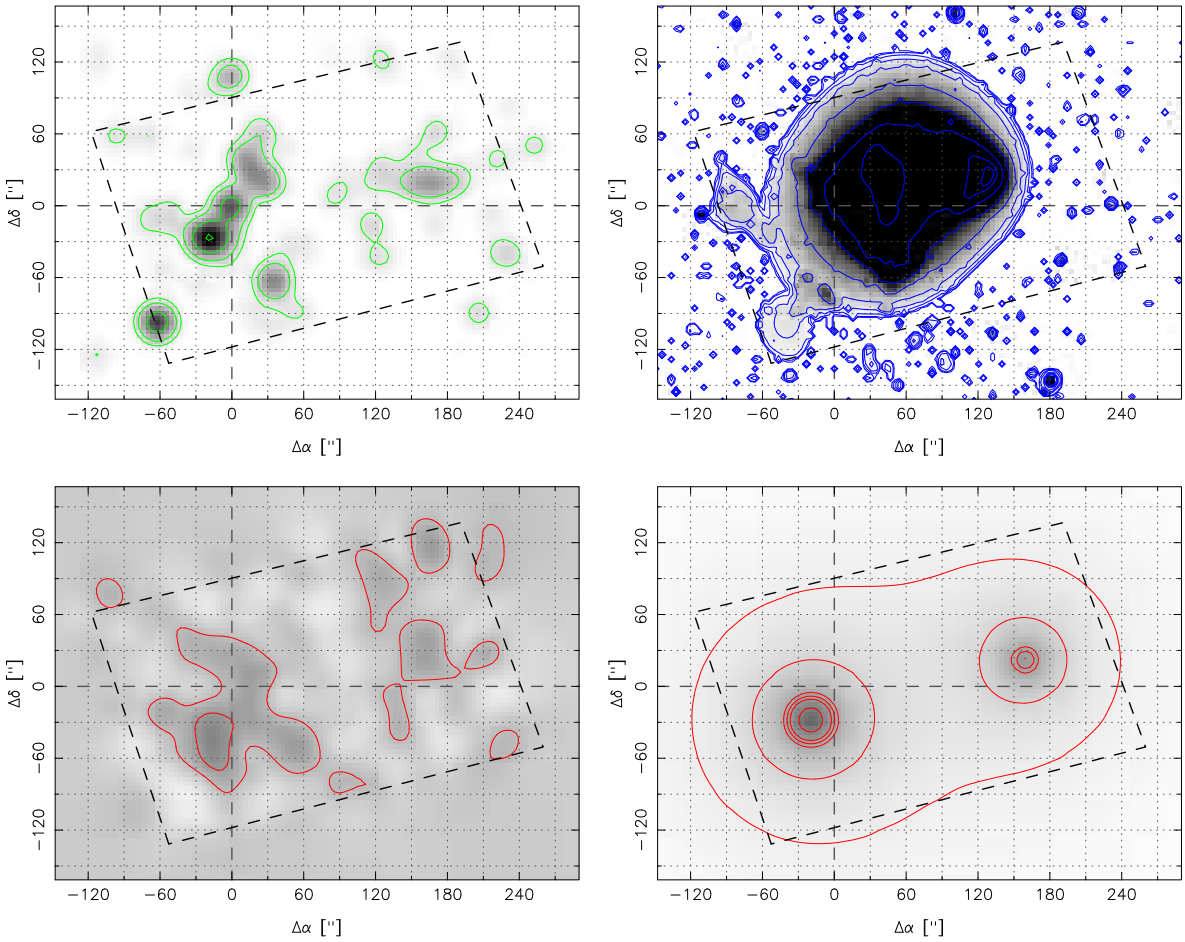

Figure A.15: 1*ES*0657−558

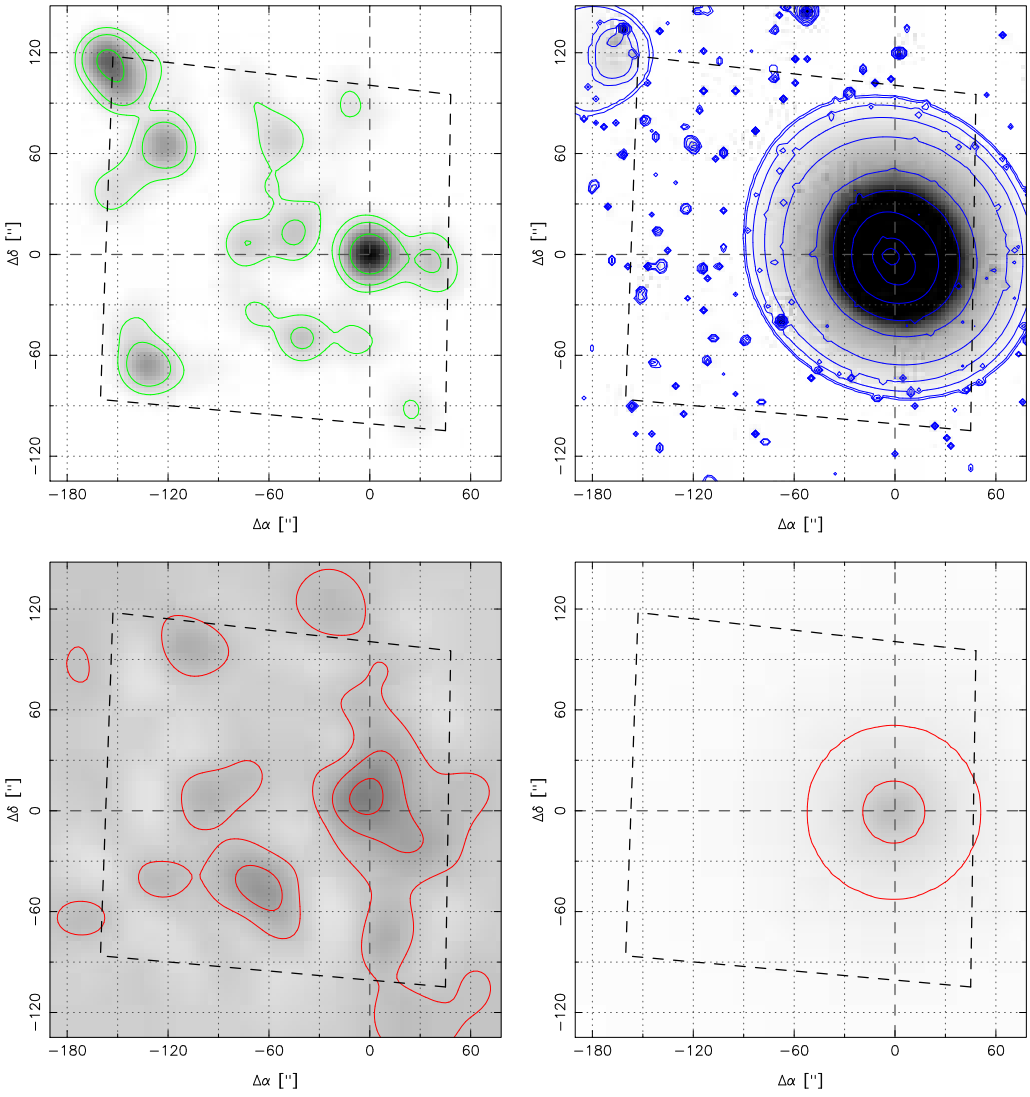

Figure A.16: *A*0611

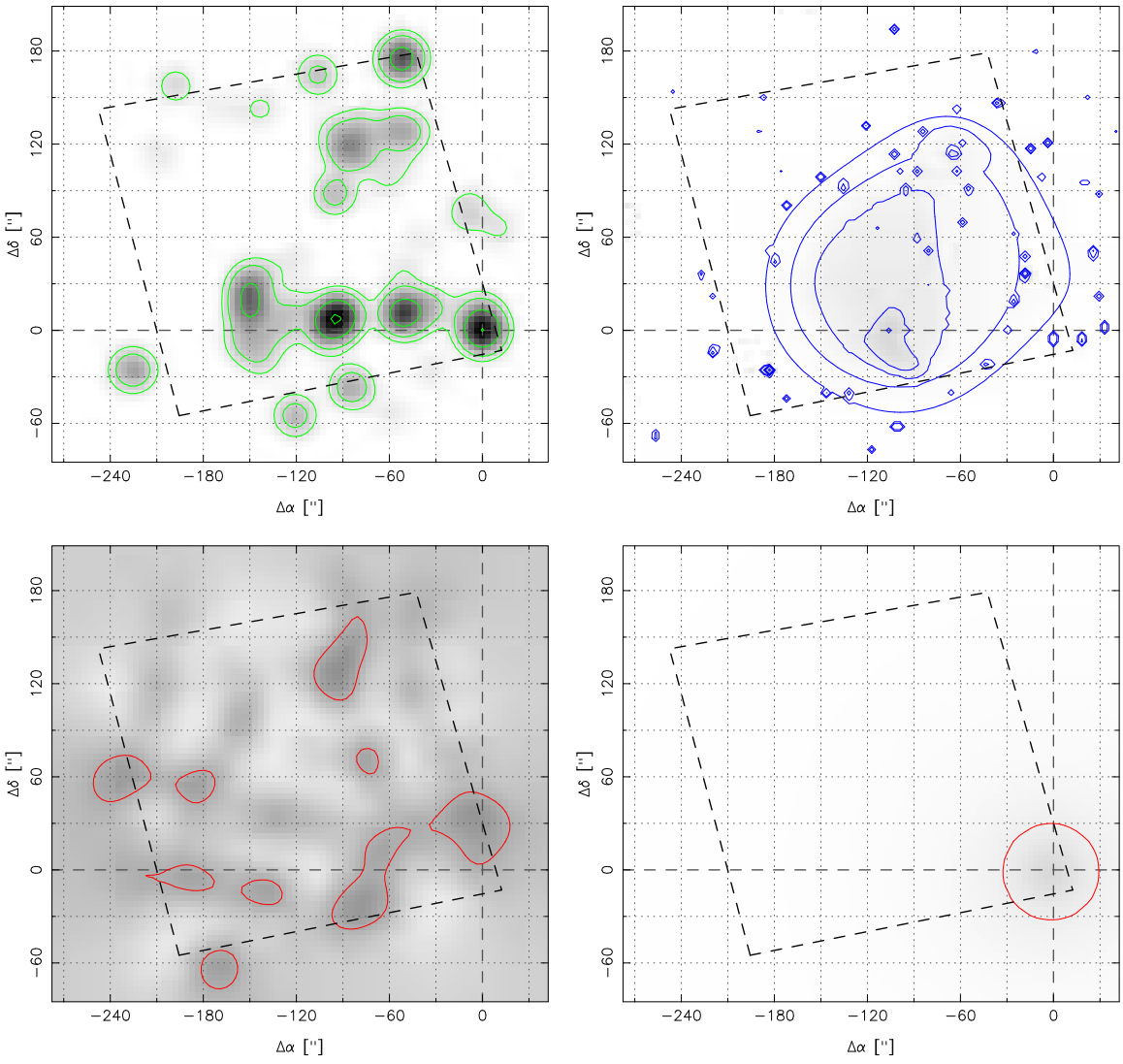

Figure A.17: *A*0781

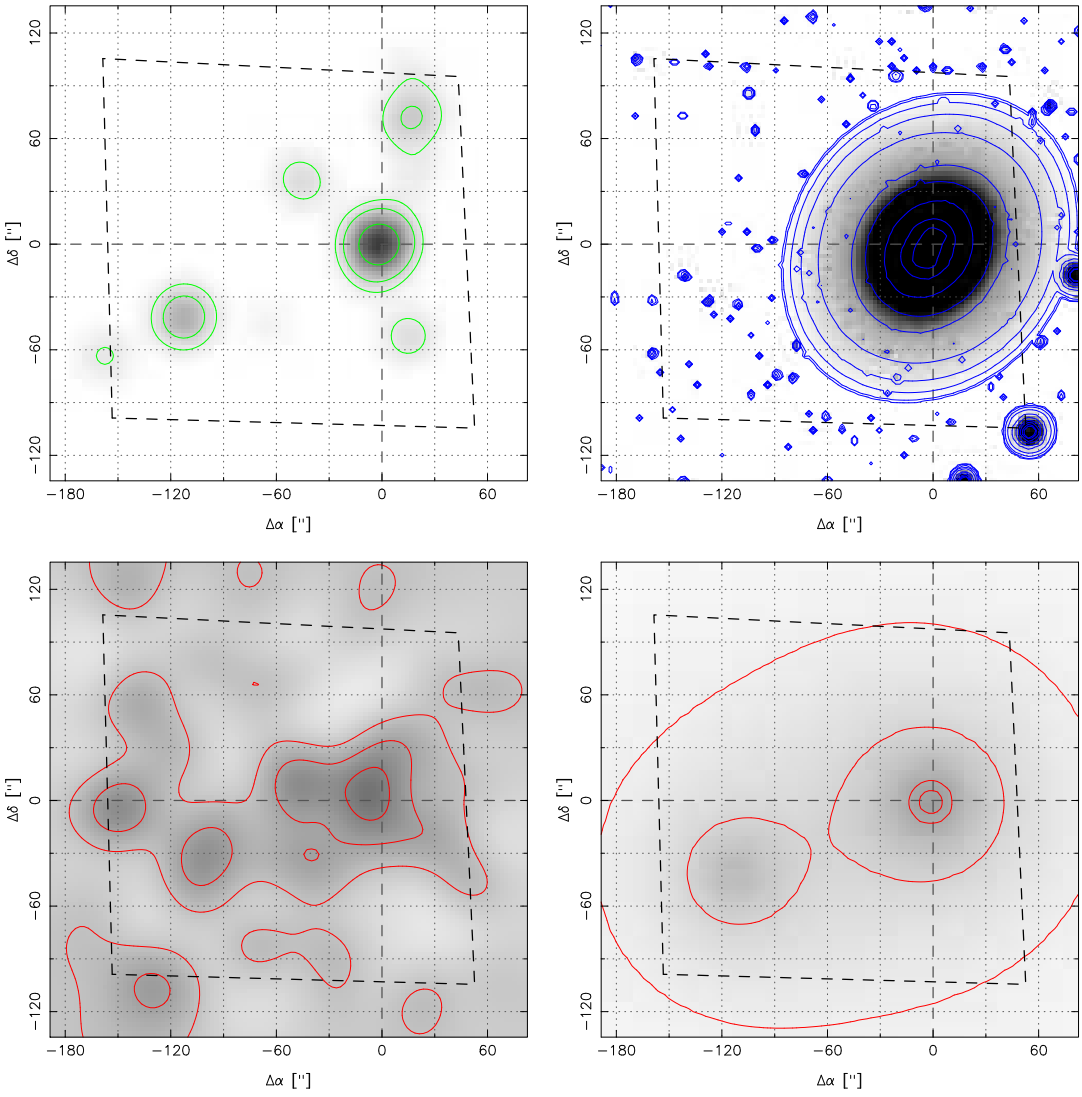

Figure A.18: Z 2701

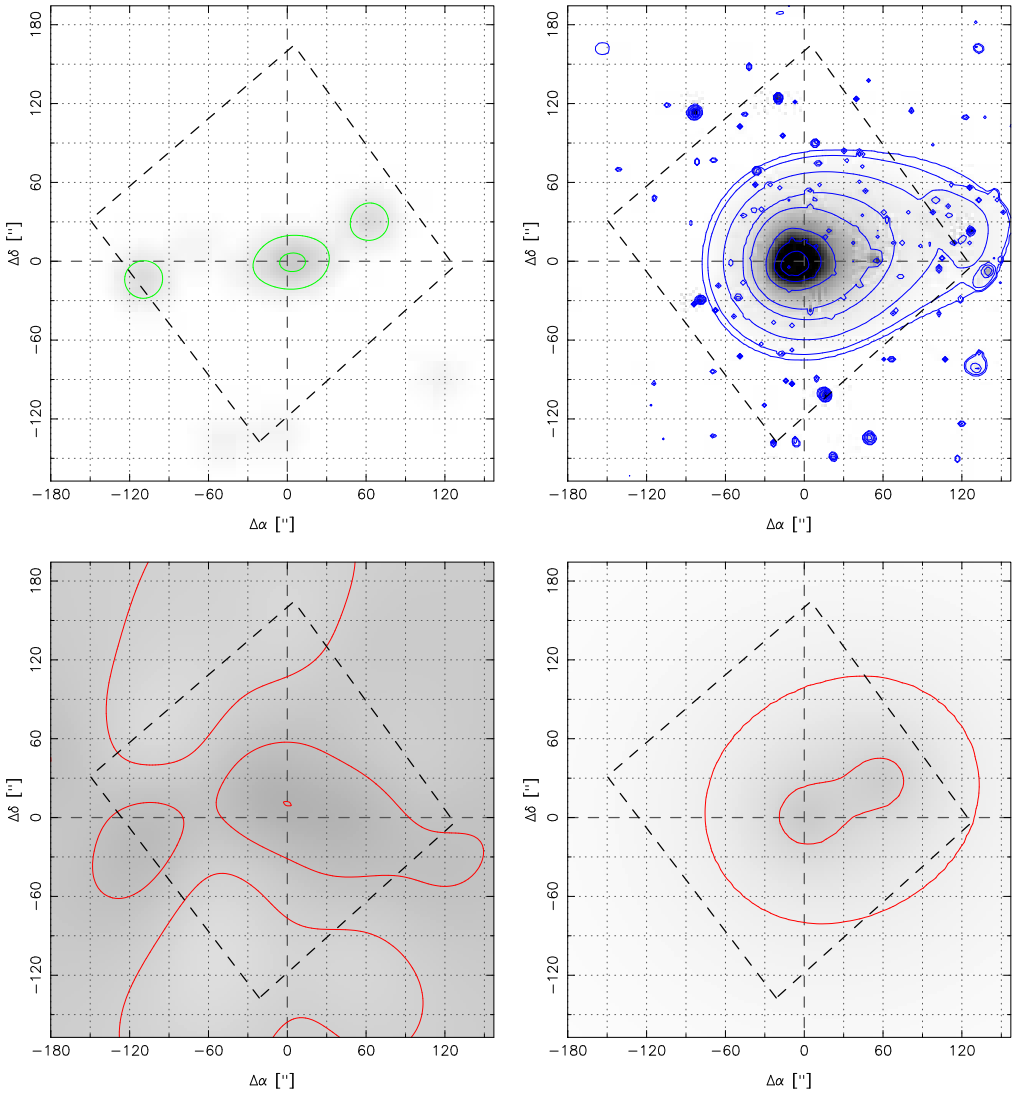

Figure A.19: *RXJ* 1000.5+4409. The κ contours in this example begin at 3σ.

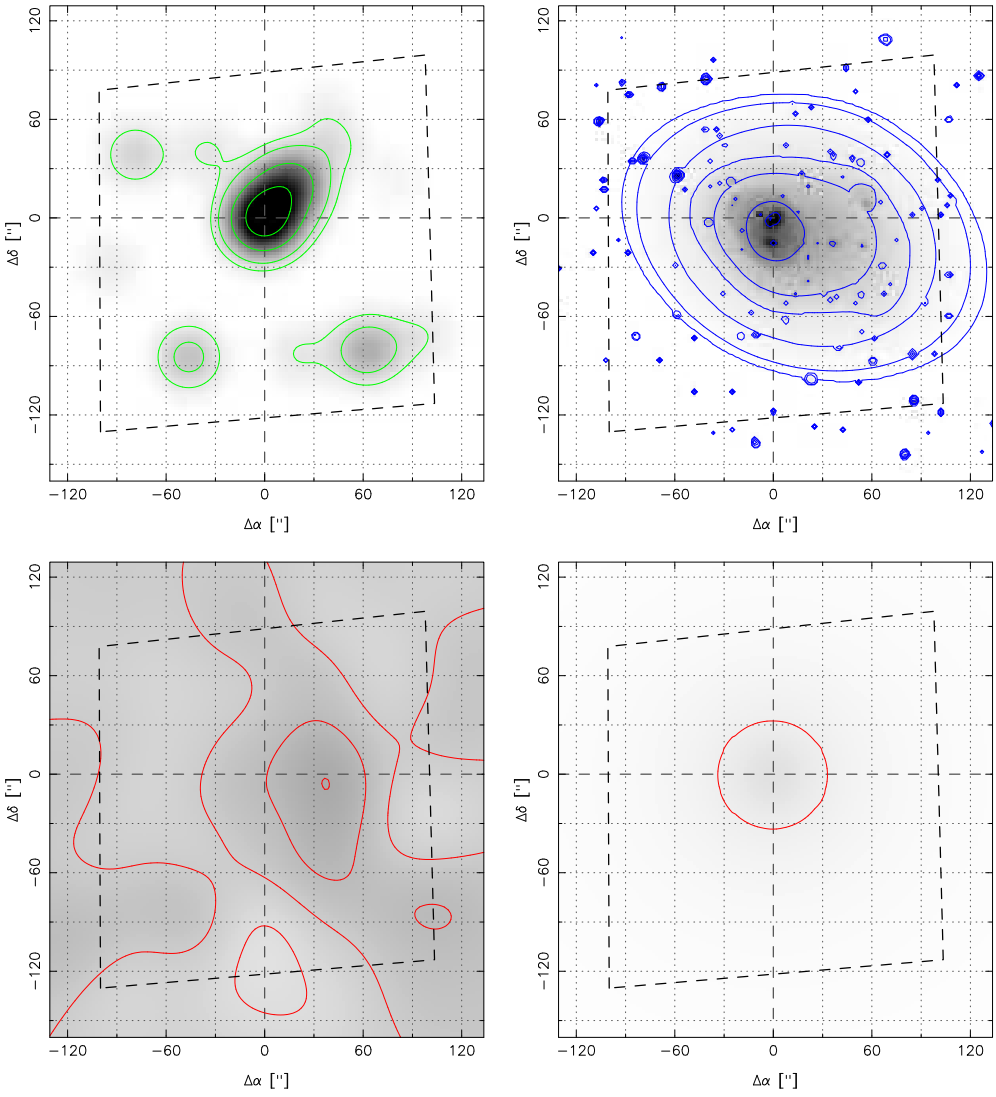

Figure A.20: *A*2187

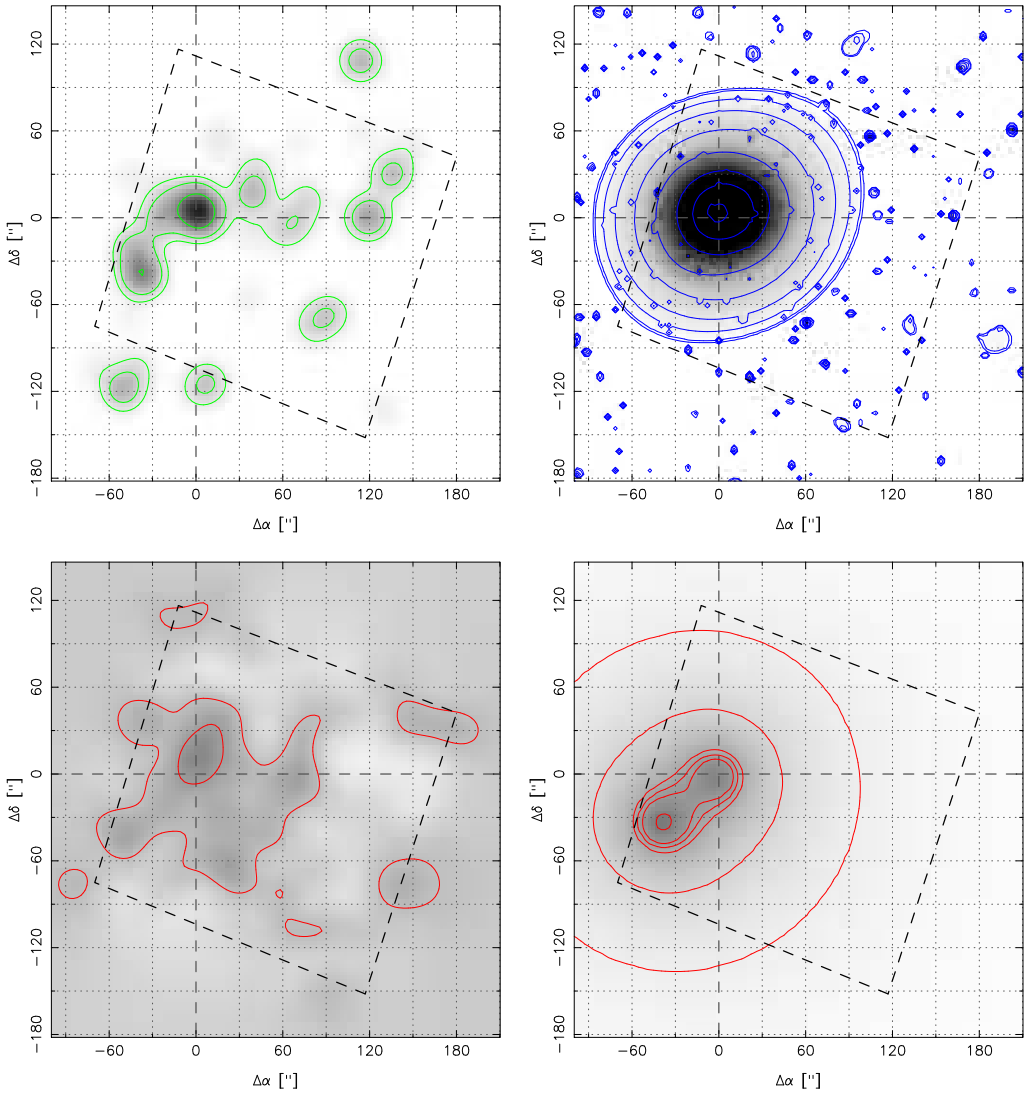

Figure A.21: *A*2537